Sustainable Devices by Design:

Thermal- and Plasma-Enabled Nanofabrication of Hierarchical Carbon Nanostructures for Bioelectronics and Supercapacitors

A thesis submitted in fulfillment of requirements for the degree of

Doctor of Philosophy

Shafique Pineda

Complex Systems, School of Physics, Faculty of Science, The University of Sydney, NSW 2006, Australia

January 2017

Table of Contents

Acknowledgements

Over the past 3 years, I have had the wonderful opportunity to work, play, and learn, alongside the most inspirational, generous, supportive, and dedicated of all individuals.

First and foremost, I sincerely thank my principal supervisor, Prof. Kostya (Ken) Ostrikov, associate supervisor, Dr. Zhao Jun Han, and auxiliary supervisor, Dr. Oliver Warschkow, for their advice, guidance, inspiration and life-long wisdom.

For the close-knit friendship, wonderful experiences, tumultuous challenges and great successes we had the opportunity to share, I truly thank Dong Han (Michael) Seo, Zhao Jun Han, and Kostya (Ken) Ostrikov, Samuel Yick, Fabricio Frizera Borghi, Timothy van der Laan, Jinghua Fang, Jungmi Hong, Hunkwan Park and Adrian Murdock.

For the countless engaging games, memorable goals, misses, and great sportsmanship, I thank my fellow soccer comrades, Bakir B., Bruce K., Christophe C., Charles L., Cibby P., Eugene T., Fernando D., Hunkwan P., James C., Jason L., Khaled C., Louis M., Malcolm L., Max M., Michael S., Mitch F., Nick G., Ning Z., Santy C., Steven W., Stephen H., Tony R., Yabai H..

For the fruitful collaborations, I would like to thank fellow researchers from CSIRO, The University of Technology Sydney (UTS), Victoria University (VU), Queensland University of Technology (QUT), and the National Measurement Institute (NMI).

Further, I would like to thank the team and group leaders at CSIRO, Kostya (Ken) Ostrikov, Katie Green, Avi Bendavid, Scott Martin, Cathy Foley and Anthony (Tony) Murphy, fellow close friends from Singapore, and The University of Sydney, for their generous support and encouragement throughout my studentship.

Additionally, I would like to acknowledge the support of the Australian Postgraduate Award (APA) scholarship, by The University of Sydney, the CSIRO's Office of the Chief Executive (OCE) Top-Up scholarship, and CSIRO's Manufacturing Flagship.

To fellow Musketeers, "one for all, and all for one"! Thank you for your life-long inspiration, guidance, and camaraderie.

Finally, and above all, I would like to thank my family, my parents, my sister, and Coco, for their ever kind and loving support.

Abstract

Graphene is promising to enable diverse technological advancements. However, major technical challenges arise in the sustainable fabrication and its practical integration as active functional materials. This thesis aims to exemplify how thermal- and plasma-based techniques may be designed and implemented to enable, enhance, and tailor the synthesis of hierarchical graphene nanostructures, and to streamline their integration for applications in bioelectronics and energy storage devices.

First and foremost, an ambient-air thermal process is designed and demonstrated, which enables graphene synthesis in a single-step, and is exemplified to be energy efficient (*i.e.,* rapid, reduced temperature), resource-efficient, green (*i.e.*, reforming renewable biomass precursors), low-cost, integration-friendly, and scalable. The graphene films show good and homogeneous physicochemical properties. On average, we observe an optical transmission of ~93.9%, a sheet resistance of ~324 Ω/sq, Raman I_D/I_G ratio of 0.15–0.25 and I_{2D}/I_G ratio of 0.95–1.50, with polycrystalline domain sizes ranging 200–500 nm.

Subsequently, sustainable plasma-based techniques were designed to realize hierarchical graphene nanostructures, namely, graphene microislands (GMs) and vertically-oriented graphene nanosheets (VGNS). The growth of GMs and VGNS were tailored by the plasma process, and feature a unique combination of a high surface area, an open morphology, interconnected arrays of graphene sheets, and a high density of reactive edges. Consequently, this enables attractive physicochemical properties for bioelectronics and energy storage devices.

In the case of GMs, plasma enables its low-temperature (200 ^{o}C) and rapid growth, and a water-mediated transfer onto arbitrary substrates. Also, plasma induces active surface functional groups on GMs, which facilitate its direct utilization in bioelectronics. Notably, GMs exhibit a biocompatibility of 80% cell viability with primary fibroblast lung cells after 5 days. The GMs were also assembled into an impedimetric genosensor with high sensitivity and selectivity. A dynamic sensing range of 1 pM to 1 nM is demonstrated, and a limit of quantification of 2.03 x 10^{-13} M is deduced, with selectivity to single-RNA-base mismatched sequences.

Further, plasma enables a single-step, low-temperature (450 ^{o}C) growth of VGNS, and its direct integration as an active material. VGNS are employed as binder-free supercapacitor electrodes, and demonstrate high specific capacitance up to 240 F/g at a scan rate of 5 mV/s, and 100% capacitance retention after 2,000 charge/discharge cycles. Also, we demonstrate that mass loading of VGNS can be increased by

regulating properties of the precursor material. By considering various precursors and respective plasma-matter interactions, the VGNS are demonstrated to achieve a high mass loading of 3.2 mg/cm^2, and a high areal capacitance of 0.46 F/cm^2.

To this end, a set of thermal- and plasma-based techniques have been designed, developed, and implemented, to realize sustainable methodologies for nanoassembly. Importantly, these techniques may be adapted, tailored, and broadly incorporated, to effectively harness the unique functional properties of graphene, and a host of other hierarchical nanomaterials. Together, these concepts may pave the realization of next-generation nanotechnologies which hold promise for a sustainable future.

Publications

[1] **Seo D.H.***, **Pineda S.***, Fang J.H., Gozukara Y., Yick S., Bendavid A., Lam S.K.H., Murdock A.T., Murphy A.B., Han Z.J., Ostrikov K., Single-Step Ambient-Air Synthesis of Graphene from Renewable Precursors and its Application as an Electrochemical Genosensor, *Nature Communications*, 2017**,** 8 (14217) (***** = equal contribution).

[2] **Pineda S.***, **Borghi F.F.***, Seo D.H., Yick S., Lawn M., van der Laan T., Han Z.J., Ostrikov K., Multifunctional Graphene Micro-islands: Low-Temperature Plasma-Enabled Synthesis and Facile Integration for Biosensing and Bioengineering Applications, *Biosensors and Bioelectronics*, 2017, 89, 437-443. (***** = equal contribution).

[3] Han Z.J., Bo Z., Seo D.H., **Pineda S.**, Wang Y., Yang H.Y., Ostrikov K., High Pseudocapacitive Performance of MnO_2 Nanowires on Recyclable Electrodes, *ChemSusChem*, 2016, 9, 1020 – 1026.

[4] **Seo D.H.*, Pineda S.***, Yick S., Han Z.J., Bell J., Ostrikov K., Plasma-Enabled Sustainble Elemental Lifecycles: Honeycomb-derived Graphenes for Next-Generation Biosensors and Supercapacitors, *Green Chemistry*, 2015, 17, 2164 – 2171 (***** = equal contribution).

[5] Seo D.H.*****,** Yick S.*, **Pineda S.**, Su D., Wang G., Han Z.J., Ostrikov K., Single-Step Plasma-Enabled Reforming of Natural Precursors into Vertical Graphene Electrodes with High Areal Capacitance, *ACS Sustainable Chemistry & Engineering*, 2015, 3 (3), 544 – 551 (***** = equal contribution).

[6] **Pineda S.**, Han Z.J., Ostrikov K., Plasma-Enabled Carbon Nanostructures for Early Diagnosis of Neurodegenerative Diseases, Materials, 2014, 7(7), 4896 – 4929.

Disclaimer

The manuscripts presented in this thesis are a revised version of the as-published copy. Non-relevant contents such as page numbers, keywords, corresponding authors, and financial interests are removed. All respective contributions and acknowledgements are presented in the chapter preambles.

Statement of Student Contribution

I certify that this thesis contains work carried out by myself as noted in the chapter preambles. All the assistance received in preparing this thesis and sources have been acknowledged. In addition to the statements above, in cases where I am not the corresponding author of a published item, permission to include the published material has been granted by the corresponding author. This thesis has not been submitted for any degree or other purposes.

Signed … 

Date …9 January 2017…

Shafique Pineda

As supervisor for the candidature upon which this thesis is based, I can confirm that the authorship attribution statements above are correct.

Signed 

Date …9 January 2017…

Kostya (Ken) Ostrikov

1

Literature Review

"Equipped with his five senses, man explores the universe around him and calls the adventure Science."

– Edwin Hubble, 1929.

1.1. Graphene

Graphene, a single atomic layer of graphitic carbon (**Fig. 1**) [1], has garnered intense attention owing to its extraordinary properties, which make it promising for a wide range of technological applications [2,3]. This one-atom-thick sheet of carbon uniquely combines extreme mechanical strength and flexibility [4], exceptionally high electronic [5] and thermal conductivities [6], as well as many other excellent physicochemical properties [7-9].

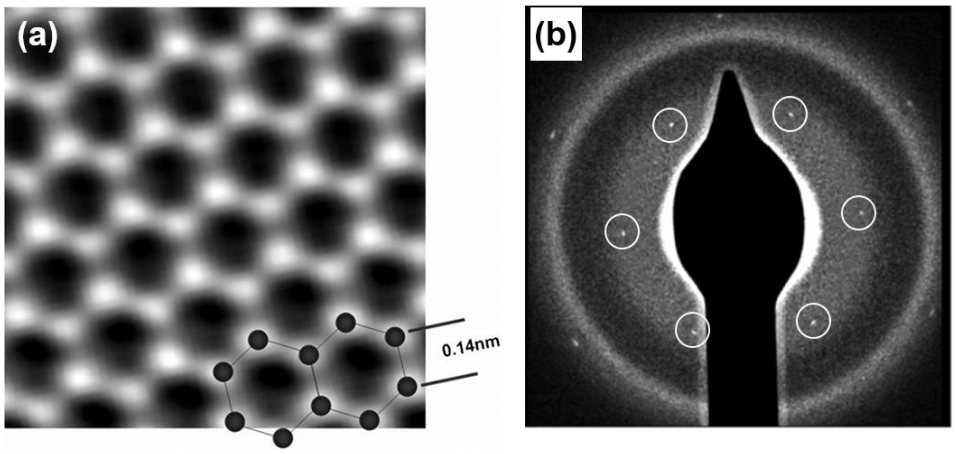

Figure 1 | Structural and crystallographic characterization of graphene. (**a**) Atomic-resolution image of the graphene lattice obtained by transmission electron microscopy. Bright spots correspond to the location of carbon atoms. Reproduced from [10], Copyright of the Royal

Society of Chemistry, 2009. (**b**) Selected area electron diffraction pattern of the graphene lattice, confirming the crystalline structure of graphene, as shown by the symmetric diffraction points (circled bright spots) in the image. Reproduced from [11], Copyright of Macmillan Publishers Limited, 2011.

Graphene has been discussed theoretically since the 1940s [12]. However, it took more than six decades before a few sheets of micrometer-sized graphene flakes were experimentally obtained (**Fig. 2**) [1].

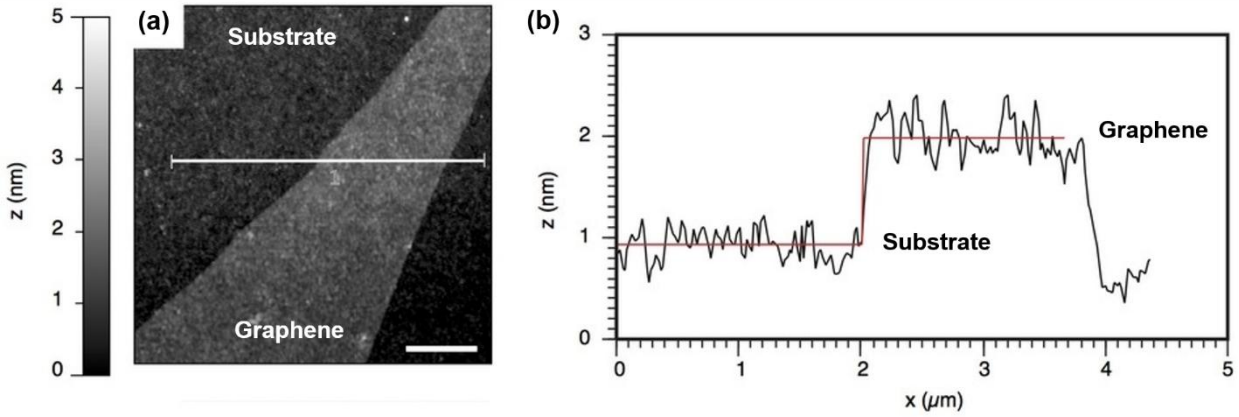

Figure 2 | Topography of graphene. (**a**) Atomic force microscopy imaging of an exfoliated flake of monolayer graphene. (**b**) Step height along the white line shown on the height (z) profile is 1.0 ± 0.3 nm. Scale bar represents 1 μm. Reproduced from [13], Copyright of Macmillan Publishers Limited, 2015.

Indeed, twelve years have progressed since graphene was first isolated from graphite by micro-mechanical cleavage (*i.e.*, the “scotch tape” method). Graphene is now synthesized by a host of versatile techniques (**Section 1.2**) [14]. These developments enable graphene nanostructures with tailored morphology and functionalities [15,16], and in instances, bulk production by the hundreds of tons, and thousands of square meters [17].

1.2. Graphene Synthesis

Small sheets and large-area thin films are the two major forms of graphene suited for diverse applications. Small graphene sheets can be used in composites and functional coatings [18], conductive inks, batteries and supercapacitors [19]. Large-area graphene

films can be used as transparent electrodes in photovoltaic devices [20], next-generation integrated circuits and optoelectronics [21], such as flexible and wearable devices [22].

Techniques for the synthesis of graphene can be classified into three categories – liquid phase exfoliation (LPE) (**Section 1.2.1**), thermal chemical vapor deposition (CVD) (**Section 1.2.2**), and plasma-enhanced chemical vapor deposition (PECVD) (**Section 1.2.3**). Notably in this thesis, original contributions on the synthesis and application of graphene derived by thermal- and plasma-based methods are demonstrated.

1.2.1. Liquid Phase Exfoliation (LPE)

Graphene flakes can be produced by exfoliation of graphite via chemical wet dispersion, followed by ultrasonication in water [23,24] and organic solvents [25,26] (**Fig. 3**). Generally, this process involves three steps: (i) dispersion in a solvent, (ii) exfoliation, and (iii) centrifugation to collect the graphene flakes. Indeed, the technique of exfoliation is recognized as a central component in the LPE process, which determines the properties of the synthesized graphene (*e.g.*, flake size, morphology, *etc.*).

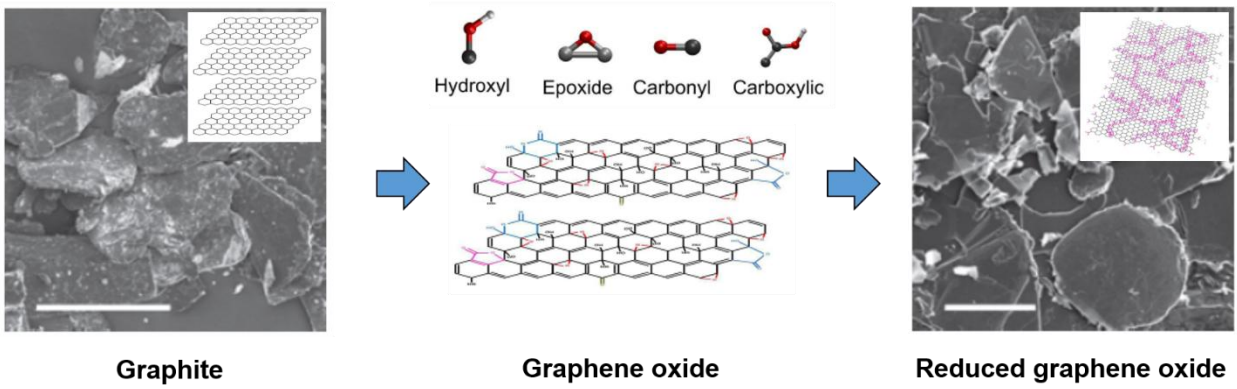

Figure 3 | Chemical exfoliation of graphite to form graphene powder (*i.e.,* Reduced graphene oxide). Scanning electron microscopy (SEM) images characterize the breakdown of large graphitic flakes. Graphene oxide flakes have the basal plane functionalized with epoxy and hydroxyl groups, both above and below it, and the edges with a variety of functional groups. This makes GO sheets defective. A partial restoration of the lattice defects is obtainable by chemical reduction. Scale bar represents 500 μm. Schematic illustrations reproduced from [27],

From the numerous advancements in graphite exfoliation (*i.e.*, intercalation, thermal expansion, oxidation-reduction, *etc.*), three dominant techniques have emerged – namely, chemical exfoliation by Hummer's method [28,29], liquid phase shear exfoliation (**Fig. 4**) [30], and electrochemical exfoliation (**Fig. 5**) [31].

In Hummer's method, a combination of strong oxidizing agents (*i.e.*, H_2SO_4, $NaNO_3$ and $KMnO_4$) is utilized to yield graphene oxide [28,29]. This conversion progresses in three stages. Firstly, graphite is exposed to an acidic medium over several days, where it undergoes intercalation with HSO_4^- / H_2SO_4 ions and molecules. Subsequently, the oxidizing agents diffuse into the intercalated graphite lattice. Finally, upon exposure to water, the covalent sulfates in the graphitic interlayers undergo hydrolysis, and graphene oxide is produced [32].

Secondly, dispersions of graphene flakes can be produced based on the shear mixing of graphite (**Fig. 4a**) [30,33]. During rotation, the shear mixer acts as a pump and pulls both liquid and solids into the mixing head. Subsequently, centrifugal forces direct the mixture towards the edge of the rotor/stator (**Fig. 4b**). Here, intense shear forces are generated and graphite is exfoliated. Finally, the processed mixture passes through the perforations in the stator, and into the main volume of the liquid. This enables the exfoliation of graphite and the bulk production of dispersed graphene platelets (**Fig. 4c**).

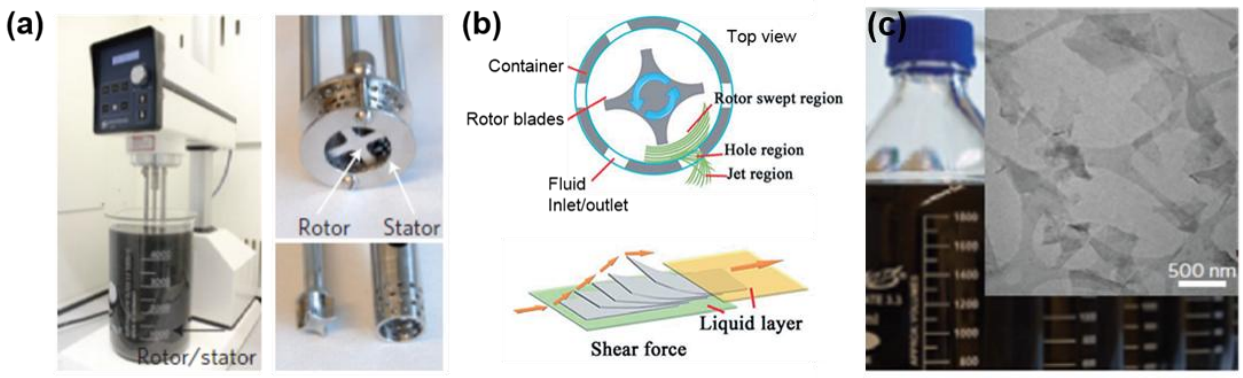

Figure 4 | Shear exfoliation of graphite. (**a**) Silverson model L5M high-shear mixer with mixing head in a 5 L beaker of dispersion containing graphitic flakes. Close-up view of the

mixing head showing the rotor and stator elements. (**b**) Schematic cross-section of the shear exfoliation setup. (**c**) Graphene dispersions in NMP solvent produced by shear exfoliation. Wide-field TEM showing the dispersed graphene flakes (inset). Reproduced from [30], Copyright of Macmillan Publishers Limited, 2014.

Finally, the electrochemical exfoliation technique utilizes electromotive forces, in order to facilitate the breakdown of graphite into a dispersion of graphene oxide [31,34]. A schematic of the electrochemical setup is illustrated in **Fig. 5a**. Pyrolytic graphite foil is employed as the working electrode, and as source of graphene for electrochemical exfoliation [35]. A Pt wire is chosen as the ground electrode. Typically, H_2SO_4 intercalants are introduced in the electrolyte [36]. At first, a low bias ~ +1V is applied to introduce the intercalation of (negatively charged) SO_4^{2-} ions into the grain boundary of graphite. Then, a high bias of ~+10V is applied, and graphite is observed to expand (**Fig. 5b – c**), and dissociate into small flakes which spread over the surface of the solution. These exfoliated graphene sheets can be collected using filtration and re-dispersed in organic solvents (*e.g.*, NMP) (**Fig. 5d – e**).

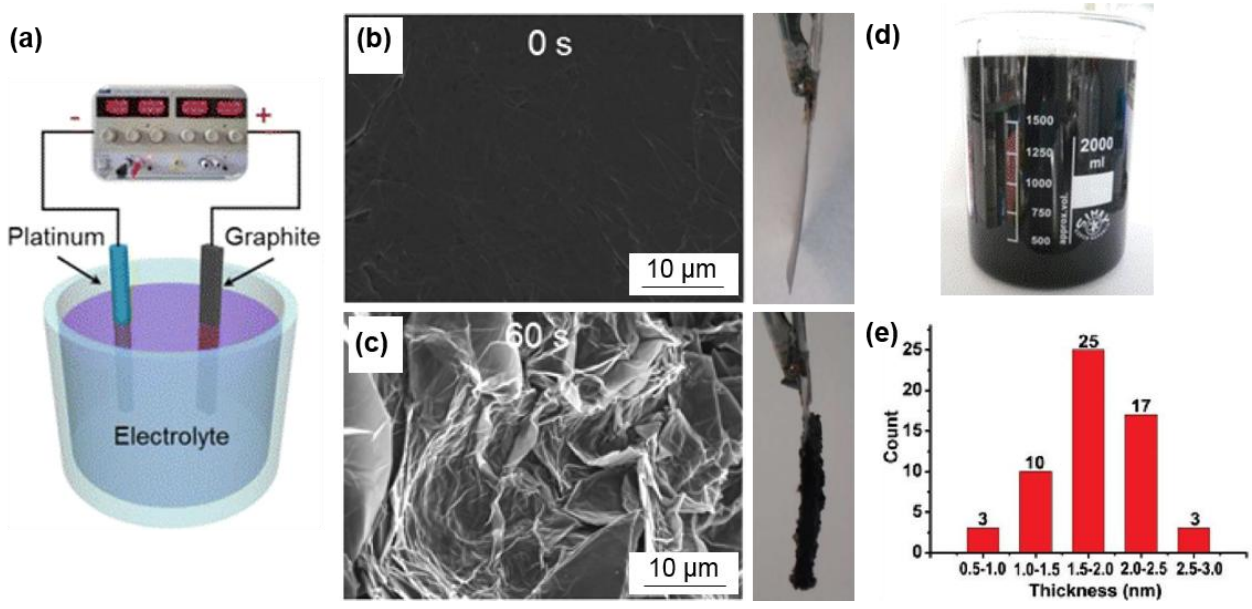

Figure 5 | Electrochemical exfoliation of graphite. (**a**) Schematic of setup. The Graphite electrode with SEM characterization of its surface (**b**) before and (**c**) after applying a +10V bias voltage for 60s. (**d**) Graphene dispersion in DMF. (**e**) Distribution in thicknesses of the electrochemically exfoliated graphene sheets. Panels (**a**) to (**d**) reproduced from [31], Copyright

of the American Chemical Society, 2014. Panel (**e**) reproduced from [34], Copyright of the American Chemical Society, 2011.

These top-down chemical approaches offer bulk production by the volume. Further, they are appealing as the as-obtained graphene sheets form colloidal dispersions in their respective solvents (**Fig. 6a**) [37]. This enables their manipulation by various processes, which include mixing, casting, impregnation, electro-spinning, or functionalization, to produce various morphologies of graphene-based materials and composites, such as fibers (**Fig. 6b**) [38], crumpled porous sheets (**Fig. 6c**) [39], and flexible conductive films (**Fig. 6d**) [40].

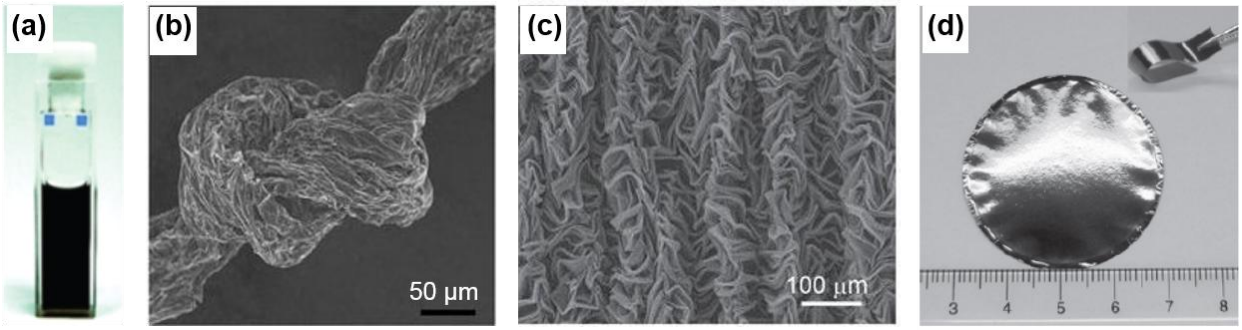

Figure 6 | Graphene dispersions post-processed into various forms. (**a**) Graphene ink produced by liquid phase exfoliation of graphite. Reproduced from [41], Copyright of the American Chemical Society, 2012. (**b**) Electrospinning of graphene fiber into a knot. Reproduced from [38], Copyright of Macmillan Publishers Limited, 2011. (**c**) Mechanically strained graphene can produce crumpled morphology with high surface area. Reproduced from [39], Copyright of Macmillan Publishers Limited, 2014. (**d**) Graphene paper prepared by vacuum filtration. Reproduced from [40], Copyright of Macmillan Publishers Limited, 2008.

However, chemical approaches for graphene synthesis inherit several drawbacks. Firstly, concentrated acids and volatile solvents are heavily used. These aggressive chemical processes disrupt the sp^2-bonded network of the graphene, and introduce hydroxyl and epoxide groups in the basal plane, and various other carboxylic and carbonyl groups to the edges [42]. This results in GO flakes being defective [43], insulating [44], and contaminated with metal impurities [45].

Secondly, chemical approaches to prepare graphene sheets are multi-staged and time consuming [46]. For instance, the LPE of graphite requires several days, and the subsequent reduction of GO sheets into graphene involves harmful reducing agents (*e.g.*, hydrazine) and surfactants [47], or additional high temperature environments to recover the graphitic structure [48,49]. Not only are graphene flakes prone to irreversible agglomeration (*i.e.*, through van der Waals interactions) [40], but also, non-conductive polymer binders are typically required to integrate the graphene flakes as functional materials for various applications [50]. In numerous instances, these result in a significant compromise in device performances [51-53]. These comparative advantages and disadvantages of chemical-based approaches for the synthesis of graphene are also summarized in **Table 1**.

1.3.2. Thermal Chemical Vapor Deposition (CVD)

The principle of chemical vapor deposition (CVD) involves the activation and heterogeneous reaction of gaseous precursors, resulting in the deposition of stable thin films on a growth substrate with suitable physical properties (*i.e.*, catalytic ability, carbon solubility, *etc.*).

In thermal CVD synthesis of graphene, a transition metal catalyst (*e.g.*, Cu, Ni, *etc.*) is employed to enable the growth of graphene films [54-56]. A schematic for the thermal CVD setup is illustrated in **Fig. 7a**. The catalytic growth substrate is typically located downstream and within the heating zone. In general, precursor gases (*e.g.*, CH_4, H_2, O_2, Ar) are firstly introduced into the reaction chamber (*i.e.*, quartz tube) [57]. Subsequently, these gases undergo high-temperature annealing (~900 – 1100 ^{o}C) [54], and the carbon precursor thermally dissociates into fragments of hydrocarbons and carbons (*e.g.*, C_xH_y, C-C) [58], which then reform on the catalyst surface into graphene films. Once the annealing stage is complete, the catalyst is rapidly quenched in order to terminate further graphene growth (**Fig. 7b**).

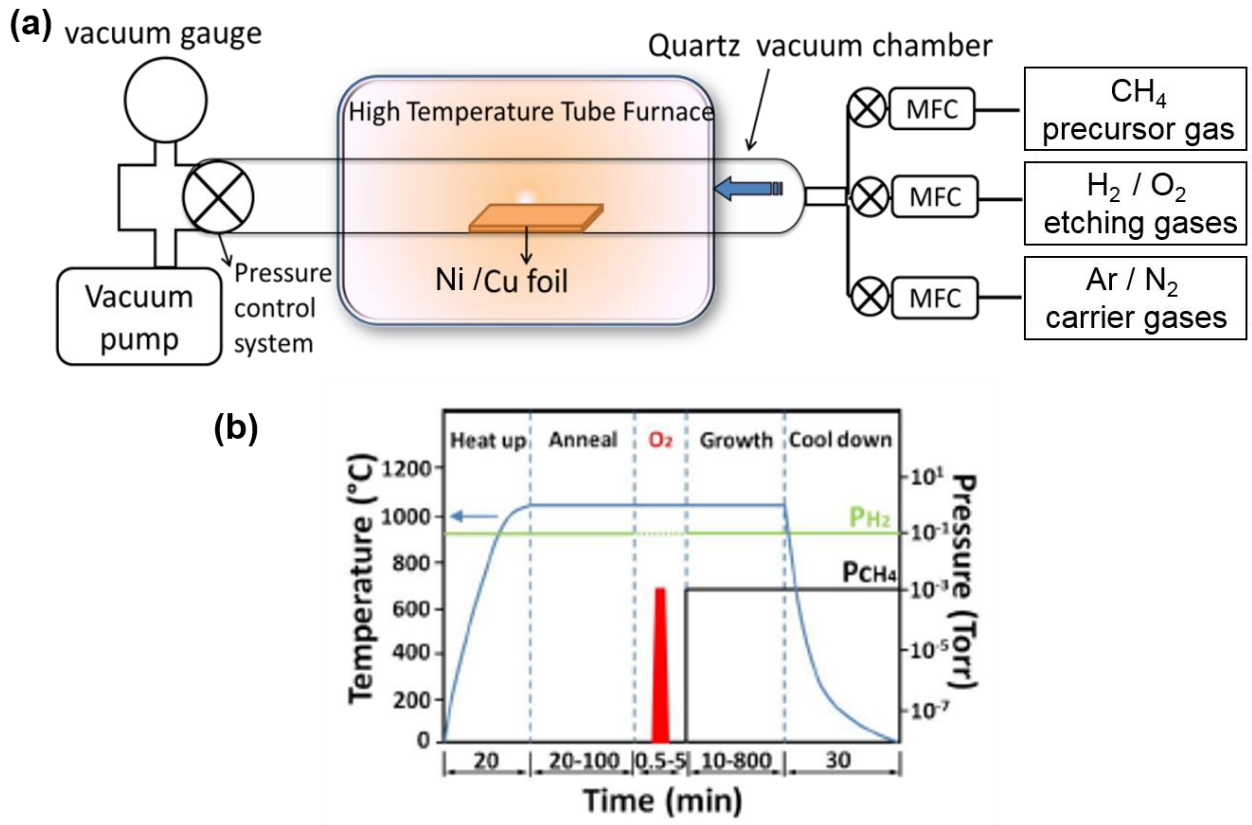

Figure 7 | Thermal chemical vapor deposition (CVD) for the synthesis of graphene thin films. (**a**) Schematic of a typical split-tube thermal furnace for graphene synthesis. The feedstock gases are fed into the heating zone, which decompose to form graphene on the Ni/Cu catalyst substrates. (**b**) Temperature and pressure profiles present in the quartz tube during the thermal CVD process. Reproduced from [57], Copyright of AAAS, 2013.

The detailed mechanism of graphene growth by CVD involves the adsorption (dissolution) of carbon on (into) the catalyst, nucleation, crystal growth and saturation, and finally termination [59-61]. A schematic of the kinetic processes are outlined in **Fig. 8** [62]. Catalyst substrates of Ni and Cu are commonly utilized in the CVD of graphene. The growth of graphene proceeds differently in Cu and Ni, notably, due to respective distinctions in carbon solubility [60], reactivity with H_2, and catalytic ability for the dehydrogenation of hydrocarbons [63,64].

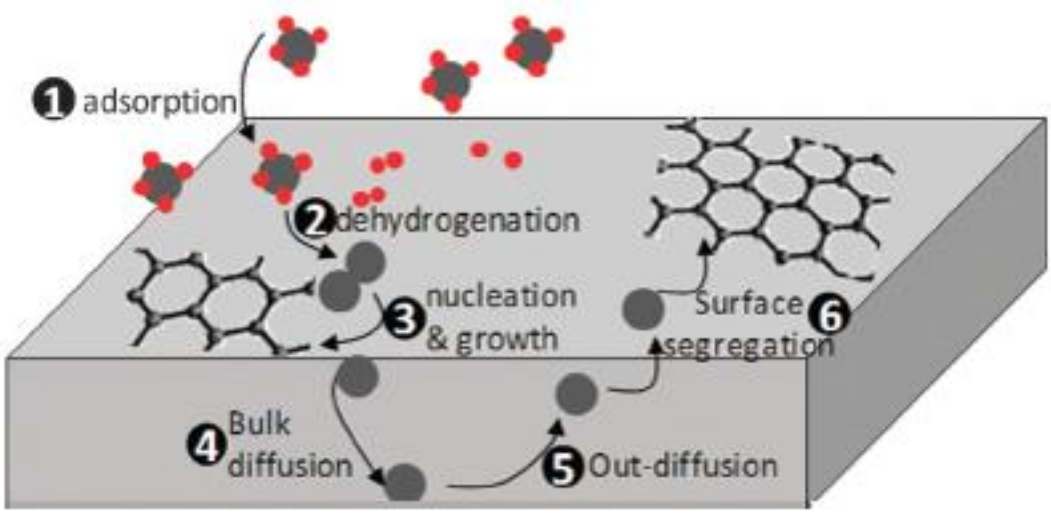

Figure 8 | Illustration of kinetic processes involved in graphene formation. Reproduced from [62], Copyright of The Royal Society of Chemistry, 2011.

In the case of Cu, graphene formation is promoted by surface adsorption of hydrocarbon fragments (reaction 1), followed by dehydrogenation (reaction 2), nucleation, and the diffusion of carbon atoms on the catalyst surface leading to the growth of graphene (reaction 3) [59,65]. The hydrogen promotes the activation of surface bound carbon for graphene growth, and also functions as an etching reagent, which controls the size and morphology of the graphene domains [66]. In the case of Ni, due to its higher carbon solubility than Cu, additional processes including the diffusion of atomic carbon into the bulk (reaction 4), its subsequent precipitation (reaction 5) and surface segregation (reaction 6), contribute to the growth of graphene layers [60,67,68].

The CVD growth of graphene is strongly mediated by the physical properties of the catalyst substrate and the reaction environment. For instance, graphene growth is highly sensitive to the crystallographic orientation of the catalyst [69], its thickness [70], surface chemistry (*e.g.*, degree of oxidation) [57], and surface morphology (*e.g.,* roughness) [71]. Likewise, the CVD environment directly influences the properties of the fabricated graphene [72-74]. Several CVD parameters which affect the quality of graphene (*i.e.*, thickness, defect content, grain size) include, the relative concentrations of feedstock gases [75], the precursor species [76,77], reaction pressure and gas-phase dynamics [78], deposition time [79], and growth temperature [80,81].

For instance, the synthesized graphene can range from large mm-sized single crystals to polycrystalline films (**Fig. 9**) [56,82]. In general, large graphene grains are possible by utilizing catalyst substrates with high purity, large crystal domains, and specific preferred orientations, combined with a long annealing duration and high temperatures during CVD.

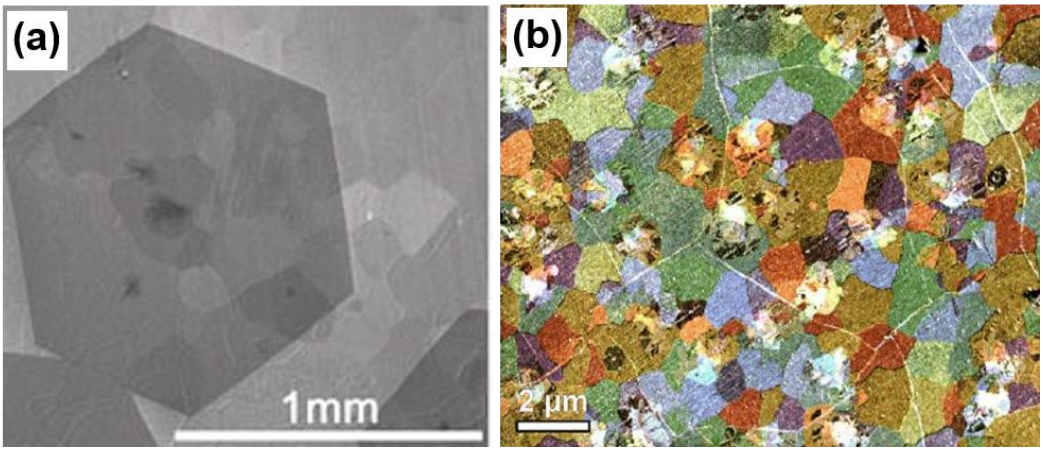

Figure 9 | Thermal CVD-produced graphene films of varying morphologies. Dark-field TEM characterizes the formation of (**a**) large millimeter-sized single crystals of graphene, to (**b**) polycrystalline films of graphene (variation in color corresponds to the different crystal orientation and hence grains). Left-sided panel reproduced from [56], Copyright of Macmillan Publishers Limited, 2012. Right-sided panel reproduced from [82], Copyright of Macmillan Publishers Limited, 2011.

Nevertheless, single-layer, defect-free, large-domain graphene is not always desired, especially for applications other than high-speed electronics (*e.g.*, water filtration, energy storage devices, sensors) [83-85]. In such cases, control of film properties such as the defect density, grain size, and thickness, are beneficial, and facilitate or enable specific performances.

Notably, disorder content in the film can be controlled by the ratio of feedstock gases [86]. An increase in the partial pressure ratios of O_2/H_2:CH_4 results in greater etching and hence introduces more defects in the graphene film. Conversely, an increase in the concentration of carbon precursor, combined with an increased annealing duration and

slower cooling rate, promotes further carbon segregation, nucleation, deposition, and aggregation, and the formation of multi-layer graphene films [87,88].

Upon the growth of graphene, it can be transferred onto arbitrary substrates by a process of polymer-assisted transfer (**Fig. 10**) [55,89,90]. First, poly(methyl methacrylate) (PMMA) is spin-coated on the surface of graphene. This adhesive polymer layer provides mechanical support for the atomically-thin graphene film. Subsequently, the graphene/PMMA film is de-coupled from the catalyst substrate by chemical etching (*i.e.*, immersion in $FeCl_3$). At this stage, the free-standing film of graphene/PMMA is transferred onto the target substrate, and the PMMA layer is dissolved by acetone.

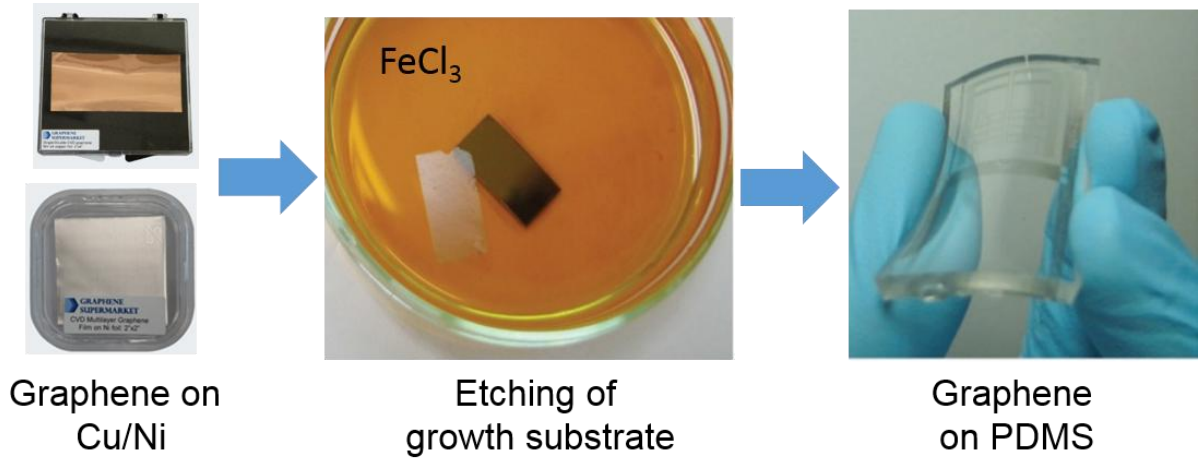

Figure 10 | Graphene as-grown on the catalyst foils can be transferred onto arbitrary substrates by a process of polymer-assisted transfer and chemical etching. Reproduced from [55], Copyright of Macmillan Publishers Limited, 2009.

The thermal CVD growth of graphene can be scaled into roll-based processes (**Fig.11**) [91-93]. For instance, graphene can be firstly fabricated on a large-area Cu film in a wide-diameter tubular furnace. Then, the graphene-deposited Cu film can be processed by a thermal roll-based system, which aids the transfer of graphene onto a desired substrate. A heated rolling interface facilitates the adhesion of the supporting polymer layer onto the graphene surface. Subsequently, the polymer-coated film is immersed into chemical etchants to promote the separation between the graphene and Cu growth substrate. Finally, the graphene film undergoes dry transfer-printing on the target

substrate. This roll-based approach has demonstrated the capability to produce graphene films up to 30-inches wide, while retaining homogeneously good optoelectronic properties. As a proof of concept, these large-area graphene films have been integrated for use as transparent touch panels [93].

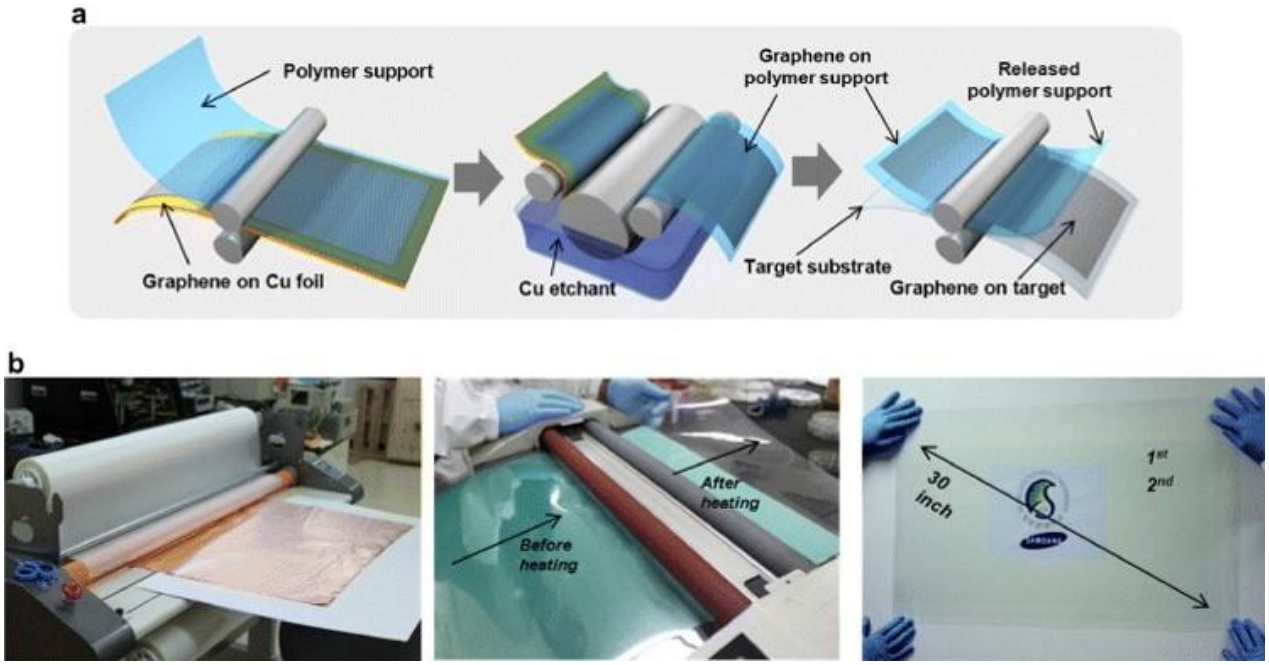

Figure 11 | Large-scale CVD fabrication of graphene. (**a**) Schematic and (**b**) respective photographs of the roll-based production of graphene films grown on Cu foil. Reproduced from [93], Copyright of Macmillan Publishers Limited, 2010.

To this end, thermal-based techniques are widely employed, and enable the controlled fabrication of high-quality, large-area, and homogenous thin films of graphene. However, these approaches for graphene synthesis inherit several drawbacks. Firstly, CVD is an energy-intensive and resource-consuming process. In particular, as CVD relies on weak neutral gas reactions, this necessitates the high temperature annealing of feedstock gases, in a continuous large-volume flow, over a prolonged duration [54,55]. These measures are required to provide sufficient energy to dissociate the hydrocarbon precursors, promote the nucleation and diffusion of carbon adatoms on the catalyst surface, and the assembly of graphene nanostructures.

Secondly, CVD is a multi-staged process. This arises from the growth dynamics of graphene, which are highly sensitive to the physicochemical properties of the catalyst substrate and the reaction environment. For instance, the catalyst growth substrate is typically required to undergo a series of pre-treatment steps [94,95]. These initiatives aid to remove surface-bound impurities and the native oxide layer, while assisting to reduce the surface roughness [96-98]. Notably, such surface artifacts have been demonstrated to compromise the growth of uniform graphene films [71,75]. Further, the CVD process often involves a sequence of controlled growth stages, which carefully modulates the reaction pressure and flow rates of precursor gases. These measures are critical in order to maintain optimal conditions for graphene growth at all phases (*i.e.*, precursor breakdown and diffusion, carbon nucleation, surface aggregation, termination, *etc.*), and to promote reproducibility in graphene quality between batches.

Lastly, graphene grown by CVD requires a series of post-treatment processes (*i.e.*, film transfer) for its integration in diverse applications. This arises from limitations of available catalyst substrates (*i.e.*, Cu, Ni) which suit to facilitate the controlled growth of good quality graphene. Further, these transfer processes are resource-consuming and damaging to the graphene. In the instance of wet-transfer, a polymer-supported graphene film is separated by dissolving the catalyst substrate in chemical etchants (*e.g.*, $FeCl_3$). The transfer process not only induces the likelihood of cracks and deformations in the graphene film [89], but also, it leaves contaminants (*e.g.*, Fe nanoparticles, aggregates, and polymer residues) firmly embedded on the graphene surface [99,100]. Indeed, these unavoidable by-products are detrimental to the quality and functionality of the graphene films (*e.g.*, reduced conductivity, increased toxicity, *etc.*). These comparative advantages and disadvantages of thermal-based approaches for the synthesis of graphene are also summarized in **Table 1**.

1.3.3. Plasma-Enabled Synthesis of Graphene

Graphene can also be synthesized by plasma-enhanced chemical vapor deposition (PECVD). In the plasma process, interactions are governed by strong Coulombic interactions between ions and charged particles [101]. Thus, plasma-based interactions are highly reactive and dynamic, and occur on a faster time scale than neutral gas

reactions present in conventional thermal CVD [102]. This enables the synthesis of graphene within a short duration (<10 mins), and at low temperatures of 200 – 450 ^{o}C [103-105].

A schematic for the PECVD setup is illustrated in (**Fig. 12a**) [106]. Precursor gases (*i.e.*, CH_4, H_2, Ar) are introduced into the reaction chamber, and an inductively-coupled RF plasma is generated. The growth substrate is typically located downstream and within the plasma generation zone, and no supplemental substrate heating is required. The mechanism of PECVD begins with the activation of heterogeneous chemical reactions between the gaseous precursors in the bulk of the plasma (**Fig. 12b**). Consequently, the precursor species undergo dissociation into building units of graphene (*e.g.*, C_xH_y, C-C). Subsequently, these building units are delivered to the substrate surface by plasma sheath effects, resulting in the formation of graphene nanostructures.

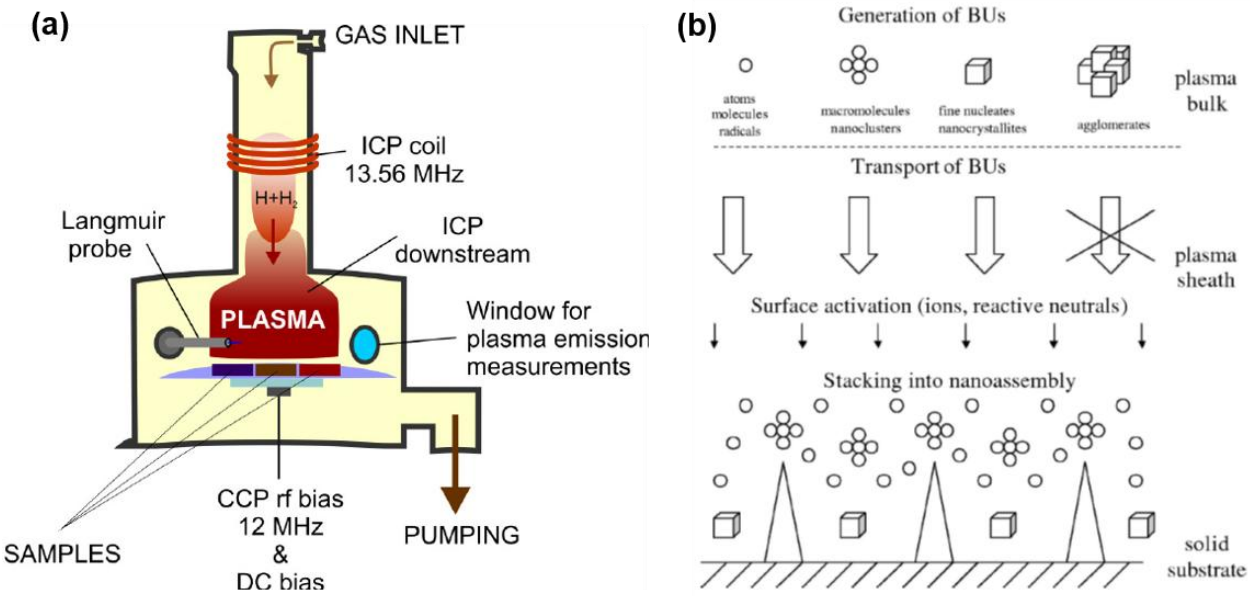

Figure 12 | Plasma nanoscience and plasma-enabled synthesis of graphene nanostructures. (**a**) Schematic of a typical inductively coupled plasma (ICP) system for graphene synthesis. Feedstock gases are fed into the reacting chamber, an RF plasma is generated, and graphene nanostructures are deposited. Reproduced from [106], Copyright of Elsevier, 2015. (**b**) Schematic of the reactive-plasma-based nanofabrication environment (building units denoted by "BU"). Reproduced from [101], Copyright of the American Physical Society, 2005.

Importantly, PECVD produces graphene nanostructures with a unique morphology, known to be vertically-oriented graphene nanosheets (VGNS) (**Fig. 13a**) [16]. VGNS feature a uniform and interconnected array of graphene sheets, arranged in an open and micro-porous structure (**Fig. 13b**) [107]. This is accompanied by thin reactive edge planes (**Fig. 13c**) [108], which extrude vertically from the growth substrate in a columnar arrangement with high aspect ratio (**Fig. 13d**) [109]. The basal planes of VGNS are comprised of thick graphitic sheets, and this tapers off to atomically-thin graphene sheets (~2 – 3 layers) at the edges (**Fig. 14**) [110,111].

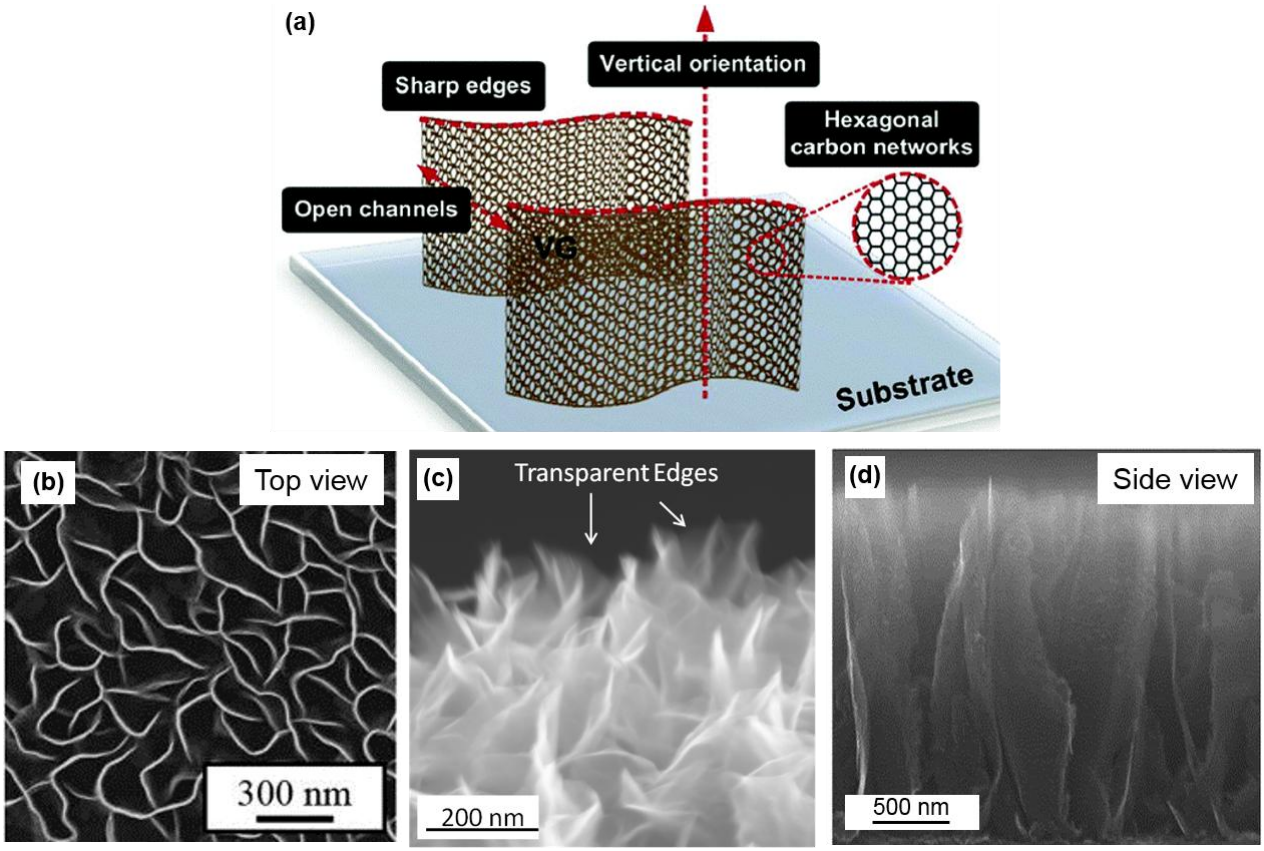

Figure 13 | Plasma-enhanced chemical vapor deposition (PECVD) enables the growth of vertically-aligned graphene nanostructures (VGNS). (**a**) Illustration of the unique morphology of VGNS, enabled by the PECVD growth process. Reproduced from [16], Copyright of the Royal Society of Chemistry, 2015. (**b**) SEM image shows the vertically-oriented and interconnected arrays of graphene nanosheets. Reproduced from [107], Copyright of AIP Publishing, 2014. (**c**) The VGNS feature thin and reactive exposed edges. Reproduced from [108], Copyright of the American Chemical Society, 2015. (**d**) Cross-sectional profile of VGNS shows a columnar

structure of high aspect ratio, which extrudes vertically from the growth substrate. Reproduced from [109], Copyright of the Royal Society of Chemistry, 2015.

The assembly of VGNS by PECVD involves the processes of nucleation, growth and saturation (*i.e.,* termination) of the free-standing vertically-aligned graphene structure [112]. Firstly, nucleation occurs at the mismatched and curved regions of the as-deposited graphitic layers at the basal plane. Subsequently, graphene growth is enabled by diffusion of carbon atoms to active sites on the surface, and further growth is limited by the rate of carbon attachment at these active sites. Notably, the termination of the open edges of the graphene lattice determines the eventual size of the graphene nanosheets. Finally, the size and curvature of the graphene nanosheets provide the necessary mechanical support for the vertical alignment, and the formation of VGNS.

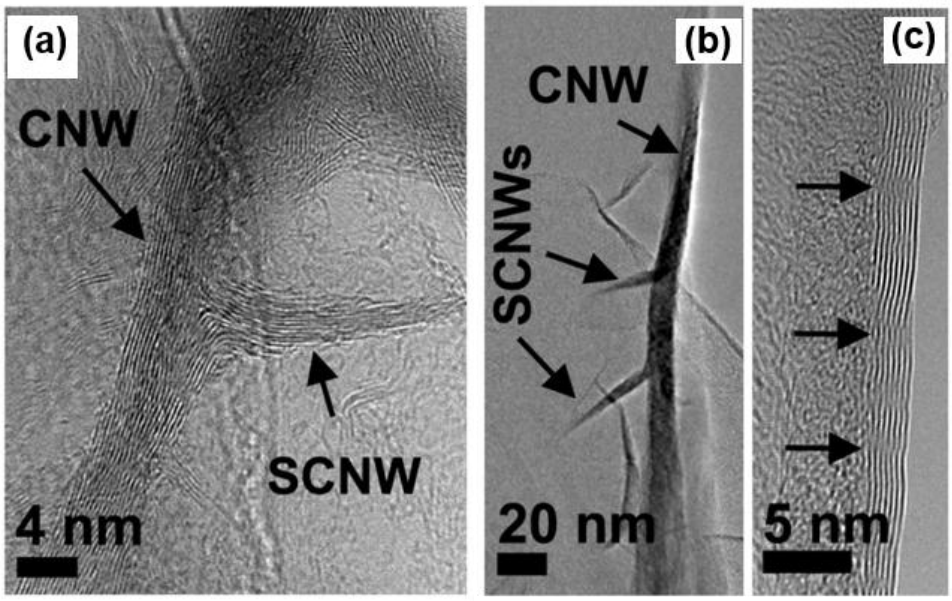

Figure 14 | HRTEM of VGNS (*i.e.*, also referred to as "CNW" and "SCNW" here, signifying carbon nanowalls and single carbon nanowall respectively). (**a**,**b**) The edges of VGNS are comprised of (**c**) few atomic layers of graphene. Reproduced from [110], Copyright Macmillan Publishers Limited, 2013.

In addition, the synthesis of VGNS by PECVD does not require any catalyst [113], and it is a substrate independent process [114]. For instance, VGNS can be fabricated on arbitrary conductive substrates, which are crystalline (*i.e.*, Si wafer) (**Fig. 15a**) [115],

amorphous (*i.e.*, carbon fiber) (**Fig. 15b**) [116], and macro-porous (*i.e.*, Ni foam) (**Fig. 15c**) [117].

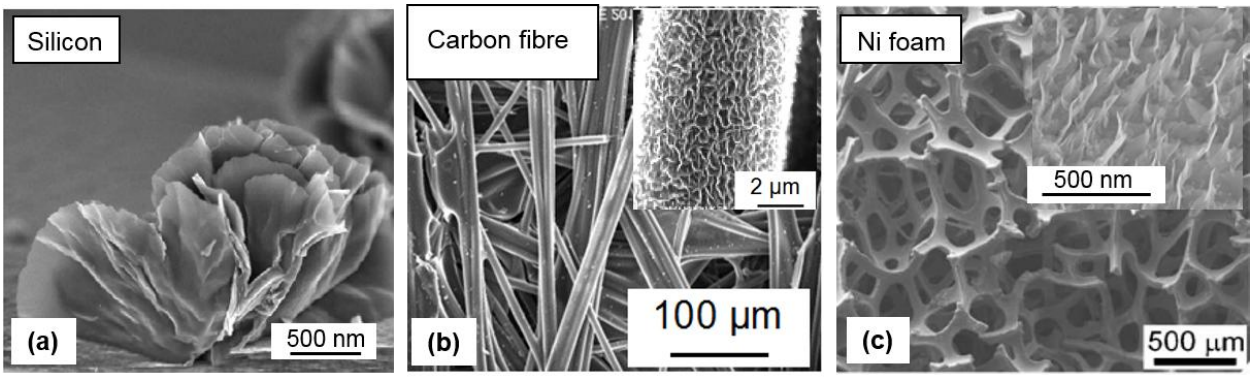

Figure 15 | VGNS grows on substrates that are conductive, crystalline or amorphous. SEM characterizations of VGNS on (**a**) silicon wafers, (**b**) amorphous carbon fiber, or (**c**) porous Ni foam. Panel (**a**) reproduced from [115] IOP Publishing, 2008. Panel (**b**) reproduced from [116], Copyright of IOP Publishing, 2013. Panel (**c**) reproduced from [117], Copyright of Wiley-VCH, 2013.

Indeed, the properties of graphene are dependent on its morphology [118-120]. The inherent reticular structure of VGNS enables a high surface area, good electrical conductivity (*i.e.*, interconnect graphene nanosheets), an ease of functionality (*i.e.*, thin reactive edges), while maintaining a good structural stability. Thus, VGNS is a promising functional material for electrochemical applications in energy storage devices and sensors.

The PECVD process enables an ease of control in the properties of the fabricated VGNS. Several plasma parameters which affect the quality of VGNS (*i.e.*, thickness, disorder content) include the partial pressure (*i.e.*, relative concentrations) of precursor gases, deposition time, and growth temperature. A shorter deposition time combined with a reduced ratio of CH_4:H_2 results in the formation of thinner graphene sheets, and overall, a decrease in the cross-sectional height of VGNS [121]. At higher growth temperatures (*e.g.*, 650 ^{o}C), the density of VGNS increases, and the disorder content in the graphene nanosheets are observed to decrease [122]. Notably, this can be

attributed to an increase in the kinetics of carbon and hydrocarbon radicals at the substrate surface and within the plasma sheath [123,124].

Plasma-based techniques for graphene synthesis feature a resource-efficient, versatile, and environmentally-benign approach. Unlike chemical- or thermal-based processes, PECVD facilitates a single-step, rapid, and low-temperature growth of graphene on diverse substrates. Further, PECVD does not produce hazardous by-products, nor does it utilize toxic reagents in the synthesis process. However, operation of the plasma deposition requires a low-pressure environment. This introduces challenges in the scale-up of the reaction chamber. In particular, increasing the volume of the plasma whilst maintaining its power results in a sharp increase in energy consumption. Thus, in order to utilize the plasma effectively, its respective purpose and plasma parameters should be carefully considered in the design of the fabrication process. For instance, the inherent advantages of PECVD may be effectively utilized in a batch-to-batch system, rather than a continuous roll-to-roll process for graphene production. These comparative advantages and disadvantages of plasma-based approaches for the synthesis of graphene are also summarized in **Table 1**.

Table 1 | Summary of the comparative advantages and disadvantages of chemical-, thermal-, and plasma-based approaches for the fabrication of graphene.

Metric	Chemical synthesis (Section 1.3.1)	Thermal synthesis (Section 1.3.2)	Plasma synthesis (Section 1.3.3)
Precursor materials	Graphite powder	Purified gases (*e.g.*, CH_4), carbon containing compounds (*i.e.*, biomass)	Purified gases (*e.g.*, CH_4), carbon containing compounds (*i.e.*, biomass)
Supplementary materials	Highly concentrated acids (*e.g.*, H_2SO_4, $NaNO_3$, $KMnO_4$), intercalating compounds and solvents (*e.g.*, NMP)	Etching gases (*e.g.*, H_2, O_2) Carrier gases (*e.g.*, Ar, N_2)	Etching gases (*e.g.*, H_2, O_2) Carrier gases (*e.g.*, Ar, N_2)
Processing time	Up to 3 days	Up to 3 hours	~ 10 minutes
Processing temperature	n/a	~ 1000 ^oC	~ 450 ^oC
Process complexity	Multi-staged	Multi-staged	Single-step
Controllability	Limited (Chemical functionality, flake size)	High (Grain size, thickness, defect content, chemical functionality)	High (Morphology, grain size, thickness, defect content, chemical functionality)
Scalability	High (Bulk production by volume)	Moderate (Roll-to-roll production)	Low-moderate (Ideal for batch-to-batch production)
Nature of produced graphene	Chemically modified flakes/powder	Pristine thin film	Pristine thin film/powder

Substrate dependence	No	Yes (Good quality growth is limited to highly crystalline catalyst substrates)	No (Any electrically conductive substrate, including amorphous surfaces)
Graphene grain size	~ nm to µm	~ µm to mm	~ µm
Graphene defect content	High	Low	Moderate
Transfer of graphene onto arbitrary substrates	Easy (*i.e.*, Graphene dispersions)	Difficult (*i.e*, Requires polymer transfer)	Easy (*i.e*, Water-assisted transfer)
Applications	Composites, energy storage devices, functional inks	Sensors, flexible and transparent electronics, heterostructure junctions, water purification membranes	Sensors, flexible and transparent electronics, energy storage devices, functional inks, capacitive deionization electrodes
References	[28,29,32,46-49]	[54-61,69,75-77,82,89,90,93]	[103-105,107,108,110-112]

1.3. Graphene Applications

The functional properties of graphene ensue from its morphology. Indeed, graphene thin films and powders are promising for numerous technological applications. In this thesis, we investigate the fabrication and design of graphene nanostructures by thermal- and plasma-based techniques. We explore their integration for two key applications – bioelectronics (**Section 1.3.1**), and energy storage devices (**Section 1.3.2**). For completeness, another emerging area of graphene application (water purification) is highlighted in **Section 1.3.3**.

1.3.1. Graphene for Biosensors

Fundamentally, a biosensor is a device comprised of two elements – a biomolecular receptor capable of specific reaction with the target analyte, and a transducer which processes the biorecognition event into a measurable signal. In particular, amongst a host of transduction platforms, electrochemical sensing methods offer great versatility and promise. Electrochemical biosensors offer attractive opportunities for numerous technologies in preventative healthcare, which require portable, fast, point-of-care, cost-effective, and low-power readout devices [125].

Indeed, a variety of electrochemical biosensors have been developed for the detection of biomarkers which cater to a wide variety of diseases [126]. However, these biosensors fall short in addressing one or more key criteria of device performance and fabrication [127-129]. In particular, this includes a high sensitivity and specificity in physiological environments, a rapid sensor response and regeneration, and an inexpensive device fabrication. Consequently, future innovations in the design of novel advanced materials towards the optimization of biosensors remain highly warranted.

Notably, carbon nanostructures (CNs) (*e.g.,* graphene, carbon nanowalls) inherit characteristics that enable their ability to function (simultaneously) as a specific receptor and a sensitive transducer (**Section 1.2.1** and **Section 1.2.3**) [130,131]. For instance, the mechanical robustness, high electrical conductivity, good electrochemical activity, and ease of functionality of CNs, have been harnessed to realize a large variety of

biorecognition nanostructures that can be tailored for the quantification of diverse biomarkers [132-134].

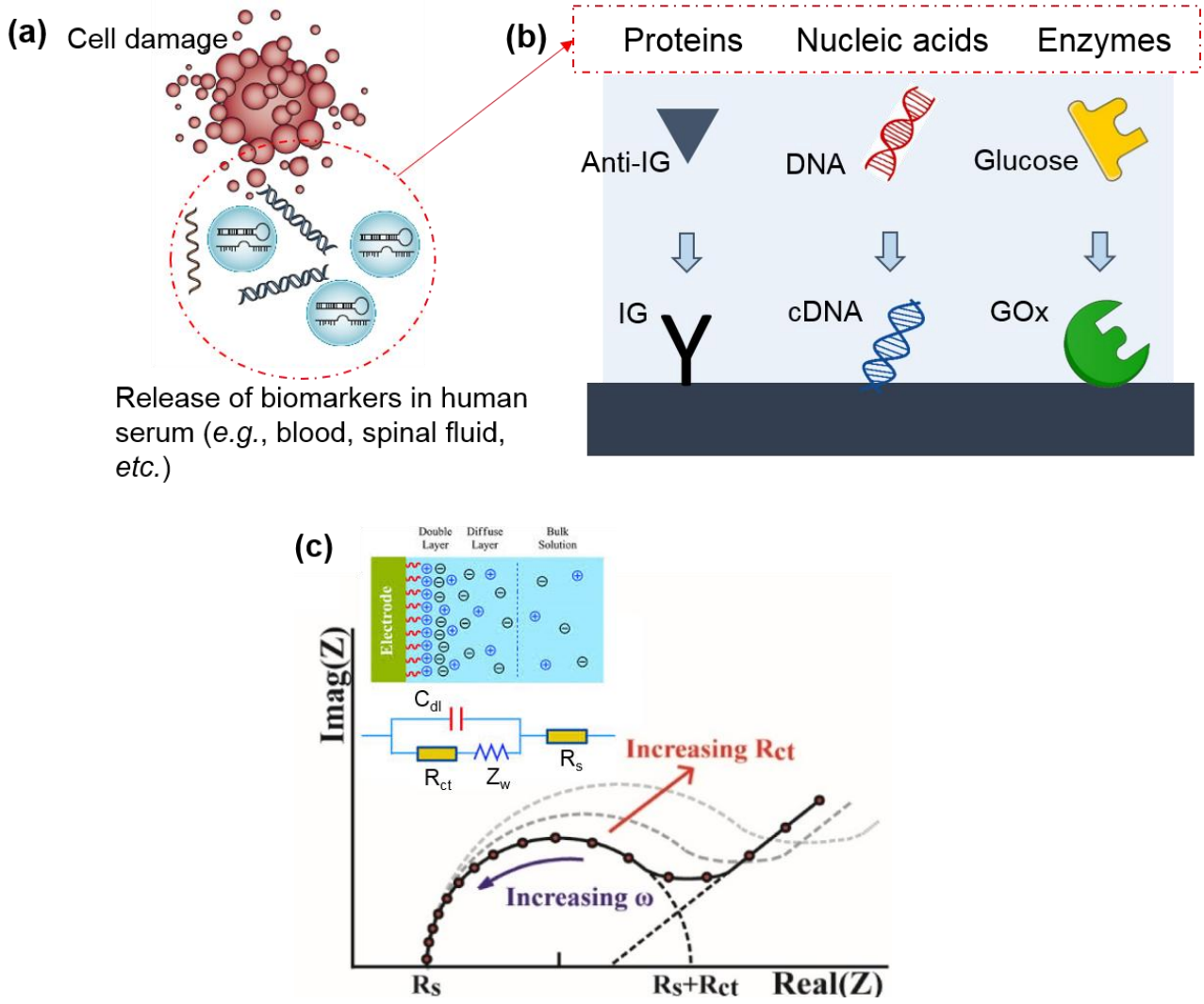

Figure 16 | Working principles of an electrochemical biosensor. (**a**) Input stage: The expression of biomarkers induced by irregularities in the biological system that are characteristic of the onset of diseases. Reproduced from [135], Copyright of Macmillan Publishers Limited, 2014. (**b**) Transduction stage: The biosensing interface. (**c**) Read-out stage: Electrochemical impedance spectra (EIS) (Nyquist plot) of the biosensing electrode in response to detection events. Here, R_s denotes the resistance of the solution, Z_w denotes the Warburg impedance at the diffusion layer, and C_{dl} denotes the capacitance at the double layer. Nyquist plot reproduced from [136], Copyright of OSA Publishing, 2015. Illustration of the electrode-analyte interface reproduced from [137], Copyright of the Royal Society of Chemistry, 2013.

The working principle of a biosensor is illustrated in Fig. 16. This begins with the expression of biomarkers (*e.g.*, in the form of proteins, nucleic acids, *etc.*) in our physiological system (*e.g.*, blood, spinal fluid, urine) [135,138]. The regulation of such biomarkers can be induced by irregularities in our biological system (*e.g.*, cell damage, apoptosis, *etc.*), and are characteristic of the onset of various diseases (**Fig. 16a**) [139,140].

Subsequently, these samples may be isolated for quantification by a sensing platform. **Fig. 16b** features the interface of an electrochemical biosensor. The biosensor is composed of an electrically conductive electrode (*e.g.*, graphene), and target-specific molecular probes (*e.g.,* immunoglobulins (IG), DNA, or enzymes) which are anchored on the electrode surface. This facilitates the selective capture of the target biomarkers which are complementary to the surface-immobilized probes.

Upon successful capture of the target analyte, the biorecognition event is transduced into an output in the form of an electrochemical signal. **Fig. 16c** illustrates an electrochemical impedance spectra (EIS) which characterizes the impedance response of an electrochemical sensor [136]. Electrochemical impedance is determined by measuring the current on an electrochemical cell from an applied AC potential. EIS offers significantly more information than DC or single frequency measurement techniques. EIS may be able to distinguish between two or more simultaneous electrochemical reactions, identify diffusion-limited reactions, provide information on the capacitive behavior of the system, and shed light on electron transfer rates in the reactions present. In particular, insights to reaction kinetics at the electrode sensing interface can be attained by an equivalent circuit model of the electrochemical system (inset of **Fig. 16c**). Typically, the equivalent circuit includes a capacitor, inductor, and several resistive elements, corresponding to the electrochemical cell [137].

In the event where target analytes are captured, this results in an increase in charge-transfer resistance (R_{ct}) at the electrode-analyte interface. Notably, the binding event may promote spatial blocking (*e.g.*, stearic re-orientation) and electrical screening (*e.g.*, charged analytes) for the transport of electrons (from the electrolyte) into the electrode material, and therefore an increase in the observed charge-transfer resistance [141,142].

Additionally, these surface impedance techniques offer opportunities to characterize the assembly of the biosensing device. For instance, it may be applied to optimize the deposition of self-assembled monolayers, and intermediate functionalization steps for the graphene-based electrode material [143,144].

In this thesis, the tailored synthesis and integration of graphene to realize effective electrochemical biosensors is explored. Thermal and plasma-assisted techniques are harnessed to achieve low-cost and sustainable fabrication of biosensors for nucleic acids and proteins, which demonstrate high sensitivity, selectivity, and ease in device assembly.

1.3.2 Graphene-Based Supercapacitors for Energy Storage

The supercapacitor is an electrochemical energy storage device, and its operation closely resembles that of a battery (**Fig. 17a**) [145,146]. A supercapacitor stores electrical charges under an applied voltage, and discharges the stored energy when an external load is connected. Unlike conventional batteries, supercapacitors promise higher power densities, increased charge retention capabilities and significantly longer life spans. Thus, supercapacitors are promising for the next-generation of energy storage devices [147].

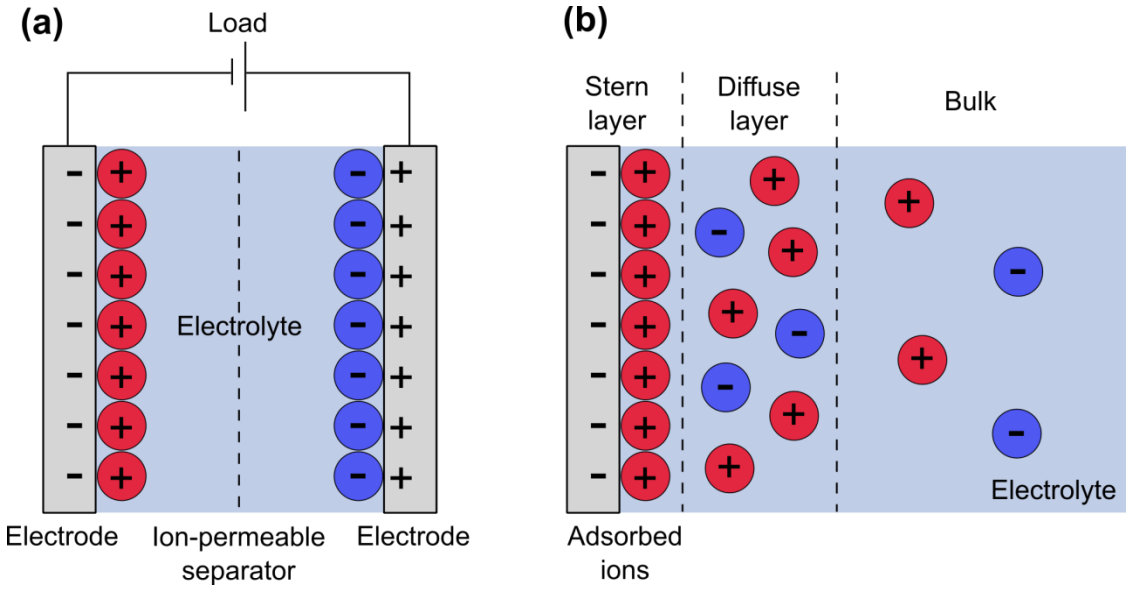

Figure 17 | Working principles of a supercapacitor. Schematic diagrams of a (**a**) supercapacitor device, and (**b**) the electrical double layer (EDL) structure at the negatively charged electrode surface. The supercapacitor consists of two electrodes, an electrolyte, and a separator that isolates the two electrodes. The positive charges in the Stern and diffuse layers contribute to the capacitance of the EDL.

Amongst the set of components in a supercapacitor, its electrode material is arguably the most important and defining characteristic [148]. In particular, the inherent properties of the electrode material (*e.g.,* surface area, porosity, conductivity, *etc.*) directly influences the amount of charge it can store (*e.g.*, capacitance, energy density), the rate at which charge can be transported (*e.g.*, rate capability, powder density), and the stability for charge storage (*i.e.*, life span). These performance metrics are central for the realization of practical energy storage devices. Thus, properties of the electrode material require careful design.

The optimal properties of an electrode material for a supercapacitor include, a high surface area, high density of meso- and micro-pores, good conductivity, open morphology, and an easy for fabrication and device integration. Notably, these characteristics may be realized in nanostructured materials. In particular, carbon nanostructures (*e.g.*, graphene, VGNS) inherit a many of such properties (*e.g.*, high aspect ratio, good conductivity, interconnected morphology, *etc.*), and thus, are promising functional materials for supercapacitor electrodes (**Section 1.2.3**) [149]. In addition, depending on the active material, the operation of the supercapacitor can be classified in two categories – electrostatic or Faradaic. Carbon-based materials are well-suited for electrostatic supercapacitors, while metal oxides are better suited for Faradaic supercapacitors.

In an electrostatic supercapacitor, charges are electrostatically accumulated within the electrical double layer (EDL) when a voltage bias is applied (**Fig. 17b**). During operation, an excess or deficit of electric charges are accumulated on the electrode surface. Correspondingly, electrolyte ions with counterbalancing charges gather at the electrolyte interface to establish electro-neutrality. In the charging process, electrons travel from the negative electrode to the positive electrode via an external load.

Simultaneously, cations in the electrolyte traverse towards the negatively-charged electrode, while anions migrate towards the positively-charged electrode. Likewise, the reverse is initiated during the discharge process.

In Faradaic supercapacitors, electrochemical redox reactions (*i.e.*, from metal oxides) occur at the electrode surface when a voltage bias is applied [150]. Here, charges are transported across the electrical double layer, resulting in the generation of a current through the device. Faradic supercapacitors enable higher working voltages and energy densities than electrostatic supercapacitors [151]. However, they demonstrate poorer capacitance retention and involve higher material costs, as compared to carbon-based supercapacitors.

In this thesis, plasma-based techniques are explored and designed, to enable the sustainable fabrication and integration of hierarchical carbon nanostructures for electrostatic supercapacitor devices.

1.3.3. Emerging Application for Graphene – Water Purification

Amongst the variety of water purification techniques, membrane distillation (MD) is a thermally-driven process that is promising [152]. MD involves the transport of water vapor through a porous and hydrophobic membrane in a discontinuous nature (**Fig. 18**) [153]. This ensures that efficiency of the MD process is independent of the salinity of the feed solution [154]. Thus, MD offers the ability to reject all non-volatile constituents (*e.g.*, ions, minerals, dissolved non-volatile organics, colloids, and pathogens) that may be present [155].

In the MD process, the membrane material is arguably the most important and defining characteristic. Notably, properties of the membrane material including, its morphology, surface energy, and porosity, directly affect its performance for water purification (*e.g.*, salt rejection, oil/water or SDS/water separation, membrane stability, likelihood of fouling) [156].

Recently, graphene has garnered interest as a membrane material for water purification, owing to its unique combination of functional properties [157]. Graphene offers for

ultrathin membranes with atomically defined nanopores, with sub-nanometer diameters approaching those of hydrated ions [158]. Consequently, this may allow for membranes with tailored selectivity and high permeance (*i.e.*, minimal resistance to fluid or ion flow), while retaining a high structural integrity [159,160].

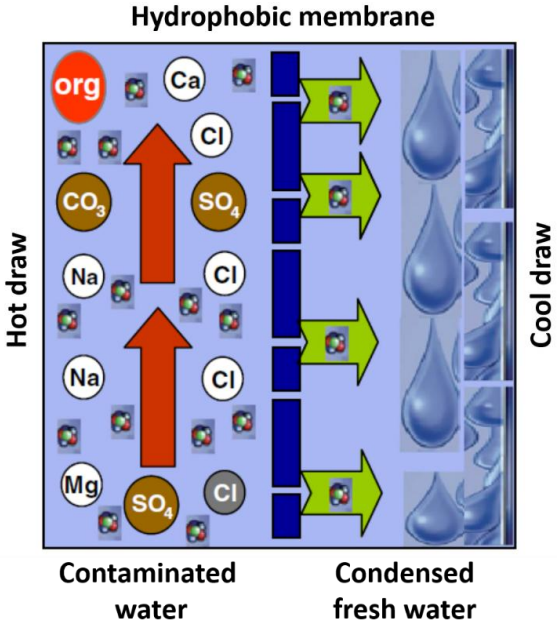

Figure 18 | Schematic of the membrane distillation process. Membrane distillation is driven by a partial vapour pressure difference due to a temperature gradient across the hydrophobic membrane material. Reproduced from [153], Copyright of Elsevier, 2013.

Recent advances in graphene processing have enabled the demonstration of atomically-thin films for water purification [161,162]. Indeed, the perfect single-layer of graphene is impermeable. Therefore, initial attempts to enable permeability of graphene have utilized a variety of reactive processes, in order to create randomly-etched pores and nanoscale apertures in the graphene film [162,163]. However, the transport of water through such pores is challenging, particularly, as this requires a large amount of pores with controlled morphology. Thus, while promising, the capability of graphene films for water purification is presently limited to small-scale demonstrations.

1.4. Material Characterization Techniques

A host of material characterization techniques are employed, supporting the development of processes for graphene synthesis, and the optimization of its properties for diverse applications.

Scanning electron microscopy (SEM)

The scanning electron microscope consists of an electron source, electromagnetic lenses, and an electron detector. It utilizes an electron beam instead of light, and functions based on its wave-particle duality. The electron beam is accelerated and focused on a sample using the lenses. The sample emits secondary electrons, which are then detected. The number of detected electrons depends on variations on the sample's surface. By scanning the beam and detecting the variations in the number of emitted electrons, the surface topography of the sample can be reconstituted. In this thesis, SEM is frequently used to characterize the microscopic morphologies for a diverse range of carbon-based nanostructures.

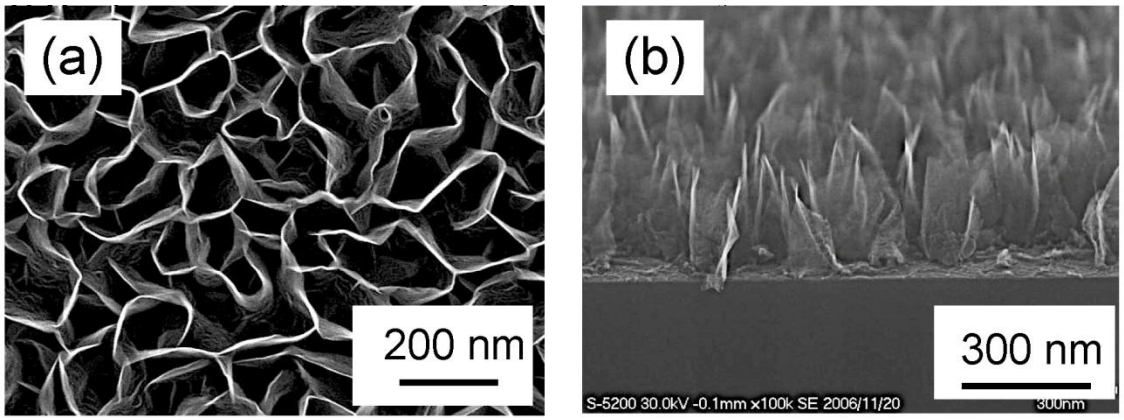

Figure 19 | SEM characterization of VGNS. (a) Top-down, and (b) side-on view. Reproduced from [114].

For instance, SEM characterizations in **Fig. 19a** and **Fig. 19b** reveal VGNS posssesses an open and interconnected morphology with sharp edge planes. In this thesis, Field-emission scanning electron microscopic (FE-SEM) images were obtained by Zeiss Auriga microscope operated at 5 keV electron beam energy with an InLens secondary electron detector.

Transmission electron microscopy (TEM)

Similar to SEM, a transmission electron microscope consists of an electron emission source, electromagnetic lenses, and an electron detector. A thin sample is positioned along the trajectory of an incident electron beam. The electron beam is produced, accelerated, and then focused on the sample by the electromagnetic lenses. The incident electron beam passes through the thin sample, and the transmitted signal of electrons are magnified into a detector. TEM allows us to magnify the image of thin samples down to atomic resolutions. Thus, TEM enables us to investigate the crystallographic properties and interatomic arrangements in the nanomaterial. In this thesis, TEM is used to characterize the atomic properties of graphene nanostructures.

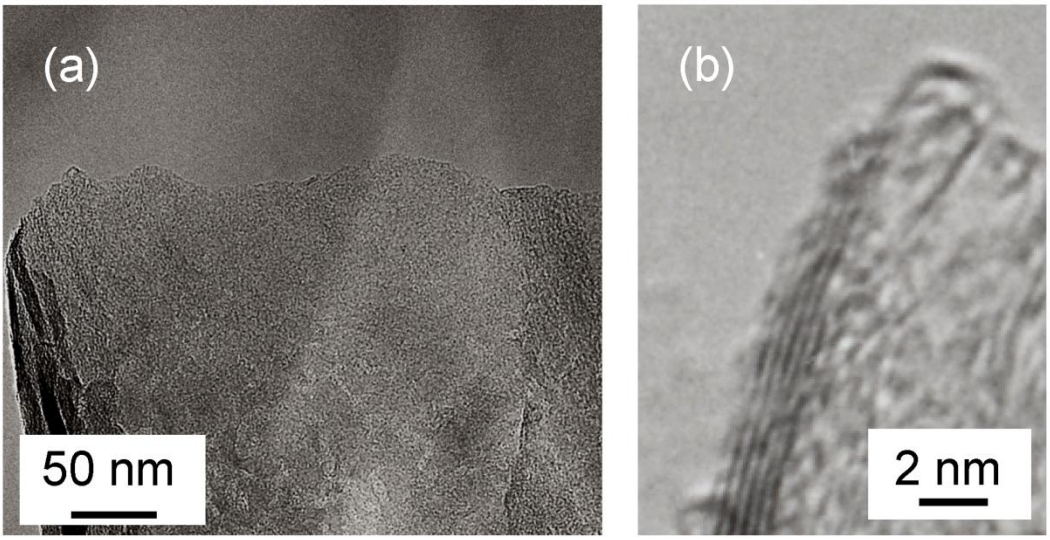

Figure 20 | TEM characterizations of a VGNS sample. (a) Low-resolution and (b) high-resolution TEM images. Reproduced from [164].

For instance, TEM characterizations show that VGNS consist of numerous nano-sized graphene domains (**Fig. 20a**). Graphene layers are observed in the high-resolution TEM (**Fig. 20b**), where interlayer spacing is approximately 0.34 nm. In this thesis, transmission electron microscopy (TEM) images were obtained with a JEOL 2200FS TEM microscope operated at 200 kV.

Raman spectroscopy

Raman is a spectroscopic technique that can be used for a variety of phases, and it is particularly useful for revealing the internal structure and bonding of the nanomaterial. This spectroscopic technique operates by the excitation of vibrational, rotational, and other low-frequency modes in the structure, by an irradiated wavelength of light (*e.g.*, UV, IR, visible range). A sample is irradiated by laser light, and the monochromatic light interacts with the molecular vibrations, phonons, or other excitations in the system (*i.e.*, inelastic scattering, Raman scattering), resulting in the energy of the laser photons being shifted. This shift in energy gives information about the vibrational modes in the system. Raman spectroscopy is particularly useful for analyzing the degree of disorder, bonding type, and interlayer lattice arrangements in carbon-based nanomaterials. In this thesis, Raman spectroscopy is frequently used to analyze the structural properties of graphene nanomaterials.

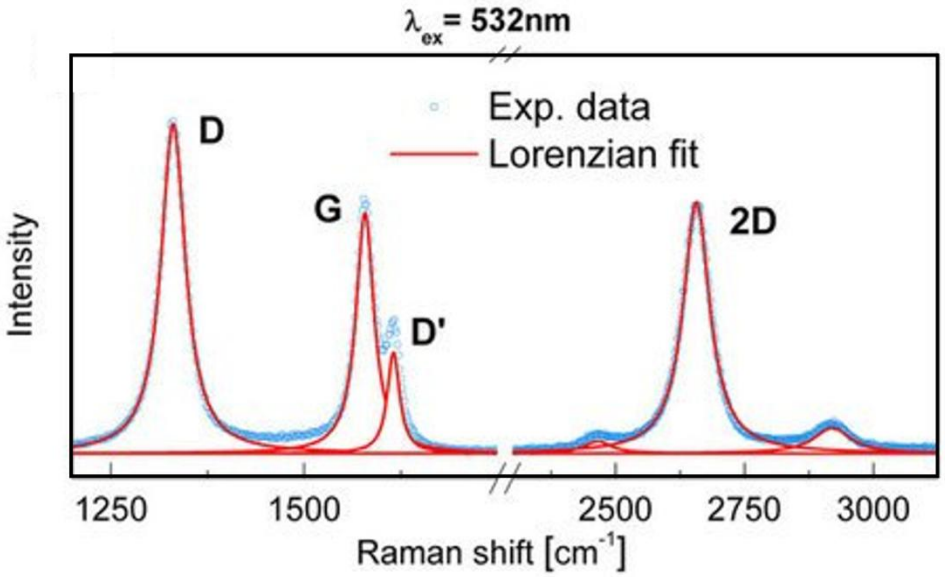

Figure 21 | Raman spectra of VGNS. Reproduced from [110].

Typically, three distinct peaks are present in the Raman spectra of graphene, namely, the characteristic disorder peak (D-band) at ~1350 cm^{-1}, the graphitic peak (G-band) at ~1580 cm^{-1}, and the second-order 2D-band at ~2670 cm^{-1} (**Fig. 21**). The D-band is attributed to the finite crystallite size effect and various defects induced in the sp^2

carbon materials; the G-band arises from the in-plane vibrational E_{2g} mode of the sp^2-hybridized carbon; and the 2D-band is a second-order Raman spectral feature due to the three-dimensional inter-planar stacking of hexagonal carbon networks [165]. This Raman spectra reveals that VGNS have a large presence of reactive edges and consist of ~ 5 graphene layers near the edge plane. In this thesis, Raman spectroscopy was performed using a Renishaw inVia spectrometer with Ar laser excitation at 514 nm and a probing spot size of 1 μm^2.

X-ray photoelectron spectroscopy (XPS)

XPS is a surface-sensitive quantitative technique that measures the elemental composition and electronic states of the elements within the top ~10 nm of a sample. XPS is based on the principle of the photoelectric effect. XPS spectra are obtained by irradiating a sample with a beam of X-rays while simultaneously measuring the kinetic energy and the number of core shell electrons being ejected. In this thesis, XPS is used to analyze the chemical and structural composition of graphene-based nanomaterials.

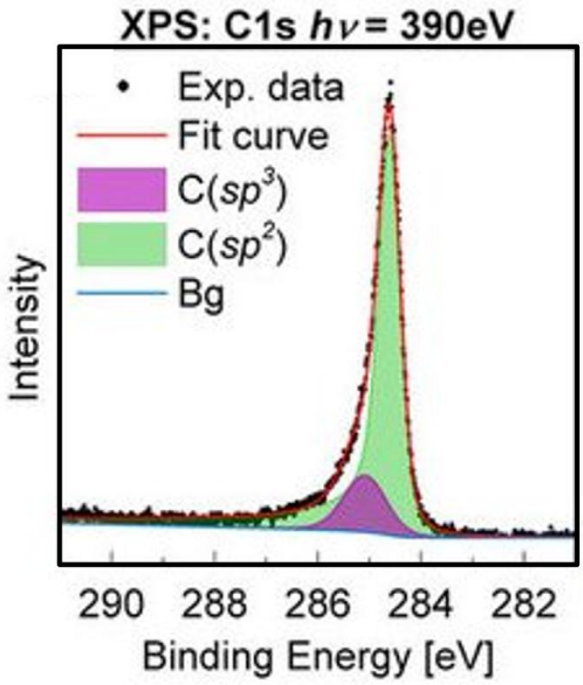

Figure 22 | XPS characterization of VGNS. Reproduced from [110].

For instance, the XPS spectra of VGNS (**Fig. 22**) can reveal valuable structural and chemical information through the ratio of graphitic sp^2 to sp^3 peaks, while also helping to indicate the presence of other functional groups (*e.g.*, oxygen, nitrogen, *etc.*) on VGNS. In this thesis, X-ray photoelectron spectroscopy (XPS) spectra were recorded with a Specs SAGE 150 spectroscope with Mg Kα excitation at 1253.6 eV. Using the CasaXPS software, a Shirley background correction was employed and the XPS spectra were deconvoluted into its respective peaks.

Atomic force microscopy (AFM)

An atomic force microscope probes the surface topography of a sample. It consists of a tip positioned at the end of a cantilever, and an optical system which uses a laser to detect deflections in the cantilever tip. Typically for imaging, the AFM operates in a tapping (repulsive) mode. When the tip is brought into contact with the sample and moved along its surface, this leads to deflections in the tip due to short-range atomic forces. Correspondingly, deviations measured by the laser allows us to measure the surface profile of the sample. AFM enables us to image the topography of the surface down to atomic resolutions. In this thesis, AFM is used to analyze the surface topography of graphene thin films.

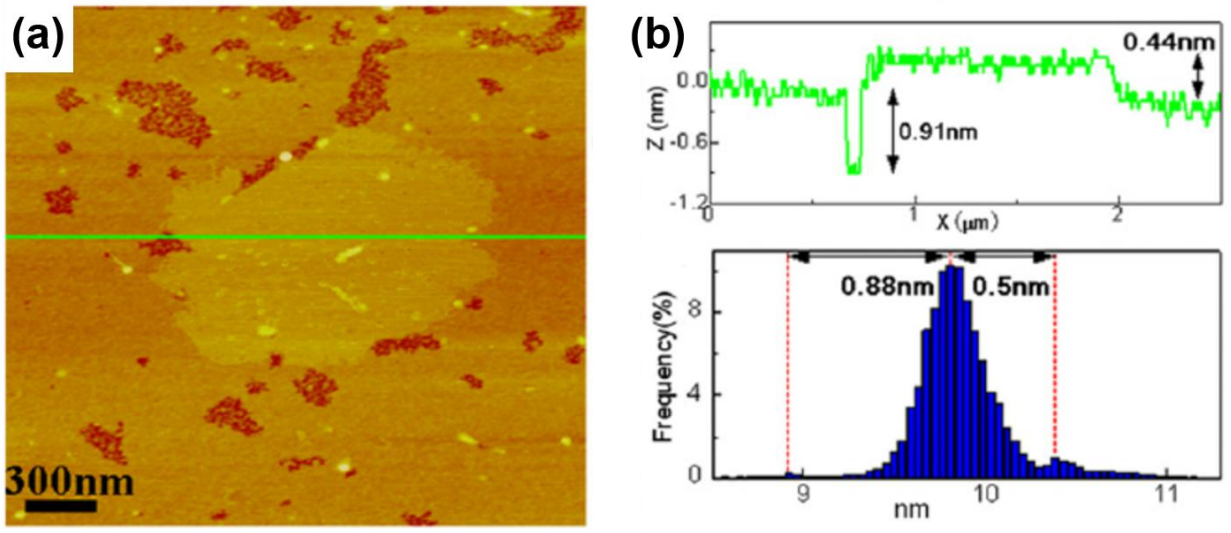

Figure 23 | AFM characterizations of a graphene flake. (**a**) AFM topography (b) height profiles across the graphene flake (indicated by the green line). Reproduced from [166].

For instance, AFM characterization of graphene (**Fig. 23**) reveals the uniformity of the graphene morphology across the surface. Here, we deduce that the graphene flake is on average 2- 3 layers thick (each layer ~0.34 nm). In this thesis, atomic force microscopy (AFM) images were acquired with an Asylum Research MFP-3D AFM operating in intermittent contact ("tapping") mode with a 5 N/m spring constant cantilever. Image analysis was performed using the Scanning Probe Image Processor (SPIP^{TM}) software produced by Image Metrology A/S.

1.5. Executive Summary

This thesis aims to exemplify how thermal- and plasma-based techniques may be designed and implemented to enable, enhance, and tailor the synthesis of hierarchical graphene nanostructures, and to streamline their integration for applications in bioelectronics and energy storage devices. This aim is achieved in the thesis by focusing on objectives 1 – 3 outlined below.

Objective 1: Re-inventing the thermal CVD process – ambient-air graphene synthesis from renewable natural precursors.

Conventional techniques for CVD synthesis of graphene film are impeded by long processing times, extensive vacuum operation, high annealing temperatures, large volumes of purified gases, and are multi-staged (**Section 1.2.2**). Such resource-consuming processes are necessary for creating a highly-controlled environment, devoid of any ambient air to enable the growth of graphene. Consequently, we explore the following questions and hypotheses (**Table 2**) to address the challenges of thermal CVD synthesis of graphene films:

Table 2. Questions and hypotheses for objective 1.

Question	Hypothesis
How can we improve the viability of the thermal CVD process for graphene production?	• By removing the use of purified gases and vacuum operation, reducing the annealing temperature, and simplifying the production process, this enables a resource-efficient synthesis of graphene. • Consequently, this necessitates using an alternative source of carbon precursor material and growing graphene in an ambient-air environment.
Aside from purified gases, can we use other forms of precursor material?	• The elevated temperature environment and catalytic properties of the growth substrate can help in reforming natural carbon-containing precursors (*e.g.*, soybean oil) into graphene with good quality and controllable properties.

How can graphene grow in an ambient-air environment at elevated temperatures?	• A closed ambient-air environment can be created for graphene synthesis. • The precursor material can dissociate and consume the reactive oxygen species (in the ambient-air) which impedes the growth of graphene. • The processing parameters (*e.g.*, precursor amount, annealing duration, substrate cooling rate, *etc.*) can be optimized to create a controlled ambient-air environment, enabling the synthesis of uniform and good quality graphene with tailored properties.

A host of materials characterization techniques were employed for optimizing and developing the ambient-air process, and providing valuable insights on the mechanisms for graphene growth. This includes:

- Scanning electron microscopy (SEM) for examining the surface morphology of the graphene film;
- Transmission electron microscopy (TEM) for studying the crystallographic properties (*e.g.*, grain size, orientation) of the graphene film;
- X-ray photoelectron spectroscopy (XPS) for analyzing the chemical functionalities at the graphene surface and sub-surface (growth substrate), which help in providing insights into the mechanisms for graphene formation in the ambient-air environment;
- Electrical 4-point probe measurements for evaluating the sheet resistance and defect content of the graphene film;
- Raman spectroscopy for analyzing the thickness, defect content and uniformity across the graphene film;
- Optical transmittance for evaluating the overall thickness of the graphene film.

In **Chapter 2**, an ambient-air CVD process is developed for the fabrication of graphene films. This enables a single-step, energy efficient (*i.e.,* rapid, low temperature), resource-efficient (*i.e.*, no purified gases), green (*i.e.*, reforming renewable biomass

precursors), low-cost, integration-friendly, technologically sustainable, and potentially scalable process for graphene synthesis.

Key takeaways for Objective 1:

We demonstrate for the first time, CVD growth of graphene in an ambient-air environment. Triglyceride-containing natural precursors (*e.g.*, soybean oil) were reformed into homogeneous, large-area films of graphene with controllable optoelectronic and structural properties. Unlike conventional CVD, this technique is single-stepped, rapid, and does not require purified gases or vacuum operation.

The thermally dissociated precursor fragments were found to promote 1) consumption of reactive oxygen species in the ambient-air, 2) a carbon-surplus environment, and the 3) formation of water vapor by-products that help maintain the catalytic ability of the growth substrate, enabling the synthesis of graphene films.

Objective 2: **Graphene for bioelectronics – Plasma-enabled synthesis and water-assisted transfer of graphene micro-islands for biosensing and bioengineering applications.**

For applications in bioelectronics, graphene powders and thin films are often considered. Chemical exfoliation methods are typically used for synthesizing graphene powders, offering production in large scale and with low cost (**Table 1**). However, these approaches for preparing graphene powders utilize harsh chemicals and introduce impurities (**Section 1.2.1**). On the other hand, CVD growth of graphene involves high temperatures (1000 ^{o}C), and is accompanied by long growth times, and is multi-staged. Further, the integration of graphene films requires the use of a transfer process. This introduces cytotoxic impurities that impede its functionality for bioelectronics (**Section 1.2.2**).

On the other hand, unlike chemical- or thermal-based processes, plasma enables a single-step, rapid, and low-temperature growth of graphene on diverse substrates, with

unique nanostructured morphology that is advantageous for applications in bioelectronics. In addition, the plasma-enabled growth of graphene does not produce hazardous by-products, nor does it utilize toxic reagents in the synthesis process.

In **Chapter 3**, we explore the following questions and hypotheses (**Table 3**) around plasma processing to address the challenges of synthesis and integration of graphene nanostructures for bioelectronics:

Table 3. Questions and hypotheses for objective 2.

Question	Hypothesis
How can we improve graphene synthesis for bioelectronics application?	• By drastically reducing the growth temperature and duration, and removing the need for wet-chemical etching in graphene transfer, this promotes a resource-efficient synthesis of graphene for bioelectronics application.
Why is plasma advantageous in graphene synthesis for bioelctronics?	• Plasma enables a low-temperature, single-step and controlled growth of graphene with unique morphology that is advantageous for developing biosensors and biocompatible coatings. • Plasma enables the as-grown graphene to easily decouple from the growth substrate and be transferred onto arbitrary target substrates, avoiding the conventional need for wet-chemical etching.

A host of materials characterization techniques were employed for optimizing the plasma-enabled graphene synthesis process, and its performance for biosensing and biocompatible coatings. This includes:

- SEM for studying the surface morphology of the graphene nanostructure;
- XPS for analyzing the surface chemical functionalities of graphene;
- Raman spectroscopy for examining the thickness, defect content and uniformity of graphene;

- Atomic force microscopy (AFM) for studying the surface topography of the graphene nanostructure;
- EIS for analyzing its performance (*i.e.*, sensitivity, selectivity) as a biosensing electrode;
- Cell viability studies for evaluating its biocompatibility.

Key takeaways for Objective 2:

Plasma enables the single-step, rapid and controlled growth of graphene micro-islands (GMs) at a low temperature (200 ^{o}C). GMs feature an interconnected morphology, reactive edges, and a high surface area. The plasma synthesis enables a water-assisted transfer of GMs onto arbitrary substrates. GMs were integrated as a functional material to realize a sensitive and selective genosensor, and as a biocompatible coating, suited for bioengineering applications.

Objective 3: Graphene for energy storage devices – Plasma-enabled reforming of natural precursors into VGNS for supercapacitors.

For energy storage devices, graphene powders derived by chemical methods are typically considered (**Section 1.2.1**). However, these powders are not only prone to uncontrolled agglomeration; but also, they require additional non-conductive binders and surfactants to integrate them for supercapacitors. Consequently, this leads to degradation in energy storage performance.

Unlike chemical methods for preparing graphene powders, plasma enables a rapid, low-temperature and single-step synthesis of graphene nanostructures with unique morphology that is particularly advantageous for application in energy storage devices. In particular, plasma synthesis enables the formation of graphene with an open and interconnected morphology, and atomically-thin reactive edges, which help to promote good electrochemical properties. In **Chapter 4**, we examine the following questions and

hypotheses (**Table 4**) around plasma processing to address the challenges of synthesis and integration of graphene nanostructures for supercapacitors:

Table 4. Questions and hypotheses for objective 3.

Question	Hypothesis
How can we improve graphene synthesis for energy storage devices?	• By drastically reducing the growth temperature and duration, preventing agglomeration, and removing the need for binders, this promotes a resource-efficient synthesis of graphene for energy storage devices.
Why is plasma advantageous in graphene synthesis for energy storage devices?	• Plasma enables the reforming of natural precursors into graphene nanostructures. • Plasma enables a low-temperature, single-step and controlled growth of graphene with unique nanostructured morphology that is advantageous for supercapacitor applications. • Plasma enables the direct integration of graphene nanostructures for supercapacitor electrodes, avoiding the need for non-conductive binders.

A host of materials characterization techniques were employed for optimizing the plasma-enabled graphene synthesis process and its supercapacitor performance. This includes:

- SEM for studying the morphology of the graphene nanostructure;
- TEM for analyzing the crystallographic properties of the graphene nanostructure;
- XPS for analyzing the surface chemical functionalities of graphene;
- Raman spectroscopy for examining the edge thickness, defect content and uniformity of graphene;
- Cyclic voltammetric tests for evaluating its performance in energy storage (*i.e.,* power density, areal capacitance, specific capacitance, rate capability, stability, *etc.*);

Key takeaways for Objective 3:

Plasma enables a single-step, low-temperature, controlled growth and direct integration of VGNS as an electrode material for supercapacitor application. Diverse natural precursors are reformed into homogeneous VGNS. The VGNS feature a high surface area, an open morphology, with interconnected arrays of graphene sheets, and reactive edges, which facilitate its excellent performance for supercapacitor applications.

References

1. Novoselov, K.S.; Geim, A.K.; Morozov, S.V.; Jiang, D.; Zhang, Y.; Dubonos, S.V.; Grigorieva, I.V.; Firsov, A.A., Electric field effect in atomically thin carbon films. *Science* **2004**, *306*, 666-669.
2. Geim, A.K.; Novoselov, K.S., The rise of graphene. *Nature Materials* **2007**, *6*, 183-191.
3. Novoselov, K.S.; Falko, V.I.; Colombo, L.; Gellert, P.R.; Schwab, M.G.; Kim, K., A roadmap for graphene. *Nature* **2012**, *490*, 192-200.
4. Lee, C.; Wei, X.; Kysar, J.W.; Hone, J., Measurement of the elastic properties and intrinsic strength of monolayer graphene. *Science* **2008**, *321*, 385-388.
5. Castro Neto, A.H.; Guinea, F.; Peres, N.M.R.; Novoselov, K.S.; Geim, A.K., The electronic properties of graphene. *Reviews of Modern Physics* **2009**, *81*, 109-162.
6. Balandin, A.A., Thermal properties of graphene and nanostructured carbon materials. *Nature Materials* **2011**, *10*, 569-581.
7. Bunch, J.S.; Verbridge, S.S.; Alden, J.S.; van der Zande, A.M.; Parpia, J.M.; Craighead, H.G.; McEuen, P.L., Impermeable atomic membranes from graphene sheets. *Nano Letters* **2008**, *8*, 2458-2462.
8. Bonaccorso, F.; Sun, Z.; Hasan, T.; Ferrari, A.C., Graphene photonics and optoelectronics. *Nature Photonics* **2010**, *4*, 611-622.
9. Xu, K.; Heath, J.R., Wetting: Contact with what? *Nature Materials* **2013**, *12*, 872-873.
10. Dato, A.; Lee, Z.; Jeon, K.-J.; Erni, R.; Radmilovic, V.; Richardson, T.J.; Frenklach, M., Clean and highly ordered graphene synthesized in the gas phase. *Chemical Communications* **2009**, 6095-6097.
11. Yu, Q.; Jauregui, L.A.; Wu, W.; Colby, R.; Tian, J.; Su, Z.; Cao, H.; Liu, Z.; Pandey, D.; Wei, D.*, et al.*, Control and characterization of individual grains and grain boundaries in graphene grown by chemical vapour deposition. *Nature Materials* **2011**, *10*, 443-449.
12. Wallace, P.R., The band theory of graphite. *Physical Review* **1947**, *71*, 622-634.
13. Blees, M.K.; Barnard, A.W.; Rose, P.A.; Roberts, S.P.; McGill, K.L.; Huang, P.Y.; Ruyack, A.R.; Kevek, J.W.; Kobrin, B.; Muller, D.A.*, et al.*, Graphene kirigami. *Nature* **2015**, *524*, 204-207.
14. Van Noorden, R., Production: Beyond sticky tape. *Nature* **2012**, *483*, S32-S33.
15. Meng, F.C.; Lu, W.B.; Li, Q.W.; Byun, J.H.; Oh, Y.; Chou, T.W., Graphene-based fibers: A review. *Advanced Materials* **2015**, *27*, 5113-5131.

16. Bo, Z.; Mao, S.; Han, Z.J.; Cen, K.F.; Chen, J.H.; Ostrikov, K., Emerging energy and environmental applications of vertically-oriented graphenes. *Chemical Society Reviews* **2015**, *44*, 2108-2121.
17. Ren, W.; Cheng, H.-M., The global growth of graphene. *Nature Nanotechnology* **2014**, *9*, 726-730.
18. Higgins, D.; Zamani, P.; Yu, A.P.; Chen, Z.W., The application of graphene and its composites in oxygen reduction electrocatalysis: A perspective and review of recent progress. *Energy & Environmental Science* **2016**, *9*, 357-390.
19. Liu, J., Charging graphene for energy. *Nature Nanotechnology* **2014**, *9*, 739-741.
20. Ahn, J.-H.; Hong, B.H., Graphene for displays that bend. *Nature Nanotechnology* **2014**, *9*, 737-738.
21. Levendorf, M.P.; Kim, C.-J.; Brown, L.; Huang, P.Y.; Havener, R.W.; Muller, D.A.; Park, J., Graphene and boron nitride lateral heterostructures for atomically thin circuitry. *Nature* **2012**, *488*, 627-632.
22. Kostarelos, K.; Novoselov, K.S., Graphene devices for life. *Nature Nanotechnology* **2014**, *9*, 744-745.
23. Lotya, M.; Hernandez, Y.; King, P.J.; Smith, R.J.; Nicolosi, V.; Karlsson, L.S.; Blighe, F.M.; De, S.; Wang, Z.; McGovern, I.T.*, et al.*, Liquid phase production of graphene by exfoliation of graphite in surfactant/water solutions. *Journal of the American Chemical Society* **2009**, *131*, 3611-3620.
24. Green, A.A.; Hersam, M.C., Solution phase production of graphene with controlled thickness via density differentiation. *Nano Letters* **2009**, *9*, 4031-4036.
25. Hernandez, Y.; Nicolosi, V.; Lotya, M.; Blighe, F.M.; Sun, Z.; De, S.; McGovern, I.T.; Holland, B.; Byrne, M.; Gun'Ko, Y.K.*, et al.*, High-yield production of graphene by liquid-phase exfoliation of graphite. *Nature Nanotechnology* **2008**, *3*, 563-568.
26. Blake, P.; Brimicombe, P.D.; Nair, R.R.; Booth, T.J.; Jiang, D.; Schedin, F.; Ponomarenko, L.A.; Morozov, S.V.; Gleeson, H.F.; Hill, E.W.*, et al.*, Graphene-based liquid crystal device. *Nano Letters* **2008**, *8*, 1704-1708.
27. Bonaccorso, F.; Lombardo, A.; Hasan, T.; Sun, Z.; Colombo, L.; Ferrari, A.C., Production and processing of graphene and 2d crystals. *Materials Today* **2012**, *15*, 564-589.
28. Marcano, D.C.; Kosynkin, D.V.; Berlin, J.M.; Sinitskii, A.; Sun, Z.; Slesarev, A.; Alemany, L.B.; Lu, W.; Tour, J.M., Improved synthesis of graphene oxide. *ACS Nano* **2010**, *4*, 4806-4814.

29. Hummers, W.S.; Offeman, R.E., Preparation of graphitic oxide. *Journal of the American Chemical Society* **1958**, *80*, 1339-1339.
30. Paton, K.R.; Varrla, E.; Backes, C.; Smith, R.J.; Khan, U.; O ¸ Neill, A.; Boland, C.; Lotya, M.; Istrate, O.M.; King, P.*, et al.*, Scalable production of large quantities of defect-free few-layer graphene by shear exfoliation in liquids. *Nature Materials* **2014**, *13*, 624-630.
31. Parvez, K.; Wu, Z.-S.; Li, R.; Liu, X.; Graf, R.; Feng, X.; Müllen, K., Exfoliation of graphite into graphene in aqueous solutions of inorganic salts. *Journal of the American Chemical Society* **2014**, *136*, 6083-6091.
32. Dimiev, A.M.; Tour, J.M., Mechanism of graphene oxide formation. *ACS Nano* **2014**, *8*, 3060-3068.
33. Varrla, E.; Paton, K.R.; Backes, C.; Harvey, A.; Smith, R.J.; McCauley, J.; Coleman, J.N., Turbulence-assisted shear exfoliation of graphene using household detergent and a kitchen blender. *Nanoscale* **2014**, *6*, 11810-11819.
34. Su, C.-Y.; Lu, A.-Y.; Xu, Y.; Chen, F.-R.; Khlobystov, A.N.; Li, L.-J., High-quality thin graphene films from fast electrochemical exfoliation. *ACS Nano* **2011**, *5*, 2332-2339.
35. Lu, J.; Yang, J.-x.; Wang, J.; Lim, A.; Wang, S.; Loh, K.P., One-pot synthesis of fluorescent carbon nanoribbons, nanoparticles, and graphene by the exfoliation of graphite in ionic liquids. *ACS Nano* **2009**, *3*, 2367-2375.
36. Ambrosi, A.; Pumera, M., Electrochemically exfoliated graphene and graphene oxide for energy storage and electrochemistry applications. *Chemistry ‐ A European Journal* **2016**, *22*, 153-159.
37. Tour, J.M., Top-down versus bottom-up fabrication of graphene-based electronics. *Chemistry of Materials* **2014**, *26*, 163-171.
38. Xu, Z.; Gao, C., Graphene chiral liquid crystals and macroscopic assembled fibres. *Nature Communications* **2011**, *2*, 571.
39. Zang, J.; Cao, C.; Feng, Y.; Liu, J.; Zhao, X., Stretchable and high-performance supercapacitors with crumpled graphene papers. *Scientific Reports* **2014**, *4*, 6492.
40. Li, D.; Muller, M.B.; Gilje, S.; Kaner, R.B.; Wallace, G.G., Processable aqueous dispersions of graphene nanosheets. *Nature Nanotechnology* **2008**, *3*, 101-105.
41. Torrisi, F.; Hasan, T.; Wu, W.; Sun, Z.; Lombardo, A.; Kulmala, T.S.; Hsieh, G.-W.; Jung, S.; Bonaccorso, F.; Paul, P.J.*, et al.*, Inkjet-printed graphene electronics. *ACS Nano* **2012**, *6*, 2992-3006.

42. Cai, W.; Piner, R.D.; Stadermann, F.J.; Park, S.; Shaibat, M.A.; Ishii, Y.; Yang, D.; Velamakanni, A.; An, S.J.; Stoller, M.*, et al.*, Synthesis and solid-state nmr structural characterization of 13c-labeled graphite oxide. *Science* **2008**, *321*, 1815-1817.

43. Mattevi, C.; Eda, G.; Agnoli, S.; Miller, S.; Mkhoyan, K.A.; Celik, O.; Mastrogiovanni, D.; Granozzi, G.; Garfunkel, E.; Chhowalla, M., Evolution of electrical, chemical, and structural properties of transparent and conducting chemically derived graphene thin films. *Advanced Functional Materials* **2009**, *19*, 2577-2583.

44. Becerril, H.A.; Mao, J.; Liu, Z.; Stoltenberg, R.M.; Bao, Z.; Chen, Y., Evaluation of solution-processed reduced graphene oxide films as transparent conductors. *ACS Nano* **2008**, *2*, 463-470.

45. Ambrosi, A.; Chua, C.K.; Khezri, B.; Sofer, Z.; Webster, R.D.; Pumera, M., Chemically reduced graphene contains inherent metallic impurities present in parent natural and synthetic graphite. *Proceedings of the National Academy of Sciences of the United States of America* **2012**, *109*, 12899-12904.

46. Gambhir, S.; Jalili, R.; Officer, D.L.; Wallace, G.G., Chemically converted graphene: Scalable chemistries to enable processing and fabrication. *NPG Asia Materials* **2015**, *7*, e186.

47. Chua, C.K.; Pumera, M., Chemical reduction of graphene oxide: A synthetic chemistry viewpoint. *Chemical Society Reviews* **2014**, *43*, 291-312.

48. Su, C.-Y.; Xu, Y.; Zhang, W.; Zhao, J.; Liu, A.; Tang, X.; Tsai, C.-H.; Huang, Y.; Li, L.-J., Highly efficient restoration of graphitic structure in graphene oxide using alcohol vapors. *ACS Nano* **2010**, *4*, 5285-5292.

49. López, V.; Sundaram, R.S.; Gómez-Navarro, C.; Olea, D.; Burghard, M.; Gómez-Herrero, J.; Zamora, F.; Kern, K., Chemical vapor deposition repair of graphene oxide: A route to highly-conductive graphene monolayers. *Advanced Materials* **2009**, *21*, 4683-4686.

50. Gwon, H.; Kim, H.-S.; Lee, K.U.; Seo, D.-H.; Park, Y.C.; Lee, Y.-S.; Ahn, B.T.; Kang, K., Flexible energy storage devices based on graphene paper. *Energy & Environmental Science* **2011**, *4*, 1277-1283.

51. Stankovich, S.; Dikin, D.A.; Dommett, G.H.B.; Kohlhaas, K.M.; Zimney, E.J.; Stach, E.A.; Piner, R.D.; Nguyen, S.T.; Ruoff, R.S., Graphene-based composite materials. *Nature* **2006**, *442*, 282-286.

52. David, L.; Bhandavat, R.; Barrera, U.; Singh, G., Silicon oxycarbide glass-graphene composite paper electrode for long-cycle lithium-ion batteries. *Nature Communications* **2016**, *7*, 10998.
53. Ji, J.; Li, Y.; Peng, W.; Zhang, G.; Zhang, F.; Fan, X., Advanced graphene-based binder-free electrodes for high-performance energy storage. *Advanced Materials* **2015**, *27*, 5264-5279.
54. Li, X.; Cai, W.; An, J.; Kim, S.; Nah, J.; Yang, D.; Piner, R.; Velamakanni, A.; Jung, I.; Tutuc, E.*, et al.*, Large-area synthesis of high-quality and uniform graphene films on copper foils. *Science* **2009**, *324*, 1312-1314.
55. Kim, K.S.; Zhao, Y.; Jang, H.; Lee, S.Y.; Kim, J.M.; Kim, K.S.; Ahn, J.-H.; Kim, P.; Choi, J.-Y.; Hong, B.H., Large-scale pattern growth of graphene films for stretchable transparent electrodes. *Nature* **2009**, *457*, 706-710.
56. Gao, L.; Ren, W.; Xu, H.; Jin, L.; Wang, Z.; Ma, T.; Ma, L.-P.; Zhang, Z.; Fu, Q.; Peng, L.-M.*, et al.*, Repeated growth and bubbling transfer of graphene with millimetre-size single-crystal grains using platinum. *Nature Communications* **2012**, *3*, 699.
57. Hao, Y.; Bharathi, M.S.; Wang, L.; Liu, Y.; Chen, H.; Nie, S.; Wang, X.; Chou, H.; Tan, C.; Fallahazad, B.*, et al.*, The role of surface oxygen in the growth of large single-crystal graphene on copper. *Science* **2013**, *342*, 720-723.
58. Liu, L.; Zhou, H.; Cheng, R.; Yu, W.J.; Liu, Y.; Chen, Y.; Shaw, J.; Zhong, X.; Huang, Y.; Duan, X., High-yield chemical vapor deposition growth of high-quality large-area ab-stacked bilayer graphene. *ACS Nano* **2012**, *6*, 8241-8249.
59. Bhaviripudi, S.; Jia, X.; Dresselhaus, M.S.; Kong, J., Role of kinetic factors in chemical vapor deposition synthesis of uniform large area graphene using copper catalyst. *Nano Letters* **2010**, *10*, 4128-4133.
60. Li, X.; Cai, W.; Colombo, L.; Ruoff, R.S., Evolution of graphene growth on ni and cu by carbon isotope labeling. *Nano Letters* **2009**, *9*, 4268-4272.
61. Kim, H.; Mattevi, C.; Calvo, M.R.; Oberg, J.C.; Artiglia, L.; Agnoli, S.; Hirjibehedin, C.F.; Chhowalla, M.; Saiz, E., Activation energy paths for graphene nucleation and growth on cu. *ACS Nano* **2012**, *6*, 3614-3623.
62. Losurdo, M.; Giangregorio, M.M.; Capezzuto, P.; Bruno, G., Graphene cvd growth on copper and nickel: Role of hydrogen in kinetics and structure. *Physical Chemistry Chemical Physics* **2011**, *13*, 20836-20843.

63. Sinfelt, J.H.; Carter, J.L.; Yates, D.J.C., Catalytic hydrogenolysis and dehydrogenation over copper-nickel alloys. *Journal of Catalysis* **1972**, *24*, 283-296.
64. Sinfelt, J.H., Catalysis by alloys and bimetallic clusters. *Accounts of Chemical Research* **1977**, *10*, 15-20.
65. Kidambi, P.R.; Bayer, B.C.; Blume, R.; Wang, Z.-J.; Baehtz, C.; Weatherup, R.S.; Willinger, M.-G.; Schloegl, R.; Hofmann, S., Observing graphene grow: Catalyst ' graphene interactions during scalable graphene growth on polycrystalline copper. *Nano Letters* **2013**, *13*, 4769-4778.
66. Vlassiouk, I.; Regmi, M.; Fulvio, P.; Dai, S.; Datskos, P.; Eres, G.; Smirnov, S., Role of hydrogen in chemical vapor deposition growth of large single-crystal graphene. *ACS Nano* **2011**, *5*, 6069-6076.
67. Baraton, L.; He, Z.B.; Lee, C.S.; Cojocaru, C.S.; Châtelet, M.; Maurice, J.L.; Lee, Y.H.; Pribat, D., On the mechanisms of precipitation of graphene on nickel thin films. *Europhysics Letters* **2011**, *96*, 46003.
68. Chae, S.J.; Güneş, F.; Kim, K.K.; Kim, E.S.; Han, G.H.; Kim, S.M.; Shin, H.-J.; Yoon, S.-M.; Choi, J.-Y.; Park, M.H.*, et al.*, Synthesis of large-area graphene layers on poly-nickel substrate by chemical vapor deposition: Wrinkle formation. *Advanced Materials* **2009**, *21*, 2328-2333.
69. Ago, H.; Ogawa, Y.; Tsuji, M.; Mizuno, S.; Hibino, H., Catalytic growth of graphene: Toward large-area single-crystalline graphene. *The Journal of Physical Chemistry Letters* **2012**, *3*, 2228-2236.
70. Weatherup, R.S.; Dlubak, B.; Hofmann, S., Kinetic control of catalytic cvd for high-quality graphene at low temperatures. *ACS Nano* **2012**, *6*, 9996-10003.
71. Han, G.H.; Güneş, F.; Bae, J.J.; Kim, E.S.; Chae, S.J.; Shin, H.-J.; Choi, J.-Y.; Pribat, D.; Lee, Y.H., Influence of copper morphology in forming nucleation seeds for graphene growth. *Nano Letters* **2011**, *11*, 4144-4148.
72. Wei, D.; Liu, Y.; Wang, Y.; Zhang, H.; Huang, L.; Yu, G., Synthesis of n-doped graphene by chemical vapor deposition and its electrical properties. *Nano Letters* **2009**, *9*, 1752-1758.
73. Wu, T.; Zhang, X.; Yuan, Q.; Xue, J.; Lu, G.; Liu, Z.; Wang, H.; Wang, H.; Ding, F.; Yu, Q.*, et al.*, Fast growth of inch-sized single-crystalline graphene from a controlled single nucleus on cu-ni alloys. *Nature Materials* **2016**, *15*, 43-47.

74. Li, X.; Magnuson, C.W.; Venugopal, A.; An, J.; Suk, J.W.; Han, B.; Borysiak, M.; Cai, W.; Velamakanni, A.; Zhu, Y.*, et al.*, Graphene films with large domain size by a two-step chemical vapor deposition process. *Nano Letters* **2010**, *10*, 4328-4334.
75. Luo, Z.; Lu, Y.; Singer, D.W.; Berck, M.E.; Somers, L.A.; Goldsmith, B.R.; Johnson, A.T.C., Effect of substrate roughness and feedstock concentration on growth of wafer-scale graphene at atmospheric pressure. *Chemistry of Materials* **2011**, *23*, 1441-1447.
76. Jang, J.; Son, M.; Chung, S.; Kim, K.; Cho, C.; Lee, B.H.; Ham, M.-H., Low-temperature-grown continuous graphene films from benzene by chemical vapor deposition at ambient pressure. *Scientific Reports* **2015**, *5*, 17955.
77. Wassei, J.K.; Mecklenburg, M.; Torres, J.A.; Fowler, J.D.; Regan, B.C.; Kaner, R.B.; Weiller, B.H., Chemical vapor deposition of graphene on copper from methane, ethane and propane: Evidence for bilayer selectivity. *Small* **2012**, *8*, 1415-1422.
78. Vlassiouk, I.; Smirnov, S.; Regmi, M.; Surwade, S.P.; Srivastava, N.; Feenstra, R.; Eres, G.; Parish, C.; Lavrik, N.; Datskos, P.*, et al.*, Graphene nucleation density on copper: Fundamental role of background pressure. *The Journal of Physical Chemistry C* **2013**, *117*, 18919-18926.
79. Li, X.; Magnuson, C.W.; Venugopal, A.; Tromp, R.M.; Hannon, J.B.; Vogel, E.M.; Colombo, L.; Ruoff, R.S., Large-area graphene single crystals grown by low-pressure chemical vapor deposition of methane on copper. *Journal of the American Chemical Society* **2011**, *133*, 2816-2819.
80. Faggio, G.; Capasso, A.; Messina, G.; Santangelo, S.; Dikonimos, T.; Gagliardi, S.; Giorgi, R.; Morandi, V.; Ortolani, L.; Lisi, N., High-temperature growth of graphene films on copper foils by ethanol chemical vapor deposition. *The Journal of Physical Chemistry C* **2013**, *117*, 21569-21576.
81. Zhang, B.; Lee, W.H.; Piner, R.; Kholmanov, I.; Wu, Y.; Li, H.; Ji, H.; Ruoff, R.S., Low-temperature chemical vapor deposition growth of graphene from toluene on electropolished copper foils. *ACS Nano* **2012**, *6*, 2471-2476.
82. Huang, P.Y.; Ruiz-Vargas, C.S.; van der Zande, A.M.; Whitney, W.S.; Levendorf, M.P.; Kevek, J.W.; Garg, S.; Alden, J.S.; Hustedt, C.J.; Zhu, Y.*, et al.*, Grains and grain boundaries in single-layer graphene atomic patchwork quilts. *Nature* **2011**, *469*, 389-392.
83. Raccichini, R.; Varzi, A.; Passerini, S.; Scrosati, B., The role of graphene for electrochemical energy storage. *Nature Materials* **2015**, *14*, 271-279.

84. Pumera, M., Graphene-based nanomaterials for energy storage. *Energy & Environmental Science* **2011**, *4*, 668-674.
85. Wang, E.N.; Karnik, R., Water desalination: Graphene cleans up water. *Nature Nanotechnology* **2012**, *7*, 552-554.
86. Jeong-Yuan, H.; Chun-Chiang, K.; Li-Chyong, C.; Kuei-Hsien, C., Correlating defect density with carrier mobility in large-scaled graphene films: Raman spectral signatures for the estimation of defect density. *Nanotechnology* **2010**, *21*, 465705.
87. Choi, D.S.; Kim, K.S.; Kim, H.; Kim, Y.; Kim, T.; Rhy, S.-h.; Yang, C.-M.; Yoon, D.H.; Yang, W.S., Effect of cooling condition on chemical vapor deposition synthesis of graphene on copper catalyst. *ACS Applied Materials & Interfaces* **2014**, *6*, 19574-19578.
88. Li, Z.; Zhang, W.; Fan, X.; Wu, P.; Zeng, C.; Li, Z.; Zhai, X.; Yang, J.; Hou, J., Graphene thickness control via gas-phase dynamics in chemical vapor deposition. *The Journal of Physical Chemistry C* **2012**, *116*, 10557-10562.
89. Liang, X.; Sperling, B.A.; Calizo, I.; Cheng, G.; Hacker, C.A.; Zhang, Q.; Obeng, Y.; Yan, K.; Peng, H.; Li, Q.*, et al.*, Toward clean and crackless transfer of graphene. *ACS Nano* **2011**, *5*, 9144-9153.
90. Li, X.; Zhu, Y.; Cai, W.; Borysiak, M.; Han, B.; Chen, D.; Piner, R.D.; Colombo, L.; Ruoff, R.S., Transfer of large-area graphene films for high-performance transparent conductive electrodes. *Nano Letters* **2009**, *9*, 4359-4363.
91. Polsen, E.S.; McNerny, D.Q.; Viswanath, B.; Pattinson, S.W.; John Hart, A., High-speed roll-to-roll manufacturing of graphene using a concentric tube cvd reactor. *Scientific Reports* **2015**, *5*, 10257.
92. Ryu, J.; Kim, Y.; Won, D.; Kim, N.; Park, J.S.; Lee, E.-K.; Cho, D.; Cho, S.-P.; Kim, S.J.; Ryu, G.H.*, et al.*, Fast synthesis of high-performance graphene films by hydrogen-free rapid thermal chemical vapor deposition. *ACS Nano* **2014**, *8*, 950-956.
93. Bae, S.; Kim, H.; Lee, Y.; Xu, X.; Park, J.-S.; Zheng, Y.; Balakrishnan, J.; Lei, T.; Ri Kim, H.; Song, Y.I.*, et al.*, Roll-to-roll production of 30-inch graphene films for transparent electrodes. *Nature Nanotechnology* **2010**, *5*, 574-578.
94. Kim, M.-S.; Woo, J.-M.; Geum, D.-M.; Rani, J.R.; Jang, J.-H., Effect of copper surface pre-treatment on the properties of cvd grown graphene. *AIP Advances* **2014**, *4*, 127107.
95. Jia, C.; Jiang, J.; Gan, L.; Guo, X., Direct optical characterization of graphene growth and domains on growth substrates. *Scientific Reports* **2012**, *2*, 707.

96. Liu, W.; Li, H.; Xu, C.; Khatami, Y.; Banerjee, K., Synthesis of high-quality monolayer and bilayer graphene on copper using chemical vapor deposition. *Carbon* **2011**, *49*, 4122-4130.
97. Vlassiouk, I.; Fulvio, P.; Meyer, H.; Lavrik, N.; Dai, S.; Datskos, P.; Smirnov, S., Large scale atmospheric pressure chemical vapor deposition of graphene. *Carbon* **2013**, *54*, 58-67.
98. Soo Min, K.; Allen, H.; Yi-Hsien, L.; Mildred, D.; Tomás, P.; Ki Kang, K.; Jing, K., The effect of copper pre-cleaning on graphene synthesis. *Nanotechnology* **2013**, *24*, 365602.
99. Lupina, G.; Kitzmann, J.; Costina, I.; Lukosius, M.; Wenger, C.; Wolff, A.; Vaziri, S.; Östling, M.; Pasternak, I.; Krajewska, A.*, et al.*, Residual metallic contamination of transferred chemical vapor deposited graphene. *ACS Nano* **2015**, *9*, 4776-4785.
100. Ambrosi, A.; Pumera, M., The cvd graphene transfer procedure introduces metallic impurities which alter the graphene electrochemical properties. *Nanoscale* **2014**, *6*, 472-476.
101. Ostrikov, K., Colloquium: Reactive plasmas as a versatile nanofabrication tool. *Reviews of Modern Physics* **2005**, *77*, 489-511.
102. Ostrikov, K.; Neyts, E.C.; Meyyappan, M., Plasma nanoscience: From nano-solids in plasmas to nano-plasmas in solids. *Advances in Physics* **2013**, *62*, 113-224.
103. van der Laan, T.; Kumar, S.; Ostrikov, K.K., Water-mediated and instantaneous transfer of graphene grown at 220 degrees c enabled by a plasma. *Nanoscale* **2015**, *7*, 20564-20570.
104. Takatoshi, Y.; Jaeho, K.; Masatou, I.; Masataka, H., Low-temperature graphene synthesis using microwave plasma cvd. *Journal of Physics D* **2013**, *46*, 063001.
105. Kim, J.; Ishihara, M.; Koga, Y.; Tsugawa, K.; Hasegawa, M.; Iijima, S., Low-temperature synthesis of large-area graphene-based transparent conductive films using surface wave plasma chemical vapor deposition. *Applied Physics Letters* **2011**, *98*, 091502.
106. Dolgov, A.; Lopaev, D.; Lee, C.J.; Zoethout, E.; Medvedev, V.; Yakushev, O.; Bijkerk, F., Characterization of carbon contamination under ion and hot atom bombardment in a tin-plasma extreme ultraviolet light source. *Applied Surface Science* **2015**, *353*, 708-713.
107. Watanabe, H.; Kondo, H.; Okamoto, Y.; Hiramatsu, M.; Sekine, M.; Baba, Y.; Hori, M., Carbon nanowall scaffold to control culturing of cervical cancer cells. *Applied Physics Letters* **2014**, *105*, 244105.

108. Seo, D.H.; Yick, S.; Pineda, S.; Su, D.W.; Wang, G.X.; Han, Z.J.; Ostrikov, K., Single-step, plasma-enabled reforming of natural precursors into vertical graphene electrodes with high areal capacitance. *ACS Sustainable Chemistry & Engineering* **2015**, *3*, 544-551.

109. Slobodian, P.; Cvelbar, U.; Riha, P.; Olejnik, R.; Matyas, J.; Filipic, G.; Watanabe, H.; Tajima, S.; Kondo, H.; Sekine, M.*, et al.*, High sensitivity of a carbon nanowall-based sensor for detection of organic vapours. *RSC Advances* **2015**, *5*, 90515-90520.

110. Krivchenko, V.A.; Evlashin, S.A.; Mironovich, K.V.; Verbitskiy, N.I.; Nefedov, A.; Wöll, C.; Kozmenkova, A.Y.; Suetin, N.V.; Svyakhovskiy, S.E.; Vyalikh, D.V.*, et al.*, Carbon nanowalls: The next step for physical manifestation of the black body coating. *Scientific Reports* **2013**, *3*, 3328.

111. Davami, K.; Shaygan, M.; Kheirabi, N.; Zhao, J.; Kovalenko, D.A.; Rümmeli, M.H.; Opitz, J.; Cuniberti, G.; Lee, J.-S.; Meyyappan, M., Synthesis and characterization of carbon nanowalls on different substrates by radio frequency plasma enhanced chemical vapor deposition. *Carbon* **2014**, *72*, 372-380.

112. Zhao, J.; Shaygan, M.; Eckert, J.; Meyyappan, M.; Rümmeli, M.H., A growth mechanism for free-standing vertical graphene. *Nano Letters* **2014**, *14*, 3064-3071.

113. Shang, N.G.; Papakonstantinou, P.; McMullan, M.; Chu, M.; Stamboulis, A.; Potenza, A.; Dhesi, S.S.; Marchetto, H., Catalyst-free efficient growth, orientation and biosensing properties of multilayer graphene nanoflake films with sharp edge planes. *Advanced Functional Materials* **2008**, *18*, 3506-3514.

114. Hiramatsu, M.; Shiji, K.; Amano, H.; Hori, M., Fabrication of vertically aligned carbon nanowalls using capacitively coupled plasma-enhanced chemical vapor deposition assisted by hydrogen radical injection. *Applied Physics Letters* **2004**, *84*, 4708-4710.

115. Alexander, M.; Roumen, V.; Koen, S.; Alexander, V.; Liang, Z.; Gustaaf Van, T.; Annick, V.; Chris Van, H., Synthesis of few-layer graphene via microwave plasma-enhanced chemical vapour deposition. *Nanotechnology* **2008**, *19*, 305604.

116. Mineo, H.; Shinji, M.; Takeyoshi, H.; Hiroki, K.; Masaru, H.; Hiroyuki, K., Fabrication of carbon nanowalls on carbon fiber paper for fuel cell application. *Japanese Journal of Applied Physics* **2013**, *52*, 01AK03.

117. Bo, Z.; Zhu, W.; Ma, W.; Wen, Z.; Shuai, X.; Chen, J.; Yan, J.; Wang, Z.; Cen, K.; Feng, X., Vertically oriented graphene bridging active-layer/current-collector interface for ultrahigh rate supercapacitors. *Advanced Materials* **2013**, *25*, 5799-5806.

118. Plummer, J., Graphene: Hierarchical fibres. *Nature Materials* **2015**, *14*, 1075-1075.
119. Yin, S.; Zhang, Y.; Kong, J.; Zou, C.; Li, C.M.; Lu, X.; Ma, J.; Boey, F.Y.C.; Chen, X., Assembly of graphene sheets into hierarchical structures for high-performance energy storage. *ACS Nano* **2011**, *5*, 3831-3838.
120. Ruffieux, P.; Wang, S.; Yang, B.; Sánchez-Sánchez, C.; Liu, J.; Dienel, T.; Talirz, L.; Shinde, P.; Pignedoli, C.A.; Passerone, D.*, et al.*, On-surface synthesis of graphene nanoribbons with zigzag edge topology. *Nature* **2016**, *531*, 489-492.
121. Zhu, M.; Wang, J.; Holloway, B.C.; Outlaw, R.A.; Zhao, X.; Hou, K.; Shutthanandan, V.; Manos, D.M., A mechanism for carbon nanosheet formation. *Carbon* **2007**, *45*, 2229-2234.
122. Cui, L.; Chen, J.; Yang, B.; Sun, D.; Jiao, T., Rf-pecvd synthesis of carbon nanowalls and their field emission properties. *Applied Surface Science* **2015**, *357, Part A*, 1-7.
123. Wang, J.; Zhu, M.; Outlaw, R.A.; Zhao, X.; Manos, D.M.; Holloway, B.C., Synthesis of carbon nanosheets by inductively coupled radio-frequency plasma enhanced chemical vapor deposition. *Carbon* **2004**, *42*, 2867-2872.
124. Krivchenko, V.; Shevnin, P.; Pilevsky, A.; Egorov, A.; Suetin, N.; Sen, V.; Evlashin, S.; Rakhimov, A., Influence of the growth temperature on structural and electron field emission properties of carbon nanowall/nanotube films synthesized by catalyst-free pecvd. *Journal of Materials Chemistry* **2012**, *22*, 16458-16464.
125. Turner, A.P.F., Biosensors: Sense and sensibility. *Chemical Society Reviews* **2013**, *42*, 3184-3196.
126. Pineda, S.; Han, Z.; Ostrikov, K., Plasma-enabled carbon nanostructures for early diagnosis of neurodegenerative diseases. *Materials* **2014**, *7*, 4896.
127. Daniels, J.S.; Pourmand, N., Label-free impedance biosensors: Opportunities and challenges. *Electroanalysis* **2007**, *19*, 1239-1257.
128. Sin, M.L.Y.; Mach, K.E.; Wong, P.K.; Liao, J.C., Advances and challenges in biosensor-based diagnosis of infectious diseases. *Expert Review of Molecular Diagnostics* **2014**, *14*, 225-244.
129. Wang, J., Glucose biosensors: 40 years of advances and challenges. *Electroanalysis* **2001**, *13*, 983-988.
130. Yang, W.; Ratinac, K.R.; Ringer, S.P.; Thordarson, P.; Gooding, J.J.; Braet, F., Carbon nanomaterials in biosensors: Should you use nanotubes or graphene? *Angewandte Chemie International Edition* **2010**, *49*, 2114-2138.

131. Pumera, M., Graphene in biosensing. *Materials Today* **2011**, *14*, 308-315.
132. Shao, Y.; Wang, J.; Wu, H.; Liu, J.; Aksay, I.A.; Lin, Y., Graphene based electrochemical sensors and biosensors: A review. *Electroanalysis* **2010**, *22*, 1027-1036.
133. Kuila, T.; Bose, S.; Khanra, P.; Mishra, A.K.; Kim, N.H.; Lee, J.H., Recent advances in graphene-based biosensors. *Biosensors and Bioelectronics* **2011**, *26*, 4637-4648.
134. Wang, Y.; Li, Z.; Wang, J.; Li, J.; Lin, Y., Graphene and graphene oxide: Biofunctionalization and applications in biotechnology. *Trends in Biotechnology* **2011**, *29*, 205-212.
135. Schwarzenbach, H.; Nishida, N.; Calin, G.A.; Pantel, K., Clinical relevance of circulating cell-free micrornas in cancer. *Nature Reviews Clinical Oncology* **2014**, *11*, 145-156.
136. Hong, B.; Sun, A.; Pang, L.; Venkatesh, A.G.; Hall, D.; Fainman, Y., Integration of faradaic electrochemical impedance spectroscopy into a scalable surface plasmon biosensor for in tandem detection. *Optics Express* **2015**, *23*, 30237-30249.
137. Luo, X.; Davis, J.J., Electrical biosensors and the label free detection of protein disease biomarkers. *Chemical Society Reviews* **2013**, *42*, 5944-5962.
138. Hardy, J.A.; Higgins, G.A., Alzheimer's disease: The amyloid cascade hypothesis. *Science* **1992**, *256*, 184-185.
139. Cheng, L.; Doecke, J.D.; Sharples, R.A.; Villemagne, V.L.; Fowler, C.J.; Rembach, A.; Martins, R.N.; Rowe, C.C.; Macaulay, S.L.; Masters, C.L.*, et al.*, Prognostic serum mirna biomarkers associated with alzheimer/'s disease shows concordance with neuropsychological and neuroimaging assessment. *Molecular Psychiatry* **2015**, *20*, 1188-1196.
140. Querfurth, H.W.; LaFerla, F.M., Alzheimer's disease. *New England Journal of Medicine* **2010**, *362*, 329-344.
141. Vogt, S.; Su, Q.; Gutiérrez-Sánchez, C.; Nöll, G., Critical view on electrochemical impedance spectroscopy using the ferri/ferrocyanide redox couple at gold electrodes. *Analytical Chemistry* **2016**, *88*, 4383-4390.
142. Bogomolova, A.; Komarova, E.; Reber, K.; Gerasimov, T.; Yavuz, O.; Bhatt, S.; Aldissi, M., Challenges of electrochemical impedance spectroscopy in protein biosensing. *Analytical Chemistry* **2009**, *81*, 3944-3949.
143. Zhang, Y.; Liu, Y.; Chu, Z.; Shi, L.; Jin, W., Amperometric glucose biosensor based on direct assembly of prussian blue film with ionic liquid-chitosan matrix assisted enzyme immobilization. *Sensors and Actuators B: Chemical* **2013**, *176*, 978-984.

144. Parlak, O.; Tiwari, A.; Turner, A.P.F.; Tiwari, A., Template-directed hierarchical self-assembly of graphene based hybrid structure for electrochemical biosensing. *Biosensors and Bioelectronics* **2013**, *49*, 53-62.
145. Zhang, L.L.; Zhou, R.; Zhao, X.S., Graphene-based materials as supercapacitor electrodes. *Journal of Materials Chemistry* **2010**, *20*, 5983-5992.
146. Faraji, S.; Ani, F.N., The development supercapacitor from activated carbon by electroless plating | a review. *Renewable and Sustainable Energy Reviews* **2015**, *42*, 823-834.
147. Simon, P.; Gogotsi, Y., Materials for electrochemical capacitors. *Nature Materials* **2008**, *7*, 845-854.
148. Wang, G.; Zhang, L.; Zhang, J., A review of electrode materials for electrochemical supercapacitors. *Chemical Society Reviews* **2012**, *41*, 797-828.
149. El-Kady, M.F.; Shao, Y.; Kaner, R.B., Graphene for batteries, supercapacitors and beyond. *Nature Reviews Materials* **2016**, *1*, 16033.
150. Augustyn, V.; Simon, P.; Dunn, B., Pseudocapacitive oxide materials for high-rate electrochemical energy storage. *Energy & Environmental Science* **2014**, *7*, 1597-1614.
151. Conway, B.E.; Birss, V.; Wojtowicz, J., The role and utilization of pseudocapacitance for energy storage by supercapacitors. *Journal of Power Sources* **1997**, *66*, 1-14.
152. Drioli, E.; Ali, A.; Macedonio, F., Membrane distillation: Recent developments and perspectives. *Desalination* **2015**, *356*, 56-84.
153. Adham, S.; Hussain, A.; Matar, J.M.; Dores, R.; Janson, A., Application of membrane distillation for desalting brines from thermal desalination plants. *Desalination* **2013**, *314*, 101-108.
154. Xie, M.; Nghiem, L.D.; Price, W.E.; Elimelech, M., A forward osmosis ¦ membrane distillation hybrid process for direct sewer mining: System performance and limitations. *Environmental Science & Technology* **2013**, *47*, 13486-13493.
155. Alkhudhiri, A.; Darwish, N.; Hilal, N., Membrane distillation: A comprehensive review. *Desalination* **2012**, *287*, 2-18.
156. Gullinkala, T.; Digman, B.; Gorey, C.; Hausman, R.; Escobar, I.C., Chapter 4 desalination: Reverse osmosis and membrane distillation. In *Sustainability science and engineering*, Isabel, C.E.; Andrea, I.S., Eds. Elsevier: 2010; Vol. Volume 2, pp 65-93.

157. Sun, P.; Wang, K.; Zhu, H., Recent developments in graphene-based membranes: Structure, mass-transport mechanism and potential applications. *Advanced Materials* **2016**, *28*, 2287-2310.
158. Robertson, A.W.; Lee, G.-D.; He, K.; Gong, C.; Chen, Q.; Yoon, E.; Kirkland, A.I.; Warner, J.H., Atomic structure of graphene subnanometer pores. *ACS Nano* **2015**, *9*, 11599-11607.
159. Celebi, K.; Buchheim, J.; Wyss, R.M.; Droudian, A.; Gasser, P.; Shorubalko, I.; Kye, J.-I.; Lee, C.; Park, H.G., Ultimate permeation across atomically thin porous graphene. *Science* **2014**, *344*, 289-292.
160. Koenig, S.P.; Wang, L.; Pellegrino, J.; Bunch, J.S., Selective molecular sieving through porous graphene. *Nat Nano* **2012**, *7*, 728-732.
161. Cohen-Tanugi, D.; Grossman, J.C., Water desalination across nanoporous graphene. *Nano Letters* **2012**, *12*, 3602-3608.
162. Surwade, S.P.; Smirnov, S.N.; Vlassiouk, I.V.; Unocic, R.R.; Veith, G.M.; Dai, S.; Mahurin, S.M., Water desalination using nanoporous single-layer graphene. *Nat Nano* **2015**, *10*, 459-464.
163. Garaj, S.; Hubbard, W.; Reina, A.; Kong, J.; Branton, D.; Golovchenko, J.A., Graphene as a subnanometre trans-electrode membrane. *Nature* **2010**, *467*, 190-193.
164. Mori, T.; Hiramatsu, M.; Yamakawa, K.; Takeda, K.; Hori, M., Fabrication of carbon nanowalls using electron beam excited plasma-enhanced chemical vapor deposition. *Diamond and Related Materials* **2008**, *17*, 1513-1517.
165. Niyogi, S.; Bekyarova, E.; Itkis, M.E.; Zhang, H.; Shepperd, K.; Hicks, J.; Sprinkle, M.; Berger, C.; Lau, C.N.; deHeer, W.A.*, et al.*, Spectroscopy of covalently functionalized graphene. *Nano Letters* **2010**, *10*, 4061-4066.
166. Zhigang, S.; Jinzhi, L.; Min, Y.; Xiaojing, Z.; Shulin, M., Preparation of graphene by jet cavitation. *Nanotechnology* **2011**, *22*, 365306.

2

Re-inventing CVD: Ambient-Air Graphene Synthesis

"But still try, for who knows what is possible?"

– Michael Faraday, 1870.

This chapter presents the ambient-air CVD technique for the synthesis of graphene from renewable precursors.

The controlled synthesis of atomically-thin crystalline films of nanostructured carbon (*i.e.*, graphene) necessitates the meticulous process of CVD. However, widely adopted techniques for the CVD of graphene films are resource-consuming, energy-intensive, and environmentally-destructive. In particular, the CVD synthesis of graphene involves high processing temperatures, extensive vacuum operation, continuous large-volume flows of purified gases, long annealing times, and are multi-staged (**Section 1.2.2**). Here, we present an ambient-air CVD technique for graphene synthesis which addresses these intrinsic limitations.

The ambient-air process enables graphene synthesis in a single-step, and is demonstrated to be energy efficient (*i.e.,* rapid, low temperature), resource-efficient (*i.e.*, no purified gases), green (*i.e.*, reforming renewable biomass precursors), low-cost, integration-friendly, technologically sustainable, and scalable.

In this chapter, fabrication and characterization of the ambient-air-derived graphene films are explored. We exemplify the essential process parameters (*e.g.,* cooling rate, precursor content, temperature, *etc.*) to enable controlled synthesis and tailored properties of the graphene film in the ambient-air process films (*i.e.*, morphology, disorder content, thickness, *etc.*). Graphene films with good optoelectronic and structural properties were obtained. On average, the graphene films demonstrated an

optical transmission of ~93.9%, a sheet resistance of ~324 Ω/sq, Raman I_D/I_G ratio of 0.15–0.25 and I_{2D}/I_G ratio of 0.95–1.50, and domain sizes ranging 200–500 nm. Further, we propose a mechanism for the growth of graphene in the ambient-air process, based on depth profiling of the as-grown film, analyses of the ambient-air composition in the reaction chamber, and reaction pathways for precursor reforming into graphene.

The ambient-air approach is compared against conventional CVD frameworks for graphene synthesis. Notably, the ambient-air technique offers numerous advantages and future opportunities for streamlined graphene production infrastructures and the realization of diverse graphene-enabled technologies.

This chapter addresses **Thesis Objective 1**.

Statement of contribution: Shafique Pineda (S.P.) and Dong Han Seo (D.H.S.) conceived the idea and together, conducted the experiments, and optimized and developed the ambient-air synthesis technique. S.P., D.H.S., Adrian T. Murdock (A.T.M.), Zhao Jun Han (Z.J.H.) and Kostya Ostrikov (K.O.) wrote the manuscript with input from all co-authors.

The following paper has been accepted for publication at **Nature Communications** [1].

References

[1] **Seo D.H.***, **Pineda S.***, Fang J.H., Gozukara Y., Yick S., Bendavid A., Lam S.K.H., Murdock A.T., Murphy A.B., Han Z.J., Ostrikov K., Single-Step Ambient-Air Synthesis of Graphene from Renewable Precursors as Electrochemical Genosensor, *Nature Communications* **2017,** 8 (14217) (***** = equal contribution).

Single-Step Ambient-Air Synthesis of Graphene from Renewable Precursors as Electrochemical Genosensor

Dong Han Seo[1,†], Shafique Pineda[1,2,†], Jinghua Fang[3], Yesim Gozukara[1], Samuel Yick[1], Avi Bendavid[1], Simon K. H. Lam[1], Adrian T. Murdock[1], Anthony B. Murphy[1], Zhao Jun Han[1,*], and Kostya (Ken) Ostrikov[4,1,2]

† These authors contributed equally to this work.

[1] CSIRO Manufacturing, P.O. Box 218, Bradfield Road, Lindfield, NSW 2070, Australia.

[2] School of Physics, The University of Sydney, Sydney, NSW 2006, Australia.

[3] School of Mathematical and Physical Sciences, The University of Technology, Sydney, NSW 2007, Australia

[4] Institute for Future Environments and Institute for Health and Biomedical Innovation, School of Chemistry, Physics, and Mechanical Engineering, Queensland University of Technology, Brisbane, QLD 4000, Australia.

Abstract

Thermal chemical vapor deposition techniques for graphene fabrication, while promising, are thus far limited by resource-consuming and energy-intensive principles. In particular, purified gases and extensive vacuum processing are necessary for creating a highly-controlled environment, isolated from ambient-air, to enable the growth of graphene films. Here we exploit the ambient-air environment to enable the growth of graphene films, without the need for compressed gases. A renewable natural precursor, soybean oil, is transformed into continuous graphene films, composed of single- to few-layers, in a single step. The enabling parameters for controlled synthesis and tailored properties of the graphene film are discussed, and a mechanism for the ambient-air growth is proposed. Furthermore, the functionality of the graphene is demonstrated through direct utilization as an electrode to realize an electrochemical sensor for nucleic acid

interactions (genosensor). Our method is applicable to other types of renewable precursors and may open a new avenue for low-cost synthesis of graphene films.

Introduction

Widely-adopted techniques for the synthesis of large-area, homogeneous, and highly-crystalline carbon nanostructures are primarily based on thermal chemical vapor deposition (CVD) methods, in which purified gases (*e.g.*, CH_4, H_2, Ar) are processed at elevated temperatures (typically around 1000 ^oC) over a prolonged period [1,2]. The use of purified gases, while critical to providing a controlled environment for generating the building units necessary for carbon nanostructure growth, is however, expensive, hazardous, and requires extensive vacuum processing. Moreover, complex and prolonged processes in the high-temperature environments incur additional operating costs, which further impede the scalability and commercialization of crystalline carbon nanostructures [3,4].

Graphene, an atomically-thin film of crystalline carbon, is a highly-promising nano-carbon material whose production is subject to the aforementioned limitations. Graphene films hold strong potential for application in diverse technologies, including water filtration and purification, renewable energy, sensors, personalized healthcare and medicine [5-7]. However, efficient, scalable, and low-cost production of graphene film with tuneable properties are essential for such technologies to be feasible. This ability remains a critical challenge.

Recent investigations have demonstrated significant progress in addressing several of these concerns to facilitate the translation of graphene technologies into commercial applications. This includes the transformation of carbon precursors of heterogeneous chemical states into graphene-related materials [8,9]. In particular, carbon-containing liquid or solid biomass precursors are attractive due to their low cost [9,10]. Nevertheless, highly-purified carrier gases and lengthy vacuum operations are still required for these precursors. The hazardous nature and high cost of these gases often reduce the production efficiency. It is thus highly topical and important to develop a

technologically and environmentally sustainable process that is free of compressed gases for the production of functional graphene films.

Here we present a single-step, rapid thermal synthesis of uniform and continuous graphene films in an ambient-air environment, using a cheap and renewable form of biomass, soybean oil, as the precursor. To the best of our knowledge, this is the first time that the synthesis of graphene film has been demonstrated in an ambient-air environment without any compressed gases. Graphene derived from this unique ambient-air process exhibits good and tuneable film properties, which are comparable to those of graphene synthesized with conventional methods [2,11]. This ambient-air process for graphene fabrication is fast, simple, safe, potentially scalable, and integration-friendly. Importantly, it offers the scope to potentially address the critical roadblocks towards large-scale, efficient graphene manufacturing.

Results

Controlled synthesis of graphene in ambient-air environment. Currently, graphene synthesis involves several key factors need to be improved: (i) lengthy high-temperature annealing processes to increase the grain size of the metal catalyst used to form graphene; (ii) utilization of purified and compressed gases to offer a homogenous and controlled delivery of carbon source materials; and (iii) the use of lengthy vacuum operation to avoid the presence of any detrimental reactive oxygen species from air [2,4]. To overcome these problems, we have designed a thermal CVD process to produce graphene in an ambient-air environment that is completely free of compressed or purified gases and requires minimum processing time.

The process is schematically illustrated in Fig. 1a, in which the precursor for graphene growth and a metal catalyst (*e.g.*, Ni foil) are placed close together inside the heating zone of a furnace, prior to heating the quartz tube. The quartz tube is then sealed and the temperature is increased. During the ramping stage, air inside the quartz tube is released through a valve to maintain atmospheric pressure. Once the annealing stage is complete, the sample is removed from the heating zone for rapid cooling. Raman

spectra of the samples grown at 800 °C in the ambient-air process indicated the presence of single-to-few layer graphene films covering the surface of the growth substrate (Fig. 1b).

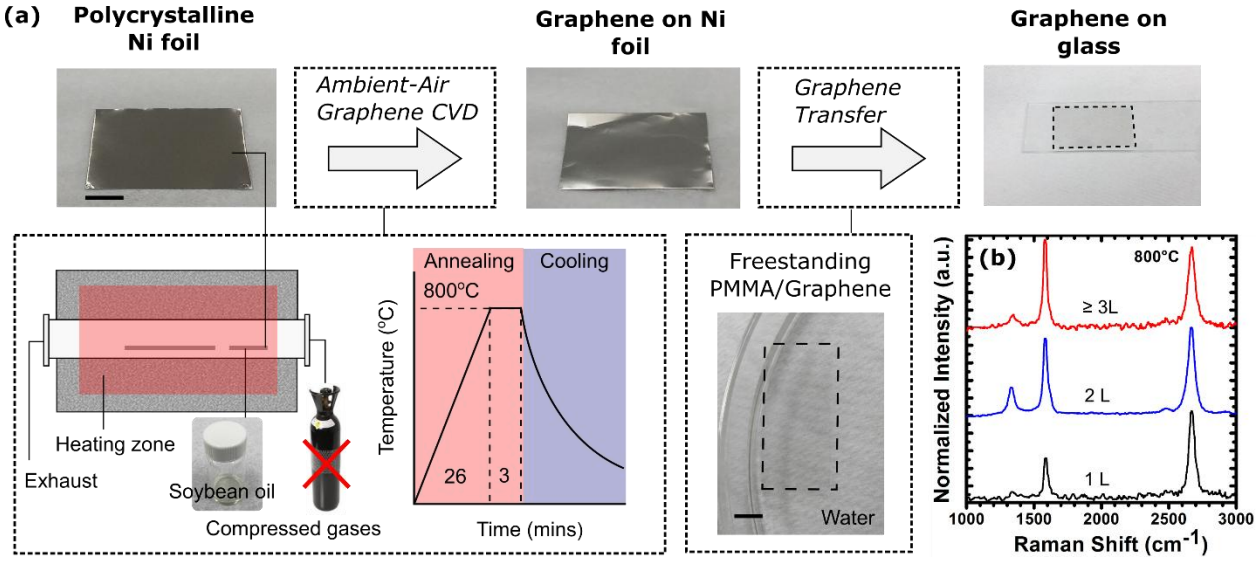

Figure 1 | Growing graphene films in the ambient-air process. (**a**) Polycrystalline Ni foil is thermally annealed together with soybean oil precursor, and the controlled synthesis of graphene is promoted in an ambient-air environment. Graphene films can then be transferred onto glass substrate. (**b**) Raman spectra indicate the presence of 1 layer, 2 layer and ≥ 3 layer regions in the graphene film grown at 800 °C. Scale bar: 1 cm in **a**.

In the standard operation, the catalyst is low-cost polycrystalline Ni foil. Graphene growth occurs by thermal reforming of a natural precursor, soybean oil, in a closed ambient-air environment. Unlike conventional CVD methods or conventional natural precursor methods for growing graphene, the technique does not require any purified gases [8,9]. Moreover, expensive vacuum processing is avoided. The natural precursors substituted for purified gases are cheaper and safer. By restricting the air flow into the quartz tube, the transformation of solid-state carbon into carbon dioxide or other gaseous species is prevented. By controlling the temperature, cooling rate and precursor amount, the process enables the growth of homogenous graphene films of good quality. A comparison of the method with other CVD processes is provided in Supplementary Table 1 and Supplementary Table 2.

The parameters observed to control the quality of graphene include temperature, processing time, precursor, substrate, and the ambient-air environment. Nickel acted as a good catalyst for the breakdown of precursor material (in this case, the soybean-oil molecules) into smaller building units that are essential for the synthesis of graphene [12].

To investigate how the transformation occurred in the process, we have analyzed the chemical composition of the annealed soybean oils at different temperatures (Supplementary Fig. 1). During the early stages of the annealing process, for instance at 300 ^{o}C, the long carbon chains in the soybean oil precursor were thermally dissociated into gaseous carbon building units such as methyl and ethyl species (Supplementary Fig. 1a). Other gaseous species were also generated, including hydrogen, water, hydroxyls, and carbon dioxide, as confirmed by mass spectrometry (Supplementary Fig. 1b – 1c). Traces of heavier hydrocarbons such as propane were also observed. Most of the oil was vaporized by about 425 ^{o}C and a rapid mass reduction of the oil was observed by thermogravimetric analysis below 500 ^{o}C (Supplementary Fig. 1d). These building units present in the vapor can diffuse through the tube during the heating stage. As the temperature gradually increases to 800 ^{o}C, these carbon building units begin to dissociate into carbon atoms and dissolve into the Ni bulk [13,14]. The sample was annealed for 3 mins at 800 ^{o}C to promote dissolution of carbon atoms in the Ni substrate. Finally, following the rapid cooling stage, carbon segregates from the bulk and crystallizes on the Ni surface forming graphene [12,15].

At elevated temperatures, long hydrocarbons in the oil decompose in the presence of O_2 to form water vapor. In particular, water vapor can promote the etching of amorphous carbon deposits on the Ni surface [16]. As such, we did not observe the formation of amorphous carbons in our sample. This also helps maintain the catalytic activity of the Ni surface in breaking down the precursor material [17]. Moreover, we have conducted a detailed analysis on the consumption of oxygen in the reactor during the growth process (Supplementary Note 1). We found that the precursor amount was critical for the consumption of reactive oxygen species. In the optimal growth condition, a slight carbon excessive environment is used to promote the growth of graphene and

deter the formation of amorphous carbon. On the other hand, an over excessive amount of precursor material led to an oversaturation of deposited carbon in the bulk of Ni, and subsequently, the crystallization of graphite on the Ni surface. This may explain the resulting formation of thick graphene sheets as observed in Supplementary Fig. 2a. Moreover, in the case of an insufficient amount of precursor, oxygen species can be present in the as-grown product in the form of C–O amorphous carbons (Supplementary Fig. 2b), consistent with the aforementioned calculations of oxygen consumption (Supplementary Note 1) [18]. These experiments indicate the critical role of the thermally-dissociated precursor materials (*i.e*., hydrocarbons) in consuming the reactive oxygen species present in the ambient-air environment, which has a profound effect in controlling the quality of the as-grown graphene films.

We have also noticed that a slow cooling can promote excessive carbon segregation from the Ni bulk, which may account for the observed formation of a graphite-like film (Supplementary Fig. 2c). Another parameter that significantly influences the growth of graphene in the ambient air environment is the annealing temperature. At an annealing temperature of 500 ^{o}C, an incomplete formation of the graphene film was observed (Supplementary Fig. 2d). This may be attributed to an insufficient amount of energy to dissociate and reform the precursor material (*i.e.*, hydrocarbon species) required for graphene formation. Conversely, at a higher annealing temperature of 900 ^{o}C, thicker graphene sheets were observed (Supplementary Fig. 2e). This may arise from the increased rate of carbon diffusion, segregation, and graphitization as a result of the elevated temperature. Importantly, these parameters allow us to obtain graphene films with tuneable average thickness and optical transmission, as characterized by Raman spectroscopy and optical transmission (Supplementary Fig. 3).

It is worth mentioning that graphene did not form on other growth substrate materials with significantly lower carbon solubility than Ni, such as the commonly-used Cu foil. Moreover, we did not observe graphene formation on graphitic surfaces such as woven carbon cloth (Supplementary Fig. 4). This suggests that the use of Ni (through, *e.g.*, carbon solubility, carbon segregation ability, catalytic effect, possibility of formation of oxide in air) and its interaction with the precursor material play a critical role in enabling

the growth of graphene films. We also investigated the possibility of transforming other types of renewable oil groups. In particular, we were able to demonstrate the ambient-air growth of similar graphene films from other types of triglyceride (carbon)-containing precursors such as butter (Supplementary Fig. 5). As such, this method is versatile and may be tailored to transform other renewable carbon-containing natural precursors into graphene films.

Structure and properties of the graphene films. The structural morphology of the graphene film was analysed by transmission electron microscopy (TEM) (Fig. 2). The distribution of domain sizes, domain orientations, and thickness within the graphene film were characterized. The energy-filtered bright-field and dark-field images were obtained on multiple regions. In the bright-field image, the graphene film appeared uniform, with dark lines representing the overlapping at the grain boundaries (Fig. 2a and Supplementary Fig. 6a). In the dark-field image, the grain boundaries and rotated polycrystalline domains are clearly observed (Fig. 2b and Supplementary Fig. 6b), as indicated by the contrast variations. In addition, the observed Moire fringes (periodic stripes) arise from the mis-oriented overlapping multilayers. This confirmed that the strips/lines of darker contrast were indeed boundaries, as also indicated by the size and shape of the graphene domains. Further, mis-oriented hexagonal graphene adlayers are observed in Fig. 2c. From these TEM characterizations, we can deduce that the graphene film is composed of domains spanning ~200–500nm.

In addition, selected-area electron diffraction (SAED) patterns were taken across a typical region of the sample, where a slight rotation between these patterns was observed (Fig. 2d and Supplementary Fig. 6c). The high-resolution TEM images at the domain edges illustrate the presence of few-layered graphene domains within the film (Fig. 2e). These results demonstrate that the graphene film is composed of mis-oriented domains of turbostratic bi/few-layer graphene [19].

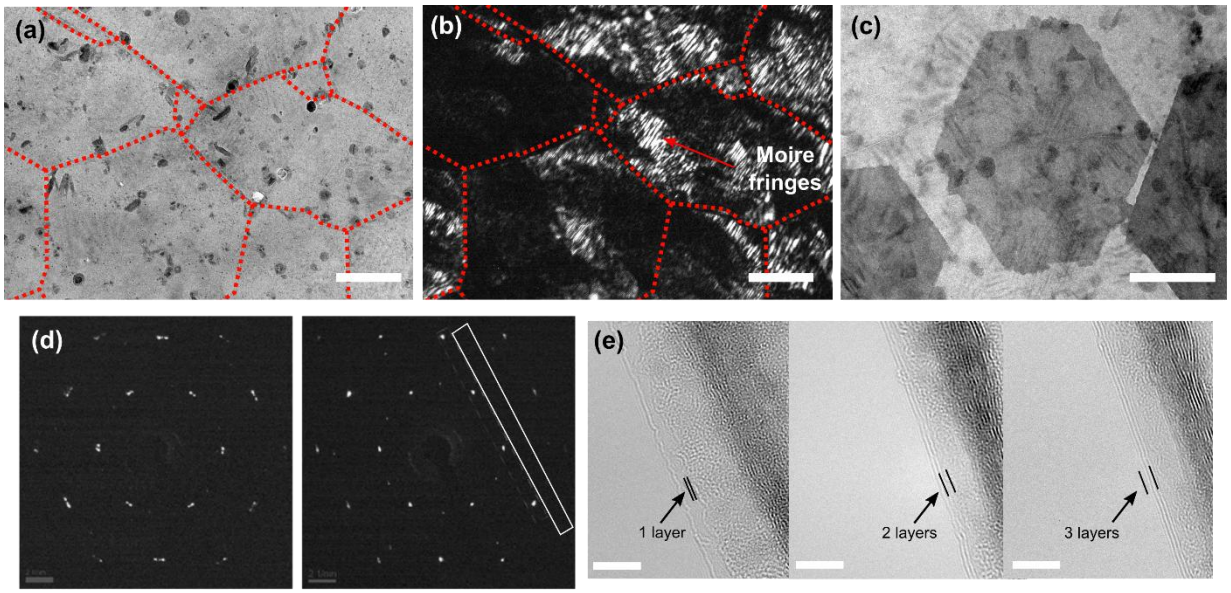

Figure 2 | TEM characterization of the graphene film grown in an ambient-air environment. (**a**) Bright-field TEM and (**b**) corresponding dark-field TEM with grain boundaries outlined in red. (**c**) TEM image of mis-oriented hexagonal graphene adlayers and (**d**) SAED patterns. The intensity profile taken from the region outlined by the white box is shown in Supplementary Fig. 6c. (**e**) HRTEM of few-layered graphene films, with the dark regions corresponding to folded edges in the film. Scale bars: 200 nm in **a,b**,**c** and 5 nm in **e**.

The structural, optical and electrical properties of the graphene film were also analyzed by Raman spectroscopy mapping, optical transmission spectroscopy, and four-point probe measurements. Before performing these characterizations, a 4x2 cm^2 graphene film grown in the ambient-air process was transferred from the Ni foil substrate to a glass surface, as demonstrated in Fig. 3a. An optical micrograph of the transferred graphene film is also included. The graphene film was observed to grow continuously over the entire Ni surface, with regions of varying thickness (Fig. 3a). To check the uniformity of graphene film, Raman spectral mapping of I_D/I_G and I_{2D}/I_G intensity ratios were taken from 4 regions R1–R4, as denoted in Fig. 3a. Typically, three distinct peaks are present in the Raman spectra of graphene, namely, the characteristic disorder peak (D-band) at ~1350 cm^{-1}, the graphitic peak (G-band) at ~1580 cm^{-1}, and the second-order 2D-band at ~2670 cm^{-1}. The D-band is attributed to the finite crystallite size effect and various defects induced in the sp^2 carbon materials; the G-band arises from the in-plane vibrational E_{2g} mode of the sp^2-hybridized carbon; and the 2D-band is a second-

order Raman spectral feature due to the three-dimensional inter-planar stacking of hexagonal carbon networks [20], and its peak position can give an indication of the number of graphene layers [21].

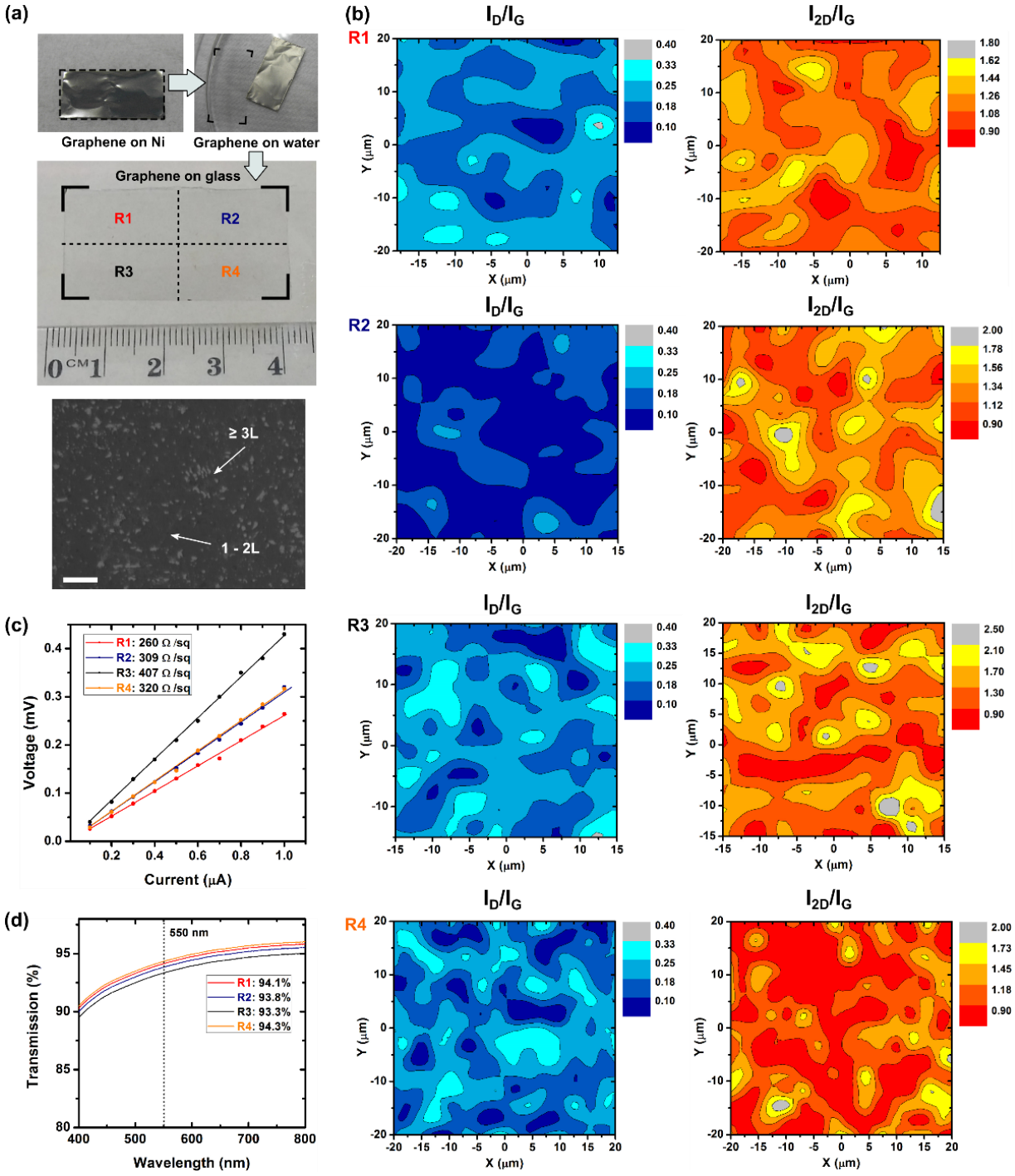

Figure 3 | Characterizations of the graphene film grown in an ambient-air environment. (**a**) A 4x2 cm^2 graphene grown on Ni foil is transferred onto glass. Measurements were taken over 4

quadrants as labelled on the graphene surface. An optical micrograph of the graphene film transferred onto glass is also included. (**b**) Raman spectral analyses of the intensity ratios of I_D/I_G and I_{2D}/I_G. (**c**) Four-point probe and (**d**) optical transmission measurements of sheet resistance of graphene films in the respective regions. Scale bar: 20 μm in **a**.

For the present film, the intensity ratios of I_D/I_G is 0.15 – 0.25, I_{2D}/I_G is 0.95 – 1.50 (Fig. 3b), and the 2D peak position resides around 2670 cm^{-1}. These values suggest that the film is composed of single- to few-layer graphene. Based on the TEM and Raman measurements, a carrier mobility of 500 – 750 $cm^2\ V^{-1}\ s^{-1}$ was estimated for the graphene film (see detailed calculation in Supplementary Note 2) [22,23]. Fig. 3c shows that the graphene film has an average sheet resistance of 324 Ω sq^{-1}, which is consistent with the observed graphene thickness, grain size and disorder content. Further, an average optical transmittance of 93.9% was obtained (Fig. 3d), suggesting a thin film structure with single-to-few layer graphene [24]. These characterizations are in good agreement with the microscopic structure of the graphene film (*i.e.,* domain size, sheet thickness) obtained by TEM.

The surface chemical properties of the graphene film were analyzed by X-ray photoelectron spectroscopy (XPS). The survey scan of Fig. 4a shows a dominant narrow C 1s peak at the binding energy of 284.5 eV, whereas other peaks were attributed to the Ni growth substrate. The C 1s narrow scan in Fig. 4b can be deconvoluted into five peaks, corresponding to the carbon sp^2 (284.5 eV), sp^3 (285.4 eV), nickel carbide (~282.8 eV), and C-O-C (~286.5 eV) and O-C=O functional groups (~288.7 eV) [25]. In particular, the graphene film has a good sp^2/sp^3 ratio of ~5.0, indicating the presence of graphene lattices with good structural quality. These characterizations provide further evidence that the graphene film grown in an ambient-air environment are comparable to those produced by the conventional CVD methods [4,11,26].

Moreover, this ambient-air process for graphene synthesis was also applicable to Ni foil growth substrates of lower purity. Graphene films of comparable quality were produced with low-purity polycrystalline Ni foils (99%) rather than high-purity foils (Supplementary Fig. 7). Such low purity foils offer significant cost reduction in the scale-up for

manufacturing graphene films. In addition, there is potential for further scale-up in the production capacity with the utilization of larger reaction chambers.

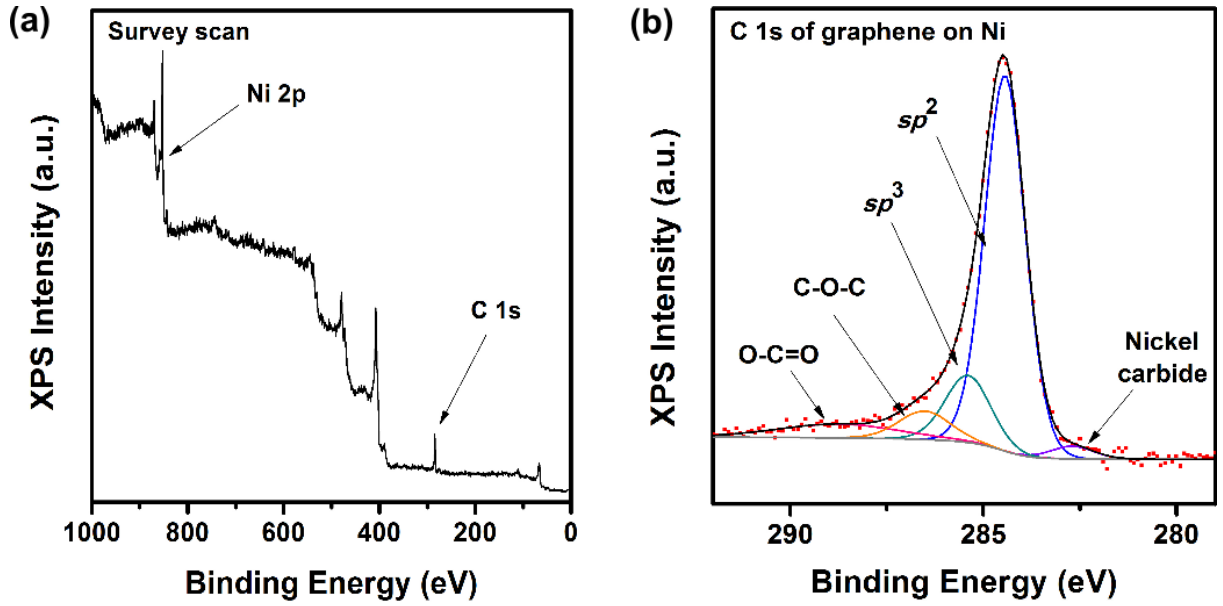

Figure 4 | Surface chemical analysis of the graphene film grown in an ambient-air environment. (**a**) XPS survey scan shows the dominant C 1s peak, where other peaks are identified from the Ni growth substrate. (**b**) C 1s narrow scan and the deconvolution show sp^2, sp^3, nickel carbide and oxygen-attached carbon functional groups.

Proposed mechanism of graphene growth in ambient-air process. The growth of graphene in an ambient-air environment may initially seem counter-intuitive, as graphene is expected to be destroyed in air at elevated temperatures (above 500 ^{o}C). However, we hypothesize that the unique processing conditions promote the controlled synthesis of graphene films in an otherwise destructive environment. Specifically, the thermally-dissociated precursor material decomposes in the presence of reactive oxygen species from the ambient-air, leading to the formation of water vapor as a by-product (Supplementary Fig. 1). The water vapor may help suppress the deposition of amorphous carbon, promote the thinning of graphene layers, and maintain the catalytic ability of the Ni substrate in breaking down the precursor material into smaller building units necessary for the growth of graphene films.

To better understand the growth process and the possible interaction with Ni substrate, we conducted experiments to probe the surface composition of Ni foils following treatments at elevated temperatures. In particular, we investigated the composition of:

(i) Ni foil heat treated in ambient environment *without* soy bean oil, where surface oxidation will be prevalent (Supplementary Fig. 8);

(ii) Ni foil heat treated in ambient environment *with* soy bean oil, following procedure as outlined previously for the growth of graphene, where surface oxidation may be prevented (Supplementary Fig. 9).

Our XPS analyses showed that when the Ni foil was heated in the ambient environment *without* soybean oil, oxygen was easily identified on the surface (Ni:O ratio of 1:1.83). However, when the Ni foil was heated with soybean oil, the oxygen content was significantly reduced (Ni:O ratio of 2.69:1). These results indicated that the breakdown of soybean oil in the reaction chamber provided a reaction pathway for the consumption of O_2, which consequently limited the surface oxidation of Ni at elevated temperatures.

Thus, we propose a growth mechanism based on these supporting evidences. Firstly, soybean oil thermally dissociates into a range of carbon building units, *e.g.* CH_3, C_2H_2, and other species, at the ramping stage (Supplementary Fig. 1). During this stage, molecular fragments of the precursor material may react with and consume O_2 inside the reaction chamber through possible reaction routes as outlined in Supplementary Note 1. Water vapour produced as a by-product of the consumption of O_2 may also help suppress the formation of amorphous carbon. The formation of water was supported by the observation of water condensation at the cool ends of the quartz tube outside the heating zone. These molecular fragments may further decompose at higher temperatures to provide a source of carbon dissolved into the Ni foil. This is supported by the detection of an extended nickel carbide peak in the XPS spectra of an etched graphene/Ni sample (Supplementary Fig. 9). Then, growth of graphene can occur through a combination of surface-mediated growth on the Ni foil and precipitation from dissolved species when the sample is cooled. The precipitation step is critical as we

observed that the cooling rate was important to control the thickness of the graphene films (Supplementary Fig. 3).

Graphene as a biosensing electrode. Electrochemical sensing methods for minute amounts of nucleic acid samples offer attractive opportunities for a plethora of preventative health technologies, which require portable, cost-effective, and low-power readout devices [27]. In particular, neurodegenerative diseases such as Alzheimer's disease are becoming more prevalent with the ageing population [28]. Alzheimer's disease is best managed with early intervention therapies provided that it can be diagnosed as early as possible. To this end, post-transcriptional epigenetic regulations of gene expressions have been found to provide highly-valuable serum-based nucleic acid biomarkers that may be utilized to enable early diagnostic strategies for the disease [29-31]. Consequently, the favourable properties of graphene motivates its applicability as a biosensing electrode.

The assembly of the electrochemical graphene-based biosensor is illustrated in Fig. 5a. Briefly, the as-grown graphene was firstly treated by oxygen plasma to introduce carboxylic functional groups on its surface. Subsequently, carbodiimide chemistry is employed to facilitate the covalent immobilization of probe miRNAs, and enable the specific detection of the complementary miRNA sequence (see Methods).

Performance of the graphene sensor was quantified by electrochemical impedance spectroscopy (EIS) technique. The charge-transfer resistance (R_{ct}) was measured to characterize the response of graphene to the surface immobilization of miRNAs. The R_{ct} was observed to increase upon successful immobilization of probe miRNAs on the graphene surface (Supplementary Fig. 10a). With the addition of target miRNAs solution, an increase in ΔR_{ct} was observed as the concentration of target miRNAs was increased (Fig. 5b). We define ΔR_{ct} by $(R_{ct} - R_0)/R_0$, where R_0 is the charge-transfer resistance of the reference sample. This increase in ΔR_{ct} is attributed to an impeded charge transport at the graphene surface, caused by spatial blocking of the captured target miRNA molecules. In addition, the hybridization between complementary genomic sequences

may induce a build-up of negative surface charge, which may repulse negatively charged ferricyanide ions and lead to an increase in R_{ct} [32].

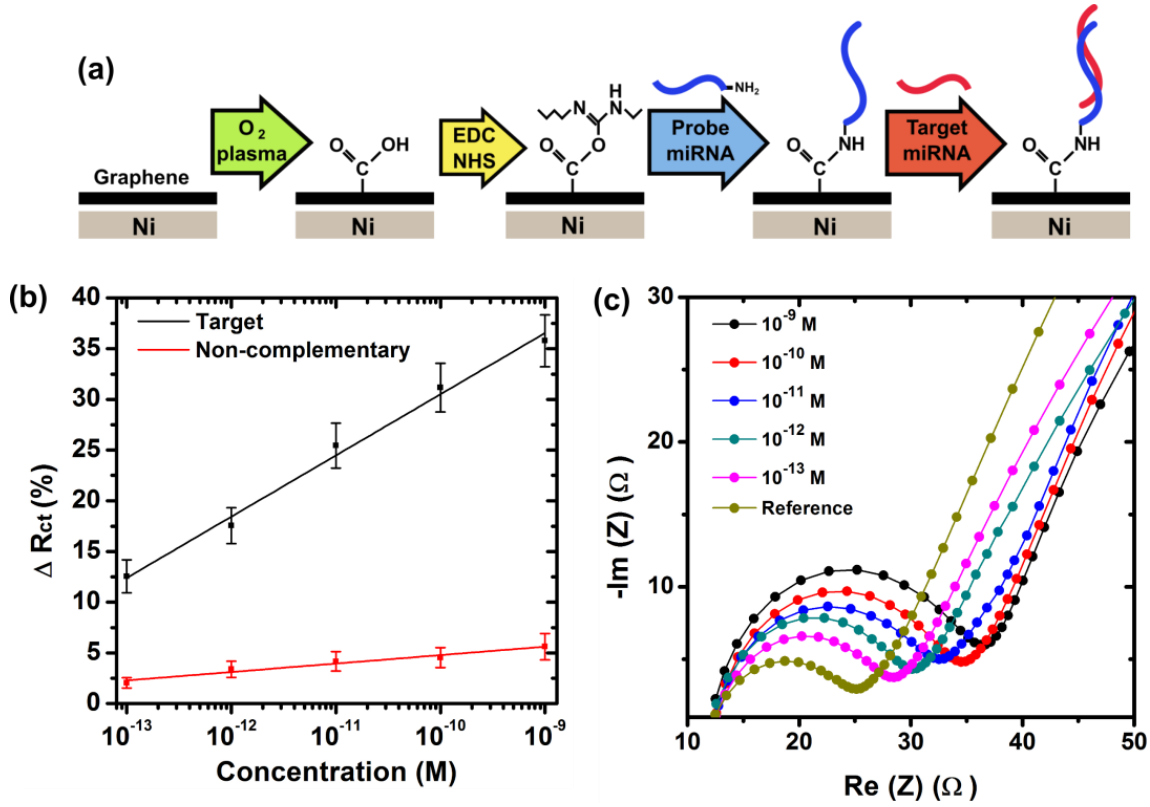

Figure 5 | Biosensor assembly and biosensing performance. (**a**) Schematics of the functionalization steps involved for the assembly of the graphene-based electrochemical biosensor. (**b**) Selectivity of biosensor is demonstrated by an increase in R_{ct} with increasing concentration of target miRNA. Error bars represent the standard error of the mean. (**c**) Individual EIS curves showing responses of the biosensor to the target miRNA at different concentrations.

The graphene-based sensor also demonstrates selectivity against miRNA sequences that are mismatched by a single RNA base, as shown in Fig. 5b. A slight increase in R_{ct} was observed at elevated concentrations of non-complementary miRNA. This may be attributed to an increase in the non-specifically adsorbed miRNAs. In contrast, the EIS response of graphene in the presence of complementary miRNAs demonstrated a dynamic sensing range spanning 0.1 pM to 1 nM, with a limit of quantification (LOQ) of 8.64 x 10^{-14} M (Fig. 5b,c). Furthermore, the sensing performance of the graphene electrode was evaluated in the presence of common interfering analytes (Supplementary Fig. 10b). The graphene-based sensor demonstrated negligible

deviation in R_{ct} in the presence of serum albumins and electroactive analytes (*i.e.*, uric acid and ascorbic acid) at physiologically-relevant concentrations. This suggests that non-specific binding at the graphene surface did not interfere with the specific binding events with the target miRNA sequence.

The above performance is comparable to other graphene-based electrochemical sensors reported in the recent literature (Supplementary Table 3). For instance, graphene oxide (GO) nanosheets decorated with perylene tetracarboxylic acid diimide (PDI) have been utilized to enable a detection limit of 5.5×10^{-13} M single-stranded (ss)DNA [33]. Similarly, reduced GO have been functionalized with tryptamine to achieve a limit of detection of ssDNA at 5.2×10^{-13} M ssDNA [34]; and graphite fibers activated to form GO interfaces were capable of detecting ssDNA down to the concentrations of 5.6×10^{-12} M [35]. The graphene film grown in ambient-air may thus be promising for future developments of early diagnostic tools, where the quantification of multiple genomic biomarkers in complex biological environments is required.

Conclusions

Graphene films demonstrate excellent functional properties and are promising for diverse applications. However, the high cost and complexities associated with graphene production impede its commercial viability. To this end, we present a novel method for the synthesis of graphene films, in an atmospheric-pressure, compressed-gas-free ambient-air environment utilizing safe, low-cost renewable precursors. This ambient-air method offers numerous advantages over conventional thermal CVD techniques for graphene synthesis, which critically rely on resource- and time-consuming procedures (Supplementary Table 1, Supplementary Table 2, and Supplementary Note 3). Graphene films with good structural and optoelectronic properties were obtained. On average, the graphene film demonstrated an optical transmission of ~93.9%, a sheet resistance of ~324 Ω/sq, Raman I_D/I_G ratio of 0.15–0.25 and I_{2D}/I_G ratio of 0.95–1.50, and domain sizes ranging 200–500 nm. We exemplify the essential process parameters (*e.g.,* cooling rate, precursor content, temperature, *etc.*) to enable controlled synthesis

and tailored properties of the graphene film in the ambient-air process. Further, we propose a mechanism for the growth of graphene in the ambient-air process, based on depth profiling of the as-grown film, analyses of the ambient-air composition in the reaction chamber, and reaction pathways for precursor reforming into graphene. The functionality of the graphene films was demonstrated through its direct integration as an electrochemical genosensor, in which sensitive and selective bio-detection was realized. Importantly, the ambient-air synthesis of graphene films from renewable precursors offers numerous advantages and opportunities for future streamlined integration into large-scale production infrastructures and the realization of diverse graphene-enabled technologies.

Methods

Ambient-air thermal synthesis of graphene. The growth of graphene was carried out in a thermal CVD furnace (OTF-1200X-UL, MTI Corp) with a quartz tube (100 cm in length, 5 cm in diameter). Polycrystalline Ni foils (25 μm, 99.5%, Alfa Aesar) were used as the growth substrate. The experimental schematic is shown in Fig. 1. Briefly, two alumina plates were placed in the heating zone of the furnace. One alumina plate was loaded with 0.14 mL of soybean oil precursor, and the other was loaded with the Ni foil growth substrate. The openings of the quartz tube were then sealed. The growth of graphene proceeds with a gradual heating and fast quenching temperature profile. Firstly, the furnace temperature was raised to 800 ^{o}C at a rate of 30 ^{o}C min^{-1}. This was followed by holding at 800 ^{o}C for 3 mins. After the growth step, the sample was immediately removed from the heating zone to enable a rapid cooling (at approximately 25 ^{o}C min^{-1}) to segregate the homogeneous and continuous graphene films. Due to the evaporation and thermal expansion of the precursor material, a small build-up in pressure within the tube was observed. Throughout the heating stage (200 to 800 ^{o}C), atmospheric pressure was maintained in the quartz tube by allowing this build-up of gases to exit via the exhaust of the tube. A controlled gas environment was created in the tube through enabling the circulation of gases produced by precursor evaporation.

Following the heating stage, pressure within the quartz tube was observed to be stabilized at atmospheric pressure. No additional gases were introduced into the quartz tube throughout the entire growth process.

Transfer of graphene. A poly (methyl methacrylate) (PMMA)-assisted transfer of graphene was adopted. Briefly, 46 mg mL^{-1} of PMMA (M_w 996,000 Sigma Aldrich) was spin-coated onto the as-grown graphene on Ni foil (3000 rpm for 1 min). The sample was then dried in open air for 12 h. Subsequently, the underlying Ni foil was dissolved in 1 M $FeCl_3$ in 30 minutes. The PMMA/graphene film then floated to the surface. This was washed several times with deionized (DI) water. Next, the PMMA/graphene was lifted off from the DI water bath and transferred onto a glass substrate. The PMMA was then dissolved with acetone, and the sample was repeatedly washed with DI water. The graphene on glass was then used for subsequent microscopy and electrical characterization.

Microscopy and microanalysis. Please refer to **Section 1.4** of Chapter 1, “Raman Spectroscopy”, “X-ray Photoelectron Spectroscopy (XPS)” and “Transmission Electron Microscopy (TEM)”, for their general experimental details. More specifically, in the XPS, both survey scans and narrow scans of C 1s and $Ni2p_{3/2}$ were conducted. The Ni and graphene/Ni surfaces were progressively etched through Ar bombardment to create a depth profile of the material.

Optical characterization. Optical images were obtained with an Olympus BX51 optical microscope. Transmittance measurements were obtained using a Varian Cary 5000 UV-Vis spectrophotometer. A graphene area of 4 cm^2 was used, and optical spectra were recorded in the wavelength range from 300 to 800 nm.

Electrical four-probe measurements. Silver paint was applied to the graphene transferred onto glass. A graphene area of 1 cm^2 was used. Four-point probe measurements were conducted at room temperature.

Inductively-coupled plasma (ICP) mass spectrometry analysis. The Netzsch STA 449 F1 instrument equipped with S-type DTA sensor was used for simultaneous thermogravimetric/differential thermal analysis (TGA/DTA) of the soybean oil precursor samples. Soybean oil samples were placed in Al_2O_3 holders, and were heated to required temperatures (300, 500 and 600 ^oC) at 10 $^oC\ min^{-1}$ heating rate under air purge gas. Correction/blank runs were carried out for each temperature range with empty reference and sample pans prior to sample thermal analysis. Evolved Gas Analysis was carried out by coupling the Netzsch system to a Thermostar Pfeiffer Quadrupole Mass Spectometry to determine gases and vapours evolving in the atomic mass range of up to 200 amu (plotted as mass to charge ratio m/z).

Biosensor device assembly. The as-grown graphene on Ni foil was treated with a low-temperature O_2 plasma (100 W, 7 s) to introduce carboxylic functional groups on its surface. The sample was placed flat and 2 cm below the plasma generation zone. The size of each sensing substrate was 2 x 1 cm^2. Then, the plasma-actived graphene was treated with 0.05 M *N*-(3-Dimethylaminopropyl)-*N*'-ethylcarbodiimide hydrochloride (EDC) and 0.03 M N-hydroxysulfosuccinimide (NHS) in phosphate buffered saline (PBS, pH=7, Sigma Aldrich) for 15 min. This enabled the formation of active ester intermediates via carbodiimide chemistry. Next, the surface of graphene was washed several times with PBS and DI water to remove excess EDC/NHS. Next, the surface of graphene was washed several times with phosphate-buffered saline (PBS, pH 7, Sigma Aldrich) and DI water to remove excess EDC and NHS. Then, NH_2-conjugated miRNAs (probe sequence: 5'-NH_2-GGTGGAGGGGACGTTTGCAGGT-3', Sigma Aldrich) were diluted in PBS to 0.2 μM, and 50 μL was pipetted onto the EDC-treated surface. This was left to incubate overnight in a wet environment and at room temperature. Next, the

sensing surface was washed with 0.05 % sodium dodecyl sufonate (SDS) (Sigma Aldrich) in 0.04 M hydroxylamine solution (Sigma Aldrich) to deactivate the remaining carboxylic functional groups and to remove non-specifically bound probe miRNAs. Then, 0.01 M Polyethylene glycol (PEG) (Sigma Aldrich) was loaded on the sensing surface to block the exposed areas of graphene to reduce further non-specific binding. Next, the (biomarker) miRNA sequence (target sequence: 5'-CCACCUCCCCUGCAAACGUCCA-3', Sigma Aldrich) was dissolved in human serum (Human Plasma AB, Sigma Aldrich) to obtain dynamic concentrations of 1 nM to 0.1 pM, which were pipetted onto the sensing surface. This was left to incubate at 45 ^{o}C for 20 min to induce hybridization between the complementary probe and target sequences. Finally, a washing step with PBS/DI water was employed to remove remaining non-specifically bounded target miRNAs. To demonstrate sensing specificity, a similar protocol was adopted by replacing the target sequence with a single-base mismatched miRNA sequence (non-complementary sequence: 5'-CCGCCUCCCCUGCAAACGUCCA-3', Sigma Aldrich). This fully-assembled device was then utilized in a three-electrode electrochemical cell for biosensing measurements.

Biosensing measurements. The electrochemical measurements were conducted in 10 mM $FeCN_6$ in 0.1 M Na_2SO_4 at room temperature. A three-electrode cell configuration was employed. The three-electrode cell used the as-grown graphene on Ni as the working electrode, a Pt wire as the counter electrode, and an Ag/AgCl reference electrode. The electrochemical impedance spectroscopy (EIS) measurements were conducted in the frequency range from 500 kHz to 1 kHz, using a BioLogic VSP 300 potentiostat/galvanostat instrument. The charge-transfer resistance (R_{ct}) of the sensing electrode was determined by the diameter of the semi-circle region in the EIS plots. The R_{ct} of the sensor following incubation with the target miRNA was expressed as a percentage of R_{ct} in the reference (blank) case, which was incubated in the human serum medium in the absence of target miRNAs. To evaluate the contribution of non-specific interactions, the interfering analytes (5 mM ascorbic acid, 5 mM uric acid and 0.3 μg mL^{-1} BSA, respectively) were diluted in the $FeCN_6/Na_2SO_4$ electrolyte prior to the

electrochemical measurements. Further, linear regression analysis was utilized to estimate a detection limit for the sensor. From the plot of ΔR_{ct} vs concentration, a relation of ΔR_{ct} = 90.89 + 6.04 log_{10} (*Concentration* [M]) was deduced (R^2 = 0.99) for sensing the target sequence. The limit of quantification (LOQ) was calculated by $10S_y/b$, with S_y as the standard deviation of the y-intercept (S_y = 7.24), and b as the slope of the linear fit (b = 6.04) [36].

References

1. Kong, J.; Soh, H.T.; Cassell, A.M.; Quate, C.F.; Dai, H., Synthesis of individual single-walled carbon nanotubes on patterned silicon wafers. *Nature* **1998**, *395*, 878-881.
2. Bae, S.; Kim, H.; Lee, Y.; Xu, X.; Park, J.S.; Zheng, Y.; Balakrishnan, J.; Lei, T.; Kim, H.R.; Song, Y.I.*, et al.*, Roll-to-roll production of 30-inch graphene films for transparent electrodes. *Nature Nanotechnology* **2010**, *5*, 574-578.
3. Yang, F.; Wang, X.; Zhang, D.; Yang, J.; LuoDa; Xu, Z.; Wei, J.; Wang, J.Q.; Xu, Z.; Peng, F.*, et al.*, Chirality-specific growth of single-walled carbon nanotubes on solid alloy catalysts. *Nature* **2014**, *510*, 522-524.
4. Kim, K.S.; Zhao, Y.; Jang, H.; Lee, S.Y.; Kim, J.M.; Kim, K.S.; Ahn, J.H.; Kim, P.; Choi, J.Y.; Hong, B.H., Large-scale pattern growth of graphene films for stretchable transparent electrodes. *Nature* **2009**, *457*, 706-710.
5. Novoselov, K.S.; Falko, V.I.; Colombo, L.; Gellert, P.R.; Schwab, M.G.; Kim, K., A roadmap for graphene. *Nature* **2012**, *490*, 192-200.
6. Ren, W.; Cheng, H.M., The global growth of graphene. *Nature Nanotechnology* **2014**, *9*, 726-730.
7. Zurutuza, A.; Marinelli, C., Challenges and opportunities in graphene commercialization. *Nature Nanotechnology* **2014**, *9*, 730-734.
8. Bonaccorso, F.; Sun, Z.; Hasan, T.; Ferrari, A.C., Graphene photonics and optoelectronics. *Nature Photonics* **2010**, *4*, 611-622.
9. Ruan, G.; Sun, Z.; Peng, Z.; Tour, J.M., Growth of graphene from food, insects, and waste. *ACS Nano* **2011**, *5*, 7601-7607.

10. Guermoune, A.; Chari, T.; Popescu, F.; Sabri, S.S.; Guillemette, J.; Skulason, H.S.; Szkopek, T.; Siaj, M., Chemical vapor deposition synthesis of graphene on copper with methanol, ethanol, and propanol precursors. *Carbon* **2011**, *49*, 4204-4210.
11. Reina, A.; Jia, X.; Ho, J.; Nezich, D.; Son, H.; Bulovic, V.; Dresselhaus, M.S.; Kong, J., Large area, few-layer graphene films on arbitrary substrates by chemical vapor deposition. *Nano Letters* **2009**, *9*, 30-35.
12. Li, X.; Cai, W.; Colombo, L.; Ruoff, R.S., Evolution of graphene growth on ni and cu by carbon isotope labeling. *Nano Letters* **2009**, *9*, 4268-4272.
13. Reina, A.; Thiele, S.; Jia, X.; Bhaviripudi, S.; Dresselhaus, M.S.; Schaefer, J.A.; Kong, J., Growth of large-area single- and bi-layer graphene by controlled carbon precipitation on polycrystalline ni surfaces. *Nano Research* **2009**, *2*, 509-516.
14. Baraton, L.; He, Z.B.; Lee, C.S.; Cojocaru, C.S.; Châtelet, M.; Maurice, J.L.; Lee, Y.H.; Pribat, D., On the mechanisms of precipitation of graphene on nickel thin films. *EPL (Europhysics Letters)* **2011**, *96*, 46003.
15. Yoon, S.M.; Choi, W.M.; Baik, H.; Shin, H.J.; Song, I.; Kwon, M.S.; Bae, J.J.; Kim, H.; Lee, Y.H.; Choi, J.Y., Synthesis of multilayer graphene balls by carbon segregation from nickel nanoparticles. *ACS Nano* **2012**, *6*, 6803-6811.
16. Hata, K.; Futaba, D.N.; Mizuno, K.; Namai, T.; Yumura, M.; Iijima, S., Water-assisted highly efficient synthesis of impurity-free single-walled carbon nanotubes. *Science* **2004**, *306*, 1362-1364.
17. Zhu, L.; Xiu, Y.; Hess, D.W.; Wong, C.P., Aligned carbon nanotube stacks by water-assisted selective etching. *Nano Letters* **2005**, *5*, 2641-2645.
18. Ferrari, A.C.; Meyer, J.C.; Scardaci, V.; Casiraghi, C.; Lazzeri, M.; Mauri, F.; Piscanec, S.; Jiang, D.; Novoselov, K.S.; Roth, S.*, et al.*, Raman spectrum of graphene and graphene layers. *Physical Review Letters* **2006**, *97*, 187401.
19. Garlow, J.A.; Barrett, L.K.; Wu, L.; Kisslinger, K.; Zhu, Y.; Pulecio, J.F., Large-area growth of turbostratic graphene on ni(111) via physical vapor deposition. *Scientific Reports* **2016**, *6*, 19804.
20. Niyogi, S.; Bekyarova, E.; Itkis, M.E.; Zhang, H.; Shepperd, K.; Hicks, J.; Sprinkle, M.; Berger, C.; Lau, C.N.; de Heer, W.A.*, et al.*, Spectroscopy of covalently functionalized graphene. *Nano Letters* **2011**, *10*, 4061.

21. Ferrari, A.C., Raman spectroscopy of graphene and graphite: Disorder, electron ‐ phonon coupling, doping and nonadiabatic effects. *Solid State Communications* **2007**, *143*, 47-57.
22. Tuinstra, F.; Koenig, J.L., Raman spectrum of graphite. *Journal of Chemical Physics* **1970**, *53*, 1126-1130.
23. Hwang, J.Y.; Kuo, C.C.; Chen, L.C.; Chen, K.H., Correlating defect density with carrier mobility in large-scaled graphene films: Raman spectral signatures for the estimation of defect density. *Nanotechnology* **2010**, *21*, 465705.
24. Nair, R.R.; Blake, P.; Grigorenko, A.N.; Novoselov, K.S.; Booth, T.J.; Stauber, T.; Peres, N.M.R.; Geim, A.K., Fine structure constant defines visual transparency of graphene. *Science* **2008**, *320*, 1308-1308.
25. Yick, S.; Han, Z.J.; Ostrikov, K., Atmospheric microplasma-functionalized 3d microfluidic strips within dense carbon nanotube arrays confine au nanodots for sers sensing. *Chemical Communications* **2013**, *49*, 2861-2863.
26. Marcano, D.C.; Kosynkin, D.V.; Berlin, J.M.; Sinitskii, A.; Sun, Z.; Slesarev, A.; Alemany, L.B.; Lu, W.; Tour, J.M., Improved synthesis of graphene oxide. *ACS Nano* **2010**, *4*, 4806-4814.
27. Turner, A.P.F., Biosensors: Sense and sensibility. *Chemical Society Reviews* **2013**, *42*, 3184-3196.
28. Ferri, C.P.; Prince, M.; Brayne, C.; Brodaty, H.; Fratiglioni, L.; Ganguli, M.; Hall, K.; Hasegawa, K.; Hendrie, H.; Huang, Y.*, et al.*, Global prevalence of dementia: A delphi consensus study. *The Lancet 366*, 2112-2117.
29. Cheng, L.; Doecke, J.D.; Sharples, R.A.; Villemagne, V.L.; Fowler, C.J.; Rembach, A.; Martins, R.N.; Rowe, C.C.; Macaulay, S.L.; Masters, C.L.*, et al.*, Prognostic serum mirna biomarkers associated with alzheimer/'s disease shows concordance with neuropsychological and neuroimaging assessment. *Molecular Psychiatry* **2015**, *20*, 1188-1196.
30. De Jager, P.L.; Srivastava, G.; Lunnon, K.; Burgess, J.; Schalkwyk, L.C.; Yu, L.; Eaton, M.L.; Keenan, B.T.; Ernst, J.; McCabe, C.*, et al.*, Alzheimer's disease: Early alterations in brain DNA methylation at ank1, bin1, rhbdf2 and other loci. *Nature Neuroscience* **2014**, *17*, 1156-1163.

31. Lunnon, K.; Smith, R.; Hannon, E.; De Jager, P.L.; Srivastava, G.; Volta, M.; Troakes, C.; Al-Sarraj, S.; Burrage, J.; Macdonald, R.*, et al.*, Methylomic profiling implicates cortical deregulation of ank1 in alzheimer's disease. *Nature Neuroscience* **2014**, *17*, 1164-1170.
32. Suni, I.I., Impedance methods for electrochemical sensors using nanomaterials. *Trends in Analytical Chemistry* **2008**, *27*, 604-611.
33. Hu, Y.; Wang, K.; Zhang, Q.; Li, F.; Wu, T.; Niu, L., Decorated graphene sheets for label-free DNA impedance biosensing. *Biomaterials* **2012**, *33*, 1097-1106.
34. Zhang, Z.; Luo, L.; Chen, G.; Ding, Y.; Deng, D.; Fan, C., Tryptamine functionalized reduced graphene oxide for label-free DNA impedimetric biosensing. *Biosensors and Bioelectronics* **2014**, *60*, 161-166.
35. Zhang, J.; Li, A.; Yu, X.; Guo, W.; Zhao, Z.; Qiu, J.; Mou, X.; Claverie, J.P.; Liu, H., Scaly graphene oxide/graphite fiber hybrid electrodes for DNA biosensors. *Advanced Materials Interfaces* **2015**, *2*, 1-6.
36. Armbruster, D.A.; Pry, T., Limit of blank, limit of detection and limit of quantitation. *Clinical Biochemistry Reviews* **2008**, *29*, S49-S52.

Supporting Information for:

Single-Step Ambient-Air Synthesis of Graphene from Renewable Precursors as Electrochemical Genosensor

Dong Han Seo[1,†], Shafique Pineda[1,2,†], Jinghua Fang[3], Yesim Gozukara[1], Samuel Yick[1], Avi Bendavid[1], Simon K. H. Lam[1], Adrian T. Murdock[1], Anthony B. Murphy[1], Zhao Jun Han[1,*], and Kostya (Ken) Ostrikov[4,1,2]

[1] CSIRO Manufacturing, P.O. Box 218, Bradfield Road, Lindfield, NSW 2070, Australia.

[2] School of Physics, The University of Sydney, Sydney, NSW 2006, Australia.

[3] School of Mathematical and Physical Sciences, The University of Technology, Sydney, NSW 2007, Australia

[4] Institute for Future Environments and Institute for Health and Biomedical Innovation, School of Chemistry, Physics, and Mechanical Engineering, Queensland University of Technology, Brisbane, QLD 4000, Australia.

† These authors contributed equally to this work.

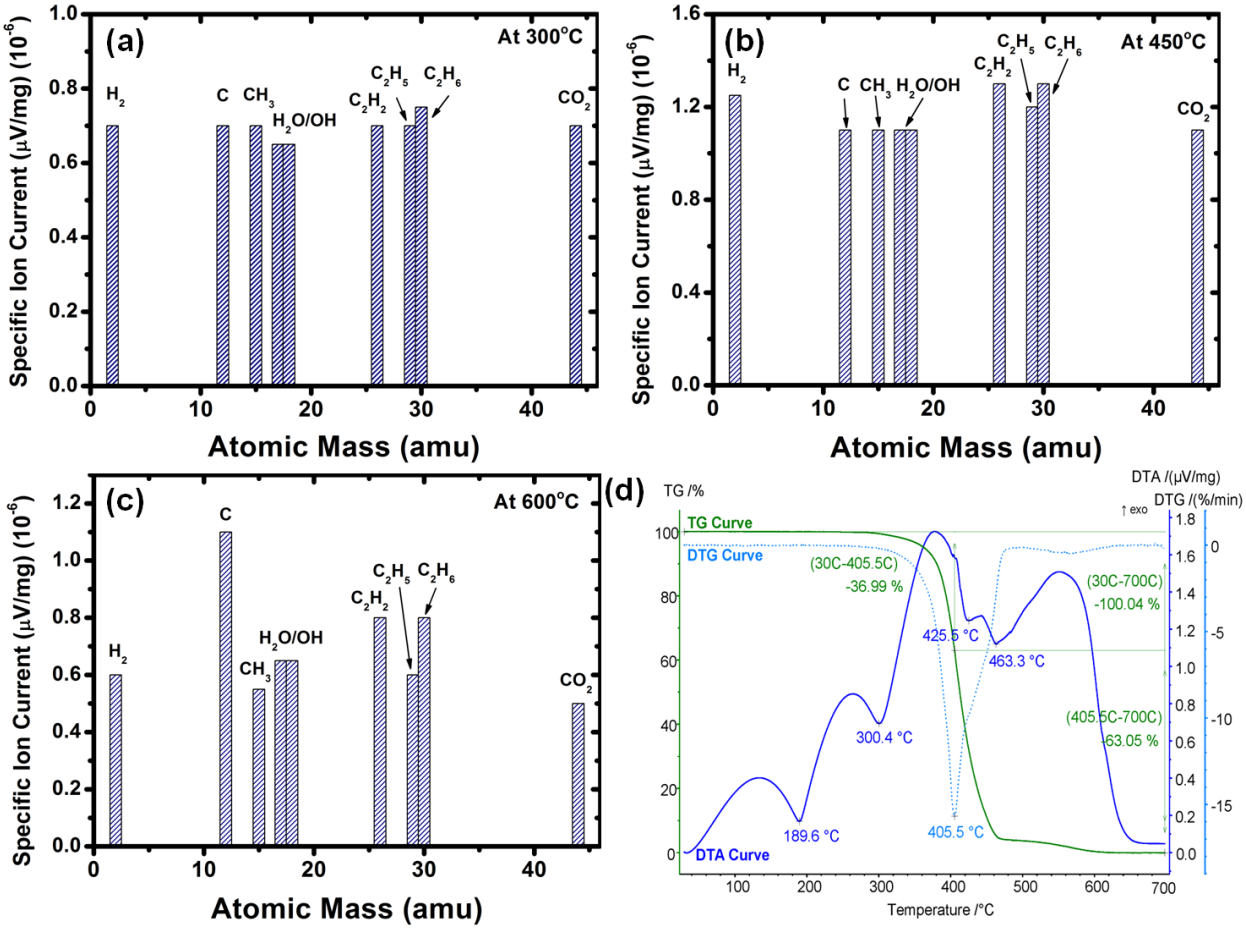

Supplementary Figure 1 | Inductively-coupled plasma (ICP) mass spectrometry analyses of vapors produced from soybean oil precursor at different temperatures. (**a**) 300, (**b**) 450 and (**c**) 600 ^{o}C. (**d**) Thermogravimetric analysis (TGA), derivative thermogravimetric analysis (DTG) and differential thermal analysis (DTA) curves of the soybean oil.

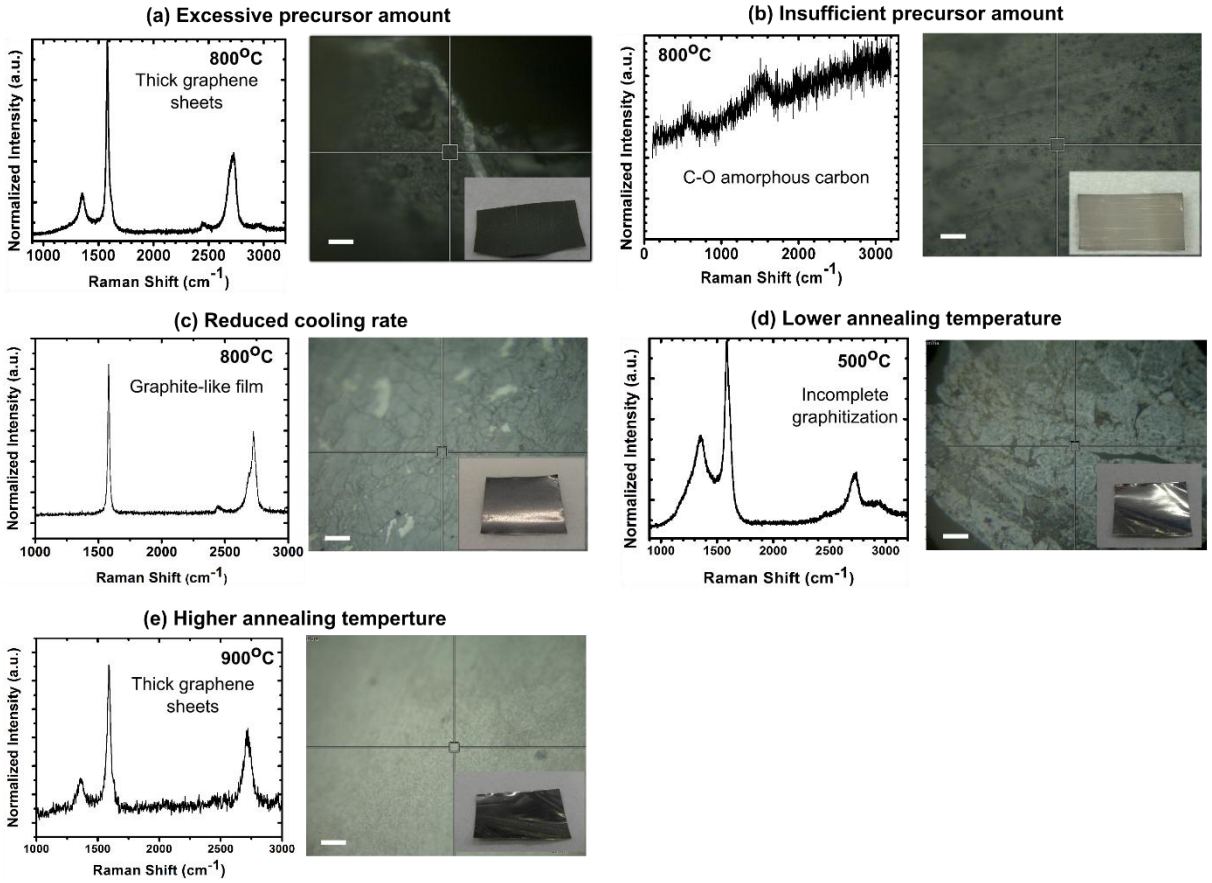

Supplementary Figure 2 | Non-optimal growth of graphene thin films and their respective Raman spectra. (**a**) An excessive amount of precursor resulted in the formation of thick graphene sheets; (**b**) an insufficient amount of precursor resulted in the formation of amorphous carbons; (**c**) a slow cooling rate resulted in the formation of graphite-like films; (**d**) a lower annealing temperature (*e.g.,* 500 ^{o}C) led to an incomplete transformation of the precursor; and (**e**) a higher annealing temperature (*e.g.,* 900 ^{o}C) led to thicker graphene sheets. Scale bars: 20 μm in **a**-**e**.

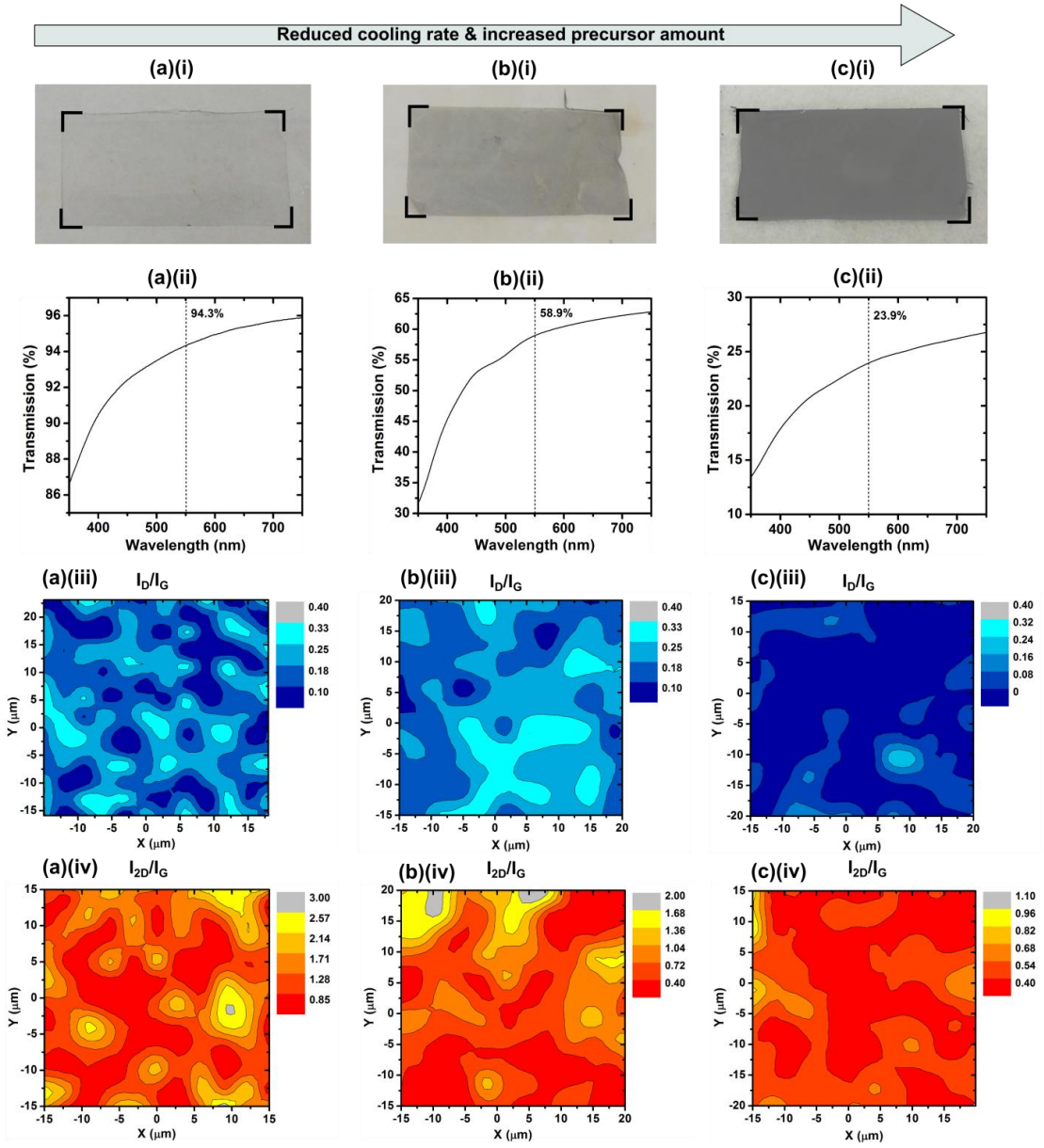

Supplementary Figure 3 | Control of graphene film thickness by adjusting the cooling rate and precursor amount in an ambient-air environment. (**a**) Fast cooling rate and an optimal precursor amount, (**b**) slower cooling rate and an increased precursor amount, (**c**) slowest cooling rate and an excessive amount of precursor. (**i**) Optical image, (**ii**) transmission spectra, (**iii**) Raman mapping of I_D/I_G and (**iv**) I_{2D}/I_G measurements of the respective graphene films.

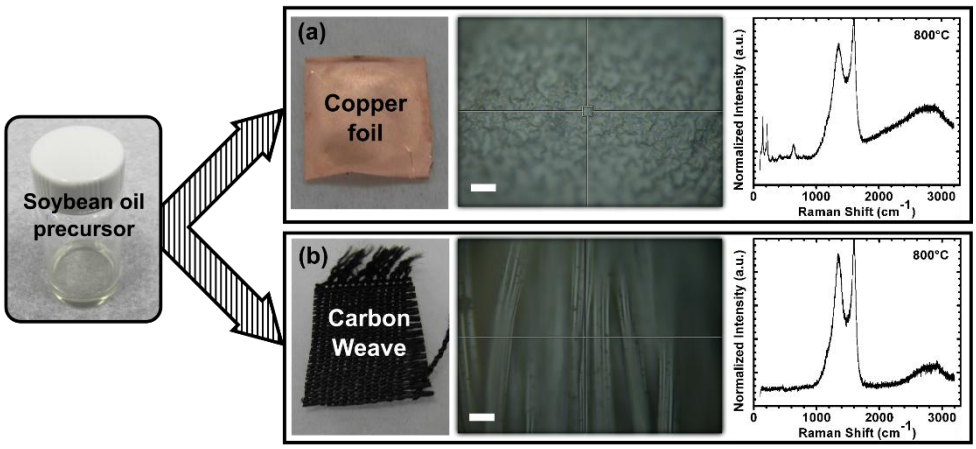

Supplementary Figure 4 | Ambient-air process applied to other substrates. Similar growth conditions applied to other substrates of (**a**) copper foil and (**b**) woven carbon. No graphene films were obtained on these substrates. Scale bars: 20 μm in **a**,**b**.

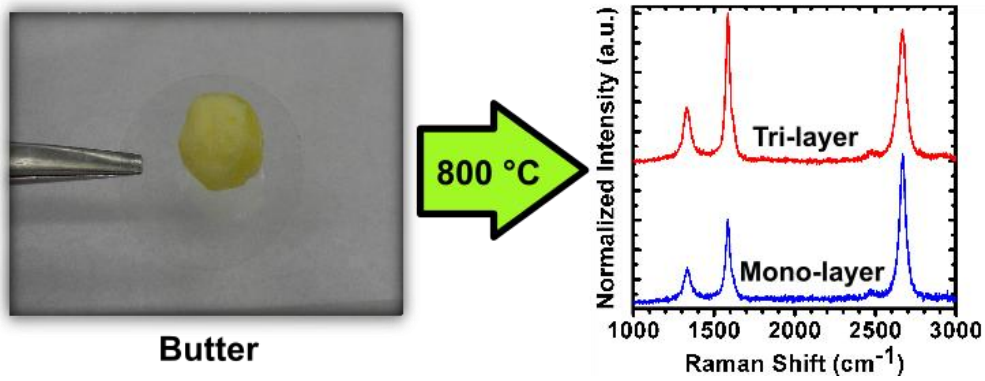

Supplementary Figure 5 | Transformation of other fat-containing precursors with the ambient-air process. Butter was used in place of soybean oil, and similar growth conditions were applied. The formation of few-layered graphene films were observed.

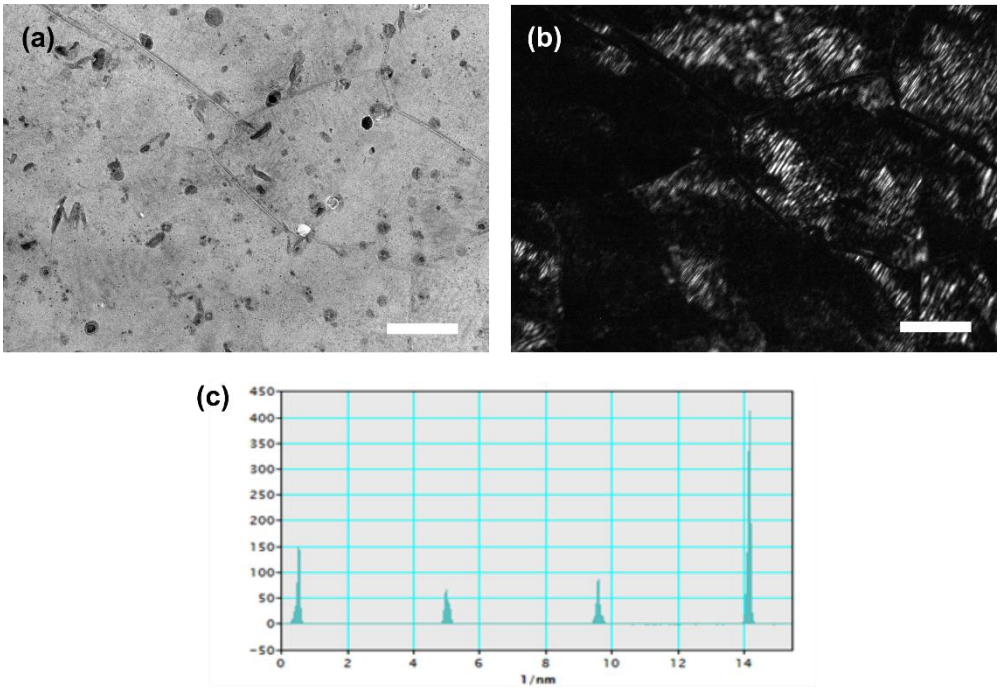

Supplementary Figure 6 | Supporting TEM characterizations of the graphene film. (**a**) Bright-field and (**b**) dark-field contrast images of the graphene film, corresponding to Fig. 2a and 2b. (**c**) Respective intensity profile of SAED pattern in Fig. 2d indicating bi/few-layered graphene. Scale bars: 200 nm in **a**,**b**.

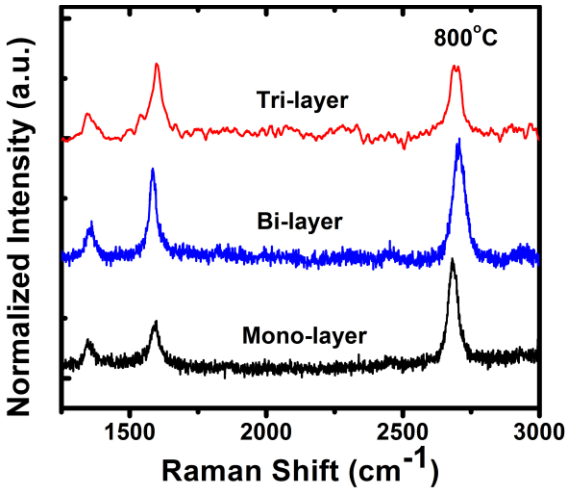

Supplementary Figure 7 | Ambient-air process applied to low-purity (99 %) polycrystalline Ni foil growth substrate. Raman spectra indicate the growth of single-to-few layer graphene films at 800 °C.

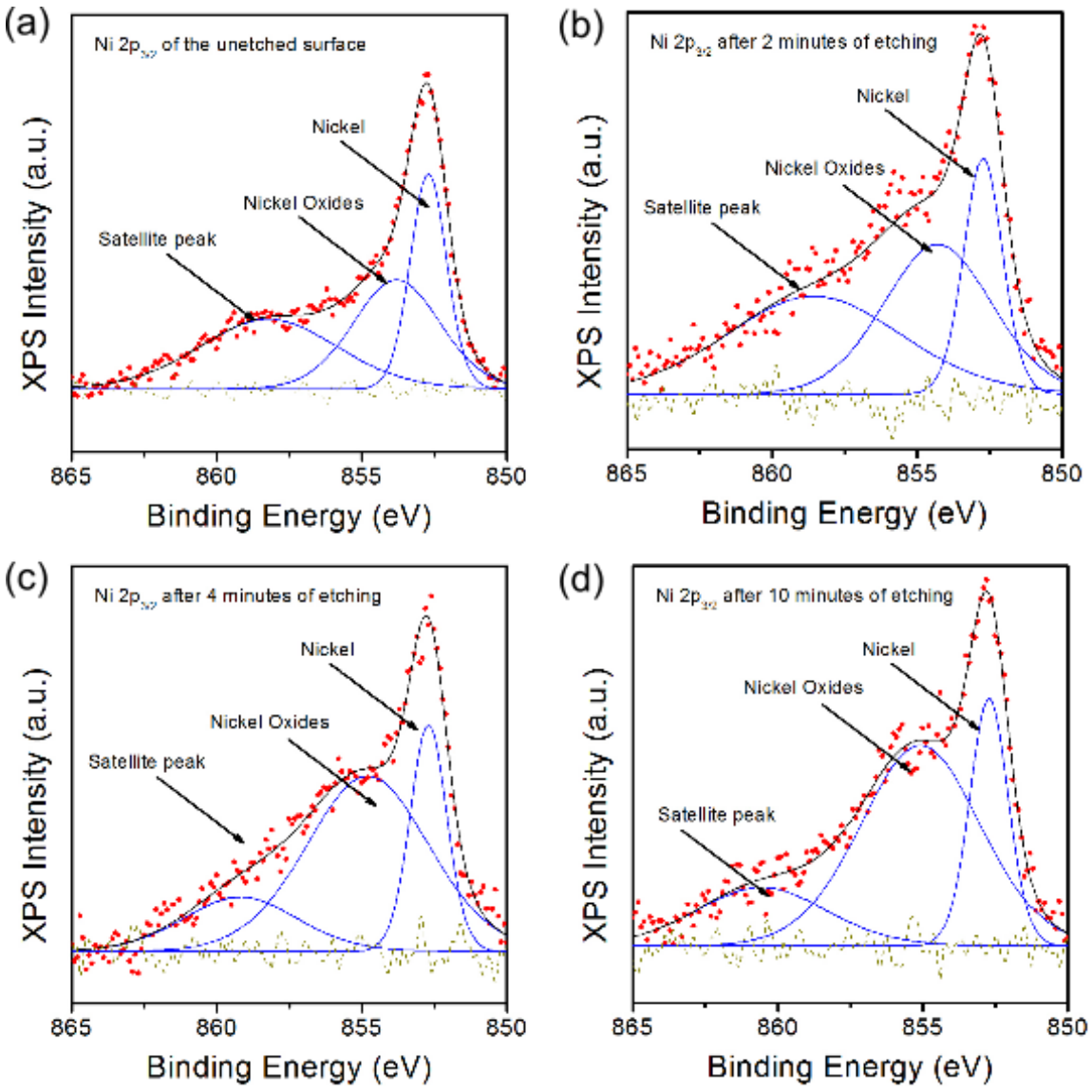

Supplementary Figure 8 | Surface analysis of Ni foil thermally heated in the absence of soybean oil. XPS Ni $2p_{3/2}$ spectra of (**a**) Ni surface heat treated without soybean oil and after the etching of (**b**) 2min, (**c**) 4 min and (**d**) 10 min.

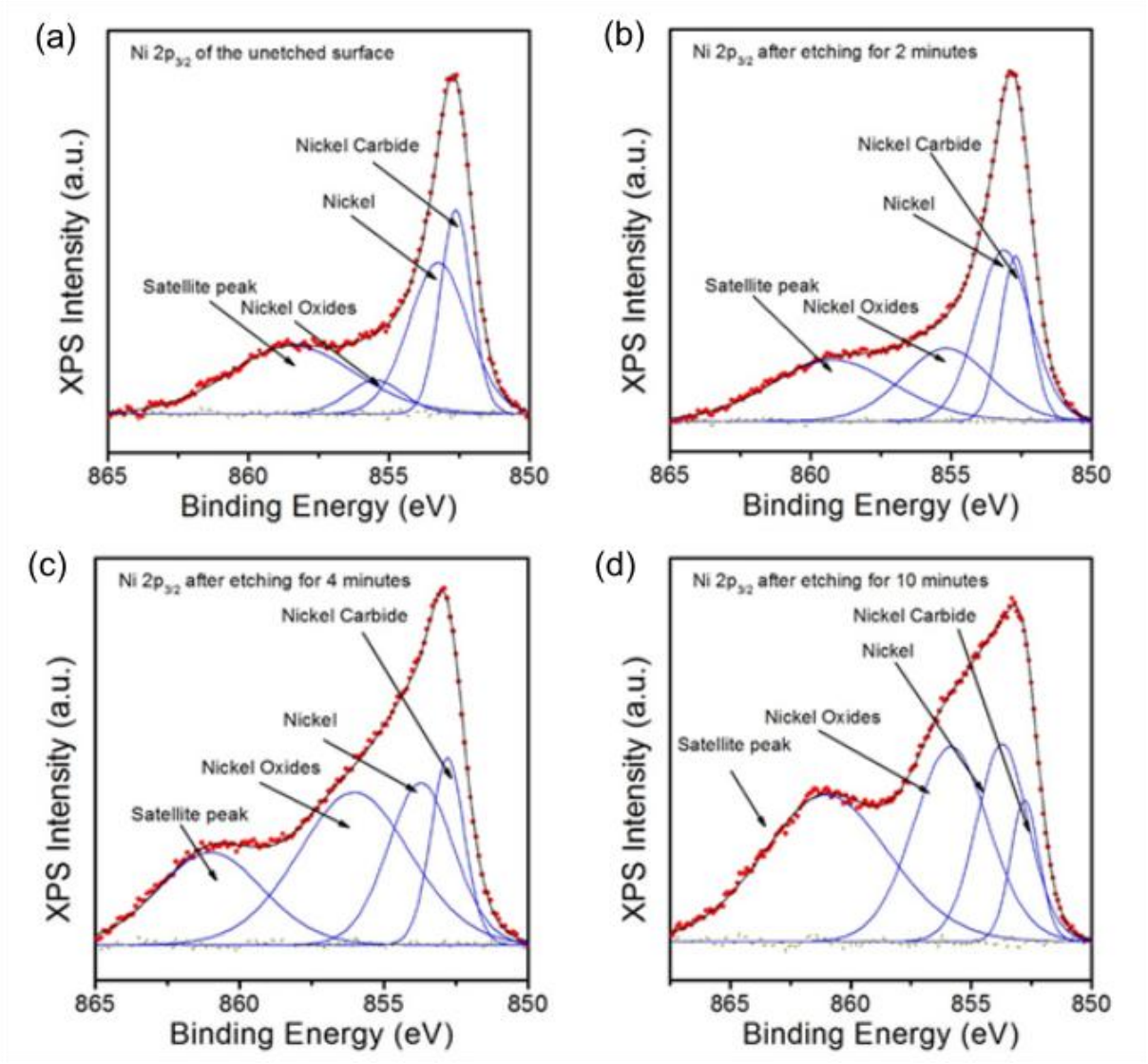

Supplementary Figure 9 | Surface analysis of Ni foil thermally heated in the presence of soybean oil. XPS Ni $2p_{3/2}$ spectra of (**a**) graphene/Ni surface and after the etching of (**b**) 2 min, (**c**) 4 min and (**d**) 10 min.

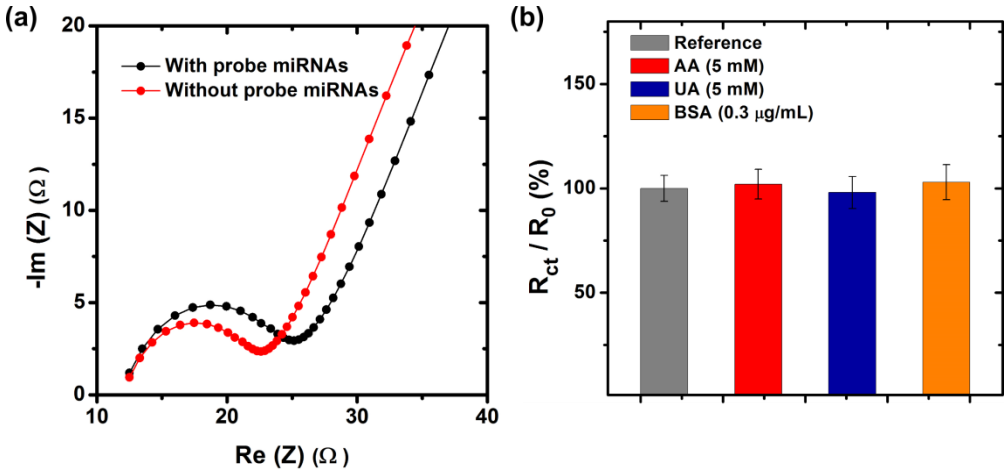

Supplementary Figure 10 | Graphene film as a bio-sensing electrode. (**a**) EIS curve showing increase in charge-transfer resistance (R_{ct}) of the graphene electrode upon immobilization of the probe miRNAs. (**b**) Response of the graphene-based biosensor to common interfering analytes, namely, ascorbic acid (AA), uric acid (UA), and BSA (bovine serum albumin), at respective physiological concentrations. Error bars represent the standard error of the mean.

Supplementary Table 1 | Comparison of the ambient-air synthesis method with conventional thermal CVD approaches for the production of graphene films.

Metric	Ruoff *et al.* [S1]	Kim *et al.* [S2]	Tour *et al.* [S3]	Bae *et al.* [S4]	This method
Carbon precursor	Methane	Methane	Carbon containing biomasses	Methane	Renewable soybean oil biomass
Feedstock gases	Hydrogen	Hydrogen & Argon	Hydrogen & Argon	Hydrogen	None
Pressure (torr)	0.04 – 0.5	n/a	9.3	0.09 – 0.46	Atmospheric
Synthesis environment	Purified gases	Purified gases	Purified gases	Purified gases	Ambient Air
Processing time (min)	150	140	150	160	< 30
Temperature (°C)	1000	1000	1050	1000	800

Supplementary Table 2 | Cost estimate of our method compared to one of the widely-adopted methods for graphene synthesis.

Object of consideration	Our method	Conventional methods†
Carbon precursor material/ Compressed gases	Renewable soybean oil biomass $0.00016 (per run)	Compressed and purified gases $1.42 (per run)
Growth substrate	Ni (25 μm, 99%)$0.038 (per run)	Cu (25 μm, 99.8%) $0.015 (per run)
Electricity for furnace heating	29 mins in total $0.33 (per run)	90 mins in total $1.04 (per run)
Operation of vacuum pump	$0.046 for 26 mins (per run)	$0.26 for 150 mins (per run)
Estimated cost (per cm^2)†	**$0.40**	**$2.74**

†Cost estimation in comparison with conventional growth methods adopted from Ruoff and co-workers, Supplementary Reference 1.

Supplementary Table 3 | Comparison with graphene-based electrochemical impedimetric biosensors in the recent literature.

Biosensor	**Performance (Detection limit)**	**Reference**
Graphene on Ni	8.64 x 10^{-14} M miRNA	This work
GO with perylene tetracarboxylic acid diimide	5.5 x 10^{-13} M ssDNA	[S5]
RGO functionalized with tryptamine	5.2 x 10^{-13} M ssDNA	[S6]
Activated GO/Graphite interface	5.6 x 10^{-12} M ssDNA	[S7]

Supplementary Note 1 | Calculation of oxygen consumption in the reactor during the growth using soybean oil.

(i) Using the dimensions of the quartz tube, the volume of the growth chamber was calculated (0.00196 m^3).

(ii) Providing the dimensions of the Ni foils (4 cm x 2 cm), the surface area of the Ni foils was calculated (as double sided, giving a total of 16 cm^2).

(iii) We clarify as previously provided that the amount of carbon source is 0.14 mL of soybean oil, which is a liquid under ambient conditions.

(iv) Calculations to demonstrate that the amount of solid carbon sources is sufficient to consume all the O_2 in the growth chamber.

In considering consumption of O_2 by the carbon in the growth chamber, we emphasise that this will be a complex process due to the decomposition of soybean oil yielding numerous molecular fragments which consume O_2 through different reaction pathways. This is clear from our results presented in Supplementary Fig. 1 which shows the variety of products (e.g. H_2, C, CH_3, C_2H_2, C_2H_5, C_2H_6 etc.) from the soybean oil precursor at different temperatures, from 300 to 600 °C. The likely combustions reactions include:

$C + O_2 \rightarrow CO_2$	1 C for 1 O_2	-- (1)
$4CH_3 + 7O_2 \rightarrow 4CO_2 + 6H_2O$	1C for 1.75 O_2	-- (2)
$2C_2H_2 + 5O_2 \rightarrow 4CO_2 + 2H_2O$	1 C for 2.5 O_2	-- (3)

$4C_2H_5 + 13O_2 \rightarrow 8CO_2 + 10H_2O$ 1 C for 3.25 O_2 -- (4)

$2C_2H_6 + 7O_2 \rightarrow 4CO_2 + 6H_2O$ 1 C for 3.5 O_2 -- (5)

$2H_2 + O_2 \rightarrow 2H_2O$ solely consumes O_2 -- (6)

Using the growth chamber dimensions and STP conditions, it is calculated that 0.0168 mol $O_{2(g)}$ is present. Also, it is noted that at the temperatures involved in the ambient-air process, CO_2 does not undergo further decomposition.

Using the average density of soybean oil (0.917 g mL^{-1}) and an average chemical composition (linoleic acid - 52%, oleic acid - 25%, palmitic acid - 12%, linolenic acid - 6%, stearic acid - 5%), it is calculated that ~0.0081 mol of C and ~0.0151 mol of H were present in the growth chamber (n.b. an additional ~0.0001 mol of O from soybean oil is also present, which we do not consider further).

If O_2 was only consumed through the reaction of C (reaction (1) above), then O_2 would be slightly in excess with a remainder of 0.0087 mol.

However, all other reaction pathways have a greater consumption rate of O_2. For instance, if O_2 was solely consumed through the reaction of C_2H_5 (reaction (3) above), then all the O_2 will be expended and C will be in excess with a remainder of 0.0035 mol.

We recognise that all these reaction pathways will likely proceed, and so the combined consumption of O_2 will yield an excess of C in the chamber. Furthermore, we noted that the presence of O_2 could be non-uniform in the growth chamber, given that the temperature inside and outside the hot-walled furnace were vastly different. This could lead to the local environment in the immediate vicinity of the soybean oil precursor and

Ni foils to have a significantly lower concentration of O_2. The calculations thus present an upper limit in estimating the amount of O_2 to be consumed by the soybean oil precursor.

We therefore can conclude that the amount of carbon source we use in the experiment- 0.14 mL of soybean oil- is sufficient to consume the O_2 in the growth chamber, yielding an excess of C from which our graphene can form.

Supplementary Note 2 | Estimation of carrier mobility for the graphene film.

The carrier mobility of the graphene film is estimated from the defect density in the film, defined by ~$(1/L_a)^2$ [cm^{-2}], in which,

$$L_a = \frac{560}{E_l^4}\left(\frac{I_D}{I_G}\right)^{-1},$$

where L_a [nm] is the crystallite size, E_l [eV] is the excitation laser energy used in the Raman measurements, and I_D/I_G is the Raman intensity ratio of the disorder content. The detailed calculation is shown below.

(i) From Raman characterizations of the graphene film (Fig. 3b in the main text), we deduced an average I_D/I_G ratio of 0.15 – 0.25.

(ii) The Raman measurements were taken with a 514 nm laser. Converting this wavelength to eV, yields excitation energy E_l of 2.41 eV.

(iii) Substituting these variables into L_a, and calculating for the defect density, yields 8.26×10^9 to 2.27×10^{10} cm^{-2}, respectively, for the lower and upper bounds of the I_D/I_G ratios. Consequently, the crystallite sizes are determined to be ~ 100 nm.

(iv) Consequently, by reference to the work by Hwang *et al.*,[S8] which correlates the defect density to the carrier mobility, we may provide an estimate for our film mobility, in the order of 500 – 750 $cm^2\ V^{-1}\ s^{-1}$. In addition, such mobility is in accordance with Salehi-Khojin *et al.*[S9] and Chen *et al.*,[S10], where a similar morphology, grain size, and defect level in the graphene films were seen.

Supplementary Note 3 | Competitive advantages of the present ambient-air graphene synthesis method.

Graphene production inherits high costs and complexities. This impedes its commercial viability. However, this ambient-air technique provides a significantly cheaper, greener, simpler and safer approach for the synthesis of graphene, as compared to the conventional thermal CVD methods (Supplementary Table 1 and Table 2). We attribute this to a key feature unique to this single-step thermal process, the growth of graphene in an ambient-air environment. Consequently, purified gases (*e.g.,* argon, hydrogen, methane) that are expensive and hazardous are not required. Instead, a safe, minimally-processed renewable precursor (soybean oil) functions as the source of carbon, and the ambient-air environment is tailored to enable the growth of graphene films.

In the conventional thermal CVD methods, the processing chamber is firstly evacuated to remove the ambient air. Next, the processing chamber is brought up to atmospheric pressure by filling the processing volume with purified gases. Finally, these purified gases are constantly circulated with extensive vacuum operation over a prolonged duration. These processes maintain an optimal flow of purified gases to enable the growth of graphene.

In the ambient-air process for graphene synthesis, these conventional steps are not necessary. Instead, graphene growth is promoted by direct control of the precursor content, process parameters (*e.g.,* cooling rate, temperature, *etc.*), and ambient-air environment, without the use of any purified gases, in a single-stepped approach. As

such, this ambient-air process has the potential to be easily integrated into existing graphene manufacturing infrastructures. Further, the ambient-air technique could also be attractive for the synthesis of large-area, high-quality graphene films. While offering the opportunity to bypass resource-consuming processes such as purified gases, extensive vacuum processing, long annealing durations and high temperatures, the ambient-air process retains good control over the quality and homogeneity of the graphene films.

Supplementary References

[S1] Li, X., *et al.* Large-Area Synthesis of High-Quality and Uniform Graphene Films on Copper Foils. *Science* **324**, 1312-1314 (2009).

[S2] Kim, K. S., *et al.* Large-scale pattern growth of graphene films for stretchable transparent electrodes. *Nature* **457**, 706-710 (2009).

[S3] Ruan, G., Sun, Z., Peng, Z. & Tour, J. M. Growth of Graphene from Food, Insects, and Waste. *ACS Nano* **5**, 7601-7607 (2011).

[S4] Bae, S., *et al.* Roll-to-roll production of 30-inch graphene films for transparent electrodes. *Nature Nanotechnology* **5**, 574-578 (2010).

[S5] Hu, Y., Wang, K., Zhang, Q., Li, F., Wu, T. & Niu, L. Decorated graphene sheets for label-free DNA impedance biosensing. *Biomaterials* **33**, 1097-1106 (2012).

[S6] Zhang, Z., Luo, L., Chen, G., Ding, Y., Deng, D. & Fan, C. Tryptamine functionalized reduced graphene oxide for label-free DNA impedimetric biosensing. *Biosensors and Bioelectronics* **60**, 161-166 (2014).

[S7] Zhang, J., *et al.* Scaly Graphene Oxide/Graphite Fiber Hybrid Electrodes for DNA Biosensors. *Advanced Materials Interfaces* **2**, 1-6 (2015).

[S8] Hwang, J. Y., Kuo, C. C., Chen, L. C. & Chen, K. H. Correlating defect density with carrier mobility in large-scaled graphene films: Raman spectral signatures for the estimation of defect density. *Nanotechnology* **21**, 465705 (2010).

[S9] Salehi-Khojin, A., *et al.* Polycrystalline Graphene Ribbons as Chemiresistors. *Advanced Materials* **24**, 53-57 (2012).

[S10] Chen, J. H., Cullen, W. G., Jang, C., Fuhrer, M. S. & Williams, E. D. Defect scattering in graphene. *Physical Review Letters* **102**, 236805 (2009).

3

Graphene Micro-Islands for Bioelectronics

"Am I to refuse to eat because I do not fully understand the mechanism of digestion?"

– Oliver Heaviside, 1850 – 1925.

This chapter presents the plasma-enabled synthesis of graphene micro-islands (GMs), and their integration as a genosensor and for biocompatible coatings.

Widely adopted forms of graphene in bioelectronics include graphene powders and graphene thin films. The former is derived by chemical methods (**Section 1.2.1**), and the latter by thermal CVD (**Section 1.2.2**). Often, graphene powders are employed as they allow versatile functional composites to be realized. However, chemical exfoliation processes utilize harsh chemicals and introduces impurities. On the other hand, graphene films are frequently utilized for their excellent optoelectronic properties. However, CVD growth of graphene involves high temperatures (1000 ^{o}C), long growth times, and is multi-staged. Further, the integration of graphene films requires a series of post-processing transfer techniques. This introduces cytotoxic impurities that impede its functionality for bioelectronics (**Section 1.3.1**).

Here, we demonstrate a plasma-enabled approach, tailored to address these limitations in graphene-based materials for bioelectronics. Plasma is shown to enable a single-step, rapid, and homogeneous growth of GMs at a low temperature (200 ^{o}C). The GMs feature an interconnected morphology, reactive edges, a high surface area, and oxygen surface functionalities, which make it readily available for implementation in bioelectronics. The plasma process for synthesis of GMs is energy-efficient (*i.e.*, low

temperature), resource-efficient (*i.e.*, rapid, water-mediated transfer), sustainable, and environmentally-friendly (*i.e.*, no hazardous by-products).

In this chapter, fabrication and characterization of GMs are explored. Control parameters for the plasma process are exemplified. We demonstrate that the properties of GMs enable its multifunctional capabilities as a bioactive interface. The plasma synthesis process is shown to enable a direct water-assisted transfer of GMs onto arbitrary substrates. Notably, GMs exhibit a biocompatibility of 80% cell viability with primary fibroblast lung cells after 5 days. Further, the GMs were assembled into an impedimetric genosensor. A dynamic sensing range of 1 pM to 1nM is demonstrated, and a limit of quantification of 2.03 x 10^{-13} M is deduced, with selectivity to single-RNA-base mismatched sequences.

Thus, the versatile nature of GMs, enabled by low-temperature reactive plasmas, may be explored to enable multi-faceted bioactive platforms for next-generation personalized healthcare technologies.

This chapter addresses **Thesis Objective 2**.

Statement of contribution: Shafique Pineda (S.P.) and Fabricio Frizera Borghi (F.F.B.) conceived the idea and together, conducted the experiments, and optimized the synthesis of graphene micro-islands and their integration for applications in biosensing and biocompatible coatings. S.P., F.F.B., Zhao Jun Han (Z.J.H.) and Kostya Ostrikov (K.O.) wrote the manuscript with input from all co-authors.

The following paper has been accepted for publication at **Biosensors and Bioelectronics** [1].

References

[1] **Pineda S.***, **Borghi F.F.***, Seo D.H., Yick S., Lawn M., van der Laan T., Han Z.J., Ostrikov K., Multifunctional Graphene Micro-islands: Low-Temperature Plasma-Enabled Synthesis and Facile Integration for Biosensing and Bioengineering Applications, *Biosensors and Bioelectronics*, 2017, 89, 437-443 (* = equal contribution).

Multifunctional Graphene Micro-Islands: Rapid, Low-Temperature Plasma-Enabled Synthesis and Facile Integration for Bioengineering and Genosensing Applications

Shafique Pineda[1,2,†], Fabricio Frizera Borghi[1,2,†], Dong Han Seo[1], Samuel Yick[1], Malcolm Lawn[3], Timothy van der Laan[1,2], Zhao Jun Han[1], and Kostya (Ken) Ostrikov[1,2,4,*]

† These authors contributed equally to this work.

[1] CSIRO Manufacturing, P.O. Box 218, 36 Bradfield Road, Lindfield, NSW 2070, Australia.

[2] School of Physics, The University of Sydney, Sydney, NSW 2006, Australia.

[3] National Measurement Institute (NMI), Nanometrology, 36 Bradfield Road, Lindfield, NSW 2070, Australia.

[4] Institute for Future Environments and Institute for Health and Biomedical Innovation, School of Chemistry, Physics, and Mechanical Engineering, Queensland University of Technology, Brisbane, QLD 4000, Australia.

Abstract

Here, we present a rapid, low-temperature (200 ^{o}C) plasma-enabled synthesis of graphene micro-islands (GMs). Morphological analyses of GMs by scanning electron microscopy (SEM) and atomic force microscopy (AFM) feature a uniform and open-networked array of aggregated graphene sheets. Structural and surface chemical characterizations by Raman spectroscopy and X-ray photoelectron spectroscopy (XPS) support the presence of thin graphitic edges and reactive oxygen functional groups. We demonstrate that these inherent properties of GMs enable its multifunctional capabilities

as a bioactive interface. GMs exhibit a biocompatibility of 80% cell viability with primary fibroblast lung cells after 5 days. Further, GMs were assembled into an impedimetric genosensor, and its performance was characterized by electrochemical impedance spectroscopy (EIS). A dynamic sensing range of 1 pM to 1 nM is reported, and a limit of quantification (LOQ) of 2.03 x 10^{-13} M is deduced, with selectivity to single-RNA-base mismatched sequences. The versatile nature of GMs may be explored to enable multi-faceted bioactive platforms for next-generation personalized healthcare technologies.

Introduction

Graphene, an atomically-thin film of crystalline carbon, has attracted significant interest for biomedical technologies owing to its exceptional physicochemical properties, determined by its unique two-dimensional structure and morphology [1]. However, green and resource-efficient production of graphene and its facile integration into biomedical devices are essential for such technologies to be feasible, which remains a challenge [2].

Recent investigations have demonstrated significant progress in addressing several of these concerns to facilitate the utilization of graphene technologies in biomedical applications. This includes reducing the production cost of graphene films grown by thermal chemical vapor deposition (CVD), by using lower growth temperatures and other carbon precursors [3,4]. However, these techniques still involve long processing times and notably high temperatures (~850°C). Moreover, while graphene dispersions prepared by chemical exfoliation are cheaper alternatives to CVD grown graphene films, their synthesis requires multi-staged complex processing, often in harsh chemical environments [5]. Also, such graphene dispersions tend to agglomerate, and utilization of graphene as a functional surface requires additional chemical binders [6]. While these graphene dispersions have shown good biocompatibility, their uses are limited by a poor electrical conductivity and a resource-consuming integration, which undermines its performance and multifunctionality for applications in bioelectronics.

In addition, there have been efforts to improve the integration of graphene into electronics, by utilizing either dry transfer techniques or improved transfer techniques based on reactive chemical etching [7,8]. However, these approaches are multi-staged and involve complex handling of graphene, and often introduce cytotoxic impurities on the surface of graphene. It is thus important to develop a simple, fast, environmentally-benign, low-temperature graphene production and integration for bioelectronics.

Plasma has been shown to grow multilayer graphene flakes, containing single layer graphene domains of sub-micrometre to just-above-micrometre size [9]. However, such graphene flakes are sparsely grown, and thus, remain unfavorable for use as bioactive coatings and biosensing interfaces, whereby a larger quantity, surface coverage, and better transferability of graphene are required. Herein, graphene micro-islands (GMs) are synthesized by a low-temperature plasma, that is resource-efficient and eco-friendly. We demonstrate the multifunctionality of GMs as a bioactive interfacial material for biocompatible coatings and electrochemical genosensing.

Results and Discussion

Fabrication and characterization of graphene micro-islands. The procedure for preparing GMs is illustrated in Fig. 1a. A low-temperature plasma process enables the growth of GMs on a copper foil. This approach is typically more resource-efficient compared to chemical vapour deposition (CVD) and represents an environmentally-benign alternative to conventional wet-chemical methods, which involve high temperatures and hazardous chemicals, respectively [10].

During the early growth process (~2 min), the methane is rapidly dissociated into carbon building units by the plasma. Subsequently, these carbon species reorganize into hexagonal carbon-rings forming graphene nanosheets. Such plasma-unique effects are mainly attributed to the strong plasma-matter interactions in the plasma sheath [11,12]. In particular, hydrogen may enhance the surface flux of these building units through the recombination-mediated energy dissipation on the surface and facilitate the nucleation

and growth of graphene nanosheets [13]. Fig. 1a outlines the process for GM synthesis. Initially, graphene nanosheets grow vertically from the substrate due to the electric field in the plasma sheath (Supplementary Fig. 1). Upon water-mediated transfer, the vertically-standing graphene nanosheets collapse to lay horizontally on the transferred substrate, in a two-dimensional open and arrayed network of GMs. Additionally, the controlled growth of GMs and its reproducibility are studied in Supplementary Fig. 2.

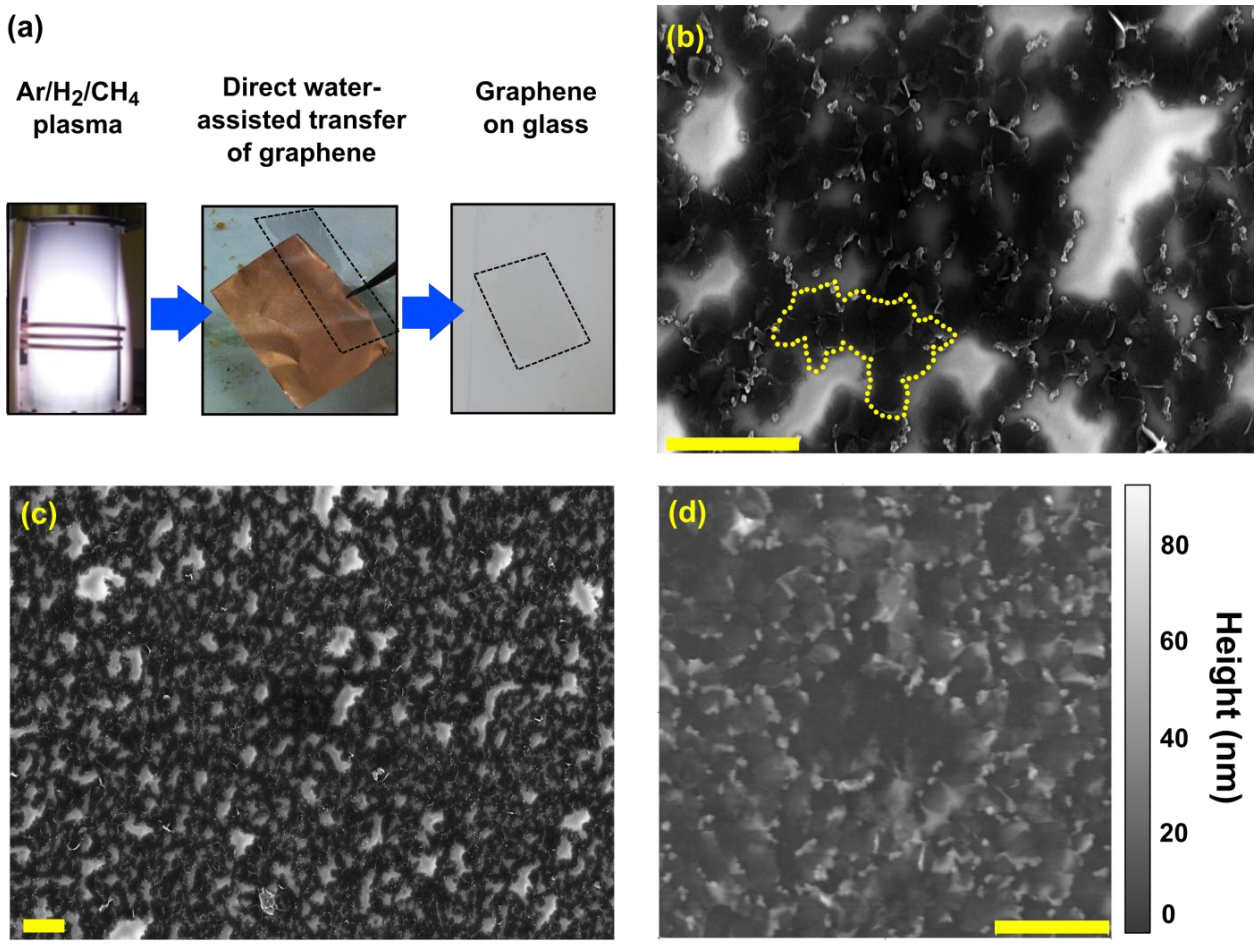

Figure 1 | Synthesis process and morphological characterization of plasma-grown graphene micro-islands. (**a**) Low-temperature plasma process for the synthesis of graphene micro-islands (GMs). High-magnification SEM (**b**) features GMs outlined in yellow. Low-magnification SEM (**c**) shows the uniform large-area coverage of GMs. (**d**) AFM topography imaging of GMs. Scale bars correspond to 1 μm in **b**, **c**, and **d**.

The microstructure and morphology of GMs are examined in Fig. 1b – d, with scanning electron microscopy (SEM) and atomic force microscopy (AFM) topography imaging. The GMs are outlined in the high-magnification SEM image (Fig. 1b). GMs are deduced to be composed of graphene domains (each 200 – 500 nm in dimension) forming an open network of micron-sized islands. These GMs are observed to provide a uniform surface coating (Fig. 1c). AFM topography imaging of GMs (Fig. 1d) feature graphene sheets (< 20nm) inter-connected in an arrayed morphology, and the presence of carbon clusters (~60 nm) along the edges of the graphene islands. Notably, these carbon clusters may be attributed to nucleation regions for the growth of graphene nanosheets in the plasma process. The morphology of individual GMs is further investigated with a close-up 3D AFM topographic map (Supplementary Fig. 3). Together, AFM and SEM characterizations demonstrate the GMs possess an inter-connected and open morphology, and GMs avoid uncontrolled agglomeration of the graphene nanosheets as commonly observed in chemically-prepared graphene flakes.

The morphology of GMs is characteristic of the low-temperature reactive plasma process [12]. Plasma enables the growth of vertically-oriented graphene nanosheets (VGNS) through strong plasma-matter interactions in the plasma sheath (Supplementary Fig. 1) [14]. For instance, H_2 can enhance the surface flux of the carbon building units (from CH_4 precursor) through the recombination-mediated energy dissipation on the surface. Also, the electric field in the plasma sheath can promote etching of defects and amorphous carbon, while guiding the delivery of building units to facilitate nucleation and growth of VGNS [15]. During the water-mediated transfer, these VGNS collapse onto their sides to form an open and interconnected network of graphene micro-islands.

The structural and chemical compositions of GMs are characterized by Raman and X-ray photoelectron spectroscopy (XPS). Three distinct peaks are present (Fig. 2a), namely, the characteristic disorder peak (D-band) at 1350 cm^{-1}, the graphitic peak (G-band) at 1580 cm^{-1}, and the second-order 2D-band at 2690 cm^{-1}.

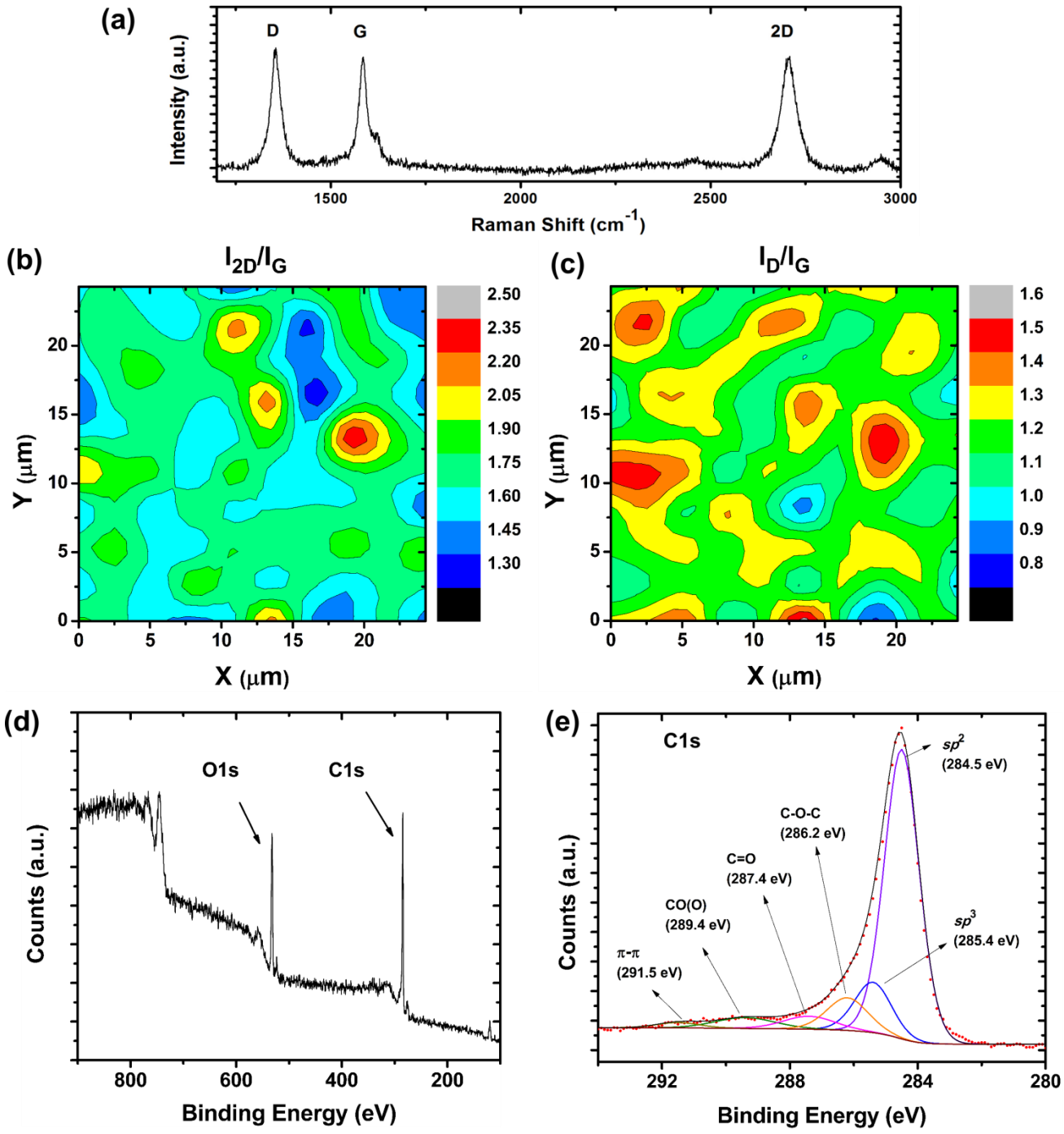

Figure 2 | Structural and surface chemical characterizations of graphene micro-islands. (**a**) A typical single-point Raman spectrum of GMs. (**b**) – (**c**) Raman spectral mapping of characteristic peak ratios ($I_{2D/G}$ and $I_{D/G}$) for GMs over a 25 μm x 25 μm area. (**d**) XPS survey scan and respective (**e**) C 1s narrow spectrum of GMs.

The G-band arises from the in-plane vibrational E_{2g} mode of the sp^2-hybridized carbon, the D-band is attributed to the finite crystallite size effect and various defects induced in the sp^2 carbon materials, and the 2D-band is a second-order Raman spectral feature due to the three-dimensional inter-planar stacking of hexagonal carbon networks [16-19]. Further, Raman spectral mapping was conducted to examine the uniformity of GMs (Fig. 2b – c). The characteristic peaks feature intensity ratios of I_{2D}/I_G ~ (1.60 – 2.10) and I_D/I_G ~ (1.1 – 1.30), which indicate the presence of homogeneously thin and reactive sheets of graphene [19,20] with enhanced electrochemical activity [21]. The single-step, low-temperature plasma process enables the synthesis of GMs with significantly improved graphitic properties as compared to chemically-derived graphene.

The chemical composition of GMs was analyzed by X-ray photoelectron spectroscopy (XPS). The survey scan (Fig. 2d) shows dominant peaks at binding energies of 284.5 eV (C 1s) and 532.7 eV (O 1s). The C 1s spectrum in Fig. 2e can be de-convoluted into six components, corresponding to sp^2 (284.5 eV), sp^3 (285.4 eV), C-O-C bonds (286.2 eV), C=O bonds (287.4 eV), O-C=O bonds (289.4 eV) and π- π* satellite orbitals (291.5 eV) [22]. Notably, such sp^3 clusters contribute to an increase in I_D/I_G. Further, an O 1s spectrum centered at 532.7 eV supports the presence of such oxygen-attached carbon species (Supplementary Fig. 4). GMs feature a sp^2 and sp^3 compositions of 68% and 12.5%, respectively, which indicates graphitic quality consistent with Raman characterizations. These oxygen moieties may have been introduced through its open edges, either following the immediate exposure of GMs to air, or through the water-mediated transfer process. Thus, Raman and XPS characterizations affirm that plasma-derived GMs possess reactive graphitic edges and oxygen functionalities.

Together, the morphological and chemical features of GMs may not only facilitate the access and surface immobilization of biological analytes, but also, may enable GMs to be readily available for integration as an interfacial material for bioengineering or electrochemical sensing applications. The plasma-enabled GMs offer multiple advantages over graphene flakes prepared by chemical exfoliation techniques (Table 1). For instance, as GMs can easily decouple from the growth substrate by a water-

mediated process, this avoids the presence of impurities from stabilizing solvents and non-conductive binders that are typically required in the chemical synthesis graphene flakes.

Table 1 | GMs compared against graphene flakes prepared by chemical exfoliation.

	Plasma-enabled GMs	**Chemically-derived graphene flakes**
Morphology	• Open, interconnected network of graphene sheets, promoting a high surface area. • Avoids agglomeration or uncontrolled stacking of graphene.	• Graphene flakes form agglomerates due to strong Van der Waals interactions between graphene sheets.
Quality	• Good graphitic quality producing thin graphene layers. • Raman I_D/I_G ~ 1.1 – 1.3, I_{2D}/I_G ~ 1.6 – 2.1.	• Poor graphitic quality producing thick graphene layers. • Raman I_D/I_G ~ 1 – 3, I_{2D}/I_G ~ 0.3 – 0.7.
Process	• Single step, rapid (<10 mins), low-temperature synthesis (200 ^oC).	• Multi-staged and prolonged process (~ 3 days).
Integration	• Water-mediated transfer allows GMs to be integrated onto arbitrary substrates. • Simple and single step transfer process, avoiding impurities and further degradation of graphene properties.	• Requires solvents to form stable dispersions of graphene flakes and non-conductive binders to integrate these graphene flakes for device application. • Complex and introduces impurities.
References	This work	[6,23,24]

Biocompatibility of graphene micro-islands. Plasma-grown GMs present surface defects, oxygen functionalities, and a large surface area. Such morphological and chemical features of GMs may increase its surface energy and polarity, which may favour the proliferation of cells [25,26]. Furthermore, the plasma-unique growth and water-mediated transfer process allows GMs to be transferred to arbitrary substrates with minimal contamination. The toxicity assay was used to study cell viability on the first and fifth days, where the cell counts were normalized by using the data for the control samples after day 1 (Fig. 3a). The cell viability over the five days showed that all samples induce and sustain cell growth (higher than 80%) with a small decrease of the number of living cells observed for all samples.

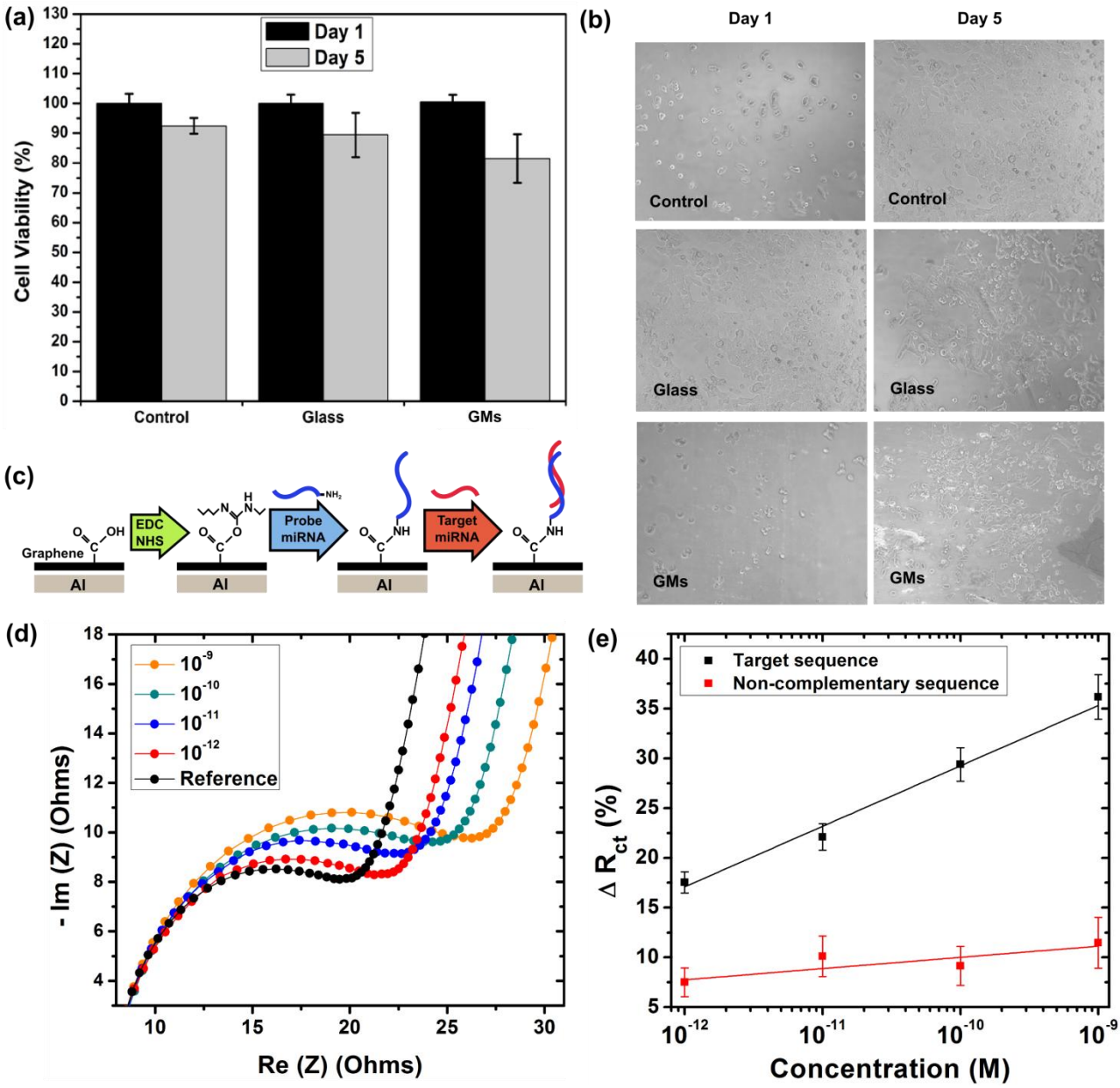

Figure 3 | Biocompatibility and biosensing performances of graphene micro-islands (GMs). Cell viability of graphene micro-islands evaluated (**a**) over 5 days of incubation, with (**b**) respective optical images of cell cultures. (**c**) Schematic for the assembly of an electrochemical biosensor based on graphene micro-islands. (**d**) – (**e**) Electrochemical impedance spectroscopy (EIS) response for GM-based biosensor with respect to the target miRNA and a single-RNA-base mismatched sequence. ΔR_{ct} is defined by $(R_{ct} - R_0)/R_0$, where R_0 is the charge-transfer resistance of the reference sample. Corresponding data are summarized in Table 1.

This is supported by the micrographs that show the altered morphology and cell counts when compared to control samples (Fig. 3b). The morphology of cells was used to determine the progression of cell proliferation in the first 24 (first row) and 120 hours (second row). From the micrographs, the cells were determined to proliferate equally on the glass surface and the GMs. After 5 days of cell culture, fewer cells were observed to be attached on the surface of GMs as compared to the first day. The cells on the control substrate were more spread out, presumably due to the different stiffness and optimized treatments applied on these surfaces for cell growth. These biocompatibility results are comparable to *in vitro* studies of graphene-based materials on the viability of mammalian cell lines. For instance, it was shown that the survival rate of human cervical cancer cells on graphene oxide was 75 – 85% after 48 hrs [27], and the survival rate of HeLa cancer cells on graphene oxide was 80 – 90% after 24 hrs [28,29]. In the case of the non-optimal growth of GMs (Supplementary Fig. 2b), the highly defective graphene results in a significant decline in cell viability (Supplementary Fig. 5). Such results can be attributed to an increase in the presence of sharp graphitic edges with defect content, increasing the likelihood that cells become ruptured. This implies that the graphitic qualities of GMs are equally important for the proliferation of cells. These results suggest that GMs represent a good interfacial material for the adhesion and proliferation of primary fibroblast lung cells. In other words, plasma-grown GMs are biocompatible and may be suitable for bioengineering applications.

Graphene micro-islands for biosensing. Electrochemical sensing methods for minute amounts of nucleic acid samples offer attractive opportunities for a plethora of preventative health technologies, which require portable, cost-effective, and low-power readout devices [30]. Diseases such as cancers are becoming more prevalent with the growing population. Importantly, cancers may be best managed with early intervention therapies followed by early-stage diagnosis. Recently, post-transcriptional epigenetic regulations of gene expressions have been found to provide highly-valuable serum-based nucleic acid biomarkers which may be utilized to enable early diagnostic

strategies for breast cancer [31,32]. Consequently, the favourable morphology and chemical features of GMs motivates its consideration as a biosensing electrode.

Assembly of the electrochemical GM-based biosensor is illustrated in Fig. 3c. Plasma-grown GMs feature active carboxyl functionalities on its surface. Through carbodiimide chemistry, this facilitates the covalent immobilization of probe miRNAs, and enables the specific detection of the complementary miRNA sequence.

Performance of the GM sensor was quantified by electrochemical impedance spectroscopy (EIS) technique. The charge transfer resistance (R_{ct}) was measured to characterize the response of GMs to the surface immobilization of miRNAs. Fig. 3D – E demonstrates an increase in ΔR_{ct} as the concentration of target miRNAs was increased. We define ΔR_{ct} by $(R_{ct} - R_0)/R_0$, where R_0 is the charge-transfer resistance of the reference sample. This increase in ΔR_{ct} may be attributed to a retarded charge transport towards the GM surface, either through spatial blocking or electrical repulsion. In particular, the hybridization between complementary genomic sequences induces a build-up of negative surface charge, and the repulsion of negatively charged ferricyanide ions, which leads to a rise in R_{ct} [33]. Further, this GM-based sensor demonstrates selectivity against miRNA sequences that are mismatched by a single RNA base. A slight increase in R_{ct} was observed at elevated concentrations of non-complementary miRNA. This may be attributed to an increase in non-specifically adsorbed miRNAs on the surface of GMs. Correspondingly, these biosensing data are summarized in Table 2.

The impedance response of GMs in the presence of target miRNAs was analyzed by linear regression (Fig. 3e). A relation of $\Delta R_{ct} = 89.99 + 6.07\ log_{10}(Concentration\ [M])$, $R^2 = 0.98$, was deduced (black curve). The limit of quantification (LOQ) was calculated by $10S_y/b$, with S_y as the standard deviation of the y-intercept ($S_y = 7.83$), and b as the slope of the linear fit ($b = 6.07$) [34]. GMs report a dynamic sensing range that spans 1 pM to 1 nM, and a LOQ of 2.03×10^{-13} M. These performances of GMs are comparable or better than graphene-based electrochemical sensors reported in recent literature (Supplementary Table 1). Notably, chemically-derived reduced graphene oxide (RGO) has been widely utilized in the assembly of such electrochemical sensors. However, GO

dispersions agglomerate uncontrollably when reduced, leading to poor graphene morphology, diminished graphene properties, and a reduction of active surface area for sensing. Additionally, the integration of GO dispersions into an electrode typically involves non-conductive surfactants or chemical binders. This significantly increases the impedance of the sensor, and leads to a compromise in sensitivity. Also, the preparation of RGO powders involves a long, multi-staged process and harsh chemicals. For instance, GO decorated with perylene tetracarboxylic acid diimide (PDI) have been utilized to enable a detection limit of 5.5 x 10^{-13} M single-stranded (ss)DNA [35]. Similarly, RGO have been functionalized with tryptamine to achieve a limit of detection of 5.2 x 10^{-13} M ssDNA [36]. Also, graphite fibers have been activated to form GO interfaces capable of detecting ssDNA down to concentrations of 5.6 x 10^{-12} M [37]. Thus, the unique morphological and surface chemical properties of GMs enable its facile integration as an impedance sensor, capable of sensitive and selective detection of miRNA. These results may be promising for future developments of early diagnostic strategies for cancer, which require the quantification of multiple biomarkers in complex biological environments. Furthermore, electrochemical genosensors based on GMs may be tailored to detect the onset and monitor the progression of other debilitating diseases.

Table 2 | Table of data for impedimetric response of GMs as presented in Fig. 3d and 3e.

Concentration (M)	**Average R_{ct} (Ω)**	**Error R_{ct} (Ω)**	**ΔR_{ct} (%)**	**Error ΔR_{ct} (%)**
0 (Reference)	15.65 (R_0)	0.35	–	–
Target sequence				
10^{-12}	18.39	0.31	17.55	1.08
10^{-11}	19.10	0.30	22.09	1.33
10^{-10}	20.25	0.26	29.39	1.67
10^{-9}	21.31	0.41	36.17	2.29
Non-complementary sequence				
10^{-12}	16.82	2.50	7.49	1.45
10^{-11}	17.23	2.72	10.12	2.04
10^{-10}	17.08	2.89	9.16	1.95
10^{-9}	17.44	3.12	11.46	2.55

Conclusions

In summary, we have presented a plasma-enabled low-temperature synthesis and water-mediated transfer of GMs. Morphological analyses by SEM and AFM reveal that GMs feature a uniform and open-networked array of aggregated graphene sheets. Structural and surface chemical characterizations by Raman spectroscopy and XPS support the presence of thin graphitic edges and reactive oxygen functional groups. We have demonstrated that these inherent properties of GMs enable its multifunctional capabilities for biocompatible coatings and electrochemical sensing. GMs exhibited a biocompatibility of 80% cell viability with primary fibroblast lung cells after 5 days. Also, GMs were assembled to realize an impedimetric biosensor for miRNAs. A dynamic sensing range of 1 pM to 1 nM was reported, and a limit of quantification of 2.03×10^{-13} M was deduced, with selectivity to single-RNA-base mismatched sequences. We envision that GMs are promising for future developments in wearable organic electronics. In principle, the active surface of GMs may enable a multitude of functionalities by hosting various heterostructures and nanocomposites. This may facilitate diverse capabilities in sensing, bioengineering, and anti-microbial coatings. For instance, GMs may be coupled to flexible polymer substrates or textiles to enable multi-faceted platforms for next-generation biomedical devices. We propose these subsequent investigations for the ongoing development of plasma-enabled medical technologies.

Materials and Methods

Plasma-enabled growth of GMs and water-mediated transfer. The deposition of GMs was carried out in a RF inductively coupled plasma CVD system. A copper foil (99.5%, Alfa Aesar) of dimensions 4 cm x 4 cm was used as growth substrate for the GMs. Firstly, a gas mixture of 10 sccm Ar and 90 sccm H_2 was fed into the chamber, and then the plasma was generated at a pressure of 2.0 Pa and RF power of 750 W, respectively. The copper foil was treated with Ar/H_2 plasma for 3 mins. Next, 2 sccm of CH_4 was fed into the chamber. Although no external substrate heating was used, during a subsequent 8 min deposition process, the substrate temperature reached ~200 ^{o}C

due to the plasma-heating effects. Next, the GMs were decoupled from the copper foil by immersion in de-ionized water. GMs floated as a film on the water surface, and were transferred onto a glass substrate for subsequent characterizations, unless stated otherwise.

Microscopy and microanalysis. Please refer to **Section 1.4** of Chapter 1, “Raman Spectroscopy”, “X-ray Photoelectron Spectroscopy (XPS)”, “Transmission Electron Microscopy (TEM)” and “Atomic Force Microscopy (AFM)”, for their general experimental details. In particular, for these XPS measurements, the GMs were transferred onto a conductive aluminium foil substrate. Both survey and narrow scans of C 1s were conducted.

Biosensing measurements. The size of each sensing substrate was 2 cm x 1 cm. The biosensing electrode consisted of GMs on aluminium foil. Subsequently, the GMs were treated with 0.05 M *N*-(3-Dimethylaminopropyl)-*N′*-ethylcarbodiimide hydrochloride (EDC) and 0.03 M N-hydroxysulfosuccinimide (NHS) in phosphate buffered saline (PBS, pH = 7, Sigma Aldrich) for 15 mins. This enabled the formation of active ester intermediates via carbodiimide chemistry. Next, the surface of graphene was washed several times with PBS and DI water to remove excess EDC/NHS. Then, NH_2-conjugated miRNAs (probe sequence: 5’-NH_2-AUUUCACGACUGUCACGUCUA-3’, Sigma Aldrich) were diluted in PBS to 0.2 μM, and 50 μL was pipetted onto the EDC/NHS-treated surface. This was left to incubate overnight in a wet environment at room temperature. Next, the sensing surface was washed with 0.05% sodium dodecyl sufonate (SDS) (Sigma Aldrich) in 0.04 M hydroxylamine solution (Sigma Aldrich) to deactivate the remaining carboxyl functional groups and to remove non-specifically bound probe miRNAs. Then, 0.01 M Polyethylene glycol (PEG) (Sigma Aldrich) was loaded on the sensing surface to block the exposed areas of graphene to reduce further non-specific binding. The (biomarker) miRNA sequence (target sequence: 5’-UAAAGUGCUGACAGUGCAGAU-3’, Sigma Aldrich) was dissolve in human serum

(Human Plasma AB, Sigma Aldrich) to obtain dynamic concentrations of 1 pM – 1 nM, which were pipetted onto the sensing surface. This was left to incubate at 45 ^{o}C for 20 mins to induce hybridization between the complementary probe and target sequences. Finally, a washing step with PBS/DI water was employed to remove remaining non-specifically bound target miRNAs. To demonstrate sensing specificity, a similar protocol was adopted by replacing the target sequence with a single-RNA-base mismatched sequence (non-complementary sequence: 5'-UAGAGUGCUGACAGUGCAGAU-3', Sigma Aldrich). This fully assembled device was then utilized in a three-electrode electrochemical cell for biosensing measurements.

Cytotoxicity testing. The cytotoxicity of plasma-grown GMs was evaluated using CellTiter 96 Aqueous Non-Radioactive Cell proliferation (MTS) Assay (Promega, C#G5421) following the protocol provided by the manufacturer. Primary fibroblasts lung cells (MRC5 cell line) were cultured in 96-well plates at 2x10^{4} cells/well on control (Tissue Culture Polystyrene - TCPS), glass and glass covered with GMs for 1 to 5 days. Optical microscopy images were taken after 24 hours and 120 hours of culture, on the 1 day and 5 days samples, respectively.

References

1. Novoselov, K.S.; Falko, V.I.; Colombo, L.; Gellert, P.R.; Schwab, M.G.; Kim, K., A roadmap for graphene. *Nature* **2012**, *490*, 192-200.
2. Zurutuza, A.; Marinelli, C., Challenges and opportunities in graphene commercialization. *Nature Nanotechnology* **2014**, *9*, 730-734.
3. Sun, Z.; Yan, Z.; Yao, J.; Beitler, E.; Zhu, Y.; Tour, J.M., Growth of graphene from solid carbon sources. *Nature* **2010**, *468*, 549-552.
4. Guermoune, A.; Chari, T.; Popescu, F.; Sabri, S.S.; Guillemette, J.; Skulason, H.S.; Szkopek, T.; Siaj, M., Chemical vapor deposition synthesis of graphene on copper with methanol, ethanol, and propanol precursors. *Carbon* **2011**, *49*, 4204-4210.

5. Hernandez, Y.; Nicolosi, V.; Lotya, M.; Blighe, F.M.; Sun, Z.; De, S.; McGovern, I.T.; Holland, B.; Byrne, M.; Gun'Ko, Y.K.*, et al.*, High-yield production of graphene by liquid-phase exfoliation of graphite. *Nature Nanotechnology* **2008**, *3*, 563-568.
6. Li, D.; Muller, M.B.; Gilje, S.; Kaner, R.B.; Wallace, G.G., Processable aqueous dispersions of graphene nanosheets. *Nature Nanotechnology* **2008**, *3*, 101-105.
7. Gao, L.; Ren, W.; Xu, H.; Jin, L.; Wang, Z.; Ma, T.; Ma, L.-P.; Zhang, Z.; Fu, Q.; Peng, L.-M.*, et al.*, Repeated growth and bubbling transfer of graphene with millimetre-size single-crystal grains using platinum. *Nature Communications* **2012**, *3*, 1-7.
8. Suk, J.W.; Kitt, A.; Magnuson, C.W.; Hao, Y.; Ahmed, S.; An, J.; Swan, A.K.; Goldberg, B.B.; Ruoff, R.S., Transfer of cvd-grown monolayer graphene onto arbitrary substrates. *ACS Nano* **2011**, *5*, 6916-6924.
9. van der Laan, T.; Kumar, S.; Ostrikov, K., Water-mediated and instantaneous transfer of graphene grown at 220 [degree]c enabled by a plasma. *Nanoscale* **2015**, *7*, 20564-20570.
10. Biswal, M.; Banerjee, A.; Deo, M.; Ogale, S., From dead leaves to high energy density supercapacitors. *Energy Environmental Science* **2013**, *6*, 1249-1259.
11. Yick, S.; Han, Z.J.; Ostrikov, K., Atmospheric microplasma-functionalized 3d microfluidic strips within dense carbon nanotube arrays confine au nanodots for sers sensing. *Chemical Communications* **2013**, *49*, 2861-2863.
12. Ostrikov, K.; Neyts, E.C.; Meyyappan, M., Plasma nanoscience: From nano-solids in plasmas to nano-plasmas in solids. *Advances in Physics* **2013**, *62*, 113-224.
13. Seo, D.H.; Han, Z.J.; Kumar, S.; Ostrikov, K., Structure-controlled, vertical graphene-based, binder-free electrodes from plasma-reformed butter enhance supercapacitor performance. *Advanced Energy Materials* **2013**, *3*, 1316-1323.
14. Zhao, J.; Shaygan, M.; Eckert, J.; Meyyappan, M.; Rümmeli, M.H., A growth mechanism for free-standing vertical graphene. *Nano Letters* **2014**, *14*, 3064-3071.
15. Bo, Z.; Mao, S.; Jun Han, Z.; Cen, K.; Chen, J.; Ostrikov, K., Emerging energy and environmental applications of vertically-oriented graphenes. *Chemical Society Reviews* **2015**, *44*, 2108-2121.
16. Lespade, P.; Al-Jishi, R.; Dresselhaus, M.S., Model for raman scattering from graphitized carbons. *Carbon* **1982**, *20*, 427-431.
17. Wang, Y.; Alsmeyer, D.C.; McCreery, R.L., Raman spectroscopy of carbon materials: Structural basis of observed spectra. *Chemical Materials* **1990**, *2*, 557.

18. Cuesta, A.; Dhamelincourt, P.; Laureyns, J.; Martinez-Alonso, A.; Tascon, J.M.D., Comparative performance of x-ray diffraction and raman microprobe techniques for the study of carbon materials. *Journal of Materials Chemistry* **1998**, *8*, 2875-2879.
19. Niyogi, S.; Bekyarova, E.; Itkis, M.E.; Zhang, H.; Shepperd, K.; Hicks, J.; Sprinkle, M.; Berger, C.; Lau, C.N.; de Heer, W.A.*, et al.*, Spectroscopy of covalently functionalized graphene. *Nano Letters* **2011**, *10*, 4061-4066.
20. Ruan, G.; Sun, Z.; Peng, Z.; Tour, J.M., Growth of graphene from food, insects, and waste. *ACS Nano* **2011**, *5*, 7601-7607.
21. Seo, D.H.; Pineda, S.; Yick, S.; Bell, J.; Han, Z.J.; Ostrikov, K., Plasma-enabled sustainable elemental lifecycles: Honeycomb-derived graphenes for next-generation biosensors and supercapacitors. *Green Chemistry* **2015**, *17*, 2164-2171.
22. Hsiao, M.-C.; Liao, S.-H.; Yen, M.-Y.; Teng, C.-C.; Lee, S.-H.; Pu, N.-W.; Wang, C.-A.; Sung, Y.; Ger, M.-D.; Ma, C.-C.M.*, et al.*, Preparation and properties of a graphene reinforced nanocomposite conducting plate. *Journal of Materials Chemistry* **2010**, *20*, 8496-8505.
23. Wang, H.; Robinson, J.T.; Li, X.; Dai, H., Solvothermal reduction of chemically exfoliated graphene sheets. *Journal of the American Chemical Society* **2009**, *131*, 9910-9911.
24. Stankovich, S.; Dikin, D.A.; Piner, R.D.; Kohlhaas, K.A.; Kleinhammes, A.; Jia, Y.; Wu, Y.; Nguyen, S.T.; Ruoff, R.S., Synthesis of graphene-based nanosheets via chemical reduction of exfoliated graphite oxide. *Carbon* **2007**, *45*, 1558-1565.
25. Wang, K.; Fishman, H.A.; Dai, H.; Harris, J.S., Neural stimulation with a carbon nanotube microelectrode array. *Nano Letters* **2006**, *6*, 2043-2048.
26. Borghi, F.F.; Rider, A.E.; Kumar, S.; Han, Z.J.; Haylock, D.; Ostrikov, K., Emerging stem cell controls: Nanomaterials and plasma effects. *Journal of Nanomaterials* **2013**, *2013*, 1-15.
27. Hong, B.J.; Compton, O.C.; An, Z.; Eryazici, I.; Nguyen, S.T., Successful stabilization of graphene oxide in electrolyte solutions: Enhancement of biofunctionalization and cellular uptake. *ACS Nano* **2012**, *6*, 63-73.
28. Peng, C.; Hu, W.; Zhou, Y.; Fan, C.; Huang, Q., Intracellular imaging with a graphene-based fluorescent probe. *Small* **2010**, *6*, 1686-1692.
29. Yang, X.; Niu, G.; Cao, X.; Wen, Y.; Xiang, R.; Duan, H.; Chen, Y., The preparation of functionalized graphene oxide for targeted intracellular delivery of sirna. *Journal of Materials Chemistry* **2012**, *22*, 6649-6654.

30. Turner, A.P.F., Biosensors: Sense and sensibility. *Chemical Society Reviews* **2013**, *42*, 3184-3196.
31. Gong, C.; Qu, S.; Lv, X.-B.; Liu, B.; Tan, W.; Nie, Y.; Su, F.; Liu, Q.; Yao, H.; Song, E., Brms1l suppresses breast cancer metastasis by inducing epigenetic silence of fzd10. *Nature Communications* **2014**, *5*, 1-15.
32. Gong, C.; Qu, S.; Liu, B.; Pan, S.; Jiao, Y.; Nie, Y.; Su, F.; Liu, Q.; Song, E., Mir-106b expression determines the proliferation paradox of tgf-[beta] in breast cancer cells. *Oncogene* **2015**, *34*, 84-93.
33. Suni, I.I., Impedance methods for electrochemical sensors using nanomaterials. *Trends in Analytical Chemistry* **2008**, *27*, 604-611.
34. Armbruster, D.A.; Pry, T., Limit of blank, limit of detection and limit of quantitation. *Clinical Biochemistry Reviews* **2008**, *29*, S49-S52.
35. Hu, Y.; Wang, K.; Zhang, Q.; Li, F.; Wu, T.; Niu, L., Decorated graphene sheets for label-free DNA impedance biosensing. *Biomaterials* **2012**, *33*, 1097-1106.
36. Zhang, Z.; Luo, L.; Chen, G.; Ding, Y.; Deng, D.; Fan, C., Tryptamine functionalized reduced graphene oxide for label-free DNA impedimetric biosensing. *Biosensors Bioelectronics* **2014**, *60*, 161-166.
37. Zhang, J.; Li, A.; Yu, X.; Guo, W.; Zhao, Z.; Qiu, J.; Mou, X.; Claverie, J.P.; Liu, H., Scaly graphene oxide/graphite fiber hybrid electrodes for DNA biosensors. *Advanced Material Interfaces* **2015**, *2*, 1-6.

Supporting Information for:

Multifunctional Graphene Micro-Islands: Rapid, Low-Temperature Plasma-Enabled Synthesis and Facile Integration for Bioengineering and Genosensing Applications

Shafique Pineda[1,2,†], Fabricio Frizera Borghi[1,2,†], Dong Han Seo[1], Samuel Yick[1], Malcolm Lawn[3], Timothy van der Laan[1,2], Zhao Jun Han[1], and Kostya (Ken) Ostrikov[1,2,4,*]

[1] CSIRO Manufacturing, P.O. Box 218, 36 Bradfield Road, Lindfield, NSW 2070, Australia.

[2] School of Physics, The University of Sydney, Sydney, NSW 2006, Australia.

[3] National Measurement Institute (NMI), Nanometrology, 36 Bradfield Road, Lindfield, NSW 2070, Australia.

[4] Institute for Future Environments and Institute for Health and Biomedical Innovation, School of Chemistry, Physics, and Mechanical Engineering, Queensland University of Technology, Brisbane, QLD 4000, Australia.

† These authors contributed equally to this work.

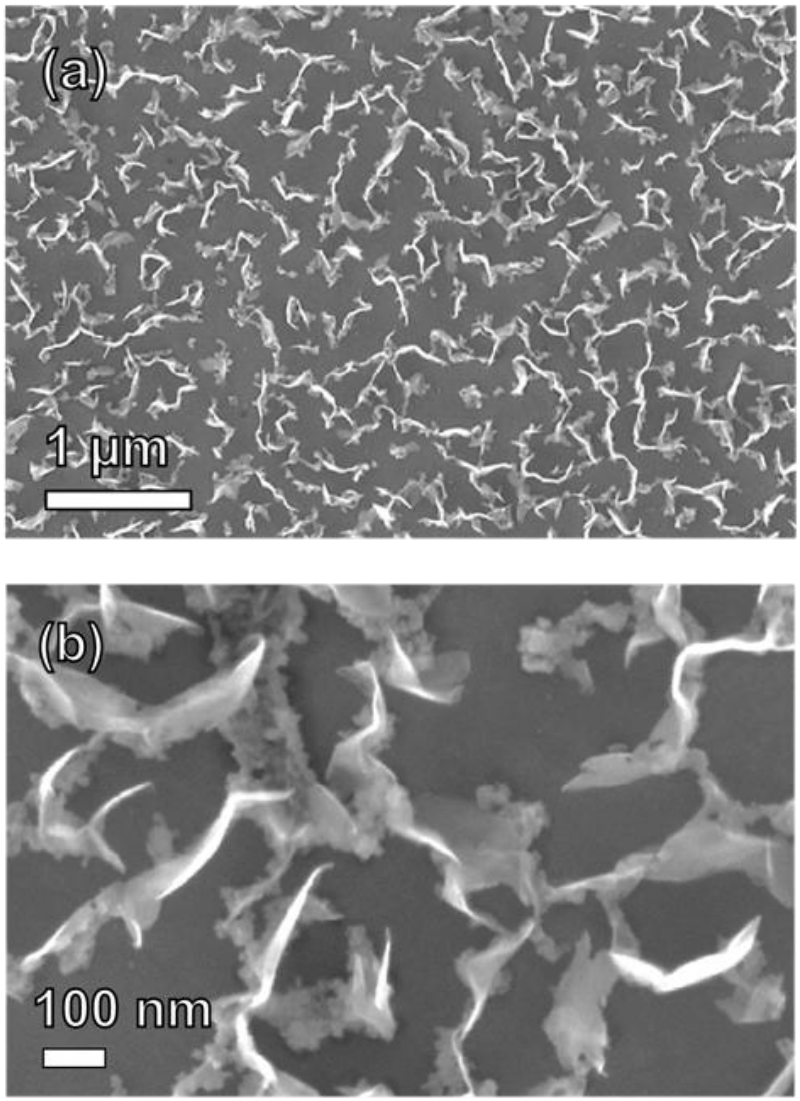

Supplementary Figure 1 | Characterization of the morphology for as-grown graphene nanosheets on copper foil. (**a**) Low-magnification SEM, and (**b**) high-magnification SEM images.

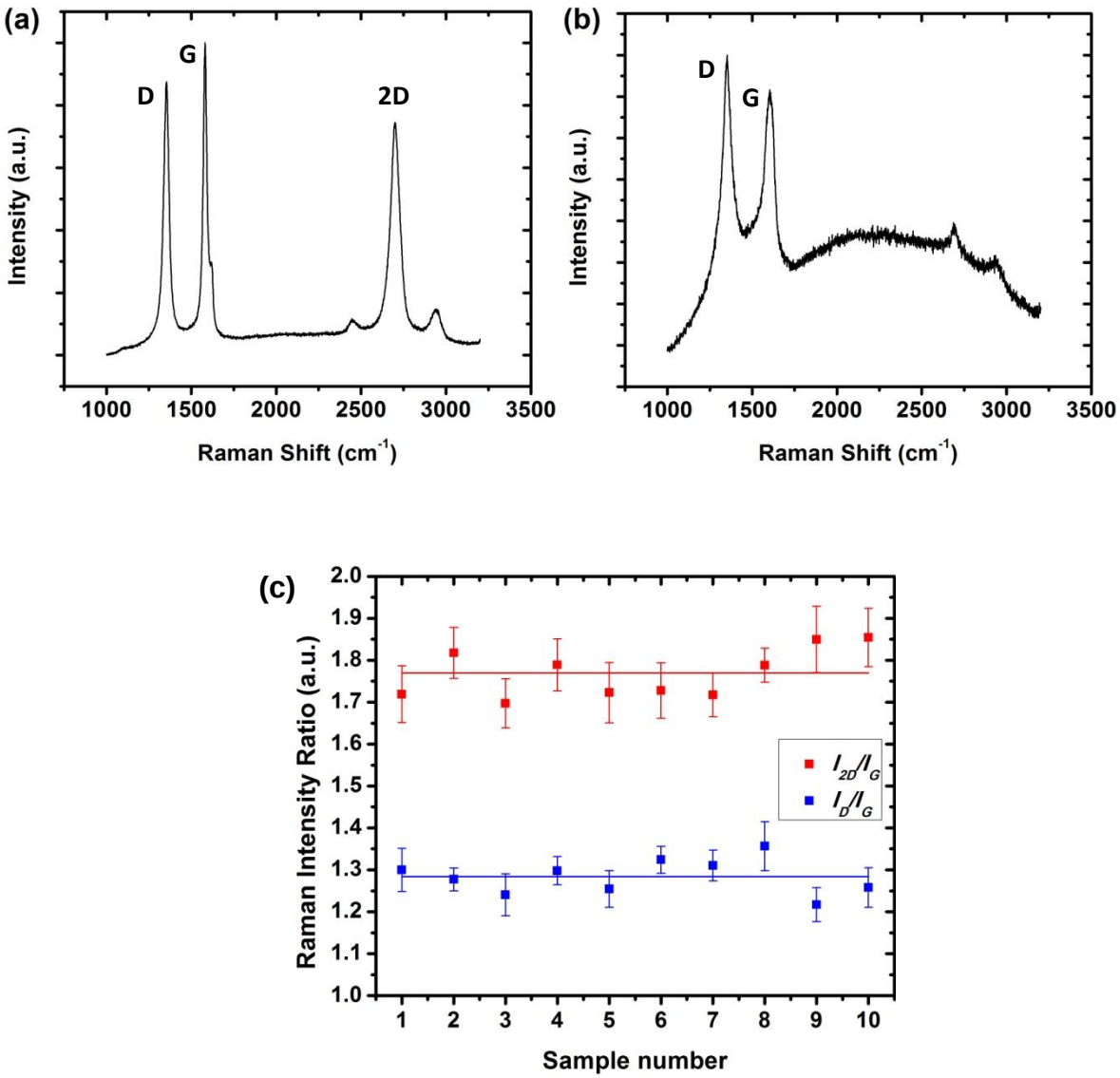

Supplementary Figure 2 | Raman spectra analysis illustrating the growth graphene micro-islands (GMs) under non-optimal conditions and reproducibility of the growth process. Characteristic D, G, and 2D peaks (labeled) are associated with lattice vibrations in the graphitic lattice. (a) With high CH_4/H_2 feedstock gas ratio and longer plasma processing time, this results in thicker graphene sheets (I_{2D}/I_G < 1). (b) Conversely, with low CH_4/H_2 feedstock gas ratio and shorter plasma processing time, this results in either overetching or an incomplete formation of graphene nanosheets (broadened D and G peaks). (c) Reproducibility of GMs, shown by repeated Raman measurements across 10 GM samples. Raman spectrum was taken at 10 different locations across the surface of each sample.

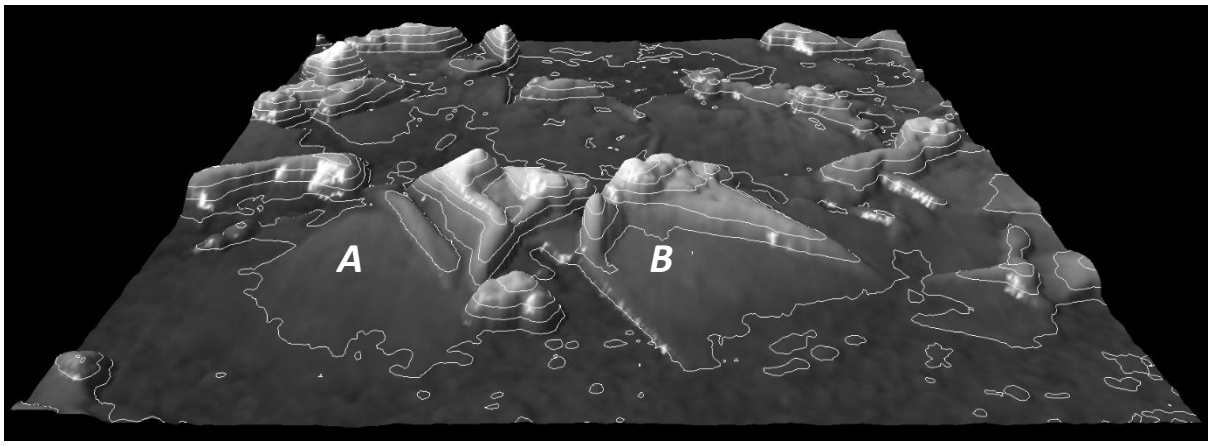

Supplementary Figure 3 | 3-D representation, with superimposed 10 nm contour lines, of a 1 μm x 1 μm AFM topography image of graphene micro-island (GM) flakes on a glass microscope slide substrate. Higher regions, indicated by the contour lines, correspond to nucleation points for growth, whilst ***A*** and **B** indicate the thin (<10 nm) flakes that emerge from the nucleation points to form GMs.

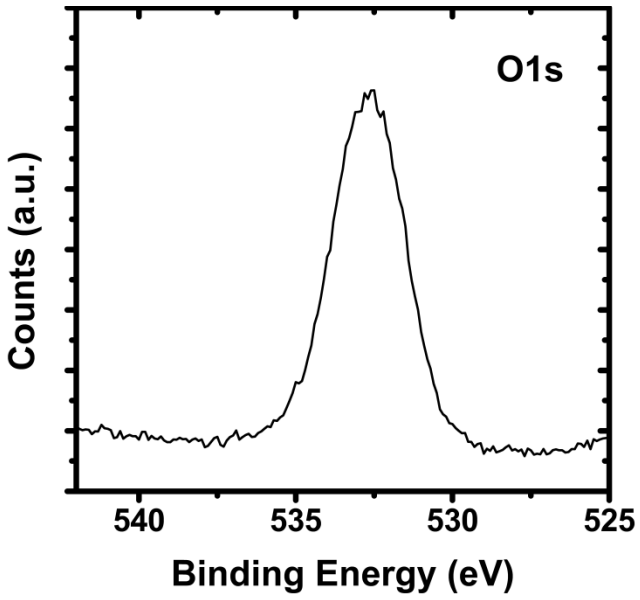

Supplementary Figure 4 | O1s narrow scan of graphene micro-islands (GMs).

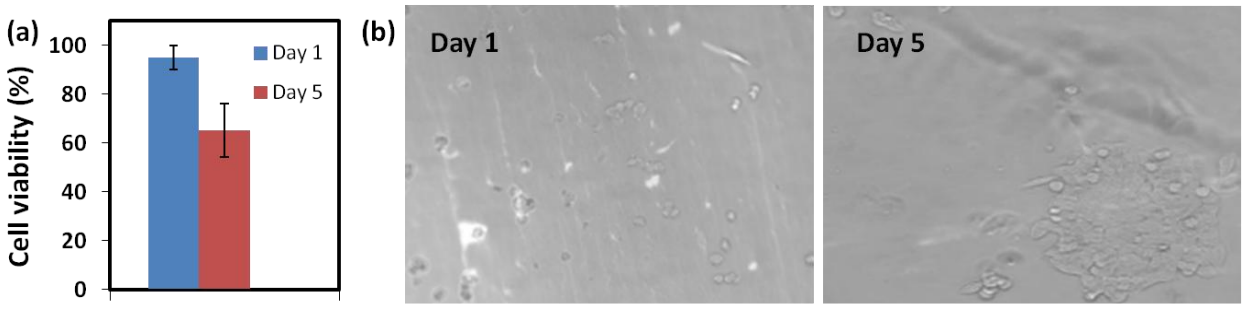

Supplementary Figure 5 | Biocompatibility performance of graphene micro-islands under non-optimal growth conditions. (**a**) Cell viability evaluated over 5 days of incubation with (**b**) respective images of cell cultures.

Supplementary Table 1 | Biosensing performance of GMs compared against other electrochemical impedance-based biosensors

Biosensor	**Performance (Limit of detection)**	**Reference**
GO decorated with perylene tetracarboxylic acid diimide	5.5 x 10^{-13} M ssDNA	[S1]
RGO functionalized with tryptamine	5.2 x 10^{-13} M ssDNA	[S2]
Activated graphite fibers	5.6 x 10^{-12} M ssDNA	[S3]
Graphene on glassy carbon, decorated with Au nanorods and polythionine	4.03 x 10^{-14} M ssDNA	[S4]
Graphene decorated with TiO_2 nanorods and chitosan nanocomposites	7.21 10^{-13} M ssDNA	[S5]
Graphene micro-islands	2.03 x 10^{-13} M	This work

Supplementary References

[S1] Hu Y., Wang K., Zhang Q., Li F., Wu T., Niu L., Decorated graphene sheets for label-free DNA impedance biosensing. *Biomaterials* **2012**, *33*, 1097-1106.

[S2] Zhang Z., Luo L., Chen G., Ding Y., Deng D., Fan C., Tryptamine functionalized reduced graphene oxide for label-free DNA impedimetric biosensing. *Biosensors Bioelectronics* **2014**, *60*, 161-166.

[S3] Zhang J., Li A., Yu X., Guo W., Zhao Z., Qiu J., Mou X., Claverie J.P., Liu H., Scaly graphene oxide/graphite fiber hybrid electrodes for DNA biosensors. *Advanced Materials Interfaces* **2015**, *2*, 1-6.

[S4] Huang H., Bai W., Dong C., Guo R., Liu Z., An ultrasensitive electrochemical DNA biosensor based on graphene/Au nanorod/polythionine for human papillomavirus DNA detection. *Biosensors Bioelectronics* **2015**, *68*, 442-6.

[S5] Gao H., Sun M., Lin C., Wang S., Electrochemical DNA biosensor based on graphene and TiO_2 nanorods composte film for the detection of transgenic soybean gene sequence of MON89788. *Electroanalysis* **2012**, *24,* 2283-2290.

4

Plasma-Enabled Synthesis of Vertically-Oriented Graphenes for Energy Storage Devices

"An ocean traveler has even more vividly the impression that the ocean is made of waves than it is made of water."
– Sir Arthur Stanley Eddington, 1927.

This chapter presents the plasma-enabled synthesis of vertically-oriented graphene nanosheets (VGNS) by reforming natural precursors, and their direct integration for supercapacitor applications.

Graphene powders are widely considered for active materials in energy storage devices (**Section 1.2.1**). However, graphene powders are prone to uncontrolled agglomeration, and require non-conductive binders and surfactants for its assembly into an electrode. Consequently, this limits the mass loading and hence, the use of graphene nanomaterials in energy storage (**Section 1.3.2)**. Indeed, this leads to significant degradation in energy storage performances (*i.e.*, reduced effective surface area, specific capacitance and stability). Here, we demonstrate a plasma-enabled approach to address these limitations in graphene-based energy storage devices.

The first half of this chapter is dedicated to developing a plasma-enabled process for VGNS synthesis, demonstrating its tailorable and attractive electrochemical properties. The second half of this chapter focuses on up-scaling the use and production of VGNS by the plasma process, while retaining its performance for energy storage devices.

Plasma is shown to enable a single-step, low temperature growth and direct integration of VGNS as an active material for supercapacitor application. Diverse natural precursors are reformed into homogeneous VGNS. The VGNS feature a high surface area, an open morphology, interconnected arrays of graphene sheets, and a high density of reactive edges, and hence, attractive electrochemical properties for energy storage.

In this chapter, fabrication and characterization of VGNS are explored. Control parameters for VGNS morphology and properties by the plasma process are investigated. The performance of VGNS for supercapacitor applications is evaluated (*i.e.*, stability, capacitance, *etc.*). Diverse precursors were demonstrated for reforming into VGNS (*e.g.*, honeycomb, butter, cheese). VGNS were employed as binder-free supercapacitor electrodes, and demonstrated high specific capacitance up to 240 F/g at a scan rate of 5 mV/s, and 100% capacitance retention after 2,000 charge/discharge cycles. Further, it is demonstrated that mass loading of VGNS can be increased by regulating properties of the precursor material. By considering various precursors and respective plasma-matter interactions, the VGNS were demonstrated to achieve a high mass loading of 3.2 mg/cm^2, and a high areal capacitance of 0.46 F/cm^2.

These results demonstrate a green and resource-efficient approach for the transformation of natural precursors into functional graphene nanostructures, promising for a variety of energy storage applications.

This chapter addresses **Thesis Objective 3**.

Two manuscripts are included in this chapter. The first manuscript has been accepted for publication at **Green Chemistry** [1]. The second manuscript has been accepted for publication at **ACS Sustainable Chemistry & Engineering** [2].

Statement of contribution for manuscript [1]: Shafique Pineda (S.P.) and Dong Han Seo (D.H.S.) conceived the idea, and together, carried out the experiments, characterizations, and testing of the VGNS material. S.P., D.H.S., Zhao Jun Han (Z.J.H.) and Kostya Ostrikov (K.O.) wrote the manuscript with input from all co-authors.

Statement of contribution for manuscript [2]: S.P. conducted the material characterizations (Raman and SEM) of VGNS with the guidance of D.H.S and Samuel Yick (S.Y.). S.P., D.H.S., S.Y., Z.J.H and K.O. wrote the manuscript with input from all co-authors.

References

[1] **Seo D.H.*, Pineda S.***, Yick S., Han Z.J., Bell J., Ostrikov K., Plasma-Enabled Sustainble Elemental Lifecycles: Honeycomb-derived Graphenes for Next-Generation Biosensors and Supercapacitors, *Green Chemistry*, 2015, 17, 2164 – 2171 (***** = equal contribution).

[2] Seo D.H.***,*** Yick S.*, **Pineda S.**, Su D., Wang G., Han Z.J., Ostrikov K., Single-Step Plasma-Enabled Reforming of Natural Precursors into Vertical Graphene Electrodes with High Areal Capacitance, *ACS Sustainable Chemistry & Engineering*, 2015, 3 (3), 544 – 551 (***** = equal contribution).

Plasma-Enabled Sustainable Elemental Lifecycles: Honeycomb-derived Graphenes for Next-Generation Biosensors and Supercapacitors

Dong Han Seo[a,b,†], Shafique Pineda[a,b,†], Samuel Yick[a,b], John Bell[c], Zhao Jun Han[a], and Kostya (Ken) Ostrikov[a,b,c,*]

[†] These authors contributed equally to this work.

[a] Plasma Nanoscience Laboratories, Industrial Innovation Program, Manufacturing Flagship, CSIRO, P.O. Box 218, Lindfield, NSW 2070, Australia.

[b] School of Physics, The University of Sydney, Sydney, NSW 2006, Australia.

[c] Institute for Future Environments and Institute for Health and Biomedical Innovation, School of Chemistry, Physics, and Mechanical Engineering, Queensland University of Technology, Brisbane, QLD 4000, Australia.

Abstract

A green and efficient conversion of redundant biomass into functional nanomaterials holds the key to sustainable future technologies. Recently, vertical graphene nanosheets (VGS) have emerged as promising nanomaterials for integration in high-performance biosensors and supercapacitors, owing to their excellent and unique structural, morphological and electrical properties. However, when considering the conventional techniques utilized in nanofabrication, such as thermal or chemical routes, these often involve complex, eco-destructive and resource-consuming processes. Here we report on a single-step, potentially scalable, environmentally-benign and plasma-enabled method to synthesize VGS from an underutilized and natural by-product precursor, honeycomb. The VGS multifunctionality is highlighted by its integration as supercapacitor electrodes for energy storage, and as an electrochemical biosensor for the detection of the neurotoxic Amyloid-beta (Aβ) biomarker of Alzheimer's disease. The

VGS were employed as binder-free supercapacitor electrodes, and demonstrated high specific capacitance up to 240 F g^{-1} at a scan rate of 5 mV s^{-1} and 100% capacitance retention after 2,000 charge/discharge cycles. Furthermore, the VGS were functionalized with curcumin bioreceptors, and exhibited good sensitivity and selectivity towards the detection of neurotoxic Aβ species, and demonstrated a detection limit of 0.1 µg/mL.

Introduction

The rationale for implementing green technologies as part of a sustainable modern society is becoming increasingly apparent [1]. In particular, recycling redundant biomass into functional nanomaterials has attracted significant attention, notably, as this promotes a more efficient route for nanomaterial fabrication, as compared to conventional methods which utilize hazardous chemicals or purified hydrocarbon gases [2,3]. Moreover, an efficient synthesis of nanomaterials remains crucial for the large-scale commercialization of high-performance energy storage and biomedical devices. However, existing techniques for the transformation of biomass into nanostructures via thermal or chemical routes are not only precursor-specific, but are also often expensive, complex, as well as energy-, time- and resource-consuming [4]. Therefore, there is a need for a process to convert these chemically heterogeneous biomasses into uniform and useful functional nanostructures. Amongst a variety of nanomaterials, carbon-based nanostructures such as graphene have attracted significant interest owing to its exceptional opto-electrical and mechanical properties [5], which are determined by its specific morphology, orientation and stacking order [6,7].

Recently, vertical graphene nanosheets (VGS) emerged as a highly-promising nanomaterial for diverse applications such as supercapacitors and biosensors [8]. VGS possess a unique morphology of few-layered graphene sheets self-organized in an open 3D-inter-networked array structure [9,10]. Such morphological features enable the properties of a high surface area and good electrical conductivity, which are particularly important for the realization of high-performance supercapcitors and biosensors.

Moreover, the presence of dense and thin reactive edge planes in VGS enhances its chemical and electrochemical activity [8]. Indeed, these reactive sites on VGS may facilitate the immobilization of biological species, and thus, makes VGS a promising base material for biosensing applications. Furthermore, while the open structure of VGS facilitates the transport of ions, its structural rigidity enhances the stability of ion storage capacitors, and thus, promotes the integration of VGS in energy storage devices.

Previous investigations have demonstrated the vital role of low-temperature plasmas for the deterministic fabrication of VGS [11-13]. In particular, such VGS structures can be formed using natural precursors in different heterogeneous chemical states by unique plasma-based processes that adhere to the basic principles of sustainability and green chemistry [2,14,15]. In particular, plasma not only enables the breakdown of chemically heterogeneous natural precursors into simpler building units of graphene, it also enables the self-organization of these building units into uniform VGS structures [15]. Therefore, plasma-based techniques present a promising approach for the effective conversion of diverse forms of biomass into functional nanomaterials. A particularly viable biomass is honeycomb. Typically after honey extraction, honeycomb is deemed to be redundant. As such, the remaining honeycomb is either disposed of, or recycled as a source of candle wax, or as an additive in cosmetics. Thus far, recycling of used honeycomb is primitive and limited. However, in this work, we utilized honeycomb, a natural wax composed of long-chain hydrocarbons, as a source for the fabrication of VGS.

Here, we demonstrate a single step, low-temperature, catalyst-free and highly efficient plasma-enabled reforming of the underutilized by-product honeycomb, into uniform VGS. Moreover, to demonstrate the multifunctionality of the honeycomb-derived vertical graphene nanosheets (HC-VGS), we directly integrated it as a supercapacitor electrode, which exhibited good electrochemical performance and stability. Furthermore, we demonstrate the functionality of HC-VGS as base material for the firm immobilization of curcumin, which in turn, enables the selective and sensitive detection of the neurotoxic Aβ biomarker of Alzheimer's disease.

Results and Discussion

Fabrication and structure of HC-VGS. Flexible and light-weight energy storage and medical devices play a central role in the future development of multifunctional electronics such as portable and wearable devices, roll-up displays, and photovoltaic cells [16]. To this end, flexible graphite paper and Ni foam were chosen as the growth substrates for HC-VGS. Due to its good electrical conductivity, Ni foam and graphite paper also functions as the current collectors in the supercapacitor and biosensing electrodes.

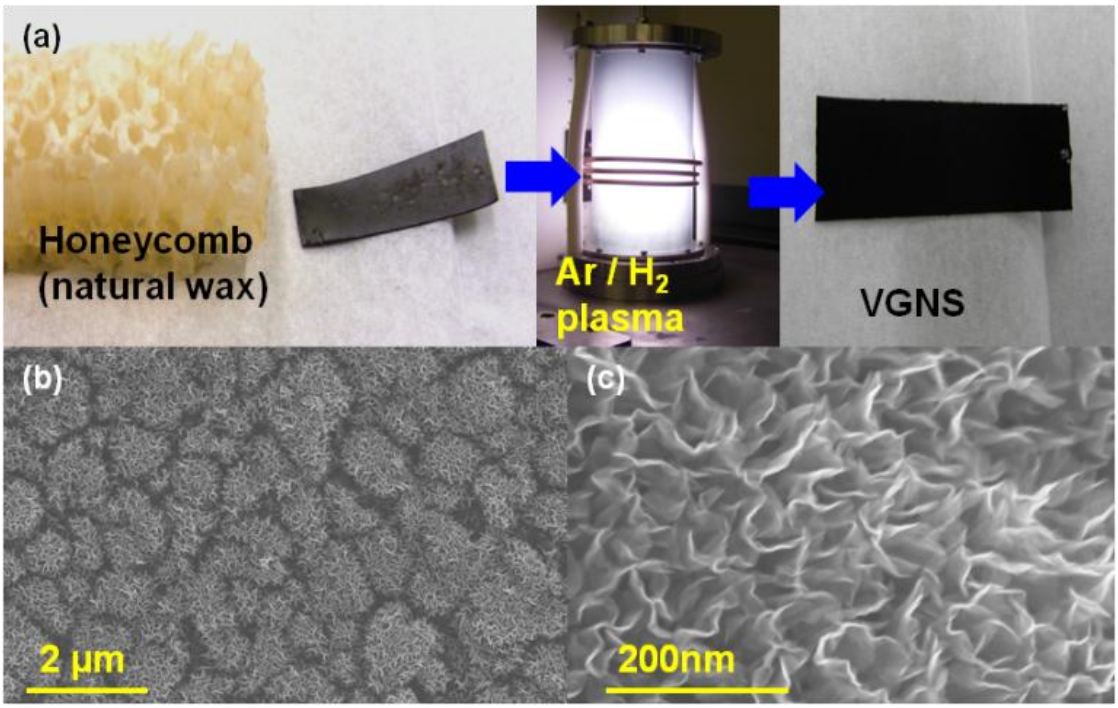

Figure 1 | Transformation of honeycomb (natural wax) into vertical graphenes in a reactive Ar + H_2 plasma-based process. (**a**) Honeycomb was liquefied on the graphite paper substrate which was placed in an ICP-CVD system, whereupon a short plasma exposure was utilized to reform the honeycomb precursor and grow the HC-VGS. As-grown HC-VGS on flexible graphite substrate with supporting (**b**) SEM; and (**c**) high-resolution SEM images featuring its morphology.

The procedure for preparing HC-VGS is illustrated in Fig. 1a. In particular, HC-VGS was formed through the unique plasma transformation of a natural by-product precursor, honeycomb. This approach features a cheap, low-temperature, and environmentally-benign alternative to the chemical vapor deposition (CVD) processes which involve highly explosive hydrocarbon precursor gases such as CH_4 and C_2H_2 [2,3].

The used natural by-product precursor, honeycomb, consisted of mostly palmitate, palmitoleate, and oleate esters of long-chain aliphatic alcohols. Honeycomb is typically solid at room temperature, and can be easily liquefied and coated on the substrates. During the early growth process (~2 min), the long chain of carbon groups in honeycomb were broken down into carbon building units owing to the rapid plasma dissociation of the material. Subsequently, these carbon building units were re-formed into hexagonal carbon-rings, which are the basic elements for the construction of graphene nanosheets. Such plasma-unique effects were presumably attributed to the strong plasma-matter interactions in the plasma sheath [17]. In particular, H_2 can enhance the surface flux of these building units through the recombination-mediated energy dissipation on the surface and facilitate the nucleation and growth of VGS [14]. Moreover, the electric field in the plasma sheath also guides the vertical growth of graphene nanosheets.

Fig. 1b and Fig. 1c show the scanning electron microscopy (SEM) images of HC-VGS obtained after the direct growth process. An inherently open, 3D network with dense and uniform graphene nanosheets was clearly observed to cover the entire surface of graphite paper (see Fig. 1a). It is known that the morphology of VGS can be controlled by the self-organization process during the plasma-enabled growth. Plasma parameters such as RF power, processing time, and gas composition will all affect the growth environment which will eventually change the structure of VGS. In our case, these graphene nanosheets were highly porous and exhibited an average sheet length of 200 nm and a typical thickness of 2 μm (Fig. 1c and Supplementary Fig. 1). This open structure may facilitate the access of biological targets and electrolyte ions to the active surfaces. Consequently, the morphology of HC-VGS not only provides a large surface area which is important for efficient charge transport in electrochemical capacitors. In

addition, the evident high density of reactive edges may also promote a facile surface-immobilization of biological analytes [17-19].

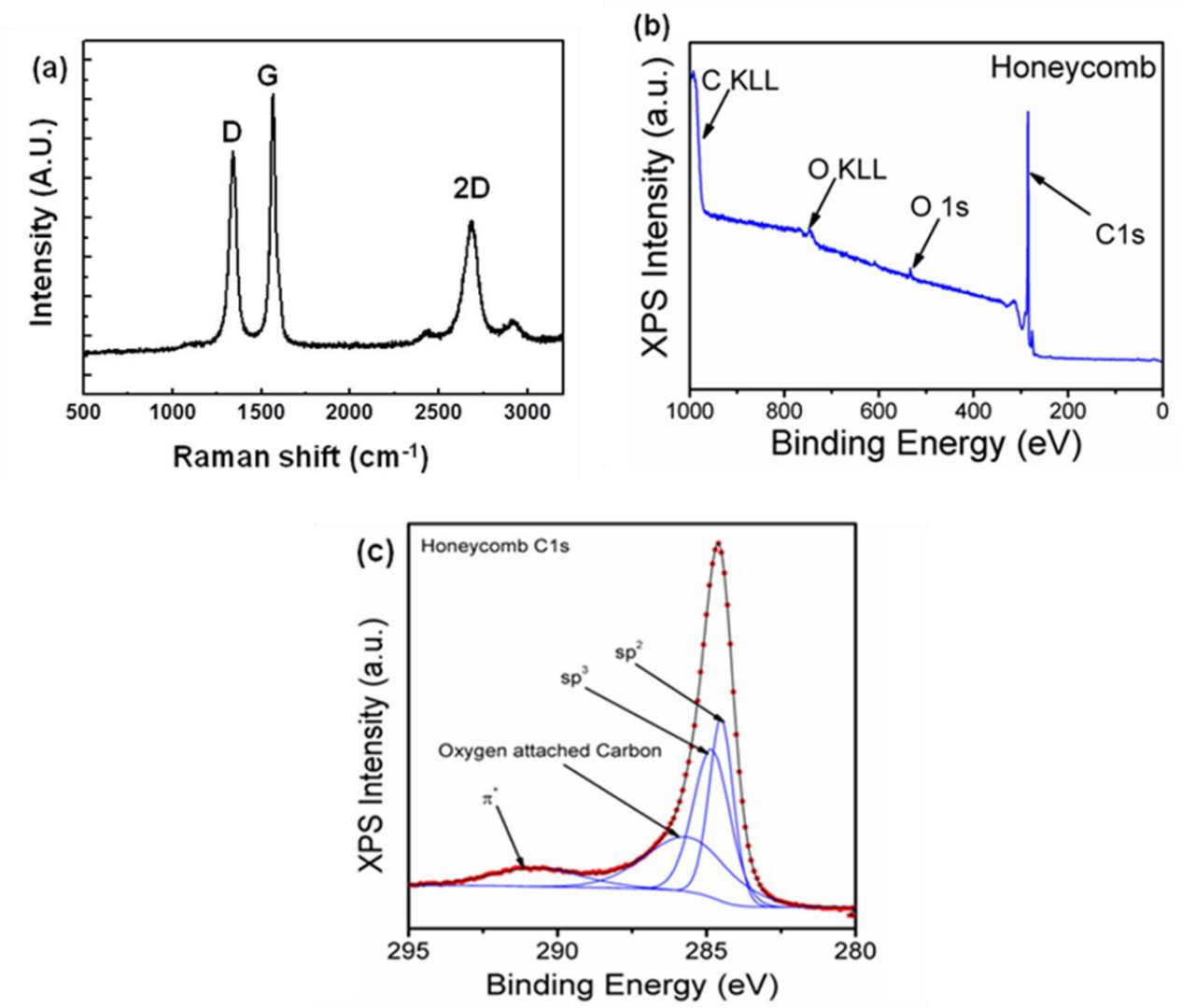

Figure 2 | Structural characterisation of HC-VGS. (**a**) Raman spectrum of HC-VGS. (**b**) XPS survey scan and (**c**) C 1s narrow scan of HC-VGS. Spectrum was fitted with the sp^2, sp^3, oxygen-attached carbon, and π-π* shake-up features.

The surface chemical information of HC-VGS was also characterized by Raman and X-ray photoelectron spectroscopy (XPS). Fig. 2a illustrates the Raman spectra of HC-VGS. Three distinct peaks were present, namely, the characteristic disorder peak (D-band) at 1350 cm^{-1}, the graphitic peak (G-band) at 1580 cm^{-1}, and the second-order 2D-band at

2690 cm^{-1}. The G-band arises from the in-plane vibrational E_{2g} mode of the sp^2-hybridized carbon, the D-band is attributed to the finite crystallite size effect and various defects induced in the sp^2 carbon materials, and the 2D-band is a second-order Raman spectral feature due to the three-dimensional interplanar stacking of hexagonal carbon networks [20-23]. The ratios of Raman I_{2D}/I_G ~(0.45) and I_D/I_G ~(0.72) indicate the presence of sharp edge planes and a dominant sp^2 graphitic structure in HC-VGS [23,24].

Fig. 2b shows the XPS measurements of HC-VGS nanostructures. A single strong C 1s peak positioned at binding energy (BE) of ~284.5 eV was evident, implying the HC-VGS was comprised of mostly carbon atoms. Fig. 2c illustrates the C 1s narrow scan for HC-VGS. The C 1s spectra could be fitted by four peaks corresponding to the carbon sp^2 (BE ~ 284.5 eV), sp^3 (BE ~ 285.4 eV), carbon-oxygen bond (BE ~286 eV), and the energy loss “shake-up” feature (BE ~ 290.2 eV) [14,17]. The sp^2 graphitic structure of HC-VGS also plays a major role in enhancing their charge storage capacity. Indeed, sp^2-bonded carbon is preferred over sp^3-bonded carbon in graphene-based supercapacitor electrodes, as the latter increases the charge transfer resistance and impedes the ability for charge storage. In particular, as HC-VGS features a large fraction of sp^2-hybridized carbon, in conjunction with a high C/O atomic ratio, this makes HC-VGS a highly desirable nanostructure for the integration in electrochemical energy storage devices.

Supercapacitor performance of HC-VGS electrodes. When considering widely available energy sources such as solar and wind power, their intermittent nature necessitates robust energy storage devices for these sources to be utilized in a commercial scale [25]. In addition, the needs for more capable energy storage devices are further stimulated by the recent advancements in portable electronics and hybrid electric vehicles [26-28]. Thus, supercapacitors which possess high power density, rapid charge/discharge rate, and a long lifespan are a particularly attractive option [29-32].

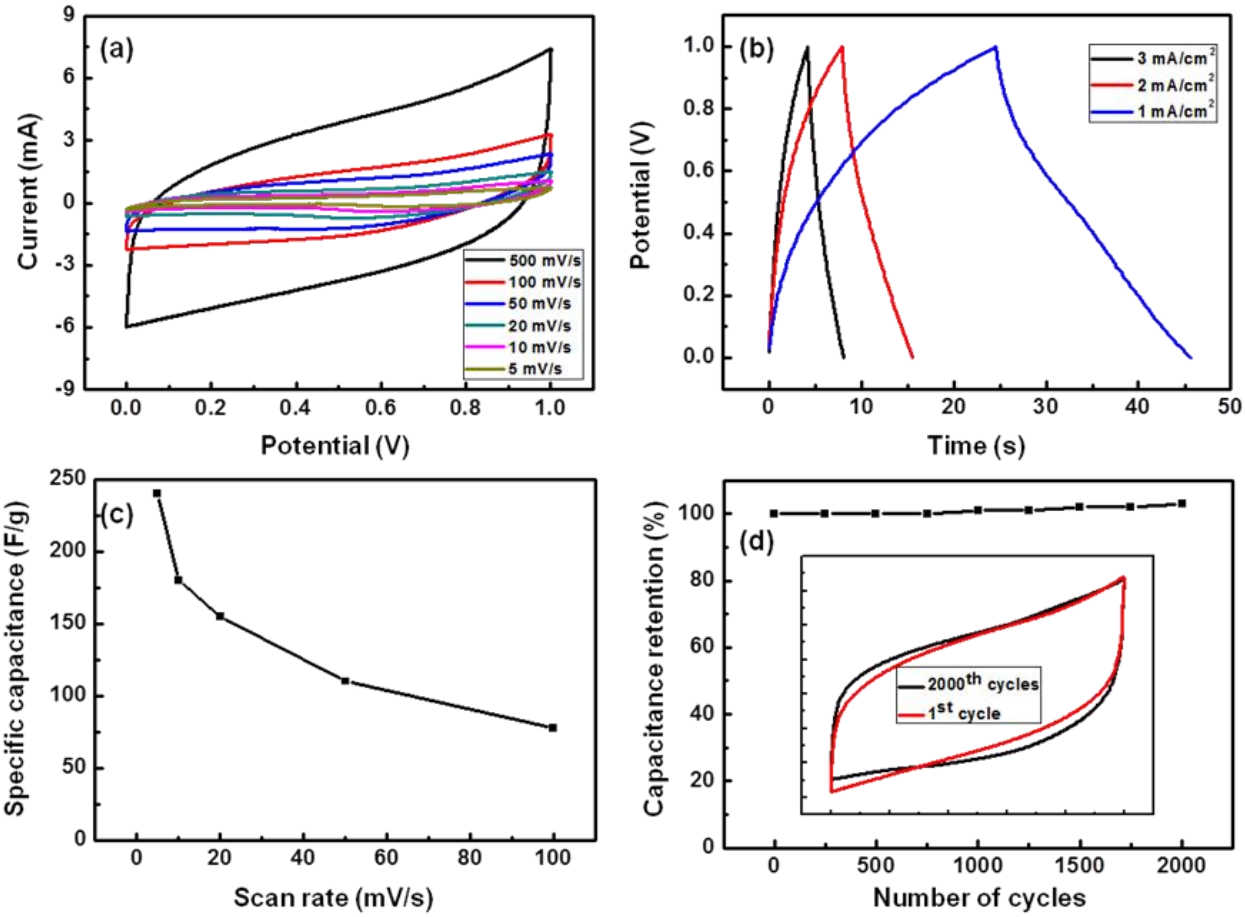

Figure 3 | Supercapacitor performance of HC-VGS. CV curves of (**a**) HC-VGS at different scan rates of 5, 10, 20, 50, 100 mV/s and 500 mV/s. (**b**) Galvanostatic charge/discharge plots of HC-VGS at current densities of 3, 2 and 1 mA/cm^2. (**c**) Rate capabilities of HC-VGS, and (**d**) cycle stability of HC-VGS at a scan rate of 400 mV/s for 2000 cycles.

The electrochemical performance of HC-VGS as binder-free supercapacitor electrodes was investigated by potentiostat/galvanostat measurements using the two-electrode configuration. Fig. 3a shows the cyclic voltammetry (CV) curves of HC-VGS in 1 M Na_2SO_4 aqueous electrolyte. Notably, the as-grown HC-VGS electrodes showed a nearly rectangular shape in CVs even at high scan rates, (*e.g.*, 500 mV s^{-1}) suggesting the efficient formation of the electric double layer (EDL) and fast ion transport in the HC-VGS structure [18]. Fig. 3b shows the galvanostatic charge/discharge curves for HC-VGS at different current densities of 3, 2, and 1 mA/cm^2, respectively. A linear

dependence between the discharge potential and time was identified in the discharge curves, further indicating the absence of major Faradaic processes [33]. These results are consistent with the structural analyses that the electrodes were composed of mostly carbon-based materials and the charge storage occurred mainly through the EDL mechanism [34].

The specific capacitance *C* calculated from the CV curves at different scan rates is shown in Fig. 3c. A decrease in the specific capacitance was observed as the scan rate was increased, similar to that of the corrugated 3D graphene sheets obtained by reduced graphene oxide [35]. It is also noted that HC-VGS exhibits a high specific capacitance of 240 F g^{-1} at a scan rate of 5 mV s^{-1} and 128 F g^{-1} with a current density of 2.5A g^{-1} (Supplementary Fig. 2). We attributed such high specific capacitance to the large surface area, high electrical conductivity, and high electrochemical activity of the HC-VGS, which enables a facile access of ions to the edge and basal planes of the nanostructure [30,36]. This value of specific capacitance for HC-VGS structure is among the highest values reported for graphene based supercapacitor electrodes, and is also superior as compared to other carbon structures with similar 3D morphology, such as the reduced graphene oxide sheets and the mechanically combined graphene/CNT hybrid structures [37,38].

The cycle stability tests are shown in Fig. 3d, in which HC-VGS exhibited 100% retention of its initial capacitance after 2,000 cycles performed at a scan rate of 400 mV/s. In addition, the inset of Fig. 3d shows almost equivalent CV curves between the 1st and the 2000th cycles, clearly evidencing the excellent stability of the electrode materials. This stability of HC-VGS is superior as compared to other typical 3D nano-carbon structures reported in the literature; for example, *Bai et al.* obtained 95% retention after 2,000 cycles for crystalline composites of NiO, reduced graphenes oxide, and carbon nanotubes; *Zhao et al.* obtained 94.4% retention after 2,000 cycles for graphene nanosheets hybridized with $Co(OH)_2$ [39,40]. A slight increase in capacitance was observed at the end of 2,000 cycles which could arise from an increased wetting of electrodes through capillary action in the successive cycles. We attribute such an good stability to the structural durability and the EDL charge storage mechanism of carbon-

based materials, as opposed to metal oxide nanostructures which often show low capacitance retention due to a significant degradation to the nanostructures through redox reactions [41].

The EIS spectrum for HC-VGS measured in the three-electrode configuration is shown in the Nyquist plot in Supplementary Fig. 3, where the frequency-dependent impedance is presented as the real (Z') and imaginary (Z'') components. As-grown HC-VGS displayed a vertical curve feature at low frequencies, indicating a near ideal capacitive behaviour [33]. We also report a low charge transfer resistance and electrode resistance of 2 Ω and 3.7 Ω respectively, which indicates that the HC-VGS possesses a highly conductive surface. In the high-frequency range, a semicircle was observed to intersect with the real (Z') axis, which could be attributed to charge transfer at the electrode-electrolyte interface [42]. We have also performed the three-electrode cell measurements to better evaluate the potential of HC-VGS electrode materials (Supplementary Fig. 4) [43]. The resulting three electrode measurement was consistent with two-electrode-based results. Our supercapacitor performance result demonstrates that HC-VGS which was derived from natural wax may be a promising material for the future energy storage devices. This advantageous characteristic may result from the highly-dense network structure and thin graphitic edges, as suggested from the morphology of HC-VGS, and may also be utilized for a good biosensing platform, which will be discussed in the next section.

Biosensing performance of HC-VGS electrodes. When considering the major life-threatening and debilitating diseases prevalent in the modern society, neurodegenerative dementias such as Alzheimer's disease (AD) present a widespread and rising incidence with far-reaching and detrimental socio-economic repercussions [44]. AD may be most effectively managed with therapeutics provided the disease is accurately diagnosed in the early stages. In order to identify and monitor the progression of AD in sufferers, the specific detection of biomarkers which hallmark the lesions associated with AD is required. One such biomarker is the aggregated form of the Aβ peptide, namely, the oligomeric Amyloid-beta (Aβ-O) which is present in the

cerebrospinal fluid (CSF) of AD sufferers [45,46]. The Aβ peptide exists in the CSF as unaggregated monomers (Aβ-M) and as aggregated oligomers, whereby the former is benign, and the latter is neurotoxic. Therefore, there is a need for a sensor which can reliably differentiate between Aβ-O and Aβ-M.

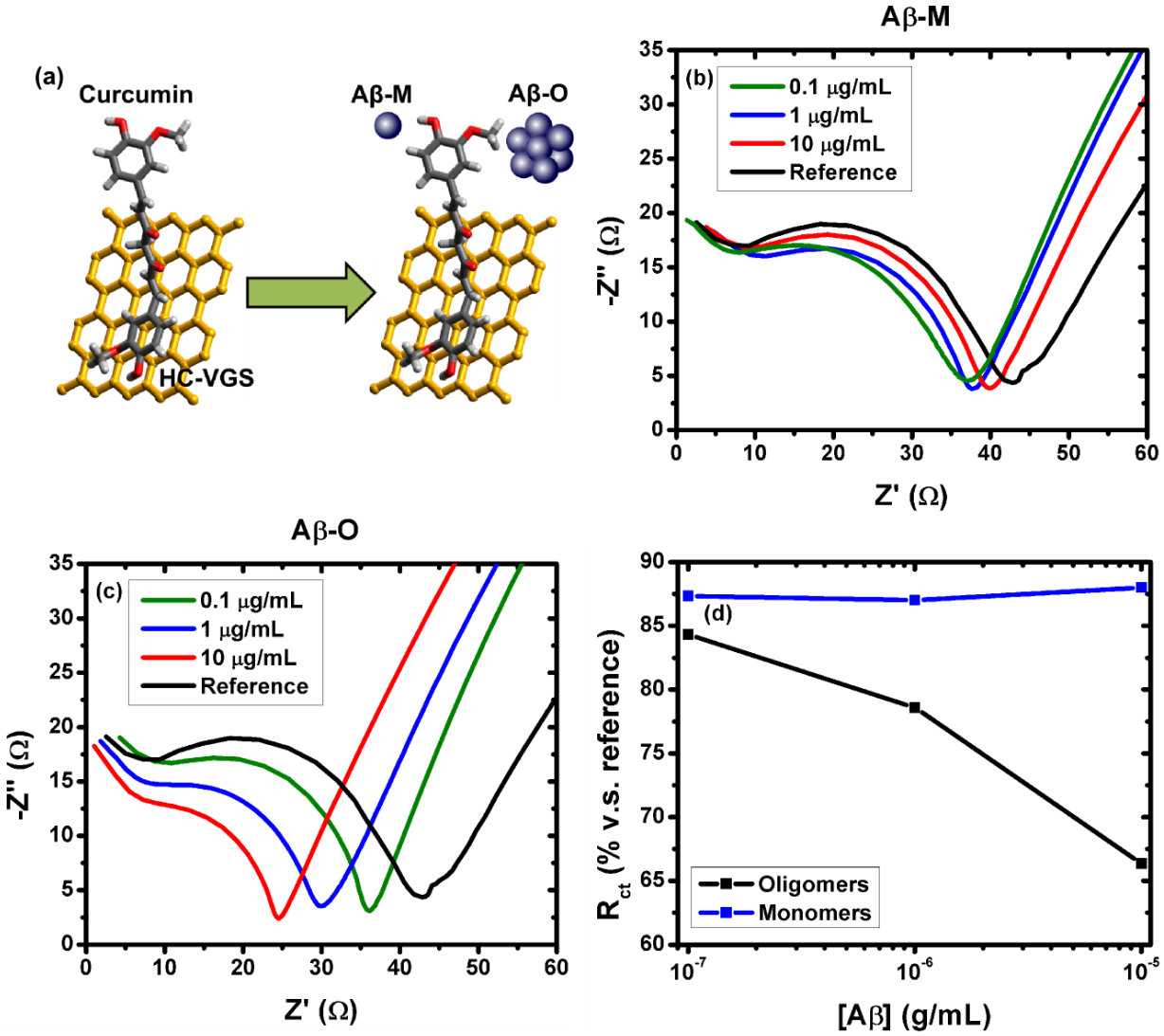

Figure 4 | Biosensing performance of curcumin-functionalized HC-VGS. (**a**) Schematic for the sensing protocol of Aβ-M and Aβ-O. (**b**) and (**c**), EIS response in the presence of Aβ-M, and Aβ-O, respectively, at different concentrations of 0.1, 1, and 10 μg/mL. (**d**) Charge transfer resistance, R_{ct}, expressed as a percentage of the blank reference, at peptide concentrations of 0.1, 1, and 10 μg/mL.

Recently, curcumin has emerged as a promising candidate which selectively binds to aggregated Aβ peptides [47]. Thus, by functionalizing our as-grown HC-VGS with curcumin, a selective sensing towards the neurotoxic Aβ-O may be enabled. Fig. 4a illustrates the sensing principle and the fabrication process of our HC-VGS-based biosensor. In particular, with the integration of HC-VGS as a sensing platform, its thin reactive open edges and inherently large surface area enable the stable and chemical immobilization of curcumin (Supplementary Fig. 5). In addition, the high electrical conductivity of HC-VGS further enables a good sensitivity for the electrochemical detection of Aβ-O.

Fig. 4b shows the EIS response of our biosensor in the presence of Aβ-M at different peptide concentrations. Overall, the radius of the semicircle region shows negligible shift from the reference. This indicates there is a negligible change in the charge transfer resistance, and may also suggest a weak interaction between the Aβ-M and curcumin bioreceptors.

On the other hand, Fig. 4c demonstrates the EIS response in the presence of neurotoxic Aβ-O. A significant decrease in the radius of the semicircle region is evident for increasing concentrations of Aβ-O. This result may indicate that curcumin possesses a greater reactivity with the aggregated form of the Aβ peptide, namely, the reaction of curcumin with Aβ-O is more favourable than with Aβ-M. Additionally, this indicates a decrease in charge transfer resistance (R_{ct}) as more Aβ-O binds to the surface-immobilized curcumin biomolecules. Correspondingly, this decrease in R_{ct} may result from a charge injection to the HC-VGS electrode by the Aβ-Os, in particular, due to the presence of electrochemically active residues in the Aβ peptide [48,49].

Further, Fig. 4d summarizes the changing trends in charge transfer resistance for the oligomeric and monomeric species at different concentrations. Unlike the case with Aβ-M, the presence of Aβ-O induces a significant decrease in the charge transfer resistance. Therefore, this result indicates that our sensor possesses a good selectivity towards Aβ peptide concentrations in the limit of 0.1 μg/mL. Moreover, we suggest that this specificity towards Aβ-O is enabled by a conformational recognition of curcumin to the secondary protein structures present in the aggregated Aβ peptide. In particular, as

curcumin is symmetrical molecule composed of two polar groups separated by a hydrophobic bridge, this allows an alignment of curcumin molecules along the axis of the stacked peptide strands present in oligomers. This in turn facilitates the electrostatic interactions between the polar groups of curcumin and the positive charges on the protonated antiparallel Aβ peptides [47].

Thus, we have demonstrated the functionality of HC-VGS as a promising and versatile base material for integration in future biosensing devices. Importantly, the favourable morphological and electrochemical properties of HC-VGS facilitate a reliable and easy-to-fabricate sensor with good sensitivity and selectivity towards the neurotoxic Aβ-O species. With future optimizations to explore the functionalization of HC-VGS and the loading of curcumin receptors, the performace of this HC-VGS-based biosensor may be further enhanced.

Conclusions

In summary, we have demonstrated an efficient plasma-enabled reforming of the natural by-product precursor, honeycomb, into VGS with excellent morphological and electrochemical properties. Furthermore, these unique and intrinsic properties of HC-VGS enabled its excellent integration as a base material for energy storage and biosensing applications. In particular, we have assembled a reliable, simple-to-fabricate, and inexpensive biosensor which capitalized on the unique properties of HC-VGS, to enable a firm surface-immobilization of curcumin, and its novel function as a bioreceptor for a selective and sensitive capture of the neurotoxic Aβ biomarkers of AD. In addition, we have demonstrated a binder-free supercapacitor electrode, which exhibited a high specific capacitance up to 240 F g^{-1} at a scan rate of 5 mV s^{-1} and 100% capacitance retention after 2,000 cycles at a high scan rate.

Importantly, these results are promising for future sustainable management of resources, through the reforming of natural by-products into carbon-based electrodes, and may also lead to better understanding of the elementary charge storage and

transfer processes, which remain critical for developments in the next-generation of energy storage and biomedical devices.

Experimental Methods

Plasma enabled growth of HC-VGS. The deposition of HC-VGS was carried out in a RF inductively coupled plasma CVD system. Flexible graphite paper and Ni foam was used as growth substrates for HC-VGS. The size of growth substrates was 6x1 cm^2. In order to provide a uniform coating of honeycomb on graphite paper, the honeycomb was first melted by heating at 100 ^oC. Subsequently, the substrates were coated evenly with the liquefied honeycomb, prior to being loaded in the reactor. A gas mixture of 10 sccm Ar and 10 sccm H_2 was fed into the chamber, then the plasma was generated at 2.0 Pa pressure and 1000 W RF power. Although no external substrate heating was used, during the 9 min deposition process the substrate temperature reached 400 ^oC due to the plasma-heating effects.

Microscopy and microanalysis. Please refer to **Section 1.4** of Chapter 1, “Raman Spectroscopy” and “X-ray Photoelectron Spectroscopy (XPS)” for their general experimental details. The mass of the electrode was determined by weighting a 10 cm long sample on an ultrasensitive balance (Δ±0.1 μg; Mettler Toledo UMT2) and calculating the fractional mass which was submerged into the electrolyte.

Supercapacitor measurements. The electrochemical measurements were performed in 1 M Na_2SO_4 at room temperature. Both three-electrode and two-electrode cell configurations were employed. The three-electrode cell used the as-grown HC-VGS sample as the working electrode, a Pt foil as the counter electrode, and an Ag/AgCl reference electrode; while the two-electrode cell used two identical testing samples as the electrodes. Cyclic voltammetry (CV), galvanostatic charge/discharge, and

electrochemical impedance spectroscopy (EIS) measurements were conducted using a BioLogic VSP 300 potentiostat/galvanostat device. CV tests were performed in the potential range of 0 – 1 V at scan rates of 5 – 500 mV s^{-1}. Galvanostatic charge/discharge curves were obtained at a constant current density of 3, 2, and 1 mA/cm^2. EIS measurements were performed in the frequency range from 0.01 Hz to 100 kHz. The specific capacitance of single electrode C_s was calculated from the CV curves in two electrode measurement by integrating the discharge current against the potential V according to $\mathrm{Cs} = (2 \int \mathrm{I}\, \mathrm{dV}/\mathrm{vm}\Delta\mathrm{V})$, where v is the scan rate (V s^{-1}), m is the mass of the active material in single electrode, and ΔV is the operating potential window (1 V). Similarly, specific capacitance was calculated from the charge/discharge curve according to $\mathrm{Cs} = 2\mathrm{I}/(\mathrm{m}\, \mathrm{dV}/\mathrm{dt})$, where I is the discharging current, m is the mass of active material, dV potential window (1 V) and dt is the discharge time. The surface mass density of active material was 0.4 mg/cm^2 and 1x1 cm^2 of the sample was used as the working electrode in the test.

Biosensing measurements. The electrochemical measurements were conducted in 20 mM phosphate buffer with 0.15 M NaCl at room temperature. A three-electrode cell configuration was employed. The three-electrode cell used the as-grown HC-VGS sample (size of 1x0.5 cm^2) as the working electrode, a Pt foil as the counter electrode, and an Ag/AgCl reference electrode.

Curcumin, from *curcuma longa* (SigmaAldrich), was dissolved to 2% w/v in DMSO and drop-cast onto HC-VGS, and left to dry overnight at room temperature and pressure. Monomeric and oligomeric Amyloid-beta 42 (Aβ) were prepared according the protocol outlined by *Youmans et al.* (Biosensis) [50]. Briefly, 45 µg of lyophilized Aβ peptide was reconstituted with 2 µL of DMSO, and 98 µL of F12K medium was added to give a total Aβ peptide concentration of 450 µg/mL. Monomeric Aβ (Aβ-M) was taken at this point, whereas oligomers (Aβ-O) were formed by incubating the solution for 24 hours at 4 ^{o}C. The curcumin functionalized HC-VGS was subjected to successive incubations with Aβ-M or Aβ-O (at concentrations of 10, 1 and 0.1 µg/mL) for 20 minutes at room temperature and pressure for each concentration. Subsequently, EIS measurements

were conducted in the frequency range from 1 Hz to 5 MHz using a BioLogic VSP 300 potentiostat/galvanostat device. The R_{ct} (charge-transfer resistance) of the sensor following incubation with Aβ was expressed as a percentage of the R_{ct} in the reference case, which was incubated in DMSO/F12K medium in the absence of Aβ.

References

1. Hunt, A.J.; Farmer, T.J.; Clark, J.H., Chapter 1 elemental sustainability and the importance of scarce element recovery. In *Element recovery and sustainability*, The Royal Society of Chemistry: 2013; pp 1-28.
2. Seo, D.H.; Rider, A.E.; Kumar, S.; Randeniya, L.K.; Ostrikov, K., Vertical graphene gas- and bio-sensors via catalyst-free, reactive plasma reforming of natural honey. *Carbon* **2013**, *60*, 221.
3. Biswal, M.; Banerjee, A.; Deo, M.S.; Ogale, S., From dead leaves to high energy density supercapacitor. *Energy Environmental Science* **2013**, *6*, 1249-1259.
4. Unarunotai, S.; Murata, Y.; Chialvo, C.E.; Mason, N.; Petrov, I.; Nuzzo, R.G.; Moore, J.S.; Rogers, J.A., Conjugated carbon monolayer membranes: Methods for synthesis and integration. *Advanced Materials* **2010**, *22*, 1072.
5. Geim, A.K.; Novoselov, K.S., The rise of graphene. *Nature Materials* **2007**, *6*, 183-191.
6. Chen, Z.; Ren, W.; Gao, L.; Liu, B.; Pei, S.; Cheng, H.-M., Three-dimensional flexible and conductive interconnected graphene networks grown by chemical vapour deposition. *Nature Materials* **2011**, *10*, 425.
7. Castro Neto, A.H.; Guinea, F.; Peres, N.M.R.; Novoselov, K.S.; Geim, A.K., The electronic properties of graphene. *Review of Modern Physics* **2009**, *81*, 109.
8. Miller, J.R.; Outlaw, R.A.; Holloway, B.C., Graphene double-layer capacitor with ac line-filtering performance. *Science* **2010**, *329*, 1637-1639.
9. Seo, D.H.; Kumar, S.; Ostrikov, K., Thinning vertical graphenes, tuning electrical response: From semiconducting to metallic. *Journal of Materials Chemistry* **2011**, *21*, 16339.
10. Shang, N.G.; Papakonstantinou, P.; McMullan, M.; Chu, M.; Stamboulis, A.; Potenza, A.; Dhesi, S.S.; Marchetto, H., Catalyst-free efficient growth, orientation and biosensing

properties of multilayer graphene nanoflake films with sharp edge planes. *Advanced Functional Materials* **2008**, *18*, 3506.

11. Ostrikov, K., Reactive plasmas as a versatile nanofabrication tool. *Review of Modern Physics* **2005**, *77*, 489-511.
12. Kato, T.; Hatakeyama, R., Site- and alignment-controlled growth of graphene nanoribbons from nickel nanobars. *Nature Nanotechnology* **2012**, *7*, 651.
13. Ostrikov, K.; Neyts, E.C.; Meyyappan, M., Plasma nanoscience: From nano-solids in plasmas to nano-plasmas in solids. *Advances in Physics* **2013**, *62*, 113-224.
14. Seo, D.H.; Han, Z.J.; Kumar, S.; Ostrikov, K., Structure-controlled, vertical graphene-based, binder-free electrodes from plasma-reformed butter enhance supercapacitor performance. *Advanced Energy Materials* **2013**, *3*, 1316-1323.
15. Bo, Z.; Yang, Y.; Chen, J.; Yu, K.; Yan, J.; Cen, K., Plasma-enhanced chemical vapor deposition synthesis of vertically oriented graphene nanosheets. *Nanoscale* **2013**, *5*, 5180-5204.
16. Nishide, H.; Oyaizu, K., Toward flexible batteries. *Science* **2008**, *319*, 737-738.
17. Yick, S.; Han, Z.J.; Ostrikov, K., Atmospheric microplasma-functionalized 3d microfluidic strips within dense carbon nanotube arrays confine au nanodots for sers sensing. *Chemical Communications* **2013**, *49*, 2861-2863.
18. El-Kady, M.F.; Strong, V.; Dubin, S.; Kaner, R.B., Laser scribing of high-performance and flexible graphene-based electrochemical capacitors. *Science* **2012**, *335*, 1326-1330.
19. Rider, A.E.; Kumar, S.; Furman, S.A.; Ostrikov, K., Self-organized au nanoarrays on vertical graphenes: An advanced three-dimensional sensing platform. *Chemical Communications* **2012**, *48*, 2659.
20. Lespade, P.; Al-Jishi, R.; Dresselhaus, M.S., Model for raman scattering from graphitized carbons. *Carbon* **1982**, *20*, 427.
21. Wang, Y.; Alsmeyer, D.C.; McCreery, R.L., Raman spectroscopy of carbon materials: Structural basis of observed spectra. *Chemical Materials* **1990**, *2*, 557.
22. Cuesta, A.; Dhamelincourt, P.; Laureyns, J.; Martinez-Alonso, A.; Tascon, J.M.D., Comparative performance of x-ray diffraction and raman microprobe techniques for the study of carbon materials. *Journal of Materials Chemistry* **1998**, *8*, 2875.
23. Niyogi, S.; Bekyarova, E.; Itkis, M.E.; Zhang, H.; Shepperd, K.; Hicks, J.; Sprinkle, M.; Berger, C.; Lau, C.N.; de Heer, W.A.*, et al.*, Spectroscopy of covalently functionalized graphene. *Nano Letters* **2011**, *10*, 4061.

24. Ruan, G.; Sun, Z.; Peng, Z.; Tour, J.M., Growth of graphene from food, insects, and waste. *ACS Nano* **2011**, *5*, 7601.
25. Yang, Z.; Zhang, J.; Kintner-Meyer, M.C.W.; Lu, X.; Choi, D.; Lemmon, J.P.; Liu, J., Electrochemical energy storage for green grid. *Chemical Reviews* **2011**, *111*, 3577-3613.
26. Tollefson, J., How green is my future? *Nature* **2011**, *473*, 134-135.
27. Service, R.F., New "supercapacitor" promises to pack more electrical punch. *Science* **2006**, *313*, 902.
28. Manthiram, A.; Fu, Y.; Su, Y.-S., In charge of the world: Electrochemical energy storage. *Journal of Physical Chemistry Letters* **2013**, *4*, 1295-1297.
29. Miller, J.R.; Simon, P., Electrochemical capacitors for energy management. *Science* **2008**, *321*, 651-652.
30. Jiang, H.; Lee, P.S.; Li, C., 3d carbon based nanostructures for advanced supercapacitors. *Energy Environmental Science* **2013**, *6*, 41-53.
31. Zhang, X.; Zhang, H.; Li, C.; Wang, K.; Sun, X.; Ma, Y., Recent advances in porous graphene materials for supercapacitor applications. *RSC Advances* **2014**, *4*, 45862-45884.
32. Wang, F.; Xiao, S.; Hou, Y.; Hu, C.; Liu, L.; Wu, Y., Electrode materials for aqueous asymmetric supercapacitors. *RSC Advances* **2013**, *3*, 13059-13084.
33. Taberna, P.L.; Simon, P.; Fauvarque, J.F., Electrochemical characteristics and impedance spectroscopy studies of carbon-carbon supercapacitors. *Journal of the Electrochemical Society* **2003**, *150*, A292-A300.
34. Simon, P.; Gogotsi, Y., Capacitive energy storage in nanostructured carbon-electrolyte systems. *Accounts of Chemical Research* **2013**, *46*, 1094-1103.
35. Yan, J.; Liu, J.; Fan, Z.; Wei, T.; Zhang, L., High-performance supercapacitor electrodes based on highly corrugated graphene sheets. *Carbon* **2012**, *50*, 2179-2188.
36. Qie, L.; Chen, W.; Xu, H.; Xiong, X.; Jiang, Y.; Zou, F.; Hu, X.; Xin, Y.; Zhang, Z.; Huang, Y., Synthesis of functionalized 3d hierarchical porous carbon for high-performance supercapacitors. *Energy Environmental Science* **2013**, *6*, 2497.
37. Zhang, L.; Zhang, F.; Yang, X.; Long, G.; Wu, Y.; Zhang, T.; Leng, K.; Huang, Y.; Ma, Y.; Yu, A.*, et al.*, Porous 3d graphene-based bulk materials with exceptional high surface area and excellent conductivity for supercapacitors. *Scientific Reports* **2013**, *3*, 1408.

38. Lee, J.H.; Park, N.; Kim, B.G.; Jung, D.S.; Im, K.; Hur, J.; Choi, J.W., Restacking-inhibited 3d reduced graphene oxide for high performance supercapacitor electrodes. *ACS Nano* **2013**, *7*, 9366-9374.

39. Bai, Y.; Du, M.; Chang, J.; Sun, J.; Gao, L., Supercapacitors with high capacitance based on reduced graphene oxide/carbon nanotubes/nio composite electrodes. *Journal of Materials Chemistry A* **2014**, *2*, 3834-3840.

40. Zhao, C.; Zheng, W.; Wang, X.; Zhang, H.; Cui, X.; Wang, H., Ultrahigh capacitive performance from both co(oh) 2/graphene electrode and k3fe(cn) 6 electrolyte. *Scientific Reports* **2013**, *3*, 2986.

41. Conway, B.E.; Birss, V.; Wojtowicz, J., The role and utilization of pseudocapacitance for energy storage by supercapacitors. *Journal of Power Sources* **1997**, *66*, 1-14.

42. Aurbach, D.; Levi, M.D.; Levi, E.; Telier, H.; Markovsky, B.; Salitra, G.; Heider, U.; Hekier, L., Common electroanalytical behavior of li intercalation processes into graphite and transition metal oxides. *Journal of the Electrochemical Society* **1998**, *145*, 3024-3034.

43. Stoller, M.D.; Ruoff, R.S., Best practice methods for determining an electrode material ˛ s performance for ultracapacitors. *Energy Environmental Science* **2010**, *3*, 1294-1301.

44. Abbott, A., Dementia: A problem for our age. *Nature* **2011**, *475*, S2-S4.

45. Blennow, K.; Hampel, H.; Weiner, M.; Zetterberg, H., Cerebrospinal fluid and plasma biomarkers in alzheimer disease. *Nature Reviews Neurology* **2010**, *6*, 131-144.

46. Querfurth, H.W.; LaFerla, F.M., Alzheimer's disease. *New England Journal of Medicine* **2010**, *362*, 329-344.

47. Yang, F.; Lim, G.P.; Begum, A.N.; Ubeda, O.J.; Simmons, M.R.; Ambegaokar, S.S.; Chen, P.P.; Kayed, R.; Glabe, C.G.; Frautschy, S.A.*, et al.*, Curcumin inhibits formation of amyloid β oligomers and fibrils, binds plaques, and reduces amyloid in vivo. *Journal of Biological Chemistry* **2005**, *280*, 5892-5901.

48. Vestergaard, M.d.; Kerman, K.; Saito, M.; Nagatani, N.; Takamura, Y.; Tamiya, E., A rapid label-free electrochemical detection and kinetic study of alzheimer's amyloid beta aggregation. *Journal of the American Chemical Society* **2005**, *127*, 11892-11893.

49. Lopes, P.; Xu, M.; Zhang, M.; Zhou, T.; Yang, Y.; Wang, C.; Ferapontova, E.E., Direct electrochemical and afm detection of amyloid-[small beta] peptide aggregation on basal plane hopg. *Nanoscale* **2014**, *6*, 7853-7857.

50. Youmans, K.L.; Tai, L.M.; Kanekiyo, T.; Stine, W.B.; Michon, S.C.; Nwabuisi-Heath, E.; Manelli, A.M.; Fu, Y.F.; Riordan, S.; Eimer, W.A.*, et al.*, Intraneuronal a beta detection in 5xfad mice by a new a beta-specific antibody. *Molecular Neurodegeneration* **2012**, *7*, 8.

Supporting Information for:

Plasma-Enabled Sustainable Elemental Lifecycles: Honeycomb-derived Graphenes for Next-Generation Biosensors and Supercapacitors

Dong Han Seo[a,b,†], Shafique Pineda[a,b,†], Samuel Yick[a,b], John Bell[c], Zhao Jun Han[a], and Kostya (Ken) Ostrikov[a,b,c,*]

[†] These authors contributed equally to this work.

[a] Plasma Nanoscience Laboratories, Industrial Innovation Program, Manufacturing Flagship, CSIRO, P.O. Box 218, Lindfield, NSW 2070, Australia.

[b] School of Physics, The University of Sydney, Sydney, NSW 2006, Australia.

[c] Institute for Future Environments and Institute for Health and Biomedical Innovation, School of Chemistry, Physics, and Mechanical Engineering, Queensland University of Technology, Brisbane, QLD 4000, Australia.

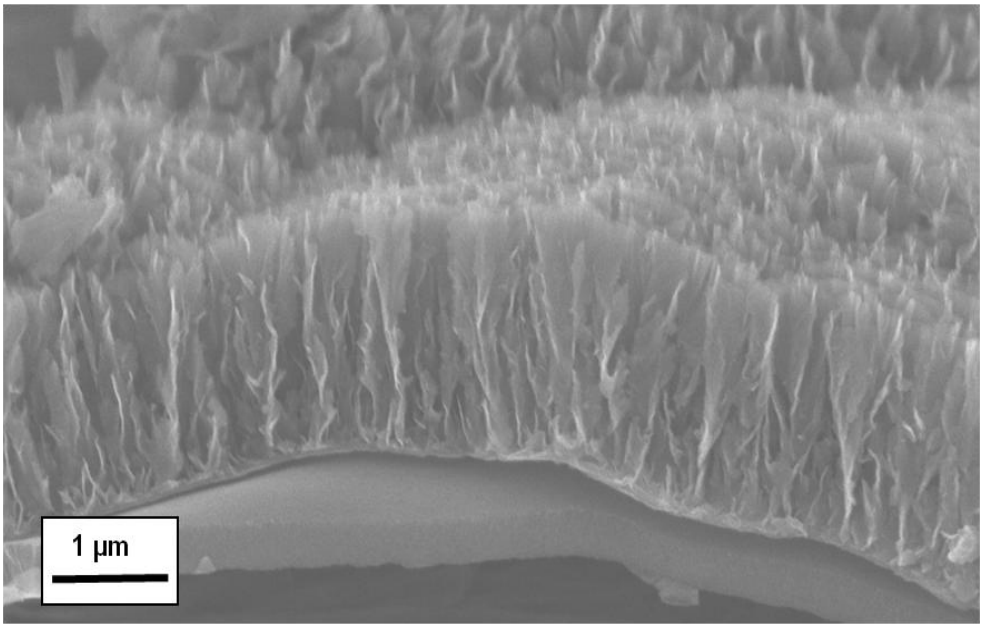

Supplementary Figure 1 | Typical cross-sectional SEM image of HC-VGS with a height of ~2 μm.

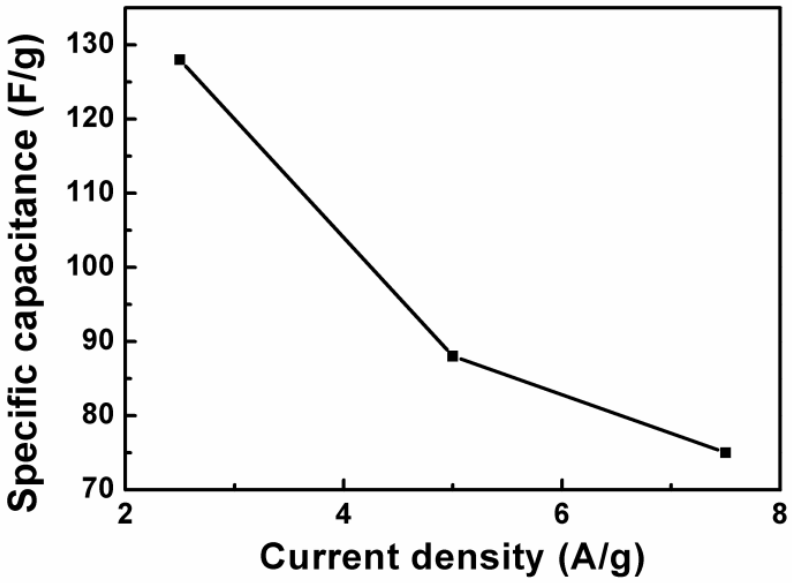

Supplementary Figure 2 | Specific capacitance of VGS calculated from the charge/discharge curves.

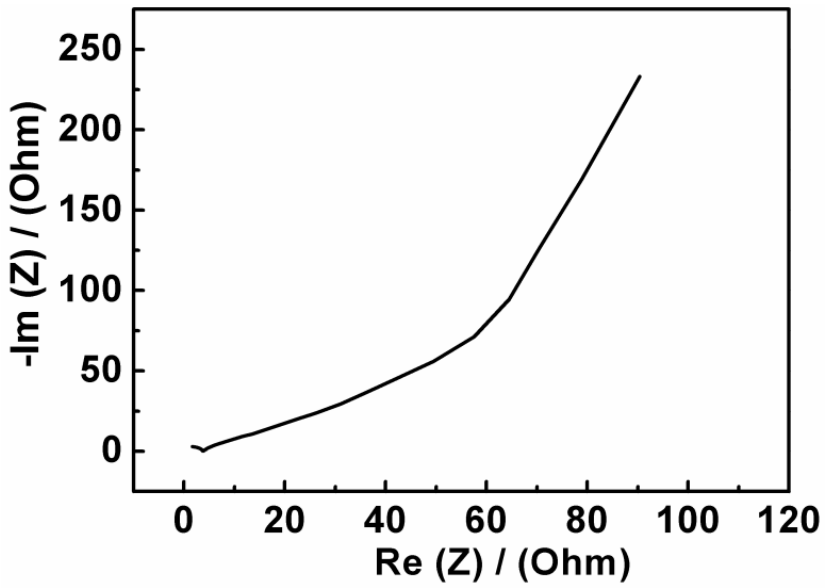

Supplementary Figure 3 | EIS measurement for pristine HC-VGS in 1 M Na_2SO_4 at room temperature using the three-electrode configuration.

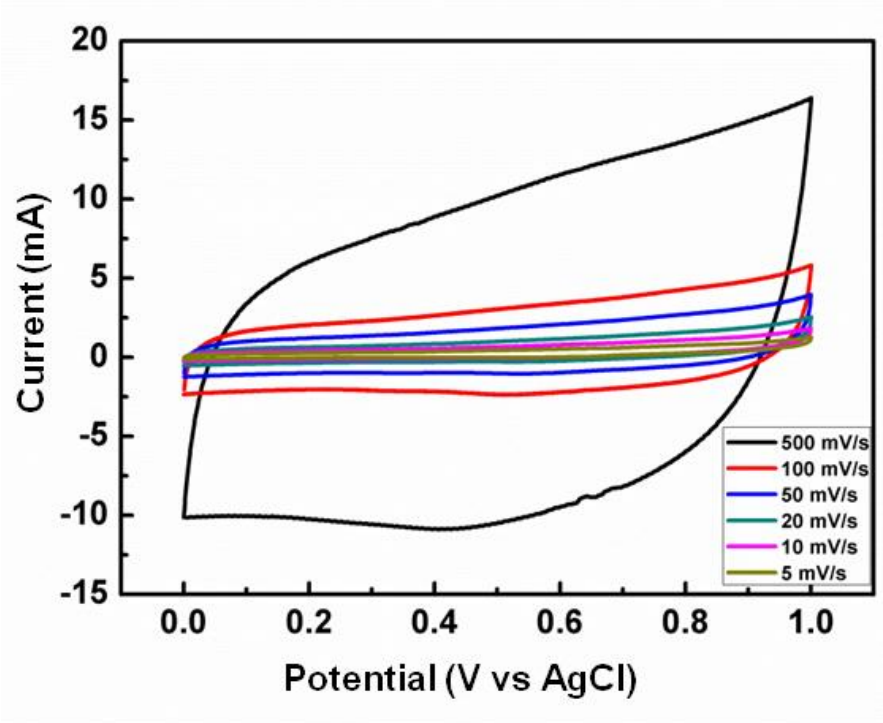

Supplementary Figure 4 | Electrochemical performance of HC-VGS in a three-electrode cell configuration. CV curves of HC-VGS at different scan rates of 5, 10, 20, 50, 100 mV/s and 500 mV/s, in 1 M Na_2SO_4 at room temperature.

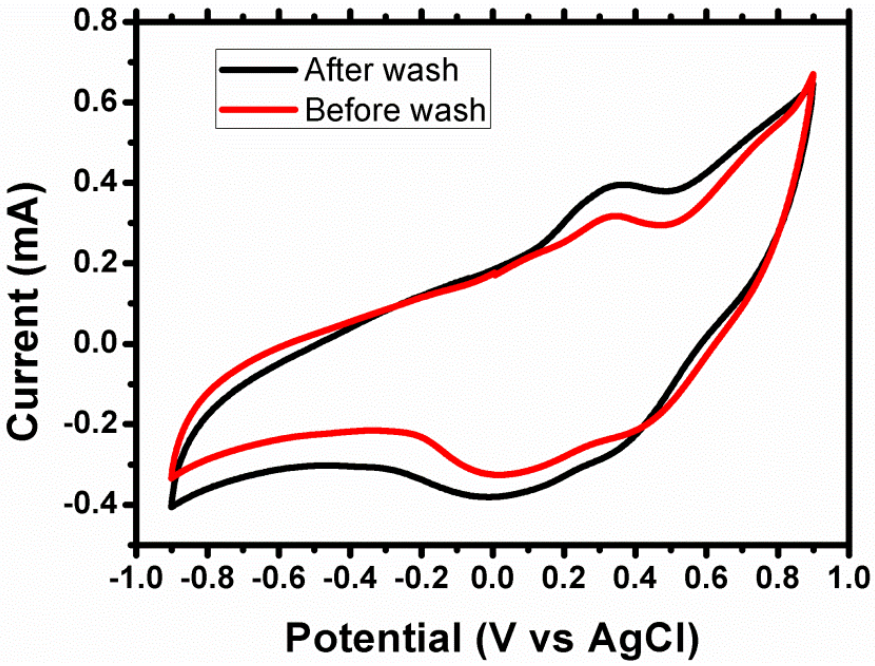

Supplementary Figure 5 | CV characterization for the attachment of curcumin onto HC-VGS. Measurements were performed in 20 mM phosphate buffer containing 0.15 M NaCl, at a scan rate of 25 mV/s, and at room temperature. The curcumin-functionalized HC-VGS was washed several times with 10% sodium dodecyl sulphate solution to remove non-specific binding.

Single-Step, Plasma-Enabled Reforming of Natural Precursors into Vertical Graphene Electrodes with High Areal Capacitance

Dong Han Seo,[†,‡,⊥] Samuel Yick,[†,‡,⊥] Shafique Pineda,[†,‡] Dawei Su,[‖] Guoxiu Wang,[‖] Zhao Jun Han,[†] and Kostya (Ken) Ostrikov[†,‡,§,*]

[⊥]These authors contributed equally.

[†]Plasma Nanoscience, Industrial Innovation Program, CSIRO Manufacturing Flagship, Lindfield, New South Wales 2070, Australia

[‡]School of Physics, The University of Sydney, New South Wales 2006, Australia

[‖]School of Chemistry and Forensic Science, University of Technology Sydney, New South Wales 2007, Australia

[§]School of Chemistry, Physics and Mechanical Engineering, Queensland University of Technology, Brisbane, Queensland 4000, Australia

Abstract

Graphene nanostructures possess excellent physical properties such as high surface area, good mechanical stability and good electric conductivity, which make them attractive as electrodes for high-performance energy storage devices. However, graphene-based nanomaterials have yet to materialized into commercial energy storage devices, mainly due to the high cost in fabrication processes and the difficulty in achieving a high mass loading. In particular, the high mass loading of active materials on the electrode represents an important step towards the translation of excellent electrochemical activity seen in the microscopic regime into the practical applications. Here, supercapacitor electrodes made of vertical graphene nanosheets (VGNS) are fabricated from a range of commercially available cheese precursors *via* green, low-temperature, plasma-based reforming processes. Taking advantage of the fast solidification of cheese molecules and the plasma-matter interactions, the produced

VGNS exhibit a high mass loading of 3.2 mg/cm^2 and a high areal capacitance of 0.46 F/cm^2. These results demonstrate a single-step, scalable, environmentally-benign, and cost-effective approach for the transformation of natural precursors into high-quality graphene structures, which could be promising for a variety of advanced electronic and energy applications.

Introduction

Research in electrochemical energy storage has recently seen a drastic expansion due to the increasing energy demands for portable electronics, electric vehicles, and utilization of renewable energy resources [1-4]. Of the various energy storage devices, supercapacitors represent a particularly attractive option, as they offer high power density, rapid charge/discharge, and a long lifespan, which are critical for a number of energy storage applications [5,6]. Fundamentally, supercapacitors operate by storing ions within the electric double layer (EDL) or through redox reactions on the electrode surface [7]. Such mechanisms allow supercapacitors to have better cycling performance and power density as compared to other energy storage devices such as batteries [6]. Nevertheless, the widespread applications of current supercapacitors are impeded by their low energy density.

The physical properties of electrode materials are known to dictate the performance of supercapacitors. In general, a large surface area with easily accessible sites and high electrical conductivity are required for an electrode to deliver high energy and power densities. The advent of carbon nanostructures such as carbon nanotubes and graphene has introduced materials with intrinsically high surface area and excellent electrical conductivity which are highly promising for energy storage applications [8,9]. A good example is the vertical graphene nanosheets (VGNS), which recently emerged as a promising electrode material owing to its highly favorable structural and electrochemical properties [10,11]. VGNS possess a unique morphology of few-layered graphene sheets self-organized in an open, interconnected, and three-dimensional (3D) array structure. While the open structure of VGNS can facilitate the rapid formation of

EDL, its structural rigidity enhances the stability by preventing the restacking of graphene nanosheets, a commonly observed problem in horizontal graphenes when immersed in liquid electrolytes [12-14]. Supercapacitor electrodes made of VGNS have shown many notable charge storage features, such as high specific capacitance, stable charge retention capability, and a low relaxation time constant τ_0 [10,15].

However, the biggest challenge of implementing VGNS into practical supercapacitors is the low mass loading. VGNS grown by chemical vapor deposition (CVD) usually have a mass loading of <0.5 mg/cm^2 (thickness <4 μm) [16]. As such, the high specific capacitance (C_s) of the materials do not always lead to a high areal capacitance (a more accurate measure for the practical supercapacitor devices) due to the limited quantity of active materials present on the electrodes [17]. This problem cannot be mitigated by a long growth time, as it often results in the formation of undesired amorphous carbons rather than thicker VGNS structure. On the other hand, a few chemical-based methods have recently reported a high mass loading of graphene-based materials [18]. However, in these chemical-based syntheses, the extraction of graphene-based materials from the natural graphite precursors is not only precursor-specific, but also expensive, complicated, as well as energy-, time- and resource-demanding. Moreover, these processes usually require additional materials, such as binders or gels, to integrate these nanostructures into functional electrodes, further complicating the process of device fabrication and reducing the scalability and sustainability [19-23]. Therefore, there is a need for developing a simple and green process which can directly produce high-quality VGNS at a high mass loading for supercapacitor applications.

In our previous work, we have demonstrated the versatility and effectiveness of plasmas as a simple and green nanofabrication tool for the efficient transformation of natural precursors into VGNS electrodes [24-26]. Notably, by utilizing precursors such as butter, this enabled the growth of VGNS with a high C_s of ~200 F/g and an excellent stability of more than 8,000 cycles. However, the areal capacitance (C_A) of these electrodes remained unsatisfactory due to the limited mass loading. In this work, we solve this problem by employing cheese as the natural precursor in the plasma-based fabrication process. We demonstrate a single-step, plasma-based reforming process to produce

VGNS electrodes with a high mass loading up to 3.2 mg/cm^2 and an excellent areal capacitance, which are superior as compared to other graphene-based materials obtained by the conventional fabrication techniques such as chemical or thermal processing. Our results thus represent significant progress towards translating the excellent capabilities of graphenes into functional high-performance energy storage devices.

Results and Discussion

Fig. 1 shows the schematic of the single-step, plasma-enabled reforming of cheese into VGNS. Ni foam was chosen as the substrate for VGNS as it provides a porous 3D scaffold for the growth of VGNS. Furthermore, due to its good electrical conductivity, Ni foam also functions as the current collector. The VGNS were grown from the cheese precursors by a 10 min exposure to plasmas in an argon and hydrogen gas mixture to enable the growth of VGNS. Commercially available processed cheese was used as the carbon source. Processed cheese is made via blending natural cheese of different age and maturity [27]. As the production of processed cheese is a standardized industrial process, this will ensure that variation between different cheese cultures which might affect the experimental reproducibility can be minimized.

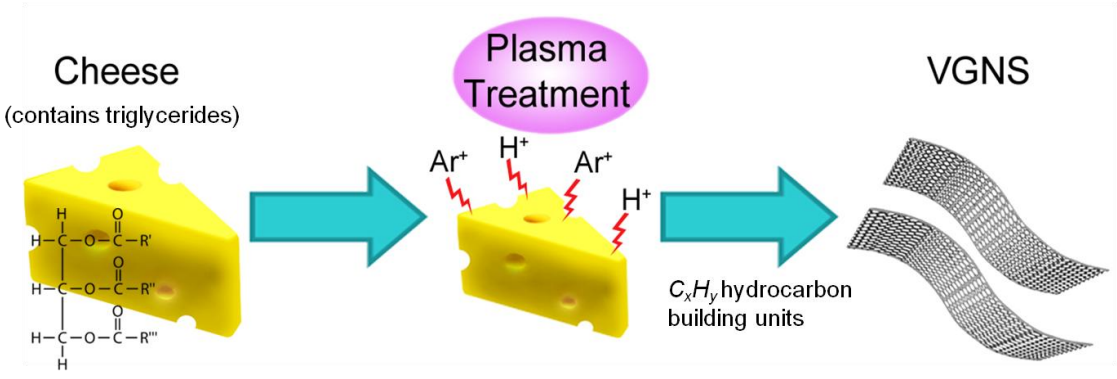

Figure 1 | Schematic of the experimental process which transforms the cheese precursor into vertical graphene nanosheets (VGNS). The plasma process enables the breakdown of the cheese precursor (containing triglycerides, proteins, *etc.*) into hydrocarbon building units for the formation of VGNS.

Processed cheese consists of fats (*i.e.*, triglycerides), proteins (*i.e.*, mostly casein) and water in 30, 22, and 40 wt.%, respectively [27,28]. In contrast, cream cheese possesses a significantly higher water content; and the fat, protein and water content of cream cheese are 30, 10, and 55 wt.%, respectively [29]. In both cheeses, there exist a small quantity of salt, emulsifying agents and other addictives. During the early growth process, the cheese precursor was promptly dehydrated by the low pressure environment and plasma heating effects. Subsequently, the heterogeneous carbon precursors (*i.e.,* fat and protein groups) were broken down into simple hydrocarbon building units by the rapid plasma dissociation of the material. These building units then self-organized into VGNS on the plasma-exposed surfaces. Such plasma-specific effects can be attributed to the strong plasma-matter interactions in the plasma sheath. The plasma process made it possible to achieve a high mass loading of VGNS which could also be extracted as high-quality graphene powder (Supplementary Fig. 1a – 1c). The typical SEM image also confirmed VGNS with the total coverage on the nickel foam substrate (Supplementary Fig. 1d).

Owing to the above mentioned advantages, VGNS produced with the two cheese precursors, *i.e.*, processed and cream cheeses, showed a mass loading of 3.2 and 0.8 mg/cm^2 respectively, which are higher than what is normally obtained from gaseous or other solid state precursors in a similar plasma process [24-26]. It was also noted that VGNS derived from liquid precursors such as honey and butter can enable a strong adhesion to the substrate. This removes the need for a binder and minimises the undesired formation of amorphous carbon [26]. However, due to their fluidic nature, this led to a significant loss of precursor material during the growth process. In particular, a large fraction of precursor material was lost during the initial growth stage when the precursor was undergoing a transformation from a liquid (precursor) to solid state (VGNS). Consequently, this leads to a significantly lower rate of mass conversion. Therefore, in order to fabricate an electrode with high mass loading while maintaining the favourable properties as inherited from liquid-based precursors, we required a liquid precursor material which rapidly solidifies upon losing its water content. In addition, a strong intermolecular bonding in the precursor would be highly desired, as this would minimize the sputtering and loss of precursor material during the plasma reformation

process. In such a circumstance, cheese represents a particularly promising candidate for the improved efficiency of reforming natural precursors into functional VGNS structures with a high mass loading, as cheese can quickly transform into the solid state after losing its water content and its strong protein matrix can minimize the loss of material during the transformation process.

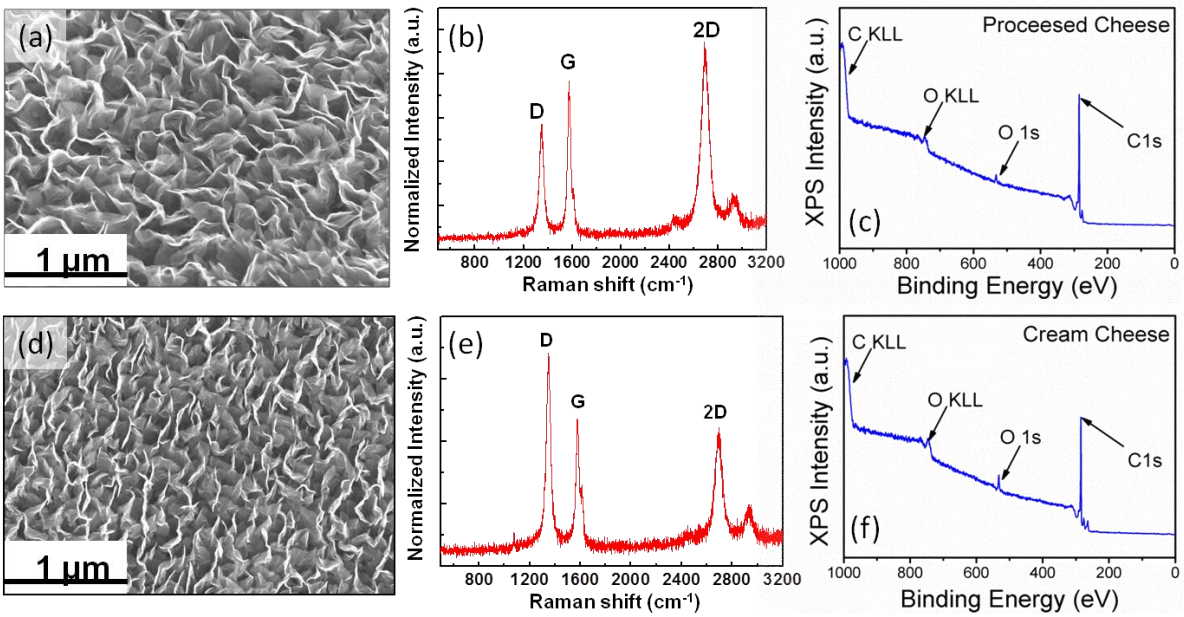

Figure 2 | Typical SEM images of VGNS produced from processed cheese (**a**) and cream cheese (**d**) precursors. Raman spectra of the VGNS obtained from processed cheese (**b**) and cream cheese (**e**). (**c,f**) XPS spectra of both cheese precursors showed that the resulting nanostructures were composed of carbon with a trace amount of oxygen.

Fig. 2a and Fig. 2d show the high-resolution SEM images of VGNS derived from processed and cream cheeses, respectively. These images show a uniform, dense, 3-D network of thin graphene nanosheets. Such uniform transformation demonstrates the merits of plasma as a nanofabrication tool to build functional nanostructures from heterogeneous natural precursors [25]. Fig. 2b and Fig. 2e show the Raman spectra of VGNS derived from processed and cream cheeses, respectively. The Raman spectra reveal the high graphitic content of the VGNS. For both the processed and cream

cheese, three distinct Raman peaks were present, namely, the characteristic disorder peak (D-band) arising from the defects within the sp^2 carbon materials at 1350 cm^{-1}, the graphitic peak (G-band) from the in-plane vibrational E_{2g} mode of the graphitic lattice at 1579 cm^{-1}, and the second-order 2D-band due to the three-dimensional interplanar stacking of hexagonal carbon networks at 2700 cm^{-1} [30-33]. By examining the ratios of intensities between the peaks, the quality of VGNS can be determined. Specifically, the I_D/I_G ratio reflects the degree of defects present within the graphene lattice, whereas the I_{2D}/I_G ratio indicates the thickness of the graphene sheets. VGNS from processed cheese showed an I_D/I_G ratio of 0.7 and a I_{2D}/I_G ratio of 1.2, whereas the one from cream cheese had an I_D/I_G ratio of 1.4 and a I_{2D}/I_G peak ratio of 0.95. The thickness of VGNS can also be deduced from the high resolution SEM (Supplementary Fig. 8) and Raman features. According to the Raman features, the I_{2D}/I_G ratios suggest that our VGNS derived from cheese consists of few-layer graphene sheets (bi-tri layer in the edge plane with a thicker basal plane) [34,35]. Moreover, the high transparency of VGNS as shown in the SEM image is usually observed for few-layer graphenes [36,37]. These results demonstrate the formation of high-quality VGNS from cheese precursors.

Fig. 2c and Fig. 2f illustrate the XPS measurements of VGNS derived from processed and cream cheeses, respectively. In both spectra, a strong C 1s peak positioned at the binding energy (BE) of ~284.5 eV was observed, together with a small amount of oxygen at the BE of 532 eV [38]. This indicates that the cheese derived structures were predominantly composed of carbon atoms with a small amount of oxygen. Chemical composition analysis of VGNS derived from processed and cream cheeses revealed C atoms at 98.4 and 95.3 at.% and O atoms at 1.6 and 4.7 at.%, respectively. Supplementary Fig. 2a and Supplementary Fig. 2b show the C 1s narrow scans of VGNS derived from processed and cream cheeses respectively. Both C 1s spectra can be deconvoluted into three distinct peaks corresponding to the C-C (BE ~ 284.5 eV), oxygenated carbon (BE ~ 285.4 eV), and the shake-up energy-loss feature (BE ~ 290.2 eV) [24,39,40]. Importantly, all VGNS samples featured a high fraction of sp^2-hybridized carbon, suggesting high quality of the graphene sheets. To demonstrate the specific surface area and materials texture of VGNS electrodes, BET measurements were also performed. The results revealed a surface area of 448 m^2/g with a typical mesoporous

structure (Supplementary Fig. 3). Also, there have been recent BET studies on plasma-grown VGNS [16], demonstrating similar magnitudes of surface area. In particular, few-layered VGNS are deduced to have a surface area ranging from 430 m^2/g [41] to 780 m^2/g [42]. Consequently, this favorable morphology is expected to facilitate the adsorption of ions for the EDL formation and enable the cheese-derived VGNS to deliver good electrochemical properties.

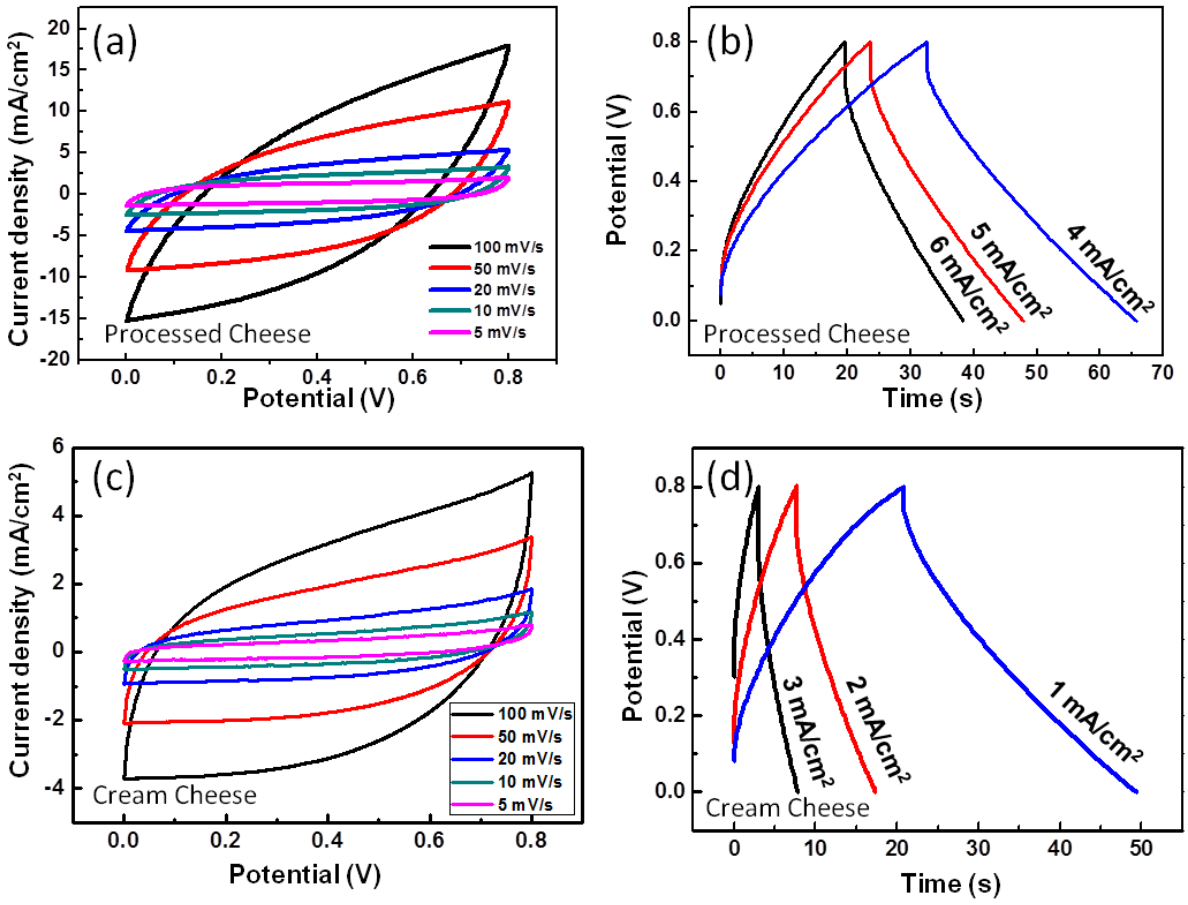

Figure 3 | Electrochemical activity of the high mass loading VGNS as obtained from processed and cream cheeses in the two-electrode configuration. Cyclic voltammetry (CV) curves of both processed and cream cheeses at various scan rates are plotted in (a) and (c) respectively. Similarly, Galvanostatic charge/discharge curves are plotted in (b) and (d).

The electrochemical performance of VGNS derived from processed and cream cheeses was then investigated by potentiostat/galvanostat with the two- and three-electrode configurations. Fig. 3a and Fig. 3c show the cyclic voltammetry (CV) curves of VGNS derived from processed and cream cheeses in 1 M Na_2SO_4 aqueous electrolyte, respectively, measured in the two-electrode configuration. It is noticeable that the CV shapes were rectangular and symmetric at low scan rates (5 – 20 mV/s), reflecting that both electrodes exhibited an efficient formation of EDL and fast ion transport. Nevertheless, the CV curves became skewed at high scan rates (*e.g.*, >100 mV/s). Fig. 3b and Fig. 3d show the galvanostatic charge/discharge curves of VGNS at different current densities from 1 to 6 mA/cm^2. Both cheese-derived VGNS exhibited a linear dependence of charge/discharge potential with time, suggesting the dominance of EDL mechanism [43]. Correspondingly, the specific capacitance C_s was calculated from the CV curves at different scan rates, as shown in Fig. 4a and Fig. 4c. Both VGNS derived from processed and cream cheeses exhibited a high specific capacitance of 156 and 151 F/g at 5 mV/s, respectively. For the calculation of specific capacitance, data from the two-electrode measurements was used to avoid potential overstatement of the device performances, which may arise from measurements conducted in a three-electrode system [44]. However, three-electrode characterizations are also necessary in evaluating the full potential of a specific nanomaterial. Therefore, both two- and three-electrode measurements were conducted. We have also calculated the specific capacitance for the three-electrode system, and it shows good agreement with the two-electrode measurements (Supplementary Fig. 9).

Typically, as the mass loading of electrode material increases, the specific capacitance of supercapacitor decreases due to the inaccessible surface areas and the impaired ion diffusion. However, this trend was not evident for VGNS obtained by the plasma reforming of cheese precursors in the present case. Despite a significant increase in the mass loading (from 0.8 to 3.2 mg/cm^2), a relatively constant C_s was obtained (151 to 156 F/g). As the graphene sheets are vertically oriented to the growth substrate, it maintains the accessible surface area and facilitates the diffusion of ions even at high mass loadings. This unique feature is important for future developments in high-capacity graphene-based supercapacitors. Furthermore, VGNS derived from cream cheese

showed a 53% capacitance retention when the scan rate increased from 5 to 100 mV/s (Fig. 4c), whereas the one derived from processed cheese also retained 41% (Fig. 4a). Such rate capabilities of cheese-derived VGNS remained superior as compared to other graphene-based electrodes. These results suggest that the ion accessibility and ion transport are greatly facilitated by the vertical alignment of graphene nanosheets in the electrode materials.

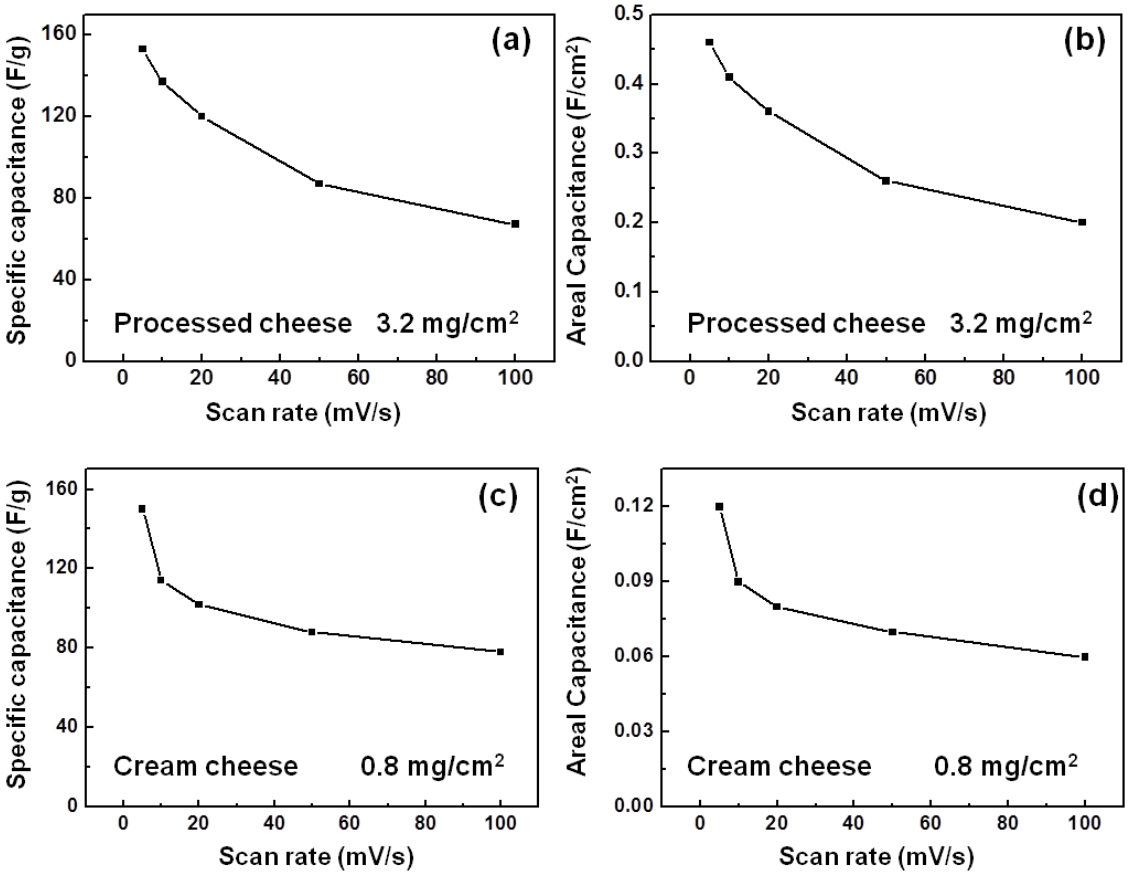

Figure 4 | Specific capacitance (a, c) and areal capacitance (b, d) at different scan rates of the high mass loading VGNS electrodes derived from processed and cream cheeses.

Fig. 4b and Fig. 4d show the areal capacitance of VGNS derived from both processed and cream cheeses at different scan rates. In particular, VGNS derived from processed cheese demonstrated a very high areal capacitance of 0.46 F/cm^2 at 5 mV/s, whereas

the one from cream cheese also exhibited 0.12 F/cm^2 at the same scan rate. The lower areal capacitance of the latter reflects the lower mass loading in that case. Notably, our results show that a 4-fold increase in mass loading leads to an approximate 4-fold increase in areal capacitance. Such linear increase in areal capacitance may be attributed to the vertical alignment of graphene sheets. The obtained areal capacitances are amongst the highest values achieved so far for pure graphene- and carbon-based supercapacitors (Supplementary Table 1) [16,18-21,45-48]. For instance, Zhou *et al.* reported a value of 0.152 F/cm^2 for chemically processed graphenes [19].

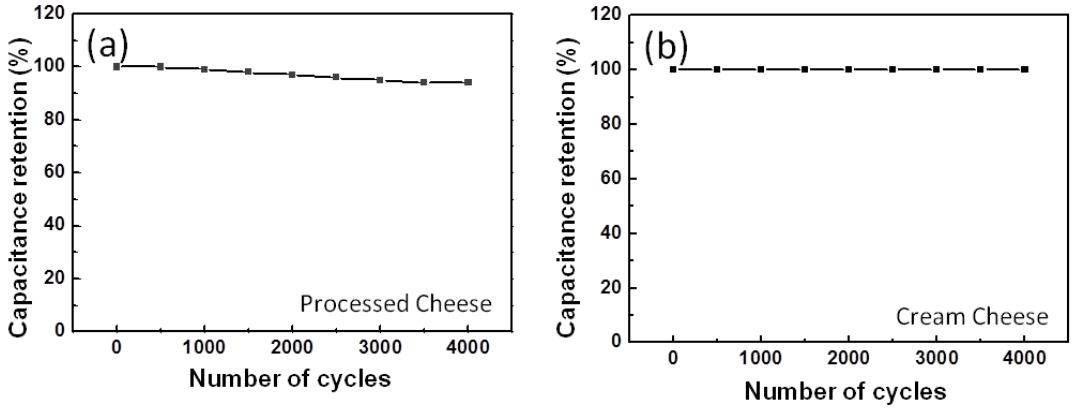

Figure 5 | Cycle stability of the high mass loading VGNS electrodes. VGNS derived from processed (**a**) and cream (**b**) cheese precursors for 4,000 cycles at a scan rate of 400 mV/s.

The stability tests of VGNS-based electrodes are shown in Fig. 5a and Fig. 5b, where the electrodes were performed over 4,000 cycles at a scan rate of 400 mV/s. Notably, VGNS derived from cream and processed cheeses exhibited the capacity retention of 99% and 94%, respectively. This stability is comparable to the many other graphene- and carbon-based supercapacitors with high mass loadings as reported elsewhere (Table S1) [20,49-51]. For instance, Maiti *et al.* reported a 97.8% retention after 5,000 cycles for graphene-based supercapacitors [20]; Zhang *et al.* obtained a 98% stability after 1,000 cycles for CNT-integrated electrodes [46]; while Puthusseri *et al.* demonstrated a 90% retention after 5,000 cycles with 3D porous carbons [51].

The electrochemical impedance spectra (EIS) for VGNS obtained from the plasma reforming processes are shown in Supplementary Fig. 4, where the frequency-dependent impedance is plotted as the real (Z') and imaginary (Z'') components. Both samples displayed a pseudo-vertical curve at low frequencies, indicating a near ideal capacitive behavior. In the high-frequency range, a semicircle was observed to intersect with the real (Z') axis in both spectra, which could be attributed to charge transfer at the electrode-electrolyte interface. This pseudo-vertical behavior may arise from the presence of amorphous carbon in the basal plane of VGNS. The equivalent series resistance can be extrapolated from the point of intersection, which was ~4 Ω for both VGNS electrodes. The good conductivity of electrodes can be attributed to the high quality of VGNS and the good binding of VGNS to the growth substrate, as enabled by the single-step plasma transformation process. In addition, we have also performed the three-electrode cell measurements to better evaluate the potential of cheese-derived VGNS electrode materials (Supplementary Fig. 5). Overall, our VGNS exhibit energy storage capabilities which are among the best for carbon-based devices (Supplementary Table 1). While the fabrication of carbon-based electrodes often involves complex and resource-consuming processes, this single-step plasma reforming of cheese precursors is clearly an energy-efficient, potentially scalable, and chemically green alternative for the direct assembly of high-performance VGNS-based supercapacitors.

To further understand the effects of precursor composition on the resulting VGNS nanostructure, we also utilized fat-reduced processed cheese as the precursor. Compared to the normal processed cheese, fat-reduced processed cheese typically contains 8-10 wt.% water and includes fat substitutes and mimetics as replacers [52]. After the same single-step plasma process, fat-reduced processed cheeses were also transformed into VGNS with a mass loading of 2.8 mg/cm^2. However, the resulting nanostructure contained more defects and thicker graphene sheets, as compared to the VGNS derived from processed cheese precursor (Supplementary Fig. 6). In addition, the fat-reduced cheese precursor resulted in VGNS with notable deposits of amorphous carbon. From the XPS elemental analysis, VGNS derived from fat-reduced processed cheese were comprised of carbon, oxygen and potassium at concentrations of 72.9,

15.5 and 11.6 at.% (Supplementary Fig. 6c). The high K and O contents of the structure were in contrast to the VGNS grown by either processed or cream cheeses. This difference most likely originated from the artificial additives and fat replacers used in the production of fat-reduced cheese. Electrochemically, VGNS derived from fat-reduced cheese exhibited a C_s of 153 F/g at 5 mV/s and an areal capacitance of 0.38 F/cm^2, similar to those obtained from processed cheese precursors. However, only 34% capacitance retention was observed when the scan rate was increased from 5 to 100 mV/s. This was significantly lower than those obtained from the processed and cream cheese precursors. Moreover, non-ideal capacitor behavior was observed, as evidenced by the skewed charge/discharge curves (Supplementary Fig. 6g). The resulting VGNS also demonstrated a higher equivalent series resistance, as compared to VGNS derived from the processed and cream cheeses (Supplementary Fig. 6h). These results reveal that the presences of artificial additives and fat-replacers in cheese precursor can reduce the graphitic content of VGNS and significantly impede their electrochemical performance. Overall, we demonstrated good supercapacitor performance using VGNS based structures derived from cheese. In addition, as VGNS is a very porous structure, it can act as a highly versatile platform material to accommodate hetero-nanostructures. Therefore, by synergizing these unused areas of VGNS with other nanostructures which exhibit good electrochemical properties, this may significantly enhance the performance of VGNS-based supercapacitors.

We denote that in the conversion of natural precursors using plasmas, the plasma parameters also play a critical role in determining the resulting properties [53]. Therefore, to demonstrate the plasma-related control and understand the temporal dynamics of the transformation of cheese into VGNS, we performed many experiments to find the optimum conditions. Over the course of experiments, the plasma treatment time and hydrogen concentration were found to be critical for the growth of VGNS. When the plasma processing time was prolonged or an excessive hydrogen concentration was used, the presence of graphitic nanostructures dramatically reduced, as evidenced by the microstructural observations and Raman spectra (Supplementary Fig. 7). Similarly, when the plasma processing time was reduced beyond the threshold or the hydrogen concentration was too low, we observed the transformation process to

be incomplete (Supplementary Fig. 7). Therefore, our experiments show that the transformation of natural precursors into VGNS requires precise control over the plasma processing parameters. This is the key for obtaining good quality graphene sheets with favourable electrochemical properties for energy storage devices.

Conclusions

In summary, we have developed a single-step, low-temperature plasma process to produce high-quality VGNS structures with a high mass loading using cheeses as the precursors. Moreover, a direct integration of VGNS with the growth substrates was successfully demonstrated. As a result of the direct integration of high-quality VGNS with a high mass loading, one of the highest-to-date areal capacitance (0.46 F/cm^2) of VGNS-based electrodes was achieved. VGNS also exhibited minimum degradation in electrochemical properties despite a significant increase in mass loading of the electrode. Furthermore, we have demonstrated that non-equilibrium low-temperature plasmas as an effective and versatile nanofabrication tool to effectively break down and rebuild diverse forms of precursors of different chemical compositions and states of matter into functional VGNS structures. These results thus provide a critical step in the development of graphene-based, high-performance energy storage devices.

Experimental Section

Fabrication of VGNS from the cheese precursors. The single-step, plasma-enabled transformation of cheese precursors into VGNS was carried out in a RF inductively coupled plasma CVD system. Commercially available processed cheese, cream cheese, and fat-free processed cheese were used as precursors. In order to provide a uniform coating on the Ni foam substrates, the cheese precursors were firstly melted at 80°C. This allowed the substrates to be evenly coated with the liquefied cheese. The cheese–laden substrates were then removed from the heater so that the cheese can re-solidify prior to loading in the plasma reactor. A gas mixture of 5 sccm Ar and 20 sccm H_2 was

then fed into the reactor, where the plasma was ignited at a pressure and RF power of 2.0 Pa and 1000 W, respectively. Although no external substrate heating was used, during the 10 min plasma process the substrate temperature reached approximately 400 °C due to the plasma-heating effects. To reduce the amount of amorphous carbon formed in the growth process, the as-grown samples were treated in air at 300 °C for 1 hour.

Material characterisation. Please refer to **Section 1.4** of Chapter 1, "Raman Spectroscopy" and "X-ray Photoelectron Spectroscopy (XPS)" for their general experimental details. The mass of electrode was determined by weighing a 10 cm long sample on a ultrasensitive balance (Δ±0.1 μg; Mettler Toledo UMT2) and calculating the fractional mass submerged into the electrolyte. N_2 adsorption–desorption isotherms of VGNS were measured by using a Micromeritics 3Flex analyzer at the temperature of 77 K. Brunauer-Emmett-Teller (BET) analysis was used to determine the surface area and was calculated using the isothermal points at a relative pressure of $P/P_0 = 0.05 – 0.25$.

Electrochemical measurements. The electrochemical measurements were performed in 1 M Na_2SO_4 electrolyte. Both three- and two-electrode cell configurations were employed. The three-electrode cell used the VGNS sample as the working electrode, a Pt foil as the counter electrode, and an Ag/AgCl reference electrode; while the two-electrode cell used two identical VGNS samples as the electrodes. Cyclic voltammetry (CV), galvanostatic charge/discharge, and electrochemical impedance spectroscopy (EIS) measurements were conducted using a BioLogic VSP 300 potentiostat/galvanostat device. CV tests were performed in the potential range of 0 – 0.8 V at scan rates of 5 – 100 mV s^{-1}. Galvanostatic charge/discharge curves were obtained at current densities of 6, 5, and 4 mA/cm^2 for VGNS derived from processed cheese and 3, 2, and 1 mA/cm^2 for VGNS derived from cream cheese, respectively. EIS measurements were performed in the frequency range from 0.01 Hz to 100 kHz. The specific capacitance of single electrode C_s was calculated from the CV curves of two-

electrode measurements by integrating the discharge current against the potential V according to $C_s = 2\frac{\int \mathrm{I}\,\mathrm{dV}}{\mathrm{m}\Delta\mathrm{V}}$, where v is the scan rate (V s^{-1}), m is the mass of the active material in a single electrode, and ΔV is the operating potential window (0.8 V). The mass loading was 3.2, 0.8, and 2.8 mg/cm^2 for VGNS derived from processed cheese, cream cheese, and fat-reduced cheese, respectively. Similarly, C_s was calculated from the three-electrode measurements by the equation, $C_s = \frac{\int \mathrm{I}\,\mathrm{dV}}{\mathrm{m}\Delta\mathrm{V}}$.

References

1. Tollefson, J., How green is my future? *Nature* **2011**, *473*, 134-135.
2. Service, R.F., New "supercapacitor" promises to pack more electrical punch. *Science* **2006**, *313*, 902.
3. Manthiram, A.; Fu, Y.; Su, Y.-S., In charge of the world: Electrochemical energy storage. *The Journal of Physical Chemistry Letters* **2013**, *4*, 1295-1297.
4. Yang, Z.; Zhang, J.; Kintner-Meyer, M.C.W.; Lu, X.; Choi, D.; Lemmon, J.P.; Liu, J., Electrochemical energy storage for green grid. *Chemical Reviews* **2011**, *111*, 3577-3613.
5. Miller, J.R.; Simon, P., Electrochemical capacitors for energy management. *Science* **2008**, *321*, 651-652.
6. Li, X.; Wei, B., Supercapacitors based on nanostructured carbon. *Nano Energy* **2013**, *2*, 159-173.
7. Simon, P.; Gogotsi, Y., Capacitive energy storage in nanostructured carbon-electrolyte systems. *Accounts of Chemical Research* **2013**, *46*, 1094-1103.
8. Staaf, L.G.H.; Lundgren, P.; Enoksson, P., Present and future supercapacitor carbon electrode materials for improved energy storage used in intelligent wireless sensor systems. *Nano Energy* **2014**, *9*, 128-141.
9. Wu, Z.-K.; Lin, Z.; Li, L.; Song, B.; Moon, K.-s.; Bai, S.-L.; Wong, C.-P., Flexible micro-supercapacitor based on in-situ assembled graphene on metal template at room temperature. *Nano Energy* **2014**, *10*, 222-228.
10. Miller, J.R.; Outlaw, R.A.; Holloway, B.C., Graphene double-layer capacitor with ac line-filtering performance. *Science* **2010**, *329*, 1637-1639.

11. Yang, P.; Mai, W., Flexible solid-state electrochemical supercapacitors. *Nano Energy* **2014**, *8*, 274-290.
12. El-Kady, M.F.; Strong, V.; Dubin, S.; Kaner, R.B., Laser scribing of high-performance and flexible graphene-based electrochemical capacitors. *Science* **2012**, *335*, 1326-1330.
13. Yang, X.; Zhu, J.; Qiu, L.; Li, D., Bioinspired effective prevention of restacking in multilayered graphene films: Towards the next generation of high-performance supercapacitors. *Adv. Mater.* **2011**, *23*, 2833-2838.
14. Cheng, Y.; Lu, S.; Zhang, H.; Varanasi, C.V.; Liu, J., Synergistic effects from graphene and carbon nanotubes enable flexible and robust electrodes for high-performance supercapacitors. *Nano Letters* **2012**, *12*, 4206-4211.
15. Sheng, K.; Sun, Y.; Li, C.; Yuan, W.; Shi, G., Ultrahigh-rate supercapacitors based on eletrochemically reduced graphene oxide for ac line-filtering. *Sci. Rep.* **2012**, *2*, 247.
16. Cai, M.; Outlaw, R.A.; Quinlan, R.A.; Premathilake, D.; Butler, S.M.; Miller, J.R., Fast response, vertically oriented graphene nanosheet electric double layer capacitors synthesized from c2h2. *ACS Nano* **2014**, *8*, 5873-5882.
17. Gogotsi, Y.; Simon, P., True performance metrics in electrochemical energy storage. *Science* **2011**, *334*, 917-918.
18. Yoon, Y.; Lee, K.; Kwon, S.; Seo, S.; Yoo, H.; Kim, S.; Shin, Y.; Park, Y.; Kim, D.; Choi, J.-Y.*, et al.*, Vertical alignments of graphene sheets spatially and densely piled for fast ion diffusion in compact supercapacitors. *ACS Nano* **2014**, *8*, 4580-4590.
19. Zhou, H.H.; Han, G.Y.; Xiao, Y.M.; Chang, Y.Z.; Zhai, H.J., Facile preparation of polypyrrole/graphene oxide nanocomposites with large areal capacitance using electrochemical codeposition for supercapacitors. *Journal of Power Sources* **2014**, *263*, 259-267.
20. Maiti, U.N.; Lim, J.; Lee, K.E.; Lee, W.J.; Kim, S.O., Three-dimensional shape engineered, interfacial gelation of reduced graphene oxide for high rate, large capacity supercapacitors. *Adv. Mater.* **2014**, *26*, 615-619.
21. Hahm, M.G.; Leela Mohana Reddy, A.; Cole, D.P.; Rivera, M.; Vento, J.A.; Nam, J.; Jung, H.Y.; Kim, Y.L.; Narayanan, N.T.; Hashim, D.P.*, et al.*, Carbon nanotube - nanocup hybrid structures for high power supercapacitor applications. *Nano Letters* **2012**, *12*, 5616-5621.

22. Dyatkin, B.; Presser, V.; Heon, M.; Lukatskaya, M.R.; Beidaghi, M.; Gogotsi, Y., Development of a green supercapacitor composed entirely of environmentally friendly materials. *ChemSusChem* **2013**, *6*, 2269-2280.
23. EPA Green chemistry's twelve principles. http://www2.epa.gov/green-chemistry/basics-green-chemistry#twelve (October) ,
24. Seo, D.H.; Han, Z.J.; Kumar, S.; Ostrikov, K., Structure-controlled, vertical graphene-based, binder-free electrodes from plasma-reformed butter enhance supercapacitor performance. *Advanced Energy Materials* **2013**, *3*, 1316-1323.
25. Seo, D.H.; Rider, A.E.; Han, Z.J.; Kumar, S.; Ostrikov, K., Plasma break-down and re-build: Same functional vertical graphenes from diverse natural precursors. *Adv. Mater.* **2013**, *25*, 5638-5642.
26. Seo, D.H.; Yick, S.; Han, Z.J.; Fang, J.H.; Ostrikov, K., Synergistic fusion of vertical graphene nanosheets and carbon nanotubes for high-performance supercapacitor electrodes. *ChemSusChem* **2014**, *7*, 2317-2324.
27. Kapoor, R.; Metzger, L.E., Process cheese: Scientific and technological aspects | a review. *Comprehensive Reviews in Food Science and Food Safety* **2008**, *7*, 194-214.
28. Bradley, R.L.V., Margaret A., Determination of moisture in cheese and cheese products. *Journal of AOAC International* **2001**, *84*, 570-592.
29. Brighenti, M.; Govindasamy-Lucey, S.; Lim, K.; Nelson, K.; Lucey, J.A., Characterization of the rheological, textural, and sensory properties of samples of commercial us cream cheese with different fat contents. *Journal of Dairy Science* **2008**, *91*, 4501-4517.
30. Lespade, P.; Al-Jishi, R.; Dresselhaus, M.S., Model for raman scattering from graphitized carbons. *Carbon* **1982**, *20*, 427.
31. Wang, Y.; Alsmeyer, D.C.; McCreery, R.L., Raman spectroscopy of carbon materials: Structural basis of observed spectra. *Chemical Materials* **1990**, *2*, 557.
32. Cuesta, A.; Dhamelincourt, P.; Laureyns, J.; Martinez-Alonso, A.; Tascon, J.M.D., Comparative performance of x-ray diffraction and raman microprobe techniques for the study of carbon materials. *Journal of Materials Chemistry* **1998**, *8*, 2875.
33. Niyogi, S.; Bekyarova, E.; Itkis, M.E.; Zhang, H.; Shepperd, K.; Hicks, J.; Sprinkle, M.; Berger, C.; Lau, C.N.; de Heer, W.A.*, et al.*, Spectroscopy of covalently functionalized graphene. *Nano Letters* **2011**, *10*, 4061.

34. Wu, W.; Yu, Q.K.; Peng, P.; Liu, Z.H.; Bao, J.M.; Pei, S.S., Control of thickness uniformity and grain size in graphene films for transparent conductive electrodes. *Nanotechnology* **2012**, *23*.
35. Seo, D.H.; Kumar, S.; Ostrikov, K., Thinning vertical graphenes, tuning electrical response: From semiconducting to metallic. *Journal of Materials Chemistry* **2011**, *21*, 16339-16343.
36. Kim, D.; Han, J.Y.; Lee, D.; Lee, Y.; Jeon, D.Y., Facile conversion of a cellulose acetate laminate film to graphene by a lamination process and post-annealing. *Journal of Materials Chemistry* **2012**, *22*, 20026-20031.
37. Park, M.H.; Kim, T.H.; Yang, C.W., Thickness contrast of few-layered graphene in sem. *Surface and Interface Analysis* **2012**, *44*, 1538-1541.
38. Datsyuk, V.; Kalyva, M.; Papagelis, K.; Parthenios, J.; Tasis, D.; Siokou, A.; Kallitsis, I.; Galiotis, C., Chemical oxidation of multiwalled carbon nanotubes. *Carbon* **2008**, *46*, 833-840.
39. Yick, S.; Han, Z.J.; Ostrikov, K., Atmospheric microplasma-functionalized 3d microfluidic strips within dense carbon nanotube arrays confine au nanodots for sers sensing. *Chemical Communications* **2013**, *49*, 2861-2863.
40. Wang, X.; Xia, T.; Ntim, S.A.; Ji, Z.; George, S.; Meng, H.; Zhang, H.; Castranova, V.; Mitra, S.; Nel, A.E., Quantitative techniques for assessing and controlling the dispersion and biological effects of multiwalled carbon nanotubes in mammalian tissue culture cells. *ACS Nano* **2010**, *4*, 7241-7252.
41. Qi, J.L.; Wang, X.; Lin, J.H.; Zhang, F.; Feng, J.C.; Fei, W.-D., Vertically oriented few-layer graphene-nanocup hybrid structured electrodes for high-performance supercapacitors. *Journal of Materials Chemistry A* **2015**, *3*, 12396-12403.
42. Zheng, Z.; Zhang, X.; Pei, F.; Dai, Y.; Fang, X.; Wang, T.; Zheng, N., Hierarchical porous carbon microrods composed of vertically aligned graphene-like nanosheets for li-ion batteries. *Journal of Materials Chemistry A* **2015**, *3*, 19800-19806.
43. Taberna, P.L.; Simon, P.; Fauvarque, J.F., Electrochemical characteristics and impedance spectroscopy studies of carbon-carbon supercapacitors. *Journal of the Electrochemical Society* **2003**, *150*, A292-A300.
44. Stoller, M.D.; Ruoff, R.S., Best practice methods for determining an electrode material's performance for ultracapacitors. *Energy & Environmental Science* **2010**, *3*, 1294-1301.

45. Chen, T.; Xue, Y.H.; Roy, A.K.; Dai, L.M., Transparent and stretchable high-performance supercapacitors based on wrinkled graphene electrodes. *ACS Nano* **2014**, *8*, 1039-1046.
46. Zhang, D.H.; Miao, M.H.; Niu, H.T.; Wei, Z.X., Core-spun carbon nanotube yarn supercapacitors for wearable electronic textiles. *ACS Nano* **2014**, *8*, 4571-4579.
47. Bai, Y.; Du, M.; Chang, J.; Sun, J.; Gao, L., Supercapacitors with high capacitance based on reduced graphene oxide/carbon nanotubes/nio composite electrodes. *Journal of Materials Chemistry A* **2014**, *2*, 3834-3840.
48. Yu, D.S.; Goh, K.; Wang, H.; Wei, L.; Jiang, W.C.; Zhang, Q.; Dai, L.M.; Chen, Y., Scalable synthesis of hierarchically structured carbon nanotube-graphene fibres for capacitive energy storage. *Nature Nanotechnology* **2014**, *9*, 555-562.
49. Salunkhe, R.R.; Hsu, S.H.; Wu, K.C.W.; Yamauchi, Y., Large-scale synthesis of reduced graphene oxides with uniformly coated polyaniline for supercapacitor applications. *ChemSusChem* **2014**, *7*, 1551-1556.
50. Peng, C.X.; Wen, Z.B.; Qin, Y.; Schmidt-Mende, L.; Li, C.Z.; Yang, S.H.; Shi, D.L.; Yang, J.H., Three-dimensional graphitized carbon nanovesicles for high- performance supercapacitors based on ionic liquids. *ChemSusChem* **2014**, *7*, 777-784.
51. Puthusseri, D.; Aravindan, V.; Madhavi, S.; Ogale, S., 3d micro-porous conducting carbon beehive by single step polymer carbonization for high performance supercapacitors: The magic of in situ porogen formation. *Energy & Environmental Science* **2014**, *7*, 728-735.
52. Johnson, M.E.; Kapoor, R.; McMahon, D.J.; McCoy, D.R.; Narasimmon, R.G., Reduction of sodium and fat levels in natural and processed cheeses: Scientific and technological aspects. *Comprehensive Reviews in Food Science and Food Safety* **2009**, *8*, 252-268.
53. Ostrikov, K.; Neyts, E.C.; Meyyappan, M., Plasma nanoscience: From nano-solids in plasmas to nano-plasmas in solids. *Advances in Physics* **2013**, *62*, 113-224.

Supporting Information for:

Single-Step, Plasma-Enabled Reforming of Natural Precursors into Vertical Graphene Electrodes with High Areal Capacitance

Dong Han Seo,[†,‡,⊥] Samuel Yick,[†,‡,⊥] Shafique Pineda,[†,‡] Dawei Su,[‖] Guoxiu Wang,[‖] Zhao Jun Han,[†] and Kostya (Ken) Ostrikov[†,‡,§,*]

[⊥]These authors contributed equally.

[†]Plasma Nanoscience, Industrial Innovation Program, CSIRO Manufacturing Flagship, Lindfield, New South Wales 2070, Australia

[‡]School of Physics, The University of Sydney, New South Wales 2006, Australia

[‖]School of Chemistry and Forensic Science, University of Technology Sydney, New South Wales 2007, Australia

[§]School of Chemistry, Physics and Mechanical Engineering, Queensland University of Technology, Brisbane, Queensland 4000, Australia

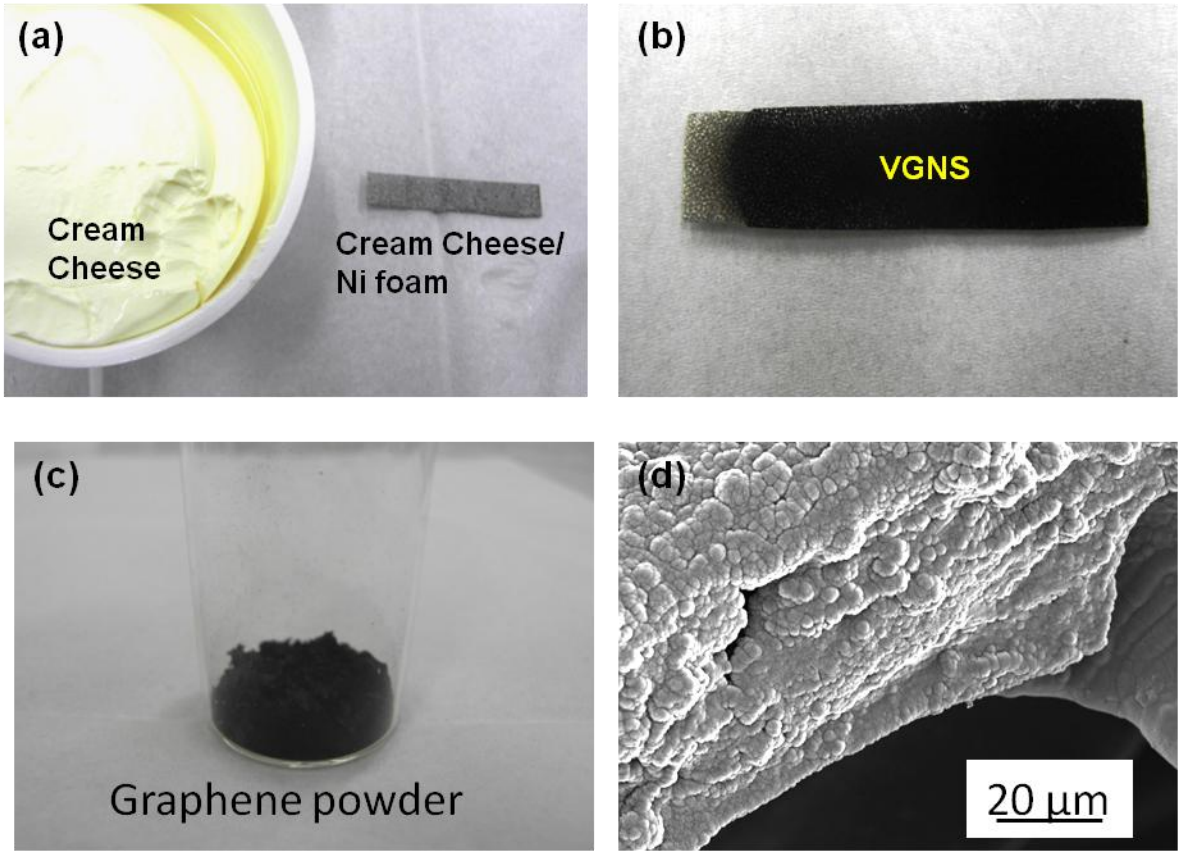

Supplementary Figure 1 | Photographs of the precursor and VGNS electrodes transformed by plasma-based process (a-c) and a typical SEM image of VGNS on the Ni foam substrate (d).

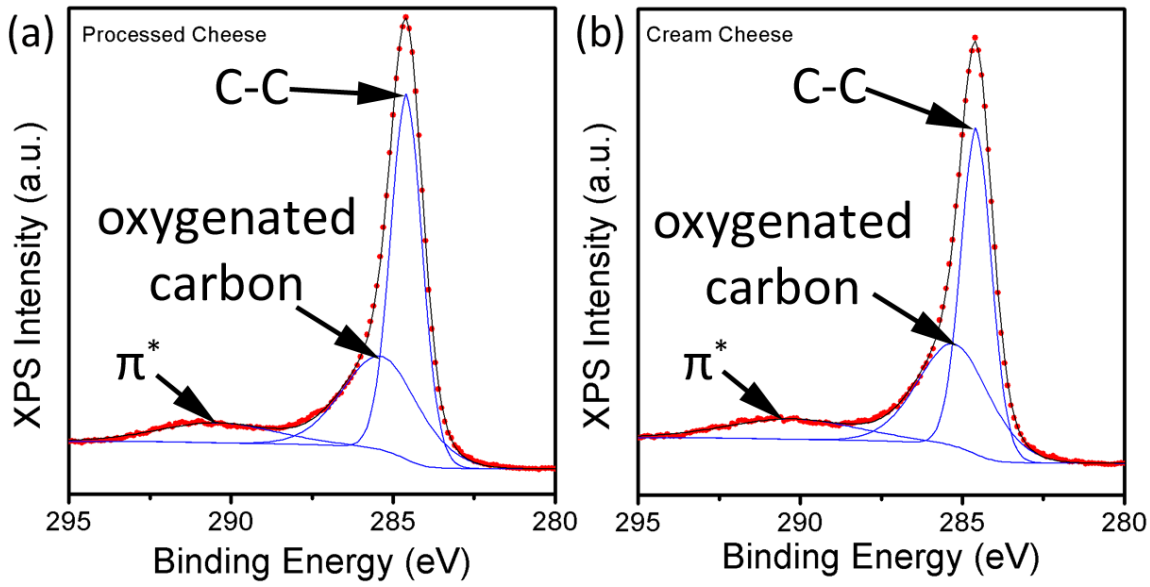

Supplementary Figure 2 | The deconvoluted C1s peaks of VGNS derived from processed cheese (a) and cream cheese (b).

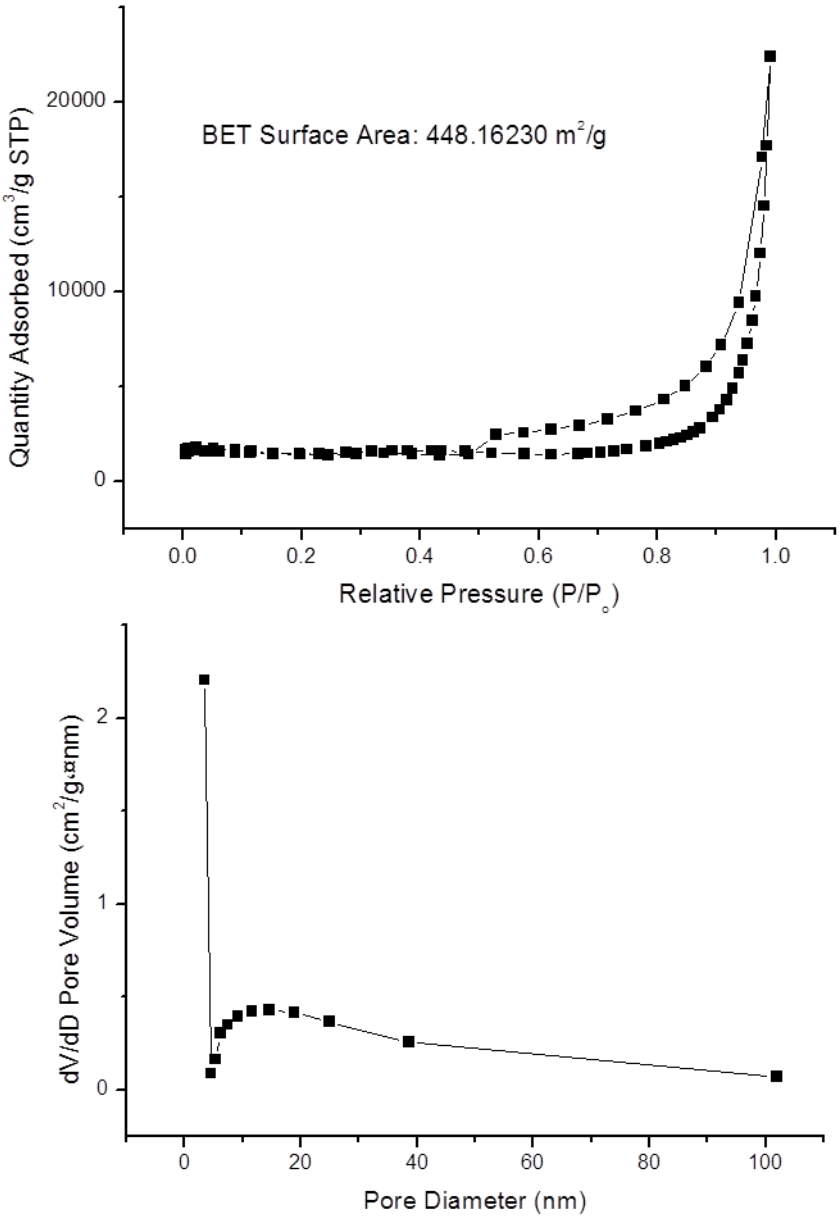

Supplementary Figure 3 | BET characterizations of VGNS. (**a**) N_2 adsorption/desorption isotherm of VGNS derived from processed cheese at 77 K . The BET surface area is ~448 m^2/g. (**b**) Pore size distribution of VGNS derived from processed cheese.

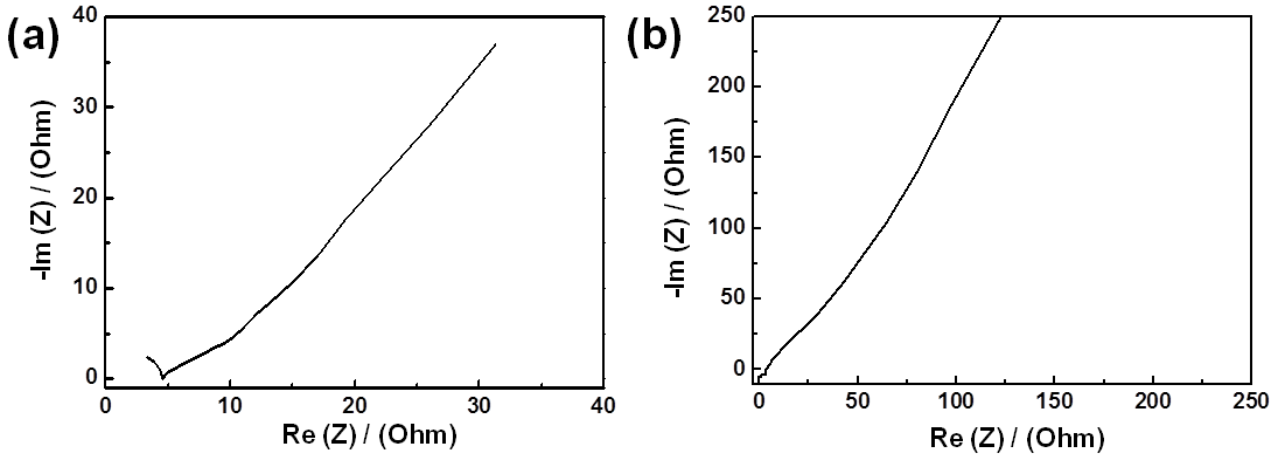

Supplementary Figure 4 | EIS spectra of the electrodes derived from processed (a) and cream (b) cheeses.

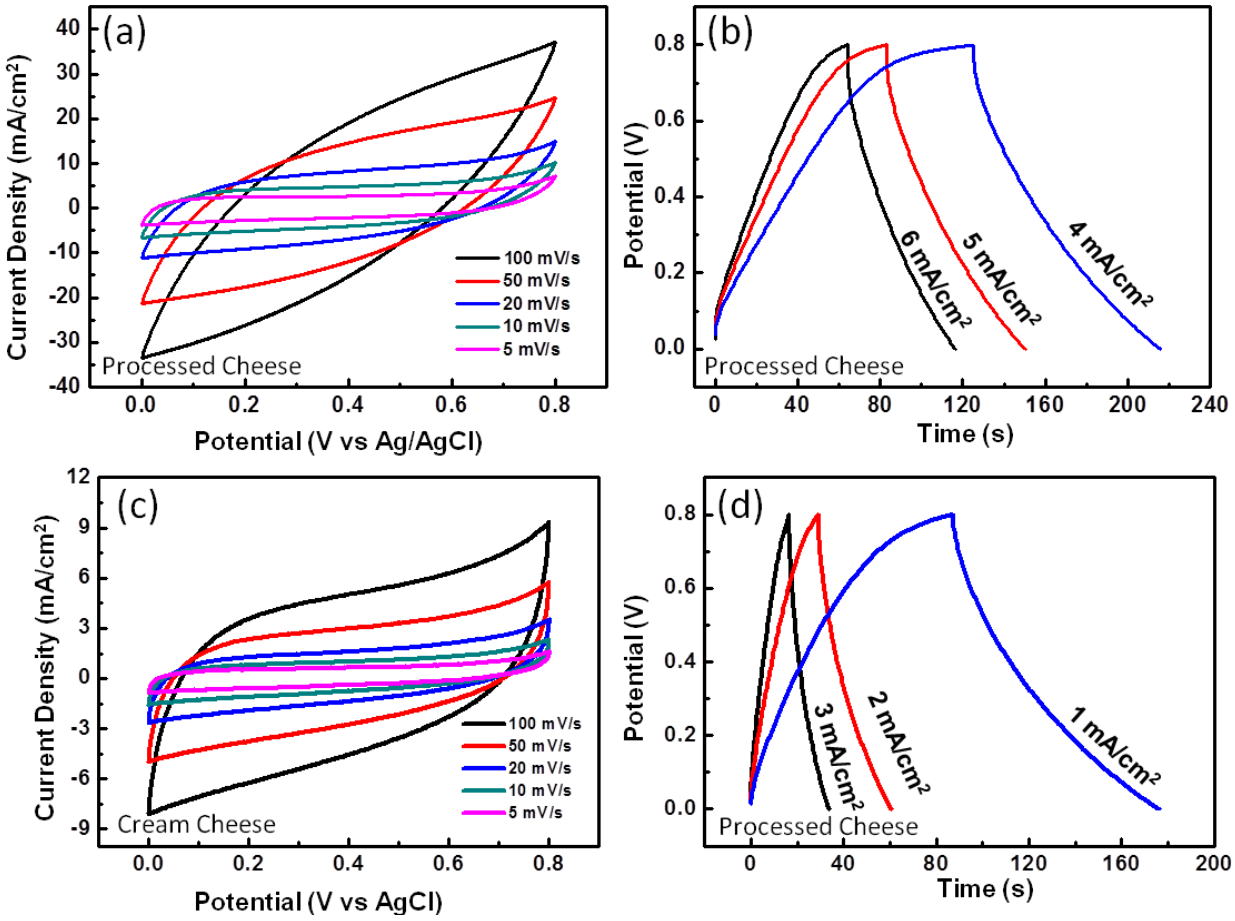

Supplementary Figure 5 | Cyclic voltammetry (CV) curves (a, c) and galvanostatic charge-discharge curves (b, d) obtained from both VGNS electrodes measured in the three-electrode setup.

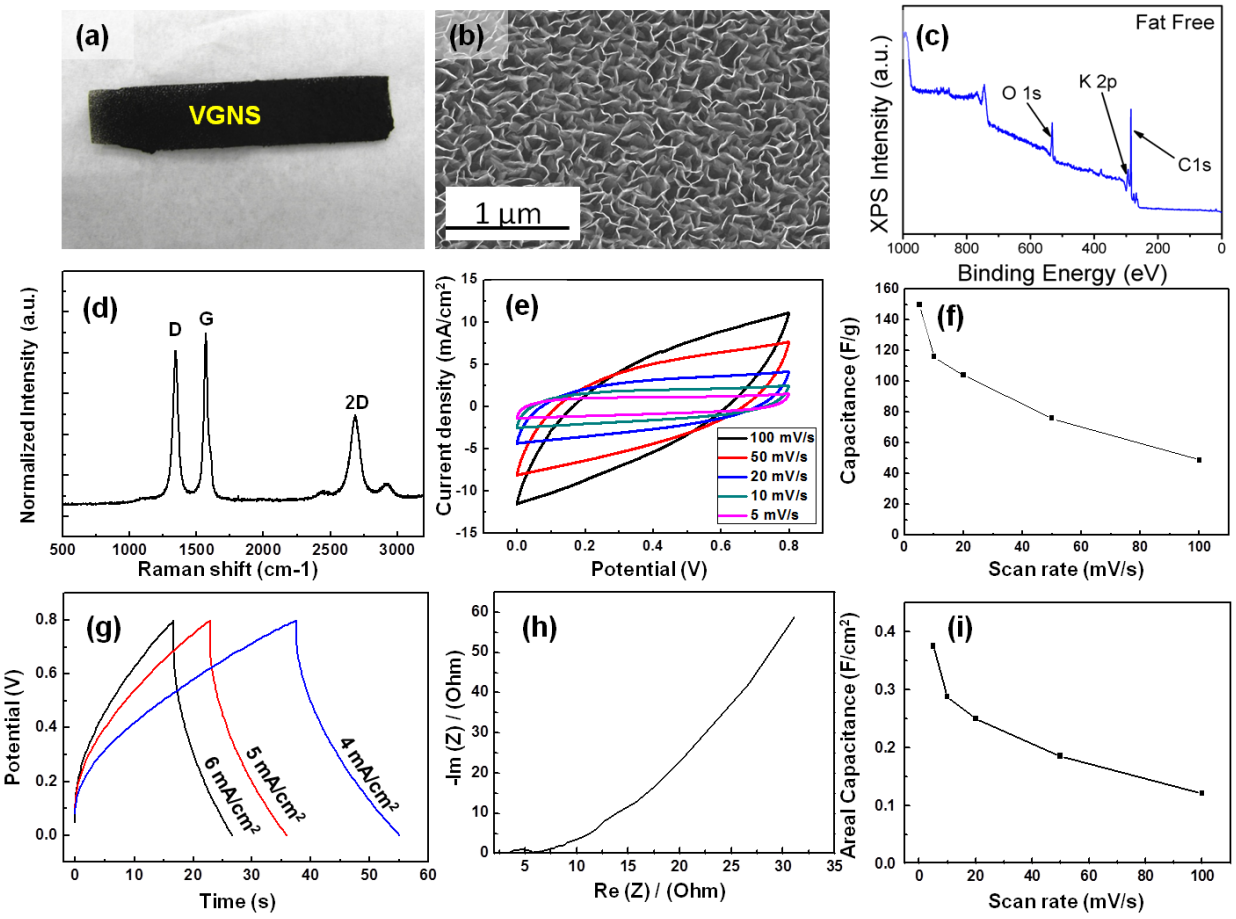

Supplementary Figure 6 | VGNS derived from fat-reduced processed cheese and its electrochemical performance. Optical photo (**a**), SEM image (**b**), XPS (**c**), and Raman spectrum (**d**) of VGNS on Ni foam. Its electrochemical performance is measured by cyclic voltammetry (**e**), C_s at different scan rates (**f**), galvanostatic charge/discharge (**g**), EIS (**h**), and areal capacitance at different scan rates (**i**).

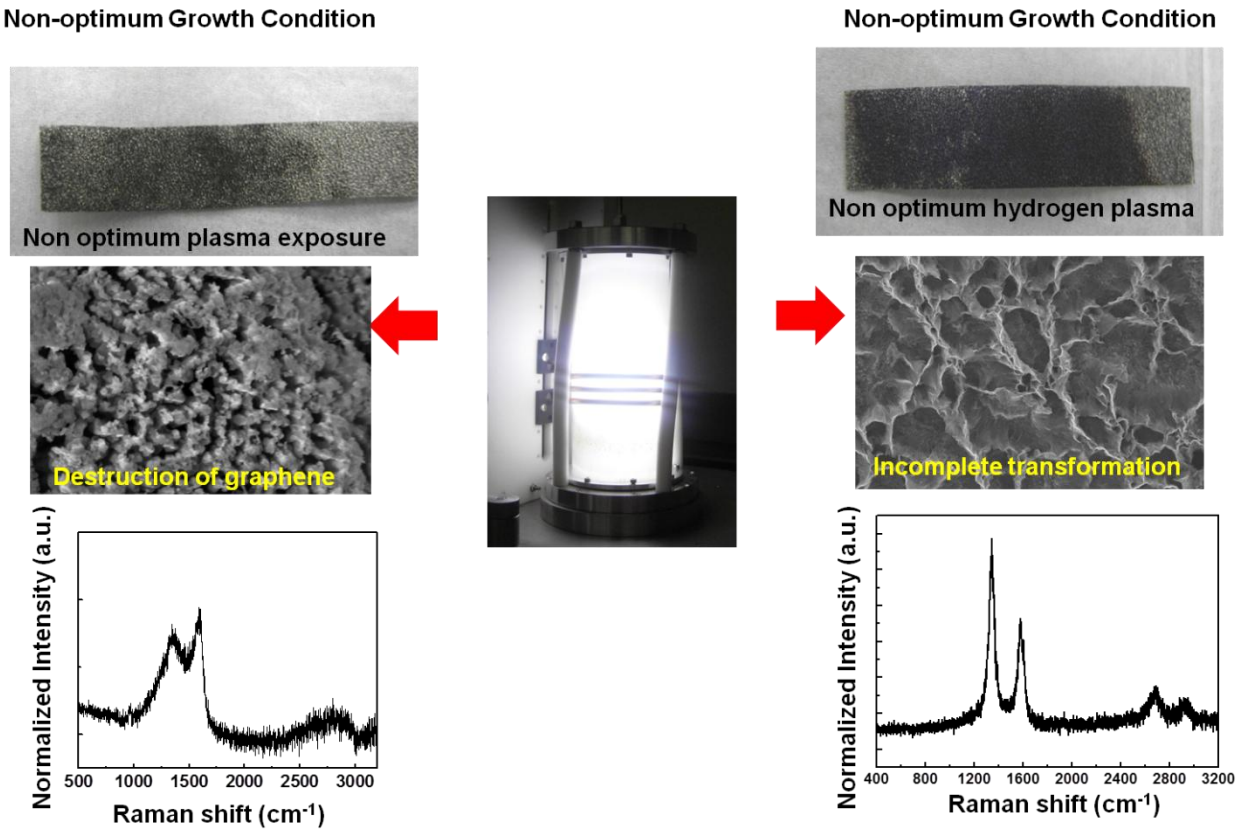

Supplementary Figure 7 | The results of non-optimal growth conditions. On the left the effects of elevated hydrogen concentration is shown, whereas the right demonstrates the effect of prolonged plasma treatment.

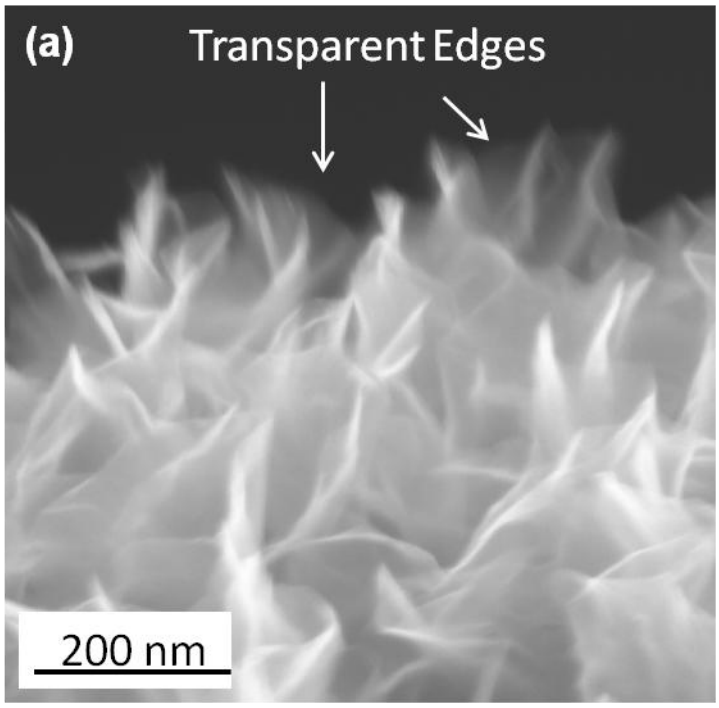

Supplementary Figure 8 | High resolution SEM image of VGNS derived from processed cheese showing highly transparent graphene sheets which are usually observed in few-layer graphenes.

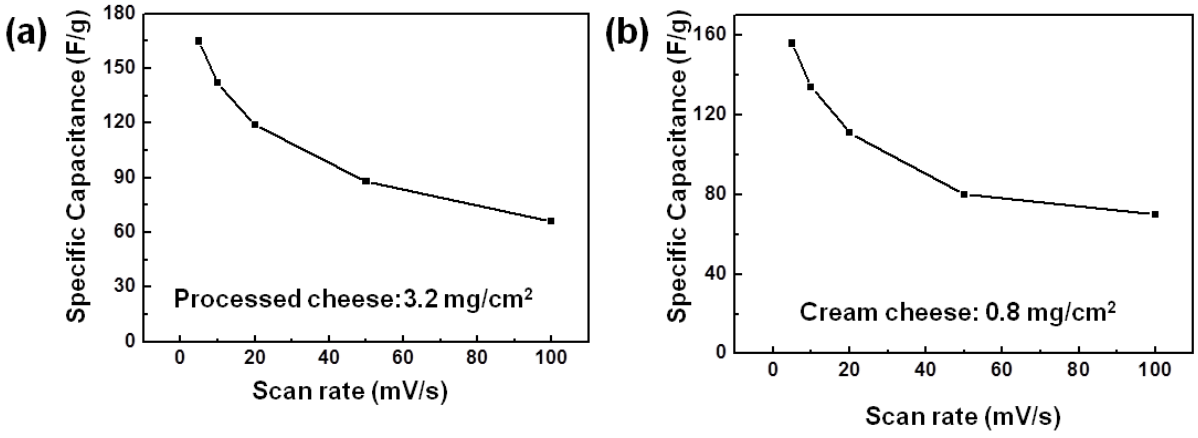

Supplementary Figure 9 | Specific capacitance of cheese-derived VGNS as calculated from the three-electrode measurements.

Supplementary Table 1 | Comparison of supercapacitor performance of graphene and carbon based nanostructures with high mass loadings.

Material	Synthesis method	Areal capacitance (mF/cm^2)	Specific capacitance (F/g)	Mass loading (mg/cm^2)	Stability	Ref
VGNS	Single-step PECVD	460	156	3.2	94% (4,000 cycles)	This work
		0.265	n/a	n/a	n/a	[S1]
		n/a	180	0.45	n/a	[S2]
Graphene / RGO/ GO	Chemical processing	152	n/a	n/a	96.4% (5,000 cycles)	[S3]
		33.8	160	0.44	97.8% (5,000 cycles)	[S4]
		n/a	286	0.5	94% (2,000 cycles)	[S5]
	CVD	0.006	7.6	n/a	n/a	[S6]
	Thermal processing	n/a	45	0.31	98 % (10,000 cycles)	[S7]
CNT	CVD	1.0	n/a	n/a	94% (1,000 cycles)	[S8]
	CVD, mechanical and chemical processing	52	86.2	n/a	98% (1,000 cycles)	[S9]
AC	Chemical processing	n/a	98.7	5.0	n/a	[S10]
Graphene /CNT composite	Chemical processing	4.97	31.5	n/a	99% (5,000 cycles)	[S11]
		116.3	n/a	n/a	93% (10,000 cycles)	[S12]
3D porous carbon	Chemical processing	n/a	343	8.1	98% (2,000 cycles)	[S13]
	Thermal processing	n/a	254	2.0	90% (5,000 cycles)	[S14]

References

[S1] Cai, M.; Outlaw, R.A.; Quinlan, R.A.; Premathilake, D.; Butler, S.M.; Miller, J.R., Fast response, vertically oriented graphene nanosheet electric double layer capacitors synthesized from c2h2. *ACS Nano* **2014**, *8*, 5873-5882.

[S2] Bo, Z.; Zhu, W.; Ma, W.; Wen, Z.; Shuai, X.; Chen, J.; Yan, J.; Wang, Z.; Cen, K.; Feng, X., Vertically oriented graphene bridging active-layer/current-collector interface for ultrahigh rate supercapacitors. *Advanced Materials* **2013**, *25*, 5799-5806.

[S3] Zhou, H.H.; Han, G.Y.; Xiao, Y.M.; Chang, Y.Z.; Zhai, H.J., Facile preparation of polypyrrole/graphene oxide nanocomposites with large areal capacitance using electrochemical codeposition for supercapacitors. *Journal of Power Sources* **2014**, *263*, 259-267.

[S4] Maiti, U.N.; Lim, J.; Lee, K.E.; Lee, W.J.; Kim, S.O., Three-dimensional shape engineered, interfacial gelation of reduced graphene oxide for high rate, large capacity supercapacitors. *Advanced Materials* **2014**, *26*, 615-619.

[S5] Salunkhe, R.R.; Hsu, S.H.; Wu, K.C.W.; Yamauchi, Y., Large-scale synthesis of reduced graphene oxides with uniformly coated polyaniline for supercapacitor applications. *ChemSusChem* **2014**, *7*, 1551-1556.

[S6] Chen, T.; Xue, Y.H.; Roy, A.K.; Dai, L.M., Transparent and stretchable high-performance supercapacitors based on wrinkled graphene electrodes. *ACS Nano* **2014**, *8*, 1039-1046.

[S7] Han, X.G.; Funk, M.R.; Shen, F.; Chen, Y.C.; Li, Y.Y.; Campbell, C.J.; Dai, J.Q.; Yang, X.F.; Kim, J.W.; Liao, Y.L.*, et al.*, Scalable holey graphene synthesis and dense electrode fabrication toward high-performance ultracapacitors. *ACS Nano* **2014**, *8*, 8255-8265.

[S8] Hahm, M.G.; Leela Mohana Reddy, A.; Cole, D.P.; Rivera, M.; Vento, J.A.; Nam, J.; Jung, H.Y.; Kim, Y.L.; Narayanan, N.T.; Hashim, D.P.*, et al.*, Carbon nanotube - nanocup hybrid structures for high power supercapacitor applications. *Nano Letters* **2012**, *12*, 5616-5621.

[S9] Zhang, D.H.; Miao, M.H.; Niu, H.T.; Wei, Z.X., Core-spun carbon nanotube yarn supercapacitors for wearable electronic textiles. *ACS Nano* **2014**, *8*, 4571-4579.

[S10] Dyatkin, B.; Presser, V.; Heon, M.; Lukatskaya, M.R.; Beidaghi, M.; Gogotsi, Y., Development of a green supercapacitor composed entirely of environmentally friendly materials. *ChemSusChem* **2013**, *6*, 2269-2280.

[S11] Sun, H.; You, X.; Deng, J.E.; Chen, X.L.; Yang, Z.B.; Ren, J.; Peng, H.S., Novel graphene/carbon nanotube composite fibers for efficient wire-shaped miniature energy devices. *Advanced Materials* **2014**, *26*, 2868-2873.

[S12] Yu, D.S.; Goh, K.; Wang, H.; Wei, L.; Jiang, W.C.; Zhang, Q.; Dai, L.M.; Chen, Y., Scalable synthesis of hierarchically structured carbon nanotube-graphene fibres for capacitive energy storage. *Nature Nanotechnology* **2014**, *9*, 555-562.

[S13] Peng, C.X.; Wen, Z.B.; Qin, Y.; Schmidt-Mende, L.; Li, C.Z.; Yang, S.H.; Shi, D.L.; Yang, J.H., Three-dimensional graphitized carbon nanovesicles for high- performance supercapacitors based on ionic liquids. *ChemSusChem* **2014**, *7*, 777-784.

[S14] Puthusseri, D.; Aravindan, V.; Madhavi, S.; Ogale, S., 3d micro-porous conducting carbon beehive by single step polymer carbonization for high performance supercapacitors: The magic of in situ porogen formation. *Energy & Environmental Science* **2014**, *7*, 728-735.

5

Outlook and Conclusion

"You're invited to come to see the Earth turn, tomorrow, from three to five, at Meridian Hall of the Paris Observatory."

– Léon Foucault, 1851.

Graphene can be classified into two forms – large-area thin films and small flakes (powder). Indeed, the properties and functionalities of graphene are dependent on its morphology. Thus, graphene is promising to enable advancements in diverse areas, including but not limited to, preventative healthcare, energy storage devices, and clean water technologies. However, major technological challenges arise in the sustainable fabrication and its practical integration as active functional materials. In this thesis, we have designed, developed and implemented thermal- and plasma-based techniques to enable, enhance, and tailor the synthesis of hierarchical graphene nanostructures, for applications in bioelectronics and supercapacitors. Below, future directions of research are proposed based on the developments presented in this thesis.

5.1. Outlook: Graphene Synthesis

First and foremost, we demonstrated the reforming of diverse natural carbon-containing precursors into homogeneous, morphology-controlled graphene nanostructures by thermal- and plasma-based techniques. This enables numerous merits including reduced production costs, resource-efficient and green processing, and sustainable elemental lifecycles. For instance, the ambient-air thermal technique enables a single-step reforming of natural precursors (*e.g.*, soybean oil) into homogeneous graphene films, and avoids the use of resource-consuming ingredients such as purified gases and

a highly-controlled vacuum environment (necessary in thermal CVD). Further, non-equilibrium plasma processes allow a low-temperature (200 ^{o}C), rapid (<10 mins) and controlled synthesis of graphene nanostructures with unique open, interconnected morphologies, demonstrating good electrochemical properties. These advancements surpass chemical exfoliation approaches on numerous fronts (Table 1 in Chapter 1). In particular, chemical techniques are multi-staged, and require long process durations (~3 days), involve highly concentrated acids, and produce graphene flakes with poor quality and limited controllability (*i.e.*, highly defective, prone to agglomeration, *etc.*).

These advancements are central to help reform the most common and desired of all biomasses, lingo-cellulosic materials (*i.e.*, plant matter and organic by-products). The transformation of cellulose into functional materials remains important to a future of advanced sustainable technologies. However, initial attempts remain limited to complex and energy-intensive processes which are used to produce biofuel. Indeed, as strong inter- and intra-molecular forces are present in the cellulose matrix structure, this necessitates high energies to breakdown cellulose into basic carbon building units for graphene. Further, cellulosic materials contain a high degree of oxygen. Consequently, the breakdown process may release reactive oxygen species which can detrimentally affect the graphene formation. In particular, this may result in uncontrolled etching, and the formation of lattice defects and amorphous carbon species.

To this end, a combination of thermal- and plasma-based approaches is promising to enable the transformation of cellulosic biomasses into functional hierarchical nanomaterials. The ambient-air (thermal) technique is shown to promote controlled reaction pathways which effectively utilize oxygen (present in the ambient air), in order to facilitate the formation of crystalline carbon nanostructures at elevated temperatures. This enables the transformation of renewable precursors into homogeneous graphene films in an otherwise destructive (*i.e.*, oxygen-rich) environment. Further, reactive plasma techniques are demonstrated to vastly accelerate and catalyze the growth of graphene nanostructures. The plasma processes are shown to enable low-temperature and rapid synthesis of graphene, with controlled multi-dimensional morphology and versatile physicochemical properties. Therefore, by designing an approach which

uniquely combines the characteristics of thermal (ambient-air) and reactive plasma processes, we may enable the reforming of cellulosic biomasses into hierarchical functional nanomaterials.

5.2. Outlook: Graphene for bioelectronics

Subsequently, we demonstrated plasma-based approaches for the synthesis of graphene micro-islands (GMs) which addresses notable challenges of functional nanomaterials in bioelectronics. Here, low-temperature reactive plasma enabled the synthesis of homoegenous GMs at 200 ^{o}C, and its water-mediated transfer onto arbitrary substrates. The GMs were realized to enable a biocompatible interface, which demonstrated sensitive and selective label-free biosensing through its controlled physicochemical properties. Future avenues of research in bioelectronics directed to address fundamental aspects such as the kinetics of binding and the diffusion/transport of species towards the sensor surface are desired. Importantly, more systematic investigations are required to evaluate the realistic performance limits of such sensors under practical and clinical conditions. An important challenge from an application standpoint includes the controlled engineering and optimization of such graphene-based devices to enable multiplexed detection. This is attractive for medical diagnostics, as often, more than one analyte species may serve as biomarkers for a single disease. Further, for the widespread adoption and application of graphene-based sensors, it requires improvements in device reproducibility, stability, and the reduction of signal drift.

5.3. Outlook: Graphene for Energy Storage Devices

Finally, we demonstrated plasma-based techniques for the synthesis of vertically-oriented graphene nanosheets (VGNS), which addresses key challenges in energy storage devices. Here, reactive plasmas enable a single step growth of VGNS and its direct integration as active materials for supercapacitor electrodes. The VGNS feature a high surface area, an open and interconnected morphology of graphene nanosheets, thin reactive edges, and hence, attractive electrochemical properties for energy storage. Also, we demonstrate control in mass loading of VGNS by the plasma process (*i.e.*, plasma-precursor matter interactions), while retaining good energy storage

performances. Indeed, graphene can be used as active or support materials in energy storage. From an application perspective, VGNS requires significantly higher mass loadings (*i.e.*, comparable to activated carbon) in order to be utilized in practical supercapacitor devices. Therefore in future developments, engineered precursor materials should be investigated, together with plasma-matter interactions, to enhance mass loadings of VGNS as active materials. On the other hand, the morphological and hierarchical structure of VGNS facilitates its effective role as a support material. In particular, future developments should focus on the utilization and design of VGNS, to host heterogeneous hierarchical nanomaterials, metal oxide crystals, and functional groups, to enhance charge storage capabilities. The large surface area, combined with reactive edges, and open morphology of VGNS, may allow for homogeneous integration of such active materials in large quantity, while retaining good stability. This is promising to enable the next-generation of supercapacitor devices with high energy and powder densities, high specific and areal capacitance, fast rate capability, and long-term charge storage stability.

5.4. Concluding Statement

Indeed, the field of graphene research has progressed tremendously over the last decade. From isolated micrometer-sized flakes of graphene, we are now at the verge of practical graphene-enabled devices. Importantly, new insights and developments in nanoassembly processes have enabled unprecedented control in the morphology, functionality, and physicochemical properties of carbon nanostructures.

In this thesis, new thermal- and plasma-enabled techniques have been developed to reform low-value, minimally-processed natural precursors into high-quality, multifunctional graphene nanostructures with controllable properties. In the thermal approach, natural precursors were transformed into homogeneous, large-area films of graphene in an ambient-air environment. Unlike conventional CVD, this technique is single-stepped, rapid, and does not require purified gases or vacuum operation. The thermally dissociated precursor fragments were found to promote 1) consumption of reactive oxygen species in the ambient-air, 2) a carbon-surplus environment, and the 3) formation of water vapor by-products that help maintain the catalytic ability of the growth

substrate, enabling the synthesis of graphene films in an otherwise destructive environment.

In the plasma approaches, this enabled the single-step, rapid and controlled growth of GMs at low temperatures (200 ^{o}C). These GMs feature an interconnected morphology, reactive edges, and a high surface area. The plasma synthesis also enabled a water-assisted transfer of GMs onto arbitrary substrates. This allowed the GMs to be integrated as functional materials to realize a sensitive and selective genosensor, and as a biocompatible coating for bioengineering applications. Further, the plasma process was developed to enable a single-step, low-temperature, controlled growth and direct integration of VGNS as an electrode material for supercapacitor application. Diverse natural precursors were reformed into homogeneous VGNS. The VGNS feature a high surface area, an open morphology, with interconnected arrays of vertically-oriented graphene sheets and reactive edges, which facilitate its excellent performance for supercapacitor applications.

To this end, this thesis compounds a set of thermal- and plasma-based techniques which have been designed, developed, and implemented, to realize sustainable methodologies for nanoassembly. Moreover, these techniques may be adapted, tailored, and broadly incorporated, to effectively harness the unique functional properties of graphene, and a host of other hierarchical and heterogeneous advanced nanomaterials (*i.e.*, 2D topological materials and van der Waals heterostructures). Consequently, these concepts may pave the emergence of sustainable nanotechnologies in renewable energy, clean water, and personalized healthcare, which promise to deliver positive and widespread socioeconomic impacts.